Dissertation

Performance and limitations of high granularity single photon processing X-ray imaging detectors

ausgeführt zum Zwecke der Erlangung des akademischen Grades eines Doktors der technischen Wissenschaften unter der Leitung von

Univ. Prof. Dr. H. Aiginger

E141

Atominstitut der Österreichsichen Universitäten

in Zusammenarbeit mit

Dr. Erik Heijne

Europäischen Zentrum für Elementarteilchenphysik CERN

CH-1211 Genf 23

eingereicht an der Technischen Universität Wien

Fakultät für Physik

von

DI Lukas Tlustos

8527411

Wien

Diese Arbeit wurde unterstützt vom Österreichsichen Bundesministerium für Bildung, Wissenschaft und Kultur.

Genf, im März 2005

CERN-THESIS-2005-032
19.04.2005

Contents

Introduction **1**

1 Semiconductor Physics **5**
1.1 Crystal Structure, Band Structure 5
1.2 Intrinsic and extrinsic Semiconductors 8
1.3 Energy deposition by ionising radiation 9
1.3.1 Photon interactions 10
1.3.2 Charged particle interaction 16
1.4 Carrier Transport 18
1.4.1 Diffusion 18
1.4.2 Drift 18
1.4.3 Current density equations 20
1.5 p-n junction diode in reverse bias 21

2 Performance measures for imaging systems **25**
2.1 Resolution, Contrast and MTF 25
2.2 Noise Transfer, SNR and NPS 27
2.3 Combined Measures, NEQ and DQE 28

3 Semiconductor Imaging Detector Concepts **31**
3.1 Applications and requirements 31
3.2 Charge Collection in a pixellated detector 32
3.3 Direct and indirect detection 34
3.4 Integrating detector systems versus single event pulse processing 36
3.5 Detector technologies 37
3.5.1 CCD 37
3.5.2 Flat Panel Imager 37
3.5.3 CMOS hybrid pixel detector 38

4 The Medipix Project **39**
4.1 Medipix1 39
4.1.1 Medipix1 chip 39
4.1.1.1 Pixel cell 42
4.1.1.2 Periphery 43
4.1.1.3 Supply and bias voltages 43
4.1.2 External read-out electronics 44

4.1.3 Threshold Adjustment procedure . . . 44
4.2 Medipix2 . . . 47
4.2.1 Medipix2 chip . . . 47
4.2.1.1 Pixel Cell . . . 50
4.2.1.2 Periphery . . . 50
4.2.2 External read-out electronics . . . 51
4.2.3 Threshold adjustment procedure . . . 52
4.2.3.1 Low threshold . . . 52
4.2.3.2 High threshold . . . 53

5 Detector Simulations 55
5.1 X-ray charge deposition . . . 56
5.1.1 Deposition in a thick Si sensor slab . . . 56
5.1.2 Deposition in a thin Si sensor slab . . . 57
5.1.3 Deposition in a pixellated Si sensor . . . 60
5.1.4 Other materials . . . 64
5.1.4.1 GaAs . . . 64
5.1.4.2 CdTe . . . 68
5.2 Charge transport and collection . . . 72
5.2.1 Simulation method . . . 72
5.2.2 Effects of charge collection on sensor response . . . 77
5.2.3 Effects of readout electronics on the single pixel response . . . 78
5.2.3.1 Spatial response . . . 78
5.2.3.2 Spectroscopic response . . . 80
5.2.4 Large area detector response . . . 80
5.2.4.1 Energy resolution including readout noise . . . 81
5.2.4.2 Homogeneity of the response across pixel borders . . . 82
5.2.4.3 SNR and DQE . . . 84
5.3 Charge sharing correction . . . 88
5.4 Energy weighting . . . 88
5.5 Summary . . . 92

6 Experimental Detector Performance Characterisation 95
6.1 Synchrotron beam measurements . . . 95
6.1.1 Experimental setup . . . 96
6.1.2 Energy calibration . . . 96
6.1.3 Single pixel response . . . 97
6.1.3.1 Pixel response profile and detector response homogeneity . 97
6.1.3.2 Electronic noise . . . 100
6.1.4 Pixel array response . . . 104
6.1.4.1 Threshold position and dispersion . . . 104
6.1.4.2 Energy resolution and electronic noise . . . 105
6.2 Flat-field-correction . . . 110
6.2.1 Threshold dispersion . . . 111
6.2.2 Sensor homogeneity . . . 117
6.3 MTF, NPS and DQE . . . 122

6.3.1 Experimental setup and parameters . . . 122
6.3.2 Modulation Transfer Function . . . 123
6.3.3 Noise Power Spectrum . . . 126
6.3.4 Detective Quantum Efficiency . . . 129
6.4 Imaging performance and applied dose . . . 129
6.5 Spectrocopic imaging . . . 134
6.6 Summary . . . 138

7 Conclusion and Outlook **141**
7.1 Conclusion . . . 141
7.2 Outlook . . . 144

List of figures **146**

List of tables **156**

Bibliography **159**

Acknowledgements **166**

List of acronyms

AMFPI	Active matrix flat panel imager
CCD	Charge coupled device
CCE	Charge collection efficiency
CMOS	Complementary metal oxide semiconductor
CSDA	Continuous slowing down approximation
CT	Computed tomography
DDL	Double Discriminator Logic
DQE	Detective Quantum Efficiency
ESF	Edge Spread Function
FPGA	Free Programmable Gate Array
FSR	Fast Shift Register
FZ	Float Zone
LVDS	Low voltage Differential Swing
MTF	Modulation Transfer Function
NPS	Noise Power Spectrum
NTD	Neutron Transmutation Doping
PET	Positron Emission Tomography
SACMOS	Self Aligned Complementary Metal Oxide Semiconductor
SDD	Silicon Drift Detector
TFD	Thin Film Diode
TFT	Thin Film Transistor
XRD	X-ray Diffractometry
XRF	X-ray Fluorescence

Abstract

Progress in CMOS technology and in fine pitch bump bonding has made possible the development of single photon counting detectors for X-ray imaging with pixel pitches on the order of 50 μm giving a spatial resolution which is comparable to conventional CCD and flat panel detectors. This thesis studies the interaction of X-ray photons in the energy range of 5 keV to 70 keV with various sensor materials as well as the response of the Medipix2 readout system to both monochromatic and wide spectrum X-ray sources.

Single photon processing offers the potential for spectroscopic imaging. However, this thesis demonstrates using simulations and measurements that the charge deposition and collection within the semiconductor sensor impose fundamental limits on the achievable energy resolution. In particular the diffusion of charge during collection in the sensor and the generation of fluorescence photons in heavier sensor materials contribute to the appearance of a low energy tail on the detected spectrum of an incoming beam. On the other hand, with the application of appropriate flat-field correction maps, the system operates to the Poisson limit. As the electronic noise in a pixel channel is around 100 e^- rms and typical energy thresholds are over 1000 e^- excellent quality images of low contrast objects have been produced using both intense and weak X-ray sources. The Modulation Transfer Function has been measured to be 9.1 lp/mm corresponding to the pixel aperture function. The Detective Quantum Efficiency is only limited by the sensor material used and does not change as a function of dose, highlighting the enormous potential for low dose imaging with such a system. The Medipix2 system has an upper threshold in each pixel too which allows an energy window of down to 1.4 keV FWHM to be selected and scanned in the range of 4 keV to 100 keV. First images using the energy threshold window demonstrate the potential of the technique to extract a spectral image when only a broad band source of X-rays is available.

Kurzfassung

Der rasante Fortschritt in der CMOS Technologie und in den Verbindungstechniken zwischen Halbleiterdetektor und elektronischem Auslesechip (Flip-Chip Technologie) erlauben die Entwicklung von photonenzählenden Detektorkonzepten für Anwendungen in der Röntgenbildgebung. Pixelabstände in der Größenordnung von 50 μm sind machbar und stellen eine Ortsauflösung zur Verfügung, die vergleichbar ist mit der von konventionellen CCDs und Flachbilddetektoren. Die Verarbeitung des Signals einzelner Photonen eröffnet die Möglichkeit, Detektoren für spektrale Bildgebung zu konstruieren.

Im Rahmen dieser Dissertation wurde sowohl die Wechselwirkung von Röntgenphotonen im Energiebereich von 5-70 keV mit verschiedenen Detektormaterialen untersucht, als auch das Ansprechverhalten des Medipix2 Detektorsystems auf monoenergetische und spektrale Röntgenquellen studiert. Die Simulationen und Messungen zeigen, dass die erreichbare Ortsauflösung und die Energieauflösung durch die Ladungsdeposition und die Diffusion in Halbleitersensor begrenzt sind.

Insbesondere die Diffusion während der Ladungsammlung im Sensor und die Emission charakteristischer Röntgenstrahlung in Sensormaterialien höherer Ordnungszahl führen zu einem niederenergetischen Hintergrund im detektierten Energiespektrum. Die daraus resultierenden Schwankungen in der Anzahl der registrierten Photonen können mit Hilfe geeigneter Flatfield-Korrekturen korrigiert werden. Das Bildrauschen folgt dann der Poisson Statistik. Das Rauschen einer Pixelelektronik des Medipix2 Chips ist $\sim$100 e^- rms und die untere Energieschwelle für die Detektion typischerweise $\sim$1000 e^-. Hervorragende Bildqualität wurde erzielt, sowohl bei Verwendung von Röntgenquellen hoher als auch niedriger Intensität. Die gemessene Modulations-Transfer-Funktion folgt derjenigen der Pixelapertur mit einer Ortsauflösung von 9.1 lp/mm. Die Detektor-Quanteneffizienz ist limitiert durch die Absorptionseffizienz des Sensormaterials und ist unabhängig von der Bilddosis. Die Ergebnisse zeigen das große Potential, das photonenzählende Detektoren für die Röntgenbildgebung, speziell bei niedriger Dosis, bieten.

Der Medipix2 Detektor verfügt über einen zweiten, oberen Schwellwert, der dazu genutzt werden kann, ein Energiefenster mit einer minimalen Breite von 1.4 keV FWHM zu definieren, das in einem Bereich von 4 bis 100 keV gesetzt werden kann. Erste Aufnahmen, die dieses Energiefenster verwenden, demonstrieren, dass mit Hilfe dieser Technik spektrale Information gewonnen werden kann, selbst wenn nur Röntgenquellen mit breitem Energiespektrum zur Verfügung stehen.

Introduction

Digital X-ray imaging detectors are used in a wide range of applications from materials analysis to medical imaging. In most current commercial detector systems, such as charge coupled devices (CCD) [1–4] and active matrix flat panel imagers (AMFPI) [5–7], the electrical signals generated in the detector pixels by each detected photon are integrated and the total charge deposited in each pixel is translated into an image.

Due to the requirements in high energy physics experiments to detect invidual high energy events, an alternative detection concept has been developed for particle tracking whereby a time and space coordinates are recorded for each passing particle. The big advances in sub-micron CMOS technology allowed to build large arrays of active pixel cells and to integrate sophisticated signal processing in each pixel.

This detector technology is now finding its way into other fields [8–15], such as single photon counting imaging detectors whereby a photon is counted only if it deposits sufficient energy in a pixel. This implies that when no incident photons are present the recorded image remains empty and free of noise. Two generations of such imaging devices, the Medipix1 [16] and the Medipix2 [17], have been developed by collaborations based at CERN and are beginning to be used successfully in a wide range of applications from X-ray imaging to neutron detection [18–22]. As the pixel size decreases in the quest for higher spatial resolution, charge sharing between adjacent pixels becomes a limiting factor for the detector performance. While this sets unavoidable limits in integrating detectors, in single photon processing detectors the processes involved can be studied and ways can be found to deal with the effects of charge sharing.

In this thesis the effects of charge sharing on the performance of high granularity pixel detectors is investigated by comparing simulation and measured data.

Outline

This thesis focuses on the effects of charge sharing on the performance of high granularity pixel detectors and presents the performance characterisation of the Medipix2/Si detector as well as results obtained with its predecessor, the Medipix1.

Chapter 1 gives an overview of the physics of semiconductor devices. The mechanisms involved in energy loss of photons in matter are described.

Chapter 2 summarizes the figures of merit used to measure the performance of imaging systems, including the modulation transfer function (MTF), the noise power spectrum (NPS) and the detective quantum efficiency (DQE). These measures are used in chapter 6 to characterize the imaging qualities of the Medipix2/Si detector system.

Chapter 3 gives an introduction to the fundamental concepts of a semiconductor radiation detector. An overview of the requirements of typical fields of application is given. The difference between the two basic concepts of direct and indirect photon detection is discussed and examples for common semiconductor detector architectures is given.

In Chapter 4 the two generations of the Medipix detector system is described. The functionality of the pixel cell is discussed and the procedures to fine tune the energy threshold are explained. A brief overview of the peripheral electronics used with the Medipix chips is given.

The simulations of photon conversion and charge transport are presented in chapter 5. The influence of the detector material and pixel geometry is investigated. The charge transport in the sensor part of the detector is modelled and the effect of read-out on the overall system response is analyzed. Particular attention is paid to the pixel geometries used with the Medipix detectors and performance parameters such as energy resolution, MTF and NPS are determined from the model calculations.

In chapter 6 the measurements performed to evaluate the detector performance are reported. The first part of the chapter describes measurements performed with the Medipix2 detector using monochromatic X-rays at the European Synchrotron Radiation Facility (ESRF). The apparent spectrum of the signal of the individual pixel is measured and the influence of charge sharing on the energy resolution and detector homogeneity are investigated. In the second part of the chapter the detector response homogeneity and the effectivity of flat-field correction techniques are investigated, using both generations of the Medipix and different X-ray spectra from conventional generators. The experimental determination of the modulation transfer function (MTF) is presented. The noise of the detector is characterised in terms of the noise power spectrum (NPS) and the detective quantum efficiency (DQE) is derived from the measurements. The influence of applied dose on the image quality is studied. The first results using the energy window mode of the Medipix2 detector are presented.

The conclusion drawn from the thesis are presented in chapter 7 and an outlook on future work is given.

Publications

First Author

- L. Tlustos, D. Davidson, M. Campbell, E. Heijne, and B. Mikulec. Fixed pattern deviations in Si pixel detectors measured using the Medipix1 readout chip. Nucl. Instr. Meth. A, 509:102-108, 2003.

- L. Tlustos, M. Campbell, E.H.M. Heijne, and X. Llopart. Signal variations in high granularity Si pixel detectors. IEEE Trans. Nucl. Sci., 51(6), 2004.

- L. Tlustos, M. Campbell, E.H.M. Heijne, and X. Llopart. Imaging by photon counting with 256x256 pixel matrix. In Optical and Infrared Detectors for Astronomy.

Edited by Holland, Andrew D. Proceedings of the SPIE, Volume 5501, pp. 78-88 (2004).

- L. Tlustos, M. Campbell, E.H.M. Heijne, K. Kincade, X. Llopart, P. Stejskal and R. Ballabriga. Imaging properties of the Medipix2 system exploiting single and dual energy thresholds. NSS2004, N43-3, 2004. Submitted to IEEE Trans. Nucl. Sci.

Named Author

- M. Chmeissani, C. Frojdh, O. Gal, X. Llopart, J. Ludwig, M. Maiorino, E. Manach, G. Mettivier, M.C. Montesi, C. Ponchut, P. Russo, L. Tlustos, and A. Zwerger. First experimental tests with a CdTe photon counting pixel detector hybridized with a Medipix2 readout chip. IEEE Trans. Nucl Sci., 51(5):2379-2385, 2004.

- D.W. Davidson, J. Watt, L. Tlustos, B. Mikulec, M. Campbell, K. Mathieson, V. O'Shea, K.M. Smith, and M. Rahman. Detective quantum efficiency of the Medipix pixel detector. IEEE Trans. Nucl. Sci., 50(5):1659-1663, 2003.

- A.R. Faruqi, R. Henderson, and L. Tlustos. Noiseless direct detection of electrons in Medipix2 for electron microscopy. Submitted to Nucl. Instr. Meth. A.

- B. Mikulec, M. Campbell, E. Heijne, X. Llopart, and L. Tlustos. X-ray imaging using single photon processing with semiconductor pixel detectors. Nucl. Instr. Meth. A, 511:282-286, 2003.

- A. Owens, H. Andersson, M. Campbell, D.H. Lumb, S.A.A. Nenonen, and L. Tlustos. GaAs arrays for X-ray spectroscopy. In Optical and Infrared Detectors for Astronomy. Edited by Holland, Andrew D. Proceedings of the SPIE, Volume 5501, pp. 241-248 (2004).

- J. Watt, D.W. Davidson, C. Johnston, C. Smith, L. Tlustos, B. Mikulec, K.M. Smith, and M. Rahman. Dose reductions in dental X-ray imaging using Medipix. Nucl. Instr. Meth. A, 513:65-69, 2003.

Chapter 1

Semiconductor Physics

Materials can be classified according to their electrical resistivity in conductors $\sim 10^{-6}\,\Omega$ cm, semiconductors $\sim 10^{-3} - 10^{9}\,\Omega$ cm and insulators $\sim 10^{12}\,\Omega$ cm. Materials with overlapping conduction and valence band are conductors, semiconductors show an energy gap of few eV that allows for thermal excitation of electrons into the conduction band at room temperature, whereas in insulators the band-gap is much lager (e.g. SiO_2 with E_g>10 eV) and such an excitation is unlikely . Exceptions to the general rule are e.g. semi-conducting diamond with a band-gap of 6 eV and GaN with 3.5 eV respectively. The temperature dependence of the resistivity differs strongly for conductors and semiconductors. Whereas for conductors resistivity rises with temperature the opposite is true for semiconductors. The most common and well known semiconductor is silicon. It is an elemental semiconductor like Se or Ge and its production and processing is much easier and better controlled than for binary compounds such as CdTe or GaAs. Common to all semiconductors is the strong influence of impurities and stoichiometry (for compound semiconductors) on the properties of the material, as detailed in the following section.

1.1 Crystal Structure, Band Structure

The most common elemental semiconductors are members of the group IV of the periodic table and show similar crystal structure. Si and Ge have diamond structure with each atom having four nearest neighbors, forming a tetrahedron cell. Also members of the group V and VI can form semiconductors, such as S, Se, Te and P and occur in various crystal structures. Binary semiconductors formed of elements of the groups III and V of the periodic table like GaAs have similar properties as the group IV semiconductor, save the increased Coulomb interaction due to a shift of electrons from the group III to the group V atoms. This results for example in an increased band-gap of 1.42 eV for GaAs. The effect can be even stronger for II-VI compounds, such as ZnS with a band-gap of 4 eV. In addition some organic compounds also show semi-conducting behavior e.g. polyacetylene $(CH)_x$ or $C_{14}H_{10}$. An overview of the properties of some common semiconductors can be found in table 1.1.

Many of the properties of semiconductors can be explained by the crystal structure and energy bands. In pure and defect free semiconductors at 0 K, the electrons fill the energy bands up to the Fermi level, leaving the conduction band completely free. This represents

Semiconductor	Si	Ge	C	GaAs	CdTe	GaN	aSe
atomic number	14	32	6	31/33	48/52	31 (0.83) 7 (0.17)	34
density $[g/cm^3]$	2.33	5.32	3.52	5.31	6.2	6.15	4.3
crystal structure	diamond	diamond	diamond	zincblende	zincblende	zincblende	
band-gap [eV] @ 300K/0K	1.12/1.17	0.66/0.74	5.47	1.42	1.56	3.2/3.0	
average energy/eh pair @300K	3.61	2.96[a]	13	4.26	4.43	8.9	50
carrier mobility @ 300K $[cm/s]$	1500	3900	1800	8500	1050	600 (1000)	$3 \cdot 10^{-7}$
	450	1900	1200	400	100	200-400 (30)	$4 \cdot 10^{-6}$
Fano factor	0.115	0.13	0.08	0.1	0.1		
direct / indirect bandgap	I	I	I	D	D	D	
dielectric constant ε	11.9	16.0	5.7	13.1	10.2	8.9	

Table 1.1: Properties of common semiconductors in radiation detection, data taken from [23–25]

the situation of an insulator. Raising the temperature results in an increasing number of electrons being lifted into the conduction band and the crystal becomes semiconducting.

The energy band structure is a consequence of the regular locations of the ionized atom cores in the crystal lattice and the conduction band electrons moving in the resulting periodic potential. To describe the dynamics of the whole system of a semiconductor a solution of the Schroedinger equation including ion-ion, electron-electron and electron-ion interaction would be required. Obviously, due to the large number of ions and electrons in a crystal, a solution for the complete equation can not be achieved without introducing certain approximations. Valence and core electrons are treated separately, with the core electrons treated within the ion core. A further simplification is the so-called adiabatic approximation, which states that the ion core is essentially at rest with respect to the electrons and ion core movements are treated separately as phonons. Furthermore the field experienced by the individual electron is assumed to be identical. Solving the Schroedinger equation with these approximations and taking into account the symmetries of the mean periodic potential, one obtains Bloch functions as eigenfunctions. These solutions are composed of a plane wave and a periodic factor governed by the wave vector $\vec{k}$. The periodic boundary conditions determine the possible energies for a given wave vector, resulting in allowed and forbidden energy regions, so called energy band. Within an allowed band an electron moves as if it were free, except that the relation between its momentum and energy is now given by

$$E(\vec{k}) = \frac{\hbar^2 \vec{k}^2}{2m_e^*} + V_0$$

with $\hbar$ the reduced Planck constant, k the wave vector of the electron and m_e^* denoting the effective electron mass and V_0 the starting energy of the allowed band. In other words the effective mass is determined by the curvature of the energy dispersion curve at the minimum.

In Fig. 1.1 the energy band structures of Si and GaAs are shown [25]. The uppermost

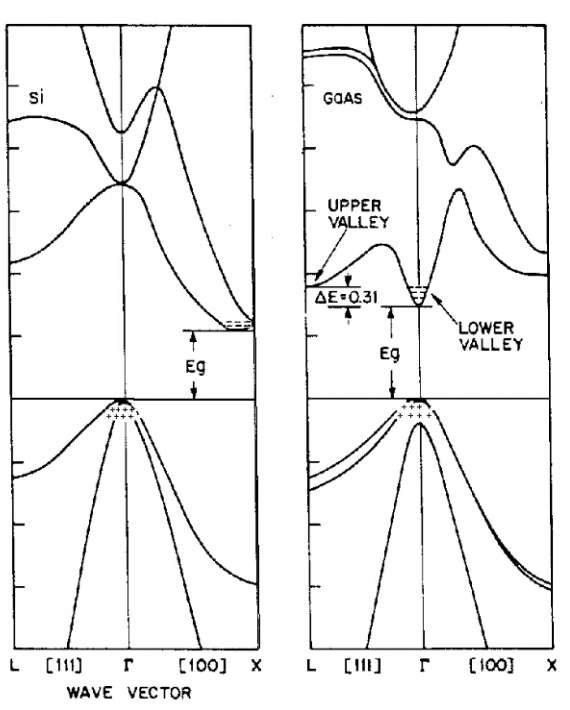


Figure 1.1: Energy band diagrams of a) Si and b) GaAs [25]. The lower band edge of the conduction bands in Si are the boundaries of the Brillouin zone, whereas for GaAs it is in the centre of the Brillouin zone aligned with the upper edge of the valence band.

occupied valence band of Si has its maximum at the Γ point (the center of the first Brillouin zone at $\vec{k} = 0$), whilst the minimum of the conduction band is situated in the X direction. Therefore, due to energy and momentum conservation, a transition from the valence to the conduction band can occur only when both the energy is equal or greater than the band-gap energy and an additional momentum is provided at the same time. This leads to a reduced probability of such a transition. On the other hand, GaAs shows a band structure with aligned valence band maxima and conduction band minima. The two types of band gap configuration are called indirect or direct band-gap.

In the case of amorphous semiconductors the energy bands are not as clearly defined as for crystalline semiconductors. The long range order and therefore the periodicity of the ion core potential is not present, but is just in place on a short range scale. This leads to a smearing of the band edges.

The magnitude of the band-gap in a given material is not a constant material property but varies strongly with stoichiometry in the case of compound semiconductors, impurities concentration, temperature and pressure.

Since the energy bands are determined by the periodic potential of the crystal any change of lattice constant will result in a change of the band-gap E_g, following the eq.

$$\Delta E_g = \left(\frac{\partial E_g}{\partial T}\right)_p \Delta T + \left(\frac{\partial E_g}{\partial p}\right)_T \Delta p$$

where T denotes the absolute temperature and p the pressure.

Empirically one finds a quadratic decrease of the band-gap at low temperature and a linear relation for high temperatures, given by [26]

$$E_g(T) = E_g(0) - \frac{AT^2}{B+T}$$

where A, B are constants

The band gap dependence on pressure is more complicated, since anisotropic deformation can give rise to different variations of the energy bands for different orientations of $\vec{k}$.

1.2 Intrinsic and extrinsic Semiconductors

The intrinsic carrier concentration of a pure semiconductor denotes the electrons and holes present in the conduction and valence band respectively .

$$n = N_C \exp\left(\frac{E_C - E_F}{kT}\right) \qquad N_C = \left(\frac{m_e^* kT}{2\pi\hbar}\right)^{3/2}$$
$$p = N_C \exp\left(\frac{E_F - E_V}{kT}\right) \qquad N_V = \left(\frac{m_p^* kT}{2\pi\hbar}\right)^{3/2}$$

with N_C, N_h the effective density of states at the conduction and valence band edge, E_F the Fermi energy, E_C the lower edge of the conduction band, E_V the upper edge of the valence band and $m_{e,p}^*$ the effective masses of electrons and holes. In intrinsic semiconductors the electron concentration in the conduction band equals the hole concentration in the valence band for any given temperature, thereby allowing to determine the intrinsic carrier concentration

$$np = n_i p_i = n_i^2 = N_C N_V \exp\left(\frac{E_g}{kT}\right). \tag{1.1}$$

The carrier concentration therefore depends only on the intrinsic properties of the semiconductor, the temperature and the width of the band-gap, but is independent of the position of the Fermi level (law of mass). The intrinsic Fermi level can be obtained as

$$E_{Fi} = \frac{E_C + E_V}{2} + \frac{3kT}{4} \ln \frac{m_h^*}{m_p^*}$$

Typical intrinsic carrier concentration are in the range of $n_i = pi = 10^{10}$ cm^{-3} at room temperature. Compared to room temperature concentration of metals in the order of 10^{21} cm^{-3} , the values for semiconductors are very small.

By adding special impurities in a controlled way the electron or hole density can be altered significantly and one speaks of extrinsic semiconductors. Although the intrinsic

carrier concentration remains unchanged, either n_i or p_i can be as low as 10^2 cm^{-3}. Impurities which create an additional allowed energy level in the forbidden band close to the conduction band can provide an electron to the conduction band, which are called donors. Acceptor impurities are able to accept an electron from the valence band in a level close to the upper limit of the valence band and create a hole in the valence band.

While the law of mass still is valid in extrinsic semiconductors, the number of holes does not necessarily equal the number of electrons, leading to the modified carrier concentrations as described by eq. 1.2 and a shifted Fermi level E_F,such that

$$\frac{n}{n_i} = \exp\left(\frac{E_F - E_{Fi}}{kT}\right) \qquad \frac{p}{p_i} = \exp\left(\frac{E_{Fi} - E_F}{kT}\right) \tag{1.2}$$

The dopant density effectively determines the carrier concentration over a wide range of temperatures.

For radiation detection purposes, as few free carriers as possible are desired in the absence of ionising radiation. However, unwanted donor and acceptor levels introduced by impurities and crystal imperfections cannot be lowered at will in the production process. One measure of the impurity concentration is the electrical resistivity, ρ, given by

$$\rho = \frac{1}{nq\mu_e + pq\mu_h} \tag{1.3}$$

with q the electron charge and $\mu_{e,h}$ the electron and hole mobilities.

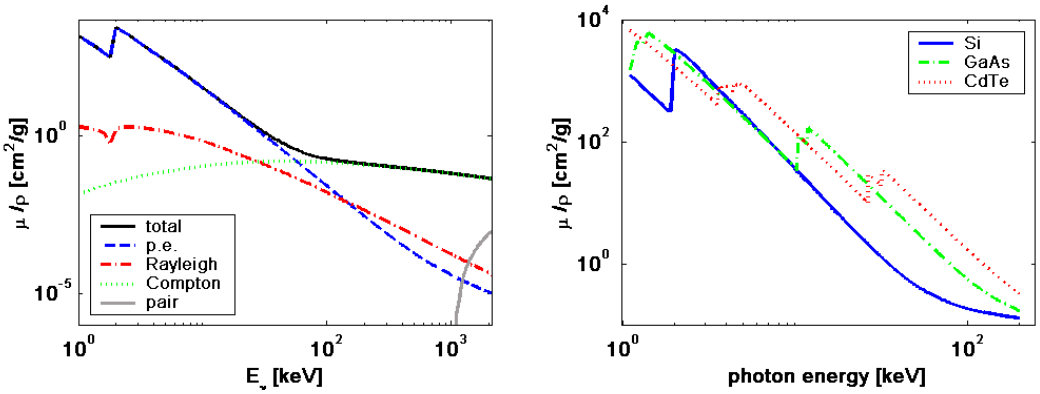
One way to increase the resistivity is to use so-called compensated materials. In compensated materials both donor and acceptors are present. Some of the electrons stemming from donor impurities are captured by acceptor impurities. In this way some of the properties of intrinsic semiconductors are provided, with a resulting carrier density approximately equal to the difference between the donor and the acceptor concentration for a n type material.

1.3 Energy deposition by ionising radiation

The first step in the detection process is always the conversion of all or a part of the energy of the incoming particle into a signal via an interaction with the detector material. Ionizing radiation can be categorized according to the involved interaction mechanism.

- Directly ionizing radiation: The energy is deposited in the medium through direct Coulomb interactions between the primary charged particle and orbital electrons of atoms in the medium.

- Indirectly ionizing radiation: Energy deposition for photon and neutrons takes place in a two-step process. Secondary charged particles, in particular electrons or positron in the case of incident photons, are generated in the medium. These secondary particles transfer energy to the medium via direct Coulomb interactions with orbital electrons.



(a) (b)

Figure 1.2: a) The total mass attenuation coefficient of Si and its contributions from photoelectric effect, Rayleigh scattering, Compton scattering and pair production in the energy range up to 2 MeV. b) The total mass attenuation coefficient of Si, GaAs and CdTe in the energy range up to 200 keV.

1.3.1 Photon interactions

When a beam of X-rays passes through matter, its intensity is reduced due to absorption or scattering processes. In contrast to charged particles, which deposit energy continuously along their track, photon interactions are localized. Photons will traverse a certain distance within a medium before depositing energy by on of the following mechanisms

- Photoelectric absorption
- Compton scattering
- Rayleigh scattering

The probability of interaction after travelling a distance d is given by

$$\eta = 1 - \exp^{-\mu(E,Z)d} \tag{1.4}$$

with μ being the linear attenuation coefficient that depends on the photon energy E and the atomic number Z. In the energy ranges used for X-ray imaging only photoelectric effect, Compton scattering and pair production contribute. The total linear attenuation coefficient is

$$\mu = \tau_{Photoelectric} + \sigma_{Compton} + \kappa_{Pair}. \tag{1.5}$$

The attenuation coefficients are usually tabulated as mass attenuation coefficients, after normalization by the material density. The mass attenuation coefficients are related to the interaction cross sections through

$$\frac{\sigma}{\rho} = \frac{N_A}{A}\sigma,$$

with N_A Avogadro's number and A the atomic mass number.

As can be seen in Fig. 1.2 for low energies the photoelectric effect is dominant.

Photoelectric Effect

During photoelectric absorption the primary photon is completely absorbed in an interaction with a tightly-bound inner shell electron. Due to momentum conservation, the photo-electric effect occurs only with bound electrons and the nucleus absorbs the recoil momentum. An electron is released with an energy $E = E_{photon} - E_{bind}$ given by the difference between the primary photon energy and the binding energy of the inner shell electron. The photo-electron subsequently looses its kinetic energy to the detector via phonon excitation and ionisation. As can be seen in Fig. 1.2b), strong discontinuities of the photoelectric attenuation coefficient occur when the photon energy exceeds binding energies of an electron shell, called e.g. K- or L-edges according to the shell concerned.

The photo-electric cross-section per atom can be approximated for photons above the K-edge as

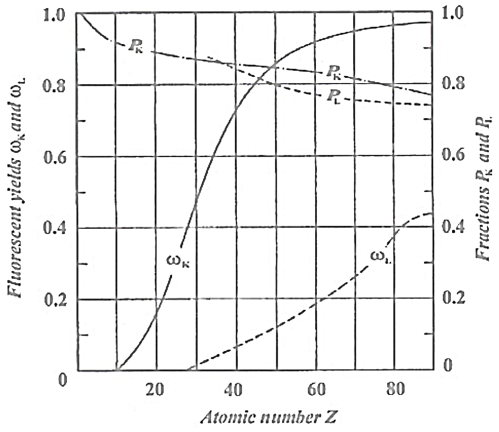
$$\tau_k = \sigma_T 4\sqrt{2}\alpha^4 Z^5 (\frac{E}{m_e c^2})^{3.5}$$

with σ_T being the Thompson cross-section and α the fine-structure constant. An approximate expression for angular distribution for the ejected K-shell photo-electron is given by [27]

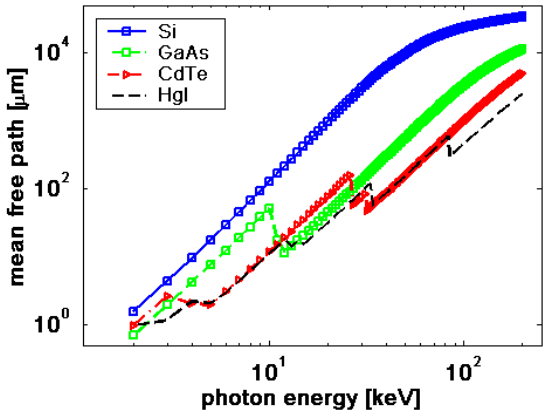
$$\frac{d\sigma_{ph}}{d\Omega_e} \sim \frac{\sin^2\theta}{(1-\beta\cos\theta)^4}\left\{1 + \frac{1}{2}(\gamma-1)(\gamma-2)(1-\beta\cos\theta)\right\},$$

where β and γ are the Lorentz factors of the photo-electron. The angular distribution extends from values of 0 up to 140 °. For lower photon energies the photoelectrons are emitted almost perpendicular to the incoming photon direction, e.g for 20 keV photons the angle of maximum intensity ∼70 °. This preferably perpendicular emission of low energy photoelectrons does not influence the final shape of the charge cloud generated, due to the strong scattering of the secondary electrons.

Photoelectric effect (and also Compton effect) vacancies are produced in atomic shells by the ejection of orbital electrons. These shell vacancies occur mainly in inner atomic shells and are followed by de-excitation, either via characteristic X-rays or Auger electrons. The number of fluorescent photons or Auger electrons emitted per orbital vacancy is expressed in the fluorescent yield ω, and $(1-\omega)$ for Auger effect respectively. The magnitude of the fluorescent yields depends on the atomic number Z of the atom and on the principal quantum number of the shell of the vacancy. Fig. 1.3a shows the fluorescence yield for K- and L-shell photo-absorption as a function of the atomic number Z. Provided that the photon energy exceeds the K-shell binding energy, about 80% of the interactions involve K-shell electrons and most of the remaining 20% eject L-shell electrons. Fig. 1.3b plots the mean free path of a selection of materials suited as sensor material for direct detection systems.



(a)



(b)

Figure 1.3: a) The fluorescence yields $\omega_{K,L}$ for the K and L-shell as a function of the atomic number and the fractions $P_{K,L}$ of all photo-effect interactions that occur in the K and L-shell [28]. b) The mean free path of photons in common semiconductor detector materials.

The shell with the highest probability of absorbing the incident photon is the inner K-shell, provided the photon energy exceeds the K-shell binding energy. The most probable transition to fill the empty position is a transition from the L shell, followed by electrons originating from the M shell. The energy difference between the two shells involved is released via emission of a secondary photon, whereas the Auger electron energy is the inner shell energy minus the energy of the two final vacancies produced during Auger emission. Whilst an Auger electron will travel only very short distances in the sensor material, a fluorescent photon has a much longer mean free path, and therefore can change considerably the spatial distribution of the charge cloud created during the conversion process.

Table 1.2 gives an overview of characteristic photons for several semiconductor sensor materials as well as for GdSO and CsI, showing the corresponding fluorescent yield and

Material	N	K_1	L_2	L_3	$K_{\alpha 1}$	$K_{\alpha 2}$	$d_{\alpha 1}$	$d_{\alpha 2}$	η[%]
Si	14	1.84	0.10	0.10	1.74	1.74	11.86	11.86	4.1
GaAs									
Ga, 48.20%	31	10.36	1.14	1.11	9.25	9.22	40.62	40.28	50.5
As, 51.80%	33	11.87	1.36	1.32	10.54	10.50	15.62	15.47	56.6
CdTe									
Cd, 46.84%	48	26.71	3.73	3.53	23.17	22.98	113.20	110.75	83.6
Te, 53.16%	52	31.81	4.61	4.34	27.47	27.20	59.32	57.85	87.3
HgI									
Hg, 44.14%	80	83.10	14.21	12.28	70.82	68.89	389.86	361.54	98.1
I , 55.86%	53	33.17	4.85	4.56	28.61	28.32	80.66	78.56	88.1
Se	34	12.66	1.65	1.47	11.22	11.18	70.09	69.44	59.3
CsI									
Cs, 51.15%	55	35.98	5.36	5.01	30.97	30.62	237.70	264.98	89.5
I , 48.84%	53	33.17	4.85	4.56	28.61	28.32	220.17	214.60	88.1
GdSO									
Gd, 83.07%	64	50.24	7.93	7.24	42.99	42.30	283.50	271.33	94.2

Table 1.2: The fluorescence properties of some semiconductor detector material. For comparison two common scintillator materials are listed as well. The energies for the K_1, L_1 and L_2 absorption edge energies and the characteristic $K_{\alpha 1}$, $K_{\alpha 2}$ energies are given in [keV]. The mean free path $d_{\alpha 1}$ and $d_{\alpha 2}$ of the $K_{\alpha 1}$ and $K_{\alpha 2}$ photons are given in [μm]. η is the total fluorescent yield for the K-shell fluorescence. As a comparison the values for two scintillator materials, GdSO and CsI, are also given.

mean free path. Characteristic photons of material with high absorption coefficients travel significant distances, up to ~390 μm in the case of HgI for the Hg line.

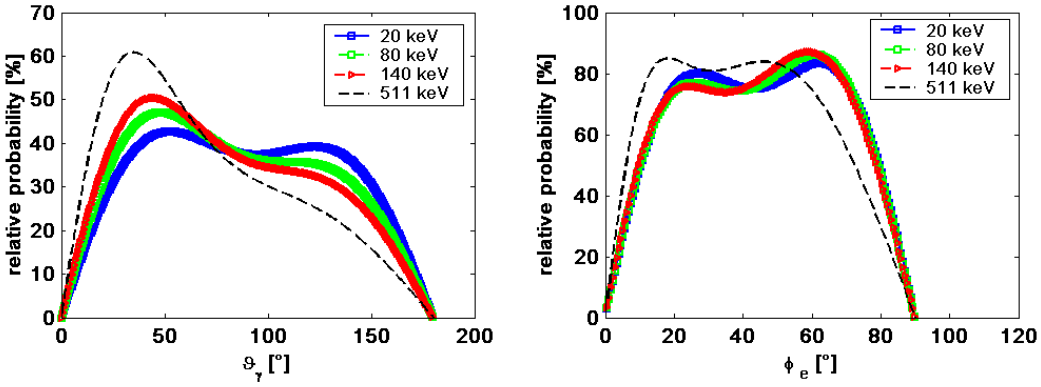
Compton Effect

The Compton effect, or incoherent scattering can involve both free and orbital electrons. The incident photon transfers a part of its energy, $h\nu$, to the electron, thereby being scattered by an angle, θ, with respect to its initial direction. If the photon energy is much larger than the binding energy of the electron, the electron can be considered as quasi-free. The scattered photon energy, $h\nu'$, and the energy of the electron, E', depend on the scattering angle only

$$h\nu' = h\nu \frac{1}{1 + \varepsilon(1 - cos\theta)}$$

$$E' = h\nu \frac{\varepsilon(1 - \cos\theta)}{1 + \varepsilon(1 - \cos\theta)}$$

with $\varepsilon = h\nu / m_e c^2$. The maximum energy transferred to the electron occurs at 180 ° and also is called Compton edge



(a) (b)

Figure 1.4: a) The angular distribution of the Compton scattered photon and b) angular distribution of the recoil electron for energies of the incident photons of 20 keV, 80 keV, 140 keV and 511 keV.

$$E'_{max} = \frac{2\varepsilon\, h\nu}{1+2\varepsilon}.$$

The differential cross section for photon scattering on free electrons can be calculated using the Klein-Nishina formula [29]

$$\frac{d\sigma_C}{d\Omega} = \frac{r_e^2}{2}\frac{E'^2}{E^2}\left\{\frac{E'}{E} + \frac{E}{E'} - \sin^2\theta\right\}$$

with r_e denoting the classical electron radius. As opposed to photoelectric absorption the emission angle for the electron here is limited to 90 °. The direction of the recoil electron is linked to the photon scattering angle by energy and momentum conservation and is given by

$$\cos\Theta = (1+\varepsilon)\tan\frac{\theta}{2}.$$

Fig. 1.4 plots the angular distributions of the scattered photon and Compton electron as a function of the respective scattering angle.

Fig. 1.5 plots the relative strength of Compton scattering with respect to the total attenuation for several typical semiconductor detector materials. In Si, Compton scattering becomes equally strong as the photoelectric effect at ∼57 keV.

Rayleigh Scattering

In Rayleigh or coherent scattering the photon interacts with a bound atomic electron without excitation of the target atom. The event is elastic in the sense that the energies of the incident and the scattered photons are identical and scattering angle is small. It is also qualified as coherent since it can be described as the emission of a photon by a coherent oscillation of all target atom electrons. Since no energy is transferred, Rayleigh

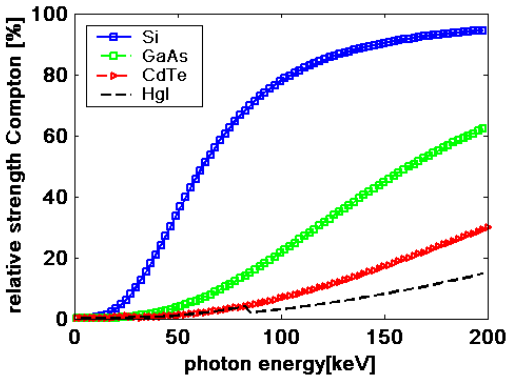
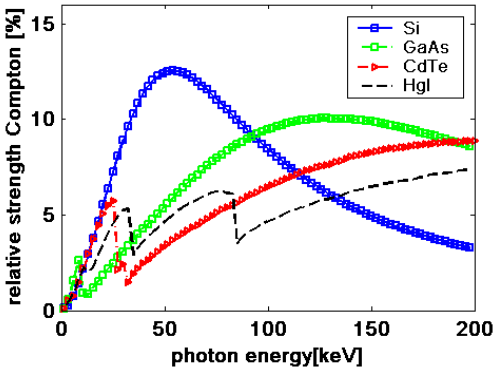


Figure 1.5: Relative attenuation Compton effect as a percentage of the total attenuation.



(a)

Figure 1.6: Relative attenuation Rayleigh scattering as a percentage of the total attenuation

scattering plays no role in the energy deposition. It still plays a role in the attenuation coefficient, since photons are scattered out of the incident beam. The differential cross section is given by

$$\frac{d\sigma}{d\Omega} = \frac{d\sigma_T}{d\Omega}\left[F(q,Z)\right]^2$$

where σ_T is the classical Thompson cross section for the scattering by a free electron

$$\frac{d\sigma_T}{d\Omega} = \frac{1}{2r_0^2}(1+\cos^2\theta)$$

and $F(q,Z)$ is the atomic form factor and q the momentum transfer. For low photon energies $F(q,Z) \sim Z$ and Rayleigh scattering is described by pure Thompson scattering. Fig. 1.6 plots the relative contribution of Rayleigh scattering to the total mass attenuation coefficient.

1.3.2 Charged particle interaction

Unlike photons, energetic charged particles moving in matter interact with the medium via Coulomb interaction, either with atomic orbital electrons or with atomic nuclei. These collisions may be elastic or inelastic. While in elastic collisions the particle is only deflected from its original direction, in inelastic collisions in addition to the deflection some of its energy is transferred to the orbital electron or emitted in the form of bremsstrahlung.

The inelastic interactions can be further categorized according to the mechanism of energy transfer. Coulomb interactions between the incident particle and orbital electrons that result either in ionisation or in excitation of the absorbing atoms are described by the so-called collision stopping power. The secondary electron created in an ionisation collision may possess sufficient energy to travel significant distances from the collision point and causing itself further ionisation. Such high energy secondary electron are also called delta rays. In Coulomb interactions between the incident electron and the nucleus the energy loss results in the production of bremsstrahlung photons. This type of energy losses is characterized by the radiative stopping power.

The total mass stopping power S can be written as

$$S_{tot} = S_{coll} + S_{rad} = -\frac{dE_{kin}}{dx}$$

and describes the loss of kinetic energy E_{kin} per unit path length. Analog to the mass attenuation coefficient for photons the mass stopping power is given by the stopping normalized to the density of the absorber ρ. The energy transfer per interaction in general is very small in comparison to the kinetic energy of the primary particle. This behaviour is modelled in the so-called continuous slowing down approximation (CSDA) as a gradual energy transfer until the particle comes to rest. The path length is given by the total distance traveled regardless of the direction and is calculated by integration of the inverse stopping power

$$R = \int_0^E -\left(\frac{dE}{dx}\right)^{-1} dE.$$

For heavy charged particle the mass stopping power is determined by the collision stopping power and is calculated using the Bethe formula [28, 29]

$$\frac{S}{\rho} = \frac{N_A Z}{A} \frac{4\pi r_e^2 m_e c^2}{\beta^2} z^2 \left[ln\left(\frac{2m_e \beta^2 c^2}{I}\right) - ln\left(1-\beta^2\right) - \beta^2 \right] \tag{1.6}$$

with N_A Avogadro's number, r_e classical electron radius, m_e the electron mass, Z, A the atomic mass and weight of the absorber, z the charge of the incident particle in units of electron charge, and I the mean excitation potential. Plotting the specific energy as a function of the particle track length results in the Bragg curve, Fig. 1.7. The curve is described correctly by eq. 1.6 for the most of the track. Close to the end of the track the curve deviates from the predicted shape since the energy transfer is reduced by electron pick-up. The difference in the shape of the curve for a single particle and a parallel beam is result of the statistical nature of the energy transfer via numerous microscopic interactions.

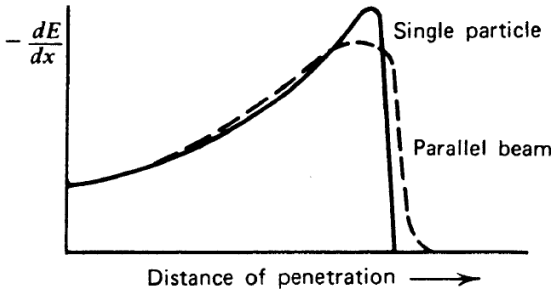


Figure 1.7: Bragg curve of an alpha particle of several MeV [29].

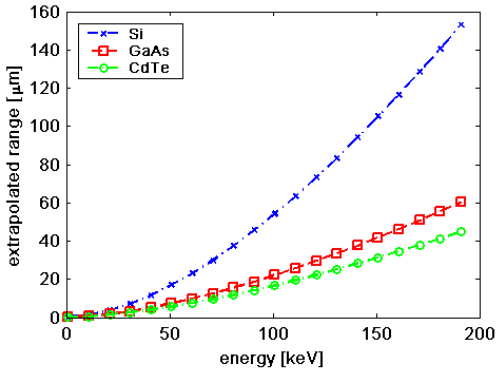


Figure 1.8: The extrapolated range for electrons in Si, GaAs and CdTe

The attenuation of electrons in matter is not described accurately by the Bethe formula, since electrons are scattered more easily due to their smaller mass. More accurate expressions for the collision stopping power for electrons and positrons is given by [28, 29]

$$\frac{S_{coll}}{\rho} = \frac{N_a Z}{A}\frac{\pi r_e^2 2 m_e c^2}{\beta^2}\left[ln\frac{\tau^2(\tau+2)}{2(I/m_e c^2)^2} + (1-\beta^2)\left[1+\frac{\tau^2}{8}-(2\tau-1)\ln(2)\right]\right] \tag{1.7}$$

where τ denotes the electron kinetic energy normalized to the electron rest mass energy. Thus the energy loss due to ionisation increases linearly with Z and logarithmically with the electron energy. In addition radiative energy loss also gives a significant contribution to the stopping power. Radiative losses scale with Z^2 and increase linear with the electrons energy. The CSDA range is a poor measure of the penetration depth of electrons in matter. Scattering effects result in very tortuous paths and lead to large variations in actual penetration of electrons into the absorbing medium. Therefore the CSDA range is a measure for the maximal electron range. A more practical measure for the penetration depth is the extrapolated or projected range and is related to the most probable range of a particle of a given incident energy. It is determined from electron transmission curves and is obtained by extrapolating the linear portion at the end of the transmission curve to zero. Fig. 1.8 plots the extrapolated electron ranges in Si, GaAs and CdTe.

The extrapolated range of low energy electrons can be approximated by [1]

$$\begin{aligned} \delta &= 0.09 \cdot \rho^{-0.8} E^{1.3} \quad E < 10keV \\ \delta &= 0.045 \cdot \rho^{-0.9} E^{1.7} \quad E > 10keV \end{aligned} \tag{1.8}$$

1.4 Carrier Transport

When an external force is applied on a system of free charge carriers, these carriers are displaced and a current results. The transport properties of a semiconductor with respect to drift of charge carriers under the influence of an electric field or diffusion due to gradients in the concentration of carrier densities play a crucial role in the signal formation. This section will deal with the transport of charge carriers generated by ionizing radiation in the detector substrate.

In absence of external forces the electrons in the conduction band and the holes in the valence band can in first approximation be considered as a gas of non-interacting charged particles. The carriers are in Brownian motion resulting from subsequent scattering on perturbations of the periodicity of the lattice potential stemming from impurities, lattice imperfections and phonons. In this case the mean carriers velocity is given by the thermal speed $m^* v_{th}^2/2 = \frac{3}{2}kT$, with m^* the effective carrier mass. This corresponds to a mean thermal speed of $10^7 cm/s$ for electrons in Si at room temperature. The mean free path between collisions is about 10-100 nm , corresponding to a relaxation time of τ_c of $\sim 10^{-12}$ - 10^{-13}s sec.

1.4.1 Diffusion

Diffusion takes place in the case of a nonuniform distribution of charge carriers in space, where carriers move from the region of high concentration to regions of lower concentration. This is described by Fick's law, stating that the compensating diffusion current density, J_{diff}, is proportional to the concentration gradient, Δn,

$$J_{diff} = -qD\nabla n$$

The diffusion constant D is a measure for the response of the carrier to a concentration gradient and is proportional to the thermal velocity v_c and the mean free path λ_c between two subsequent collisions

$$D \propto v_{th}\lambda_c.$$

The total diffusion current density from holes and electrons is given by

$$J_{diff} = qD\nabla n - qD_h\nabla p.$$

1.4.2 Drift

Without electrical field $\vec{E}$ and in absence of diffusion processes the free carrier motion will be a random thermal motion with zero average displacement. An electric field will accelerate the carriers between subsequent collision leading to an average drift velocity, $v_{n,p}$ of electron and holes

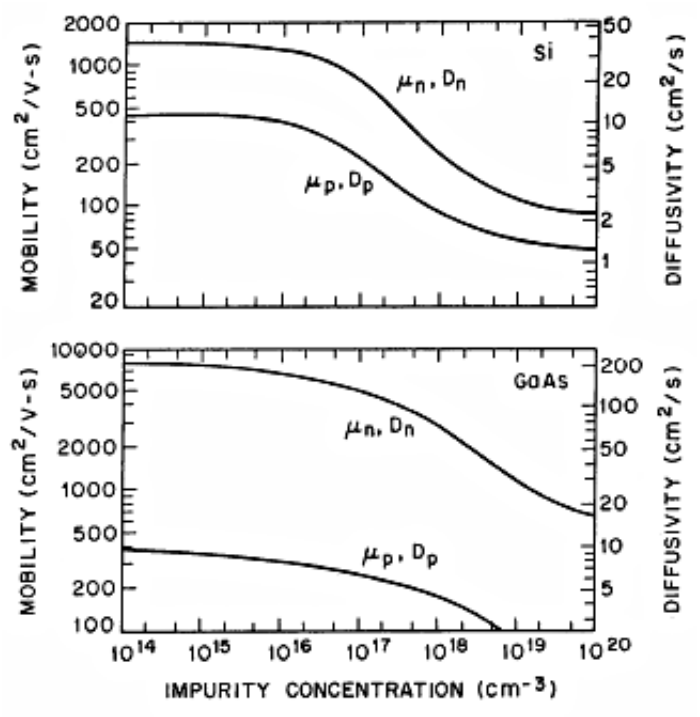


Figure 1.9: The electron μ_e and hole μ_h mobilities and the respective diffusivities $D_{e,h}$ for in Si and GaAs as a function of impurity concentration. [25].

$$v_{n,p} = \mp \frac{q\tau_C}{m_{n,p}} \vec{E} = \mp \mu_{n,p} \vec{E}$$

with τ_c is the relaxation time, giving rise to a total macroscopic current density, J_{drift}, given by

$$J_{drift} = (n\mu_e + p\mu_p) q\vec{E} = \sigma \vec{E}.$$

where σ denotes the material conductivity $\sigma = (n\mu_e + p\mu_p)q$.

The relationship with constant carrier mobility μ is valid only in the case of low electric fields, when transport can be regarded as drifted equilibrium, and carriers scatter elastically with optical phonons, thus leading to a linear relation between electric field and carrier velocity. The different scattering mechanisms contribute following Matthiesen's rule, stating that the total scattering rate is the sum of the rates of contributing processes

$$\frac{1}{\mu_{tot}} = \Sigma_i \frac{1}{\mu_i}$$

Therefore mobility is limited by the mechanism with the shortest relaxation time. Carrier mobilities decrease strongly with increasing impurity concentration, see Fig. 1.9, since the carriers scatter elastically on the impurities. The higher mobility of electrons is related to their lower effective mass.

With increasing field strength the carrier energies become appreciably larger than the thermal energy. The carriers start to scatter more and more inelastically until the energy

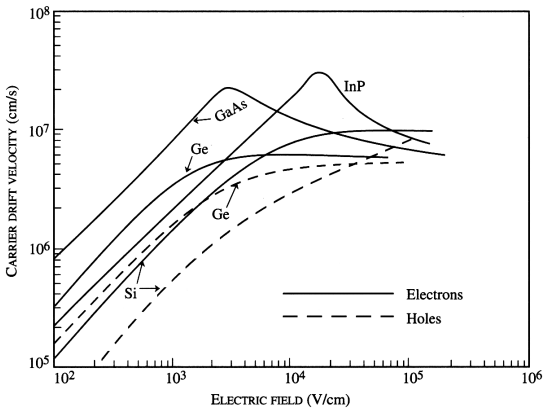


Figure 1.10: The dependence of the drift velocity on the electric field for electrons and holes in Si, Ge, GaAs and InP. Electron in GaAs and InP show a velocity overshoot above the saturation velocity [30].

gain from the field is exactly balanced by the energy loss rate. This leads to a saturation velocity of

$$v_s = \sqrt{\frac{E_{op}}{m*}}$$

with $E_{op}$the optical phonon energy and m^* the effective carrier mass. In Si, velocity saturation occurs at about $5 \cdot 10^5 V/cm$ with an electron velocity of $1.07 \cdot 10^7 cm/s$ and a hole velocity of $8.37 \cdot 10^6\, cm/s$, c.f. 1.10. In this case the mobility can be written as [25]

$$\mu(E) = \frac{\mu_{low}}{1 + \frac{\mu_{low} E}{v_{sat}}} \tag{1.9}$$

Mobility and diffusion are related to each other via the Einstein relation

$$D_{n,p} = \frac{kT}{q}\mu_{n,p}$$

1.4.3 Current density equations

When both concentration gradients and an electric field are present the current density is given by

$$\begin{aligned} \vec{J_n} &= q\mu_n n\vec{E} + qD_n\nabla n + G_n - R_n \\ \vec{J_p} &= q\mu_p p\vec{E} - qD_p\nabla p + G_p - R_p \end{aligned} \tag{1.10}$$

where $G_{n,p}, R_{n,p}$ are the generation and recombination rates for electrons and holes respectively. For a complete description of the transport processes in a semiconductor one has to solve the eq. 1.10 together with the Poisson equation

$$\Delta\Phi = \frac{\rho_e}{\varepsilon} = \frac{q}{\varepsilon}(p - n + N_D^+ - N_A^-). \tag{1.11}$$

where ρ_e denotes the space charge density and ε is the dielectric permittivity, N^- and N^+ the concentrations of the ionized donor and acceptor impurities. An analytical solution of these three coupled differential equations cannot be found for most cases and they have to be solved numerically.

1.5 p-n junction diode in reverse bias

A p-n junction diode is created when joining together opposite doped extrinsic semiconductors. This type of structure shows rectifying characteristics and allows current flow mainly in one direction. After joining the two regions electrons diffuse into the p-material and holes into the n-material. As a result a surplus of negative charges will be created in the p-region due to the remaining ionized acceptor atoms and the positive donor ions in the n-type side of the structure. This carrier concentration gradient creates an electric field across the junction, counteracting the diffusion process. A region completely depleted of free charge carriers extends over a distance W_p into the p-type side and W_n in to the n-type side. In thermal equilibrium the drift currents cancel out with the diffusion currents and the two Fermi levels align. The built-in potential V_{bi} of the junction in the absence of an external bias is given by

$$V_{bi} = \frac{k_B T}{q} \ln \frac{p_p}{p_n} = \frac{k_B T}{q} \ln \frac{n_n}{n_p}, \tag{1.12}$$

where $n_{n,p}$ are the electron densities in the n- and the p-side of the junction and $p_{n,p}$ the respective hole densities.

The total width of the depletion region can be calculated as

$$W(V_{bi}) = W_p + W_n = \left[\frac{2\varepsilon V_{bi}}{q} \frac{N_A + N_D}{N_A N_D}\right] \tag{1.13}$$

with N_A the acceptor density on the p-type region and N_D the donor density in the n-type region.

The depletion region is not necessarily symmetric around the junction but extends further into the lighter doped side. By applying an external voltage the width of the depletion region can be reduced or extended. The basic idea of semiconductor diode radiation detectors is to extend the carrier free region to the entire detector volume. This is done by reverse biasing the diode applying an external bias voltage V_{bias} of the same polarity as V_{bi}. Electron-hole pairs created within this depletion layer by ionising radiation will be separated and drift under the influence of the electric field towards the collection electrodes. In the absence of recombination or charge trapping during the drift time the charge collected gives an absolute measure of the deposited energy in the detector volume. In general the diode structure is created by a very thin but heavily doped rectifying layer on one side of the detector diode, whereas on the other side of the lightly doped detector volume a ohmic contact is implemented. If the diode is p^+n, then $N_A \gg N_D$ and the depletion region extends mainly into the n-side. In this asymmetric junction the depletion

depth is mainly determined by the donor concentration and can be approximated using the effective doping concentration

$$n_{eff} = |N_D - N_{A,n}|$$

with $N_{A,n}$ the compensating acceptor distribution in the n-type material. Complete depletion occurs when the width W of the depleted zone reaches the thickness of the substrate d. Since the $V_{bias} \gg V_{bi}$ the width of the depleted layer in the bulk region of the detector diode can be approximated by

$$W = \sqrt{\frac{2\varepsilon V_{bias}}{q n_{eff}}} = \sqrt{2\varepsilon\mu\rho V_{bias}} \tag{1.14}$$

where ε is the permittivity and ρ is the resistivity of the n-type region. The diode is fully depleted when the external voltage exceeds the depletion voltage V_{dep}

$$V_{dep} = \frac{q n_{eff} d^2}{2\varepsilon} \tag{1.15}$$

For voltages below this value the electric field is given by

$$E(z) = \frac{2(V_{bias} - V_{bi})}{W}\left(\frac{z}{W} - 1\right) \tag{1.16}$$

If the external voltage exceeds V_{dep}, the resulting electric field is given by

$$E(z) = \frac{2V_d}{d}\left(1 - \frac{z}{d}\right) + \frac{V_{bias} - V_{dep}}{d}. \tag{1.17}$$

The collection times t_{coll} for charge carriers generated at a depth z can derived from eq. 1.16 and eq. 1.17. For under-depletion one the collection time, t_{coll}, is given by

$$t_{coll}(z) = \frac{\varepsilon}{\mu q n_{eff}} \ln \frac{W}{W - z}$$

and for overdepletion

$$t_{coll}(z) = \frac{\varepsilon}{\mu q n_{eff}} \ln \frac{V_d + V_{bias}}{V_d + V_{bias} - \frac{2V_{dep}}{d} z}. \tag{1.18}$$

In first order approximation the collection time in overdepletion becomes $t(z) = zd/\mu V_{bias}$.

The width of the charge cloud at the end of the collection time is determined by the lateral diffusion and can be approximated by $\sigma = \sqrt{2Dt_{coll}} = \sqrt{2k_B T\, zd/qV_{bias}}$, with D the diffusion constant.

The continuity equation including drift and diffusion currents is given by

$$\frac{\partial n_{n,p}}{\partial t} = \mp\mu_{n,p} n_{n,p} \nabla \cdot E + D_{n,p} \Delta n_{n,p}$$

The motion in z-direction perpendicular to the detector planes is defined by the equation

$$\frac{\partial^2 n_{n,p}}{\partial^2 z} - \frac{1}{D_{n,p}}\frac{\partial n}{\partial t} \mp \frac{\mu_{n,p}}{D_{n,p}}\left(\frac{2V_{dep}}{d^2} + E_z(z)\frac{\partial n_{n,p}}{\partial z}\right) = 0$$

Under the influence of the field gradient the charge spread of one carrier type is increased, whereas the diffusion of the other type is counteracted leading to an equilibrium spread of the charge cloud of $\sigma^2 = \varepsilon D/(e \cdot n_{eff}\mu)$.

Chapter 2

Performance measures for imaging systems

The general task of X-ray imaging systems is to measure the intensity distribution of an incident photon beam. Due to the wide possible range of applications the requirements on imaging systems are equally diverse. To detect a small object with high contrast poses different requirements than the detection of large objects of low contrast. Commonly the characterisation of imaging systems is done in terms of physical quantities related to particular aspects of the imaging process such as resolution or noise performance. Linear systems analysis can be applied to imaging systems showing a linear response to input signal and have transfer properties that are independent of location at the input signal. Using this formalism, signal and noise can be decomposed into their Fourier components and input and output signal can be related in terms of the spatial frequency.

The aim of this chapter is to give a brief description of some of the standard quantities used to measure the performance of imaging systems.

2.1 Resolution, Contrast and MTF

Contrast: One basic figure of merit is the image contrast. It describes mainly the density difference between two adjacent areas in the image. The contrast C of the signal may be defined as

$$C = \frac{2(S_2 - S_1)}{(S_1 + S_2)} \tag{2.1}$$

where $S_{1,2}$ are the mean pixel values in the two regions. A measure of the performance of the imaging process is given by the ratio of the image contrast, C_{out}, to the contrast in the original signal, C_{in}. This is described by the contrast transfer, T_C, and can be measured using an object of known contrast

$$T_c = \frac{C_{out}}{C_{in}} \tag{2.2}$$

The visibility of the object in the image also depends on the object dimensions. Therefore the contrast transfer on its own is not a meaningful measure, but has to be combined

with resolution measurements.

MTF: The modulation transfer function MTF combines contrast transfer and resolution in one figure of merit. It expresses the contrast transfer as a function of the spatial frequency. In the description of linear systems theory the MTF is given by the Fourier transform of the system response to a delta function as input. The formation of the image function, $g(x, y)$, can be seen as the convolution of an object function $f(x, y)$ with a linear position invariant operator $h(x, y)$ [31]

$$g(x, y) = h(x, y) * f(x, y) \tag{2.3}$$

or in the frequency domain

$$G(u, v) = H(u, v) \cdot F(u, v) \tag{2.4}$$

with u, v the spatial frequencies in x and y direction.

In imaging $H(u, v)$ is called the object transfer function (OTF). It can be seen as the Fourier transform of the output of a system having a delta function as input. The object transfer function at a certain spatial frequency f represents the system response to an sinusoidal input of the same spatial frequency. The different stages of the imaging process can be separated into three components, a presampling OTF, a digital OTF and a display OTF. The presampling OTF is given by

$$H_{pre} = H_{geom} \cdot H_{analog} \cdot H_{aperture} \tag{2.5}$$

where H_{geom} includes geometric unsharpness due to focal spot blurring and geometrical magnification for X-ray imaging. H_{analog} describes the broadening of the spatial response due to physical processes in the detector system, e.g. scattering. $H_{aperture}$ takes into account the finite size of the active area of a pixel. The presampling OTF can be seen as the transfer function of a single isolated pixel.

The digital transfer function is obtained by the Fourier-domain convolution of the presampling OTF the with the two-dimensional sampling comb, H_{comb},

$$H_{digital} = H_{pre} * H_{comb}. \tag{2.6}$$

Finally before displaying the resulting image, filtering can be applied to the data, which then gives rise to the final output

$$H_{sys} = H_{digital} \cdot H_{filter} \cdot H_{display}. \tag{2.7}$$

The Modulation transfer function is defined as the normalized modulus of the OTF, and therefore the presampling and the digital MTF are obtained as

$$MTF_{pre}(u, v) = \frac{|H_{pre}(u, v)|}{|H_{pre}(0, 0)|} \quad \text{and} \quad MTF_{dig}(u, v) = \frac{|H_{dig}(u, v)|}{|H_{dig}(0, 0)|}. \tag{2.8}$$

In digital systems the spatial sampling leads to aliasing of signal frequencies above the Nyquist frequency. As a consequence the resulting MTF_{dig} at a certain frequency

does not describe the frequency response of a single sinusoidal input, but has additional contributions from the overlap due to the aliasing. This leads to difficulties with the interpretation of the MTF_{dig} and limits its significance as a measure of performance of different systems. Nevertheless it can be used for for system comparison purposes, but for a direct comparison the data is required to be taken under exactly the same conditions.

The experimental determination of a realistic measure for the digital MTF_{dig} is complicated by the fact that in pixellated detectors shift invariance on sub-pixel scale is not present. As a result the system response also depends on the relative phase of the input signal with respect to the sampling comb given by the segmentation, in other words the relative position of the edge with respect to the pixel border.

One approach to overcome this uncertainty is to measure the MTF with the edge positioned at all possible locations within the pixel boundaries and calculate the average of the individual MTFs. A method to obtain an estimate for this expectation MTF or EMTF from the measured presampling MTF without increasing the experimental complexity has been proposed by [32], by averaging the digital MTF over one period of the sampling pitch, a,

$$EMTF = \frac{1}{a}\int_0^a db \frac{|H_{dig}(u,b)|}{|H_{dig}(0,b)|} \qquad 0 \leq u \leq u_{Nyquist}. \tag{2.9}$$

However, by including the effects of phase dependency of the MTF_{dig} the ambiguity for frequencies above the Nyquist frequency is not removed and two detectors with completely different MTF_{pre} can have identical an EMTF. Therefore the MTF_{pre} and EMTF together give the best description even though in practice the mostly only the MTF_{pre} is used. The MTF_{pre} of a two dimensional digital detector can be estimated using a method proposed in [33], in which the two dimensional geometry of the detector is used to oversample the response of the detector to a line edge input.

2.2 Noise Transfer, SNR and NPS

Image noise results from the unwanted fluctuations in the signal level, which can mask a real fluctuation in the signal and therefore leads to a degradation of image quality. In X-Ray imaging the number of detected photons in a detector layer should ideally obey Poisson statistics, resulting in a mean number of N absorbed photons as a standard deviation of $\sqrt{N}$. Several other sources of noise contribute in addition to the inherent fluctuations of the photon beam, such as dark current in the detector, secondary quantum noise in indirect detection systems, noise generated in the readout electronics and fixed pattern noise due to beam inhomogeneities or variations in detector response.

SNR: A measure for the noise level in an image is given by the signal to noise ratio

$$SNR = \frac{\sigma}{\mu}. \tag{2.10}$$

where σ is the measured variance of the pixel values and μ is the mean pixel value. The SNR is generally less than the ideal $\sqrt{N}$ of Poisson statistics.

Frequently the SNR also is given with respect to the separability of two distributions and is reported in terms of the separation of their means divided by their standard deviation

$$SNR = \frac{|\langle S_1 \rangle - \langle S_2 \rangle|}{\sqrt{\sigma_1^2 + \sigma_2^2}}. \tag{2.11}$$

NPS: The signal to noise relation alone is not sufficient to characterise the noise, for it does not include information about the statistical correlations of the fluctuations. The noise power spectrum NPS describes both the intensity of the noise and the spatial correlations. It is defined as the Fourier transform of the autocorrelation function ACF of the signal variations, g', around the mean signal

$$g' = g - mean(g)$$

$$ACF(a,b) = g'(x,y) * g'(x+a, y+b) \tag{2.12}$$

$$NPS(u,v) = Fourier\{ACF(a,b)\} = |G'(u,v)|^2 \tag{2.13}$$

Therefore the noise power spectrum of an imaging device can be regarded as the output power spectrum of a white noise input

$$NPS_{out}(u,v) = |h(u.v)|^2 \cdot NPS_{in}(u,v). \tag{2.14}$$

The NPS tends to be flattened if an stochastic process is under-sampled, which is the case for almost every digital imaging system. But unlike for the MTF, the presampling NPS cannot be measured, since the power spectrum of the input is white and will always contain components above the Nyquist frequency. Only the digital noise power spectrum can be measured, including the aliased contributions.

2.3 Combined Measures, NEQ and DQE

The description of the SNR given above is sufficient only when the signals and background are normally distributed. A better description of the SNR is the noise equivalent quanta (NEQ) [34–37]. It denotes the apparent number of photons used in image formation for a given image frequency. Or, put in another way, it is the number of photons necessary to obtain a given SNR in the image

$$NEQ(f) = \frac{\mu^2 \cdot MTF^2}{NPS} \tag{2.15}$$

The upper limit of the NEQ is given by the number of incident photons in case of loss-free photon conversion, ideal MTF and noise free detection.

A closely related measure is the detective quantum efficiency, DQE [34–37]. Whilst the NEQ describes the image quality, the DQE refers the image quality to the incoming signal, thus characterising the system performance. It gives the fraction of incident

quanta contributing to image quality, in other words the degradation of information in the signal in the detector system. It is therefore suitable for comparing the internal noise performance of different detector systems, independent of the input signal

$$DQE(f) = \frac{SNR_{out}^2}{SNR_{in}^2} = \frac{NEQ(f)}{\Phi} = \frac{I(q)^2 \cdot MTF^2(f)}{\Phi \cdot NPS(f)} \leq 1 \tag{2.16}$$

q ... X-ray dose
I ... Intensity transfer function
Φ... Number of incident quanta

At present it is common practice to determine the DQE using the presampling MTF, although the DQE derived in this way is not entirely unambiguous.

This is a consequence of the fact that the presampling MTF_{pre} presented above describes the resolution properties of the system including the pixel aperture and signal in the sensor part of the detector but does not take into account the effects of digitalization in the pixellated readout. The NPS on the other hand cannot be measured without the effects of aliasing present. The measured DQE therefore always will include the effects of aliasing, which suggests that in fact the digital MTF_{dig} or the EMTF would provide a more useful and precise input to the calculation of the DQE. On the other hand this average value of the EMTF is no longer related to the point spread function at any location, and strictly speaking cannot be used as a measure of the contrast transfer. Furthermore it also assumes that the frequency content in the image is uniformly distributed above the Nyquist frequency, which is not necessarily the case. Since there is no entirely unambiguous solution to calculate the DQE, the best approach is to provide both the presampling and the digital version of the DQE.

Chapter 3

Semiconductor Imaging Detector Concepts

This thesis seeks to understand the strength and limitations of hybrid pixel detectors system in X-ray imaging. In this chapter some basic concepts of semiconductor imaging detectors are discussed and the special case of a hybrid pixel detector is introduced.

3.1 Applications and requirements

Although the detector technology used in this thesis has its origin in the position sensitive detectors in HEP, the exact requirements for a particular X-ray imaging applications can differ significantly.

In particle physics experiments individual charged particles have to be detected and tracked with high spatial resolution and timing precision. The readout of a detector may be self-triggered or triggered by an event registered in another detector. In imaging applications on the other hand the readout is determined by a fixed acquisition time and the signal is accumulated over the active time. Whilst the effective frame rate in HEP can very high, the single pixel occupancy may be very low. The exact opposite is true in most imaging applications. Whilst Si as detector material offers excellent properties for charged particle detection, its stopping power is rather weak for photon energies above 20 keV, notably in energy ranges used in general medical radiography.

- Medical applications: X-ray imaging in the medical domain ranges from relatively low photon energies up to 35 keV in mammography, to 140 keV in computed tomography (CT) or even 511 keV in positron emission tomography (PET). The major requirement is dose efficiency in order to keep the patient dose as low as possible. Pixel sizes range from 50 μm to 200 μm [38–40].

- Baggage inspection: several X-ray imaging techniques are in use in baggage inspection system. Dual energy imaging is employed, either as planar transmission or volume imaging, to determine the effective atomic number and the effective density

of the examined objects, allowing for a distinction of organic and inorganic material. In order to increase the detection rates this technique is usually combined with scatter imaging techniques since these are more specific in the detection of explosives [41, 42].

- Materials analysis: Within the broad range of X-ray methods used in materials analysis based on the scatter, emission and absorption properties of X-radiation, the two most common are X-ray fluorescence (XRF) spectrometry and X-ray diffractometry (XRD). In general characteristic emission lines of metal targets in conventional X-ray tubes are used in the range of 4-20 keV. Frequently XRF and XRD are used in combination, applying XRF for quantitative elemental analysis and XRD to differentiate phases in the sample [43, 44].

- Synchrotron radiation: The high intensity and tunability of synchrotron radiation allows experiments to be performed that would either be impossible or require excessive times using conventional X-ray sources. For example the excellent monochromaticity together with the high photon flux allows to resolve weak diffraction peaks that previously could not be obtained. This also means that very high demands are made with respect to detector performance, in particular for protein crystallography. Currently no detector system can fulfill all requirements simultaneously [22, 45, 46].

The new imaging detector concept based on CMOS technology described in this thesis is a very promising candidate having the potential of satisfying at least some of the requirements summarized in table 3.1.

3.2 Charge Collection in a pixellated detector

When a charge pair is created in the detector volume signals are created on the collection electrodes before the charge carriers arrive physically. While moving under the influence of the electric field all charge carriers contribute to these currents induced on the electrodes. Since electrons and holes move in opposite directions, the polarity of the induced currents is of the same sign at a given electrode. The shape of the induced current depends on the position of the creation point of the initial charge cloud. The total current in the electrodes is the sum the displacement current and the conduction current. The displacement current density J_D is given by the temporal change in dielectric displacement D

$$J_d = \frac{dD}{dt} = \varepsilon \frac{dE}{dt} \tag{3.1}$$

Integrating over the whole collection time, the overall charge collected due the displacement current is zero, Fig. 3.1, unless charge recombination or trapping with a time constant longer than the collection time takes place.

LHC	Radiography	Crystallography
Individual particles	Image	Image
MIP	γ, e^-	γ, e^-
Several ke^- signal	Mammography, ∼17-30 kV Autoradiography, ∼1 ke^- ^{99}mTc, 140 kV	8-20 kV
10^{-2} mm^2 pixel size	10^{-3}-10^{-2} mm^2 pixel size	10^{-2} mm^2 pixel size
Low mass sensor	High conversion efficiency	High conversion efficiency
Count rate ∼kHz per pixel	> MHz per pixel	1-10 MHz per pixel
Low power consumption <50-100μW/pixel	Comparable to HEP, but less stringent	Comparable to HEP, but less stringent
Radiation hardness >2,10,40 Mrad	Mrad	>Mrad
Readout single events	Readout whole matrix	Readout whole matrix
average frame rate ∼100kHz	not critical, except CT	frame rate 100 Hz and more

Table 3.1: Example of detector requirements in HEP, radiography and protein crystallography. [8, 44, 45, 47–50]

Weighting field and small pixel effect: A convenient way to calculate the total current induced on the collection electrode has been developed by Ramo [51]. For a charge q moving at a distance d towards the collection electrode, the induced charge, Q, in the electrode is

$$dQ = q\frac{dx}{d}. \tag{3.2}$$

In the case of charge trapping or recombination during charge collection, eq. 3.2 has to be modified to include the charge losses. The Hecht relation [29] describes the dependence of the total induced charge on the position z of the initial charge generation under the assumption of exponential decrease of charge carriers with time

$$Q^* = qN_0\left\{\frac{v_h\tau_h}{d}\left[1-exp(\frac{z-d}{v_h\tau_h})\right]+\frac{v\tau_{ee}}{d}\left[1-exp(\frac{-z}{v_e\tau_e})\right]\right\}. \tag{3.3}$$

$v_{e,h}$ denote the electron and hole drift velocities and $\tau_{e,h}$ the respective carrier lifetimes. A related figure is the charge collection efficiency (CCE) defined as the total charge induced at the electrodes normalized to the total charge created in the detector volume

$$CCE = \frac{Q^*}{q_eN_0}. \tag{3.4}$$

For a segmented electrode geometry the calculation of the induced current is more complex. In this case Ramo's theory is described in terms of a weighting field

$$I_j(t) = \Sigma_i q_e\vec{v}_i(r,t)\cdot\vec{E}_{Wj}(r). \tag{3.5}$$

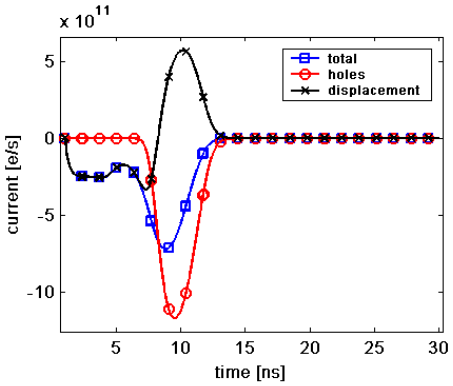


Figure 3.1: Induced charge on the p^+ electrode of a p^+n diode for a 10 keV photon converted in 150 µm distance from the pixel collection electrode in a 300 µm thick Si sensor of 55 µm pixel size.

with $\vec{v_i}$ the velocity of the i^{th} carrier in the detector volume. The weighting field is calculated by solving the Poisson equation for the detector geometry with the j^{th} electrode set to a unity potential and all other electrodes kept at zero potential. In the case of a planar detector geometry with an electrode size much larger than the electrode distance eq. 3.5 becomes $I = q_e \mu \vec{E}/d$. By integrating eq. 3.5 over the drift time the total charge induced can be written as the difference of a weighing potential Φ_{Wj} between the point of charge creation and charge collection

$$Q = q_e \Delta \Phi_{Wj}.$$

The shape of the weighting potential depends on the pixel geometry. With the common electrode on the back side of the detector and an array of small pixel electrodes on the front-end side the weighting field is strongest close to the pixel electrode. The smaller the pixel size as compared to the detector thickness, the more the weighting potential field is restricted to regions close to the pixel contact. This is also called the small pixel effect and is beneficial in particular if charge trapping occurs [52–55]. The very localised weighting fields of pixels with a large aspect ratio allows to minimize the contribution of the trapped carrier type by collecting it via the common electrode. The induced signal on the pixel electrode will only contribute significantly if the charge generation takes place very close to the pixel electrode. A further consequence of the small pixel effect is that the electrode signal rise time becomes almost independent of the position of charge generation interaction. Fig. 3.2 shows the weighting potential along the pixel symmetry axis for different pixel aspect ratios.

3.3 Direct and indirect detection

Depending on the type and energy of the incident radiation there are two possibilities to convert ionizing radiation into an electrical signals: direct and indirect conversion. In the case of direct conversion the incoming radiation directly generates e-h pairs in

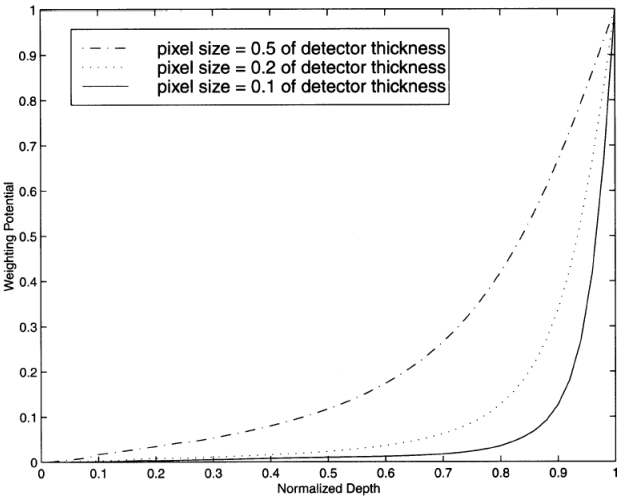


Figure 3.2: The weighting potentials for three different pixel sizes in dependence of the normalized detector depth [29].

the semiconductor detector volume. Common materials for direct detection systems are Si and amorphous Se in combination with active matrix flat panel imagers (AMFPI), charged coupled devices (CCD) or complementary metal-oxide-semiconductor (CMOS) readout electronics. Direct detection systems offer high spatial resolution and high energy resolution. At photon energies in the range of general medical applications Si offers only reduced stopping power. Alternative materials like GaAs or CdTe present higher stopping power, but large areas of homogeneous material are difficult to produce. Amorphous Se can be deposited over large areas and provides a stopping power comparable to GaAs. On the other hand charge trapping and detrapping leads to ghosting and lag in image formation [56].

The indirect detection approach increases the quantum detection efficiency by placing a scintillator layer on top of a semiconductor detector which is sensitive to visible light. The scintillator first converts the primary radiation into visible light, which then is converted into an electrical signal in the semiconductor detector. The most common indirect detector systems use CCD or AMFPI readout schemes. The main differences in image formation in these systems as compared to direct detection systems is given by the much less favourable statistics of secondary photon generation and the transport of optical photons within the scintillator. The mean energy necessary to produce a secondary photon is in the range of $>\sim$20 eV as compared to 3.6 eV per electron hole pair in Si. Light spread in the conversion layer lead to a reduction of contrast and spatial resolution. Secondary quantum noise and the loss of optical photons and the escape of K-edge fluorescent photons lead to a reduction of the achievable SNR. In addition the lateral light spread in the scintillator depends on the depth of the X-ray conversion, introducing a X-ray energy depended blurring. Since the overall system performance depends both on resolution and contrast as well as the detection efficiency, the choice of detection type is application dependent. Comparative measurement between direct and indirect detector AMFPI and CCD systems in medical radiography can be found in [4, 39, 57].

3.4 Integrating detector systems versus single event pulse processing

There are two competing concepts to translate the information contained in the charge pulse per converted photon: signal integration or single event pulse processing. Apart from the technical implementation the principal difference lies in the way the information is translated into image data.

Signal integration: In this approach the collected current pulse produced by each X-ray interaction is added to an potential well or a capacitor without any further treatment. This implies that any currents originating from other sources than the detected signal, such as detector leakage currents, are also added and introduce noise to the accumulated signal. Main sources are leakage currents, background radiation. Especially in low count rate applications, where long acquisition times are required, the integrated noise becomes more pronounced.

The number of charges generated by a photon is directly proportional to its energy. Therefore the contribution of the converted photons is weighted by their energy. Image contrast is generated by the absorption of photons in the object. Since low energy photons are attenuated more strongly in the object, they carry more information. By weighting the photon by its energy, image contrast carried by low energy photons has a weaker weight and the Poisson noise contributions from high energy photons is enhanced. The result is a decrease in image SNR.

Single event pulse processing: A different approach is used in single event processing systems. Here the quantity accumulated in a pixel is not necessarily proportional to the energy deposited by the individual particle, but rather a derived value which only is added after being tested against a selection criteria.

In the case of photon counting the selection criteria is the allowed range for the measured pulse height and the derived value the binary result of the thresholding process. In this way the contribution of detector leakage currents to the image noise can be excluded. Photon counting removes this built-in weighting of photons and only registers the validity of an event, thereby increasing the SNR.

Energy weighting: Single event pulse processing opens the possibility to counteract the effects of the energy dependent attenuation of X-rays in matter on the SNR. As mentioned above simple integration of the energy deposited by each photon over-emphasizes the signal carried by high energy photons, leading to an enhanced noise contribution of those photons carrying the least information. By appropriately selecting the weighting factor, w, as a function of photon energy, E, the image SNR can be optimized. For a photon energy spectrum passing trough two adjacent regions with different absorption coefficients, the SNR can be written following eq. 2.11

$$SNR = \frac{\int_E w(E)\left(\langle n_1(E)\rangle - \langle n_2(E)\rangle\right)}{\sqrt{w_i^2\left(\langle n_1\rangle + \langle n_{2,i}\rangle\right)}} \tag{3.6}$$

where $n_{1,2}$ denotes the number of photons recorded in two adjacent regions. It has been shown that the optimal weighting function is given by [58–60]

$$w_{opt}(E) = \frac{T_1(E) - T_2(E)}{T_1(E) + T_2(E)}. \tag{3.7}$$

with $T_{1,2}$ the transmission trough region one and respectively. This optimal weight function can only be calculated if the exact composition and thicknesses in the object are known already. For low contrast objects the weight function can be approximated to be $w \sim E^{-3}$. The effects of energy weighting on the achievable image SNR will be discussed in detail in sec. 5.4.

3.5 Detector technologies

3.5.1 CCD

A charge coupled device imager (CCD) consists of an array of potential wells in a metal-oxide-semiconductor chip. Gate electrodes built on top of the insulating oxide layer and create a depleted zone in the semiconductor underneath the oxide. The pixels are organized in parallel columns by implanted potential barriers [1, 23]. Photo-charges generated in the semiconductor are accumulated in the potential wells. The readout is accomplished by clocking the gate potentials in such a way that the accumulated charge packets are shifted down the pixel columns. At the end of the columns an analog output shift register transports the charge packets to an on-chip preamplifier. The main advantage of this structure is the very low input capacitance presented to the preamplifier, which allows for noise figures down to a few electrons rms in devices cooled to $<\sim 130°$ C. The main disadvantages are that the detector is still sensitive to radiation and leakage currents during the readout charge transport from pixel to pixel and that the pixels values have to be processed serially by the preamplifier. This limits the achievable readout speed and also links the noise performance to the readout speed. Furthermore the dynamic range is limited by the potential well, usually is in the order of 10^5 e^- [1] and the minimal charge signal of $\sim$100 e^-.

The CCD itself is weakly sensitive to X-rays, since the depletion is only several μm. Therefore most X-ray imaging CCD are coupled to scintillating materials like CsI(Tl) or Gd^2O^2S. As already described, in this indirect detection scheme the achievable spatial resolution is limited by the light spread of the scintillator layer. Although pixel sizes for CCD systems in medical application may be as small as 25 μm, the spatial resolution is in the order of $\sim$5 lp/mm [4, 61].

3.5.2 Flat Panel Imager

Active matrix flat panel imagers (AMFPI) use thin film transistor (TFT) or thin film diode (TFD) arrays as readout electronics. In such devices each pixel element contains a converter, a charge storage node, and readout switch. Flat panel imagers are based on amorphous silicon and use a similar manufacturing process as liquid crystal displays, allowing for large areas to be covered. Typically the readout electronics is deposited onto

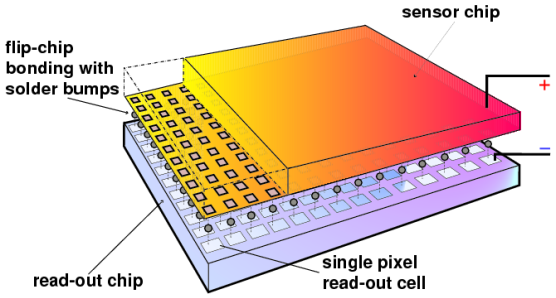


Figure 3.3: Schematic of a hybrid pixel detector with the sensor chip and the electronics chip connected via bump bonds.

a glass substrate. Pixel sizes range from 100 to 400 μm [40, 57, 62]. In the case of a direct detection system, the converter layer, e.g. amorphous Se [40], is deposited directly on the readout. In indirect systems a layer of light sensitive photodiode is deposited on top of the TFT, followed by the scintillator. The necessity to implement the photodiode leads to a reduced fill factor, i.e. a reduction in active area per pixel cell. The readout switches connect a row of pixels to charge amplifiers located at the bottom of the columns. In this way the readout time can be significantly improved with respect to CCD systems. The main advantage of AMFPI over CCDs is that large areas can be covered. The biggest drawback is the relatively high readout noise of $\sim$1300 e^- [63].

3.5.3 CMOS hybrid pixel detector

The advances in CMOS technology made it possible to integrate sophisticated readout electronics on the pixel scale. As opposed to the detector systems described above this approach allows for real time signal processing per detected particle and digitalization already in the pixel cell. The electronics noise in the pixel cell is much lower than in the AMFPI, since the detector pixel elements are directly connected to the readout electronics, therefore keeping the input capacitance to the preamplifier very low. Originating in HEP, where the objective is to detect the crossing point of a minimum ionising particle with high spatial and temporal precision this detection technique has also been adapted to imaging purposes, c.f. 4.

In the hybrid pixel detector architecture, Fig. 3.3, the radiation sensor element and the readout are processed separately. The sensor is segmented with the same geometry as the readout chip and detector and readout cells are connected individually. The connection is provided by small indium or solder bumps with a diameter in the order of 20 μm. This interconnect can be achieved by standard flip-chip technology. The separation in processing allows for independent optimisation of readout and sensor and different sensor materials can be used with the same readout. By developing the readout electronics using standard CMOS technology the increase in component density can be fully exploited and advanced signal processing such as energy discrimination and digitalisation can be performed on the pixel level.

Chapter 4

The Medipix Project

Hybrid pixel detectors were developed at CERN since 1998 [64], were first tested in a three pixel-chip telescope in 1991 [65] and finally successfully used in the lead beam experiment WA97 at CERN [66]. Since then pixel detectors have become key components in particle physics experiments, notably for tracking detectors with high detector occupancy. They provide high spatial resolution, high detection efficiency and make it possible to reconstruct tracks in an high-multiplicity environment [67]. Radioactive sources have been used routinely to calibrate the test-input charge for tracking detectors which proved their ability to detect X-rays and γ-rays. The requirements for the readout in HEP still differs substantially from the ones for imaging, the most obvious one being the rectangular pixel shape used in HEP, c.f. table 3.1.

An attempt to transfer the know-how gained in HEP to the design of a general purpose X-ray imaging detector was undertaken in the microelectronics group at CERN within the framework of the Medipix1-collaboration [68] and resulted in the Medipix1 or PCC (Photon Counting Chip) readout chip [16]. This chip has been tested successfully and has been used in a wide range of applications[1]. It proved that the photon counting approach can provide high resolution images of excellent dynamic range and an image noise approaching photon statistics. The performance of the system was limited mainly by the size of the pixel (170 μm x 170 μm), which was determined by the component density of the 1 μm CMOS process used. Encouraged by the results the successor, Medipix2, was designed, providing improvements in several key characteristics.

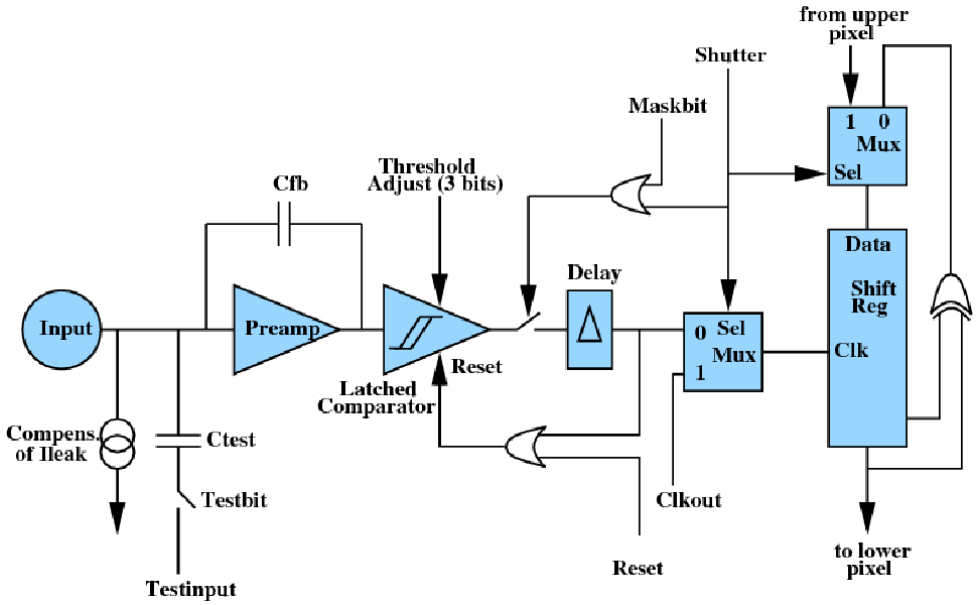
The following section describes the functionality of both generation of the Medipix readout chip. Furthermore a description of the readout systems used with the chips and their calibration procedures will be given.

4.1 Medipix1

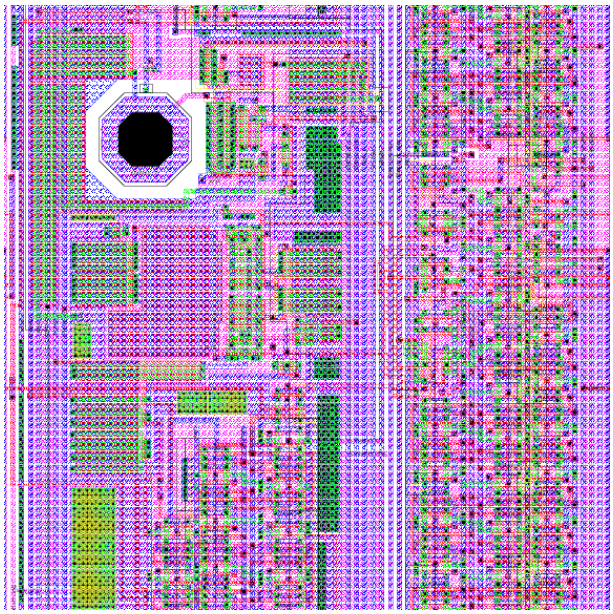
4.1.1 Medipix1 chip

The Medipix1 chip [16] has been developed as a direct spin-off from HEP using building blocks of the Omega3-LHC1 chip [69] by adapting functionality and pixel shape to imaging

[1] For a list of publication the reader is referred to the collaboration homepage: http://medipix.web.cern.ch/MEDIPIX/



(a)



(b)

Figure 4.1: a) The functional block diagram of the Medipix1 pixel cell. b) The CAD layout of the pixel cell.

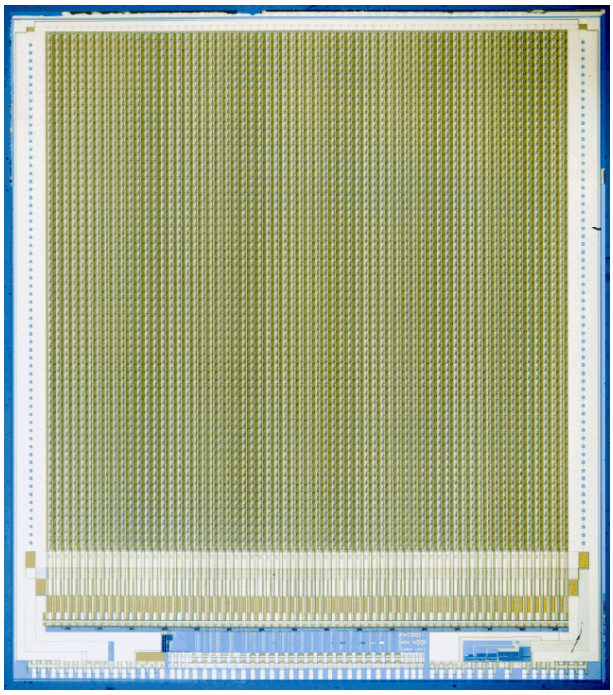


Figure 4.2: A photograph of a Medipix1 chip without the sensor chip mounted. The 64x64 pixel array in the upper part is the active chip area that will be connected to the sensor chip. Two pixel row at the lower end of the array are not used for particle detection purposes but serve for leakage-current sensing and connect the sensor guard-ring to the chip ground. The bottom part of the chip contains the I/O functionality.

requirements. The chip was designed as a multi purpose readout chip for various imaging applications and was fabricated in a 1 μm SACMOS (Self-aligning Complementary Metal-oxide Semiconductor) process with a component density comparable to a 0.6 μm CMOS process. The total chip area covers ∼12.25 mm x ∼14 mm, whilst the active area of 1.18 cm^2 consists of a 64x64 array of square photon counting pixels of 170x170 μm^2. The bottom of the pixel array is not sensitive to input from the radiation sensor chip and is used to implement auxiliary functionality, including

- An additional 65$^{\text{th}}$ pixel row, which consists of dummy pixels for sensing of the sensor leakage current. The detected leakage current is first mirrored and then inversed in polarity. A copy is fed back into the input of each pixel in the column to correct for signal offset due to dark currents. Note that this scheme assumes the leakage current to be uniform in each column of pixels. This assumption does not hold true for some sensor materials [70]. The leakage current compensation can compensate up to 10 nA per pixel (∼35 μA/cm^2).
- A 66th row of bump bonds to connect the sensor guard-ring with ground. The guard-ring structure is a continuous p^+ implant in the sensor chip similar to the one of the pixel electrodes. It surrounds the pixel array on the front-end side of the sensor parallel to the sensor edge and shields the pixel array from leakage currents generated by defects at the diced edge of the sensor. The width of the guard ring structure is of the same order of magnitude as the sensor thickness in order to ensure controlled electrical field conditions at the outer pixels.
- Wire-bonding pads for power supply and signal lines.
- A 16-bit bus used for both writing the configuration bits and reading out the data.

4.1.1.1 Pixel cell

Each cell comprises a charge sensitive preamplifier, a comparator with variable threshold and a 15-bit pseudo-random counter. Fig. 4.1 shows the pixel functional schematic and the layout.

Preamplifier: The charge sensitive preamplifier is sensitive to positive input signals only. The feedback capacitance of C_{fb}= 3.5 fF yields a voltage gain of 285 mV/fC input charge. The signal rise time is controlled by V_{bias} and is typically in the order of 150 ns. V_{comp} controls the leakage current compensation circuit and the return-to-zero time of the preamplifier.

Comparator: The preamplifier signal is fed into a latched comparator, whose threshold is set globally on the entire pixel array via V_{th}. To adjust the threshold level in every pixel, a 3-bit threshold adjustment circuitry is added in each pixel, which allows to scale

an adjustment bias V_{tha} in 8 steps individually for each pixel. If the preamplifier signal exceeds the threshold level, a digital pulse is produced by the latched comparator and sent to the counter. The width of this pulse is determined by V_{dl}. It controls an adjustable delay line, which feeds back the comparator output to its reset. In this way an artificial but controlled non-paralyzeable dead-time is introduced, ensuring a well-defined relation between registered counts and real number of events even at very high count rates.

Counter: The 15-bit pseudo-random counter/shift register [71] of each pixel is connected serially with its neighbouring pixels in a column and has two operation modes: counting and readout. The operation mode is selected via an external shutter signal lines, which controls the acquisition time. When the shutter signal level is low, the chip is in acquisition mode and the output pulse signals from discriminator circuit are sent to the counter. When the shutter signal is high, the output from the comparator is disconnected from the delay line and shift register is switched to readout mode.

4.1.1.2 Periphery

In readout mode an external clock is used to shift out the contents of the 4096 counter registers via a 16-bit bidirectional data bus at the bottom of the chip. The maximum frequency for the external readout clock is 10 MHz, resulting in a readout time of the whole chip of 384 μs. Each pixel has five configuration bits, of which three are used for the threshold fine-tuning, and one for each masking not-working pixels and to set a pixel to test input mode. The bidirectional 16-bit bus is also used to load the configuration bits to the five configuration bits per pixel, which are connected in series in the columns.

4.1.1.3 Supply and bias voltages

The chip needs four supply voltages, namely

- V_{dd}: the digital power supply
- V_{dda}: the analog power supply
- V_{gnd}: the analog reference ground
- V_{ss}: the system ground.

The standard values for these voltages are $V_{dd} = V_{dda} = 3V$, $V_{gnd} = 1.5V$ and were supplied by an external DC power supply[2]. The values for V_{bias}, V_{comp}, V_{th} and V_{tha} have to be optimized individually for each chip, depending on the application requirements. These five bias voltages have to be supplied externally by the readout electronics

[2]Gossen Konstanter LSP.

4.1.2 External read-out electronics

Two distinct readout system for the Medipix1 exist at CERN . The system used for almost all measurements in this thesis with the Medipix1 was the VME based **MRS** (Laben Medipix Readout System) system [72], which was fabricated by Laben together with INFN Pisa. The main components are a PCB chipboard, a motherboard and a VME card.

The chipboard, onto which up to two Medipix1 chips can be glued and wired-bonded, provides mechanical support for the chip and connects the chip to the supply and control lines. It also holds the connector for the sensor bias.

The operation of the VME-card is controlled via a VME bus-master card and a VME-PCI interface card. The readout software used was a modified and extended version of the readout software Medisoft 2.2 provided by the University of Napoli [72].

The main functionality of the motherboard is to to act as level translators from 5 V TTL down to 3 V CMOS logic and to forward the test pulse and the chip bias voltages to the chipboard. The VME card contains all the logic required for the readout as well as DACs to provide the five analogue bias voltages.

A more compact set-up has been developed by NIKHEF, Amsterdam [73]. It is based on standard commercial analogue and digital I/O boards[3] and a dedicated interface board **Muros1** (Medipix1 re-Usable Read-Out System). In principle no other hardware components are necessary, apart from the high voltage supply for the sensor. The main functionality of the Muros1 is to provide the power supply for the Medipix circuit, the clamping of the digital TTL signals to CMOS level and to generate the test pulse for chip testing and calibration. Only the standard values for the supply voltages given above are provided by the Muros1. In practice the five bias voltage have been taken from a analogue DC power supply, since in some cases differing values are needed.

4.1.3 Threshold Adjustment procedure

The detector performance of the Medipix1 depends strongly on the values chosen for the analog bias voltages for V_{bias} and V_{comp}. As already mentioned in sec. 4.1, the preamplifier gains can vary slightly from pixel to pixel. The pixel threshold values across the array have a Gaussian distribution with a typical spread of 450-600 e- rms without threshold adjustment. In order to reduce the threshold spread the optimal values for the 3-bit threshold adjustment per pixel has to be determined.

The readout chain of each pixel can be tested by injecting a test pulse on the test input capacitance of 24.3±1 fF [74]. Test pulses of 300 ns width are supplied by the Muros1 pulse generator. Normally a burst of 1000 pulses is used at a fixed global threshold voltage V_{th}, and the value of the pulse amplitude is increased in fine steps until all 1000 pulse are counted, leading to an s-curve of registered counts over pulse amplitude. The actual threshold of a pixel then is determined by the pulse amplitude at which 50 % of the pulses are counted. If a pixel fails to count more then 50% of the pulses even at high pulse amplitudes then it is regarded as not working. Pixels are considered as noisy if the

[3] Analogue board AT-AO-10, digital board PCI-DIO-32HS. Manufacturer: National Instruments Corporation, 6504 Bridge Point Parkway, Austin, TX 78730-5039.

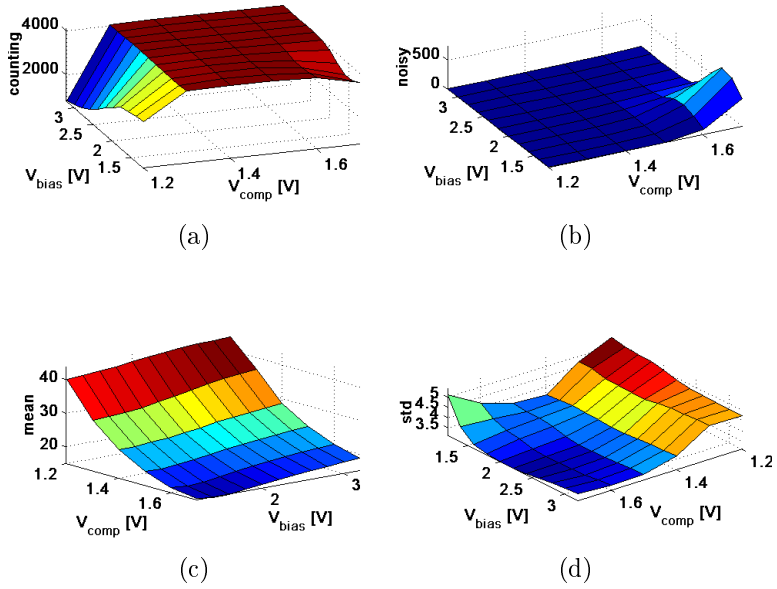


Figure 4.3: A typical result of a V_{bias}/V_{comp} scan to find the optimal working point for a given application. Plotted are a) the number of counting pixels, b) the number of noisy pixels, c) the mean threshold , c) the standard deviation of the threshold plotted against the bias voltage.

count exceeds a given threshold count, usually 3 counts, for pulse amplitudes well below the threshold. The values for the minimal achievable mean threshold, its unadjusted spread across the pixel array, the number of correctly counting and the number of noisy pixels are linked and depend on the settings of the analog bias voltages V_{bias} and V_{comp}. A 3-bit threshold adjustment fine-tunes the globally set threshold for the individual pixel, with the range of the maximal adjustment controlled by V_{tha}. The procedure of threshold tuning consists of three steps:

- First a working point for the values of V_{bias} and V_{comp} has to be selected. This is done by scanning the range of possible combinations for the values of V_{bias} and V_{comp} and measuring the mean threshold, the threshold spread, the number of counting pixels and the number of noisy pixels as described above. The value for V_{th} has to be set so that the full width of the threshold distribution is above the noise floor of the electronics. In the selection of the working point for V_{bias} and V_{comp} the number of working and noisy pixels and the threshold spread has to be optimised against the minimal average threshold. An example of such a scan is given in Fig. 4.3.

- Next the optimal value of the adjustment bit has to be found by measuring the threshold distribution for all 8 possible values of the adjustment set uniformly over the whole array. Here the value of V_{tha} has to be set so that the threshold distribu-

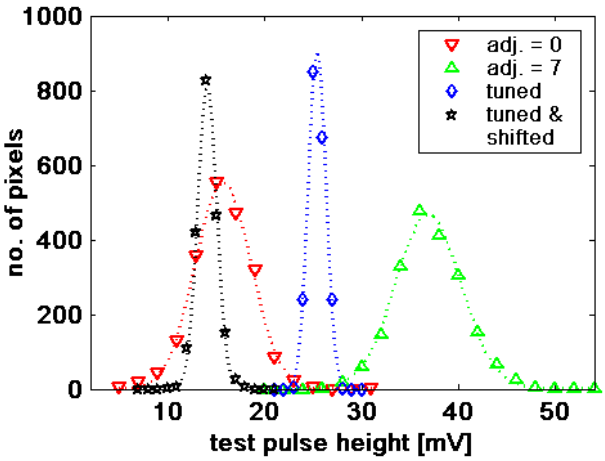


Figure 4.4: The Medipix1 3-bit threshold adjustment. Plotted are the threshold distribution with the adjustment value set to 0 in all pixels and the one with the adjustment value set to 7 (the distributions for the intermediate adjustment values are not plotted for reason of clarity). To obtain the best compression of the threshold dispersion, these two curves should overlap by $1/8^{th}$ of their full width. The adjustment mask is generated by selecting for each pixel the adjustment value which results in the threshold closest to the midpoint between the two curves. The fine tuned threshold distribution then is centered at this midpoint and can be shifted to lower mean threshold values by lowering the global bias voltage V_{th}.

tions for the adjustment bit equal to 0 and the one equal to 7 overlap for 1/8 of the distribution width.

- The mid-value between the mean threshold with adjustment set to 0 and the one with adjustment set to 7 marks the targeted center of the adjusted threshold distribution. For each pixel the adjustment value giving the threshold closest to the targeted center value is selected for the final adjustment map.

The procedure is illustrated in Fig. 4.4. The threshold distributions corresponding to the adjustment values set uniformly to 0 and 7 respectively are plotted, together with the compressed distribution centered around the overlap of the unadjusted distributions. The spread of the threshold values is reduced from a value of 3-4 mV down to 0.8-1.2 mV, corresponding to 120-180 e^- rms. After this optimization the tuned distribution can be shifted to lower or higher thresholds by changing the value for V_{th}. For high thresholds it has to be kept in mind, that the mean threshold characteristic is linear only for values for of $V_{th} \leq 1.5\,V$ [74].

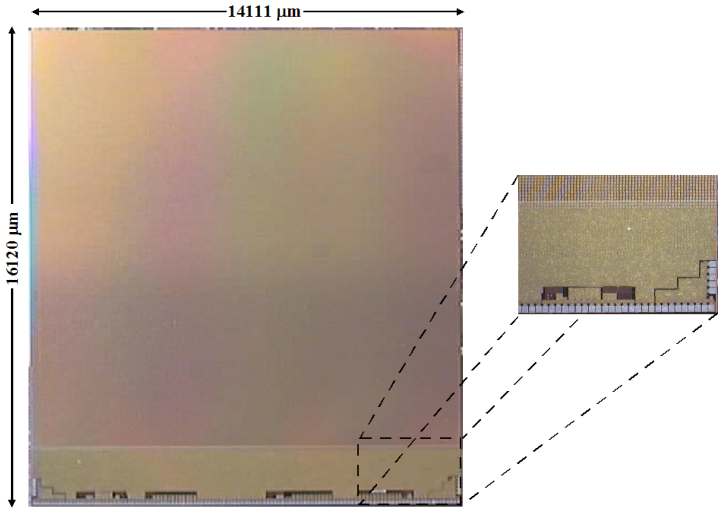


Figure 4.5: A photograph of the Medipix2 readout chip. The zoom shows the area implementing the five lateral I/O wire-bonding pads that can be used to form a daisy-chain of multiple chips.

4.2 Medipix2

The excellent performance of the Medipix1 served as a proof-of-concept for the single photon counting approach for imaging applications. The performance of the Medipix1 was limited mainly by its pixel size of 170x170 μm, which was determined by the component density of the 1 μm CMOS process available at the time of design. To benefit from the much more advanced 0.25 μm CMOS technology a complete redesign of the readout chip was undertaken in the microelectronics group at CERN within the framework of the Medipix2 collaboration [17].

4.2.1 Medipix2 chip

The main objective in the design of the Medipix2 chip was to reduce the pixel size to 55x55 μm^2 in order to obtain a spatial resolution comparable to commercially available integrating detectors like CCD or AMFPI systems. The big increase in component density offered by 0.25 μm CMOS technology, due to shrinking component size and increasing number of metal interconnect layers, allowed not only to decrease the pixel size but also to add new functionality:

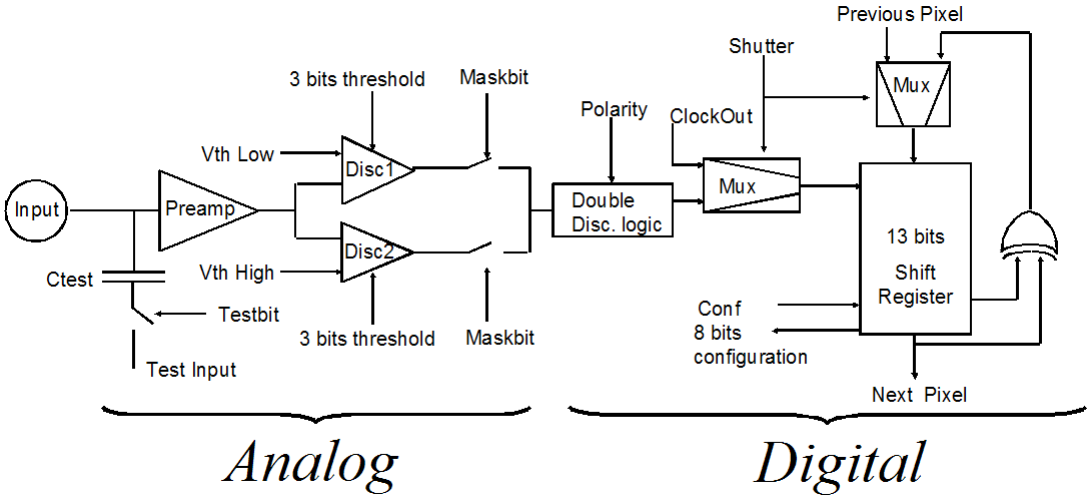
- the charge sensitive preamplifier accepts both polarities as input signal, opening the possibility to use alternative detector materials
- leakage current compensation per pixel
- serial and parallel readout

0.25 μm CMOS design technology		
Butt-ability on three sides, daisy chain connection between chips		
Window threshold discrimination		
Square pixel size	55 μm	
Sensitive area	14.08 $\times$ 14.08 μm^2	
Ratio (sensitive area/total chip area)	87%	
Analogue and digital supply voltage	2.2 V	
Total static power consumption	500 mW	
Pixel counter depth	13 bit	
Max. count rate per pixel	1 MHz	
Test input capacitance	8 fF	
Threshold dispersion rms (adjusted)	500 e$^-$ (100 e$^-$)	
Serial read-out time @ 100 MHz	9.17 ms	
Parallel read-out time @ 100 MHz	280 μs	
Radiation tolerance	200 krad (10 keV x-ray)	
	electrons	holes
Preamplifier Gain	12.5 mV/1ke$^-$	13.25 mV/1ke$^-$
Peaking time	150 ns	150 ns
Linearity	$<$3 % up to 100 ke$^-$	$<$3 % up to 80 kh$^+$
Leakage current compensation	-7 to 0 nA per pixel	0 to $\sim$20 nA per pixel
	-2.3 to 0 mA/mm^2	0 to $\sim$6.6 mA/mm^2
Electronic Noise	$\sim$90 e$^-$ @ I_{leak}=0 nA	$\sim$120 e$^-$ @ I_{leak}=10 nA
DDL pulse width	300 ns-1.2 μs	300 ns-1.2 μs

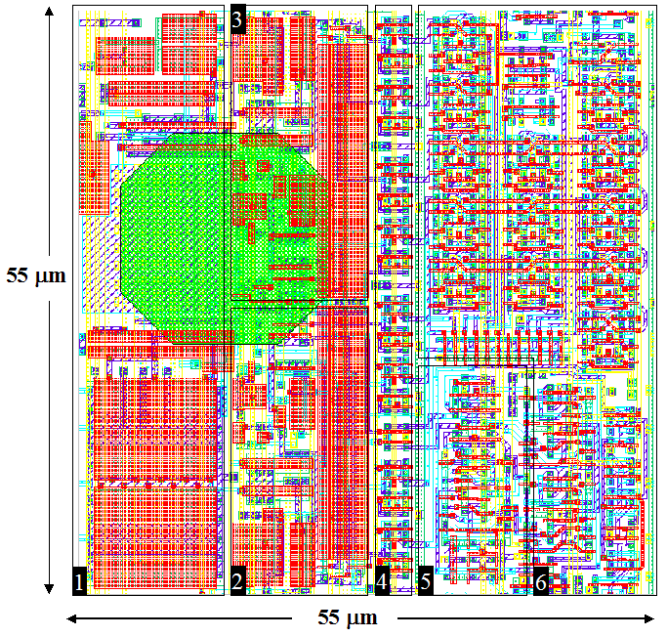
Table 4.1: A breakdown of the system and performance parameters of the MPX2

- on-chip DACs that set the biasing conditions to operate the chip, providing improved temperature stability
- three side butt-able to cover large areas
- two energy thresholds allowing for energy window discrimination

The total number of transistors per pixel increased to $\sim$500, giving around 33 m transistors per chip (comparable to a Pentium IV processor) and a static power consumption of $\sim$8 μW per pixel. Thirteen 8-bit DACs control the chip operation and set the working point globally for the whole pixel array. Each pixel has eight independent configuration bits. Six bits are used for the per-pixel fine tuning of the two thresholds (three bits for each discriminator), one bit for masking noisy pixels and one to enable the input charge test through the 8 fF on-pixel capacitance. An overview of the main feature and characteristic figures of the Medipix2 is given in table 4.1.



(a)



(b)

Figure 4.6: Medipix2 pixel cell layout [17]. a) Functional block diagram. b) 1: Preamplifier. 2: High threshold Discriminator. 3: Low threshold discriminator. 4: 8-bit configuration register. 5: Double discriminator logic. 6: Shift register and control logic. The octagonal bump bond opening has a diameter of 20 µm.

4.2.1.1 Pixel Cell

Each pixel cell comprises a charge sensitive preamplifier, two discriminators, a Double Discrimination Logic (DDL) and a counter. The functional schematics of the pixel cell is shown in Fig. 4.6a). Fig. 4.6b) shows the layout of the pixel cell.

Charge preamplifier Particular care has been taken in the design of the charge preamplifier to reject noise stemming from the chip substrate or from the power supplies. The working point of the preamplifier is controlled by four DACs: $PREAMP$, GND, FBK and $IKRUM$. $PREAMP$ controls the preamplifier gain and the rise time of the voltage output pulse. GND sets the preamplifier DC input level, FBK determines DC output voltage of the the preamplifier and is used to optimize the dynamic range. $IKRUM$ determines the return-to-zero of the output voltage pulse and also sets the limit for the leakage current compensation in electron collection mode.

Discriminator The output of the preamplifier is fed into two identical but independent discriminators. The pulse heights of the preamplifier output is compared simultaneously with the upper threshold, $VthHigh$, and the lower threshold, $VthLow$. Two different DACs control the threshold levels: THL sets the value for $VthLow$ and THH for $VthHigh$. Three adjustment bits are used per threshold to fine tune the respective level in each pixel in order to minimize the threshold dispersion across the array.

DDL The output of the two discriminators is then processed in the DDL. It can be operated in two modes: single threshold mode or energy window mode. If the $VthHigh$ is set lower than $VthLow$, the chip is in single threshold mode and all particles exceeding the lower threshold are counted. In energy window mode the difference of the two levels determines the range of valid pulse heights, corresponding to the energy window into which the incoming particle energy has to fall in order to increment the counter. For each valid events a pulse of adjustable length is generated at the output of the DDL and sent to the counter. The length of this pulse controlled via the $DelayN$ DAC. In this way the dead-time behaviour of the chip can be kept in a non-paralyzeable regime and the relation between count rate and true event rate is kept unambiguous even at very high count rates.

Counter The counter is implemented as a 13 bit pseudo-random counter/shift register with a counter depth of 8001 counts, providing about twice dynamic range per unit area as the Medipix1. Analogous to the Medipix1 the operation mode is controlled by a shutter signal. When the Shutter is low the shift register works as a pseudo-random counter. When the Shutter is high the counter contents are shifted out column-wise in a serial fashion using an external clock. The same shift register is used both for setting the 8 configuration bits and for reading the 13-bit counter information.

4.2.1.2 Periphery

One of the aims in the design was to provide the possibility to cover larger areas. In order to achieve this goal, the dead space between chips had to be kept as low as possible. The

entire periphery was placed at the bottom of the chip and the non-sensitive area in the other three edges was reduced to less than 50 μm, leaving 87 % of the total area that can be covered by a sensor that is sensitive to radiation.

The periphery contains 13 8-bit DACs, which set the different bias voltages in the chip, a 256-bit Fast Shift Register (FSR) to write to or read from the pixel array, 127 wire bonding pads for power supply and signal lines and Low Voltage Differential Signaling (LVDS) drivers and receivers. To read out the pixel counters or to write configuration bits into the pixels, the whole array is organized in 256 columns of 256x13 bits. Therefore each chip has 851968 bits to be read or written for any array I/O operation. All I/O operations, including setting the values of the thirteen 8-bit DACs and the 8-bit configuration registers per pixel, can be performed using the a high-speed LVDS output drivers. For applications requiring a high frame rate, an alternative parallel readout via a 32-bit single-ended CMOS bus is provided. The readout time for the entire array using an external clock of 100 MHz is ~9 ms using the serial port. The parallel reduces the readout time to 280 μs.

Five lateral I/O wire-bonding pads can be used to form a daisy-chain of multiple chips. Since the minimal space between two neighbouring chips in such a daisy chain is ~150 μm, a row or a column of 165 μm wide pixels is introduced inbetween two neighbouring chips. A chip board for a 2x4 multi chip detector without any dead-space has been fabricated by NIKHEF [75].

4.2.2 External read-out electronics

The Muros2 (Medipix2 re-Usable Readout System version 2) board has been designed by NIKHEF [76]. The following section summarizes the functionality of the Muros2. A detailed description can be found in [77].

The Muros2 acts as an interface between a board carrying a maximum of eight Medipix2 chips and a commercial data acquisition card[4]. The only additional equipment needed to operate the Muros2 is a 3.3 V DC power supply. All the supply voltages for the different Muros2 circuits and the voltages for the analog and the digital power supply for the Medipix2 are generated. The clock signals for the communication between the Muros2 and the data-acquisition card and the Medipix2 respectively are provided. The data transmission and the chip control logic are implemented using a FPGA. In addition, the external clock for the Medipix2 and the clock for the data transmission between the FPGA and the PC is generated in the FPGA. This clock is also used to hardware-control the acquisition time.

The Muros2 board supports only serial communication with the Medipix2 via LVDS drivers and receivers. Level converters handle the differences in the logic levels of the data acquisition card (TTL), the FPGA (3.3V CMOS) and the Medipix2 chips (2.2V CMOS).

A test-pulse generator is realized on the board for chip-testing and for fine-tuning the energy thresholds. The height and the length of the test pulse is set via 2 on-board 12-bit DACs. A third on-board 12-bit DAC can be used to override one of the internal DACs in the Medipix2 chip if a higher precision than the 8-bit on-chip DAC is needed. A forth DAC gives the opportunity to control an external high-voltage supply for the sensor chip.

[4]National Instruments DIO-653X board.

The value of the bias voltages generated inside the Medipix2 can be monitored using an 16-bit ADC on the Muros2.

The read-out software to operate the Medipix2/Muros2 system has been developed by the University of Napoli [78].

4.2.3 Threshold adjustment procedure

The threshold adjustment procedure foreseen for the Medipix2 follows the same approach as the one described above for the Medipix1. Despite additional analog buffers placed at the bottom of every column, in order to minimize the voltage pulse rise-time over the whole column, an attenuation of the test pulse due to the capacitance and resistance of the internal electrical connections has been found. Therefore an alternative approach has been used to determine the threshold adjustment mask.

4.2.3.1 Low threshold

As opposed to the Medipix1 routine, where the signal height is scanned over a fixed discriminator threshold, here the input signal is kept constant while scanning the threshold level over a fixed height input signal for all eight possible values for the adjustment mask. In this way eight different s-curves are obtained per pixel. The fixed height input then can either stem from a pulse generator or any other source, like a monochromatic line of a radioactive source, e.g. ^{109}Cd. The criteria for a pixel to be regarded counting here is the threshold setting applied at which 50% of the input signal pulses is counted. The further calibration procedure is analogous to the pulser calibration described above for the Medipix1.

The limited activity of available radioactive sources renders this adjustment procedure extremely time consuming, and ,since the recorded number of counts in a pixel obeys Poisson statistics, a very large number of counts is required for accurate determination of the s-curves. Alternatively the so-called noise floor of the readout chip, meaning the noise signal induced at the input of the preamplifier by the digital part of the pixel electronics, can be used as reference signal. Since all pixels in the readout chip are identical, apart from process related mismatch of transistors, the level of this noise signal is considered to be uniform across the active array. The midpoint of the s-curve as criteria to mark a pixel counting has to be replaced by a minimum number of counts, since the number of noise counts per time unit cannot be predicted. The result of the 8 threshold scans are Gaussian distributions of threshold voltages. The tuning parameter THS determines the overlap of the individual scurves. To obtain an optimal compression of the threshold spread THS has to be chosen so that the Gaussian distributions obtained with the adjustment value set to 0 and 8 overlap by 1/8 of the width. Then for each pixel the adjustment value giving the threshold closest to the crossing point of the uncompressed distributions is chosen to obtain the compressed threshold distribution, Fig. 4.7. It has been shown [79], that differences in adjustment maps obtained using noise floor and radioactive sources lie within the accuracy of the 8-bit DAC setting the values for THS and THL and FBK respectively.

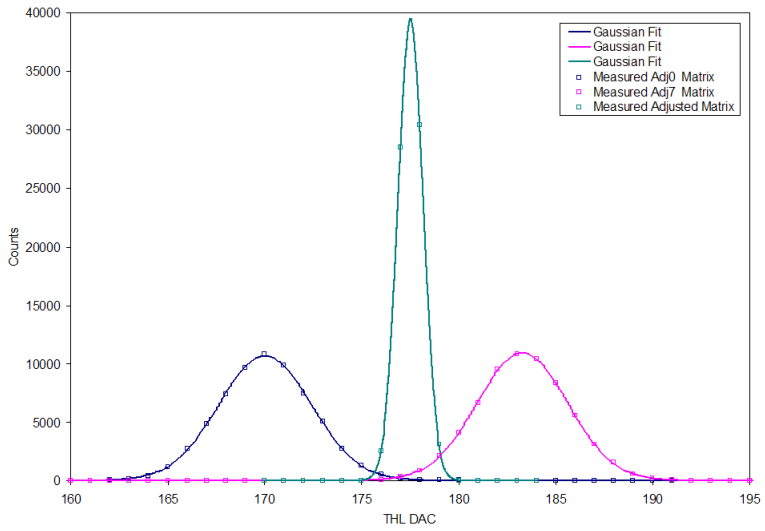


Figure 4.7: Example for the Medipix2 threshold tuning using the noise floor method [79]. Plotted are the threshold distribution with the adjustment value set to 0 in all pixels and the one with the adjustment value set to 7. The fine tuning is achieved by selecting for each pixel the adjustment value which results in the threshold closest to the midpoint between the two curves.

4.2.3.2 High threshold

The high threshold was kept at a fixed value and a very high input test pulse well above the high threshold was used. The energy window logic is such that if the high threshold DAC, THH, is set to a value lower than the low threshold DAC, THL, only the low threshold is used. In this way energy window operation or single threshold operation can be selected. This transition point between single threshold and double threshold mode is used as the reference point for the fine tuning of the high threshold. At the moment the high threshold crosses the lower threshold, the pixel switches to window mode and starts to count. The pixels were binned according to the high threshold value at which they began counting and an upper threshold mask thus derived. No correlation between upper and lower threshold masks could be found, which indicates that the threshold variation is not dominated by the common preamplifier.

Chapter 5

Detector Simulations

The design and the evaluation of a detector system as well as the correct interpretation of measured data necessitate the understanding of the characteristics and the limitations of each individual component of the system. In any detector system the first step of image formation is the conversion of incident X-ray energy into electric signals, which are to be further processed by the readout electronics.

For materials analysis and crystallographic applications the photon energy is normally limited to well below 100 keV. In medical radiography the photon energies of up to 200 keV may be used, whilst in nuclear medicine and other imaging applications the energy required can be even higher [9, 46]. Compton scattering, see Fig. 1.4, is the dominant effect above ∼40 keV for Si as sensor material, accounting for almost 80 % of the energy transfer at 100 keV. Together with a mean free path in the range of 2 cm and a most probable scattering angle of ∼40° for the scattered photon, c.f. 1.4c), this leads to significant decrease of resolution properties. As a comparison the corresponding values for CdTe at 100 keV are 6.5 % relative attenuation strength of the Compton effect and 800 μm mean free path length for the scattered photon. The inherent spatial and energy resolution provided by a given sensor material therefore strongly depends on the photon energy and detector geometry.

The charges generated in the sensor part of the detector are transported to the collection electrodes and processed in the readout electronics. The signal seen on the collection electrodes is influenced by several factors, e.g. the position of charge deposition in the pixel, the pixel geometry, the collection field, the bulk doping and charge trapping. In a counting system the number of counts recorded in a single pixel also depends on the threshold settings and electronic noise.

In sec. 5.1 the charge deposition is simulated. In order to quantify the influence of charge deposition on the achievable spatial and energy resolution Monte Carlo simulations have been carried out for Si, GaAs and CdTe. Detector thicknesses ranging from 50, 100, 300, 700 and 1000 μm and square pixel with side lengths ranging from 25 to 2000 μm were used in the simulations. In particular included are the geometries and sensor materials currently in use with the Medipix1 and Medipix2 readout chips.

In sec. 5.2 the charge transport in the sensor part of the detector is modelled and the effect of the read-out on the overall system response is analyzed and discussed. The charge transport simulations focus on the detector geometry of the Medipix2. Performance

parameters such as energy resolution, MTF and NPS are determined from the model calculations.

5.1 X-ray charge deposition

All charge deposition simulations presented in this chapter are based on PENELOPE [80], a Monte Carlo code for the simulation of coupled electron-photon transport. PENELOPE has been chosen over alternative packages such as EGS4 [81] and MCNP [82] because it uses the most up-to-date Evaluated Photon Data Library (EPDL97) from the Lawrence Livermore National Laboratory (LLNL) as discussed in [83]. A recent benchmark [84] recommends PENELOPE for low energy photon simulations. The package supplies a library of FORTRAN subroutines that are used to write a customized program, which takes care of the simulated tracks and keeps score of the relevant quantities. Its models provide reliable results down to a few hundred eV and have also been included as an optional model into Geant4 [85]. It is relatively straightforward to tailor a PENELOPE based code to the specific problem of charge deposition in a segmented semiconductor detector.

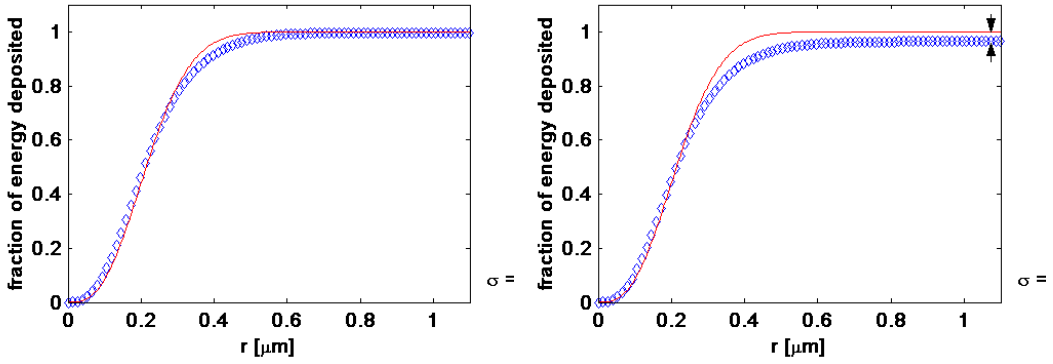
PENELOPE simulates in detail hard interactions with an energy transfer of greater than a selected cutoff energy, whereas soft interactions with scattering angle or energy-loss less than the corresponding cut-off values, are described by means of multiple scattering approximations. Particles with energies below 100 eV are considered to be absorbed locally. One of the advantages of this approach is that the simulation of particle tracks does not include a minimum step length between two consecutive interactions. This is particularly of interest for the simulation of high granularity pixellated detectors with a very large interface region between adjacent pixels, since this simulation scheme handles lateral displacements and interface crossing appropriately and provides a consistent description of the energy straggling.

The minimum bin-size for the simulated energy distribution is determined by the selected cutoff-energies for the simulation of hard inelastic collisions and Bremsstrahlung emission. In order to tally the energy distribution of photons energies as low as 8 keV, all cutoff energies were set to 250 eV.

In sec. 5.1.1 the average charge deposition profile without the effects of the sensor surface and pixel borders will be studied. Sec. 5.1.2 describes the deviation from complete charge deposition due to surface losses in thin sensors of 55 to 700 μm thickness. In sec. 5.1.2 the combined effects of both the finite sensor thickness of 300 μm and the segmentation on the mean charge cloud are investigated. The limitations in energy resolution and spectroscopic response for square pixel with side lengths in the range from 25 μm to 1mm are discussed.

5.1.1 Deposition in a thick Si sensor slab

In order to investigate the energy deposition without the effects of the finite sensor thickness and segmentation and to establish a reference for the average radial deposition profile, simulations have been carried out with the hypothetical configuration of a point-like photon source, which is coincident on the center of a 100 cm thick and laterally infinitely



(a) (b)

Figure 5.1: Mean radial energy deposition profiles (circles) with respect to the center of mass of the deposited charge in a laterally infinite Si sensor slab of 100 cm thickness for photons of 10 keV. Plotted is the fraction of energy contained within a sphere of a radius given on the abscissa. The solid line marks the Gaussian distribution fitted to the simulation data with a width 0.14 μm in both cases, representing the situation without fluorescence photons present. a) No fluorescence photons are taken into account and b) . The effects of the 4.1% fluorescence yield in Si result in the offset on the right hand side.

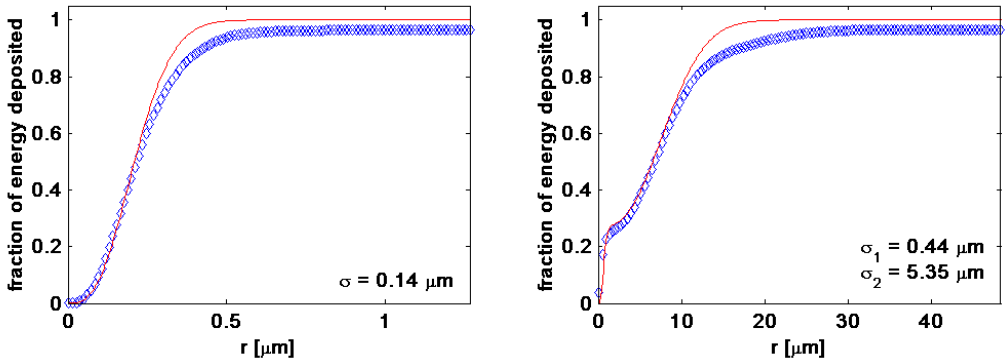
large slab of sensor material. In this geometry all photons generated in the center of the slab deposit their energy within the slab and no transmission and no backscattering of particles takes place. To estimate the average charge density distribution generated by a photon, the radial distribution of the energy deposited with respect to the center of mass of the charge cloud was calculated for each photon and compiled into a histogram.

To see the maximum achievable energy resolution for Si as detector material and a given detector geometry, the radial distribution of the deposited charge, Fig. 5.1a), and the distribution obtained with all contributions due to characteristic photons omitted in the analysis, Fig. 5.1b) were calculated with an energy of 10 keV, i.e. well above K-edge of the Si sensor material. The obtained radial profiles have been fitted with $4\pi r^2 \cdot \exp(-r^2/(2\sigma))$. It can be seen that the shape of the average charge clouds without fluorescence follows closely a Gaussian shape, and more than 90 % of the charge is deposited within the Gaussian profile. The offset in Fig. 5.1b) is a consequence of the fluorescence photons travelling quite long distances from the interaction point.

5.1.2 Deposition in a thin Si sensor slab

In a thin sensor the energy deposited by the individual photon can deviate from the results presented in the previous section. In this case losses due to backscattering and transmission of primary and secondary particles cannot be neglected, leading to changes to both spatial and energy resolution with respect to a thick sensor.

Also the mean deposition profiles may be modified with respect to a sensor which is much thicker than the mean free path of the incoming photons. Fig. 5.2 illustrates



(a) (b)

Figure 5.2: a) The energy deposition profiles in a 300 μm thick Si sensor of 10 keV photons impinging perpendicular on the sensor surface. The solid line marks the Gaussian distribution fitted to the simulation data. b) The deposition profile in the case of 80 keV photons. Plotted is the fraction of energy contained within a sphere of a radius given on the abscissae. The very localized deposition for 80 keV photons stems from Compton recoil electrons, since almost all Compton scattered photon leave the detector without depositing their total energy. The solid line is a fitted double Gaussian distribution.

this effect for selected photon energies in a 300 μm thick an laterally infinite sensor slab. In this simulation the photons impinge perpendicular on the sensor surface. For photons of 10 keV, Fig. 5.2a), the energy deposition profiles essentially follow the pure Gaussian shape, and 89% of the charge deposited is contained in the Gaussian profile. At 80 keV photon energy, Fig. 5.2b), only 67 % are contained within the fitted Gaussian profile, of which ∼23 % are related to Compton scattering. The main mechanism in Si leading to incomplete energy deposition in the sensor volume is Compton scattering. The spatial width of the Compton related deposition in Si is one order of magnitude below the diameter of the charge cloud generated by photoelectric absorption. Although the cross section for Compton scattering is much smaller than the one for photoelectric absorption at lower photon energies the effect can already be seen from 30 keV.

To estimate the surface escape losses simulations have been carried out for infinitely wide sensor slabs of thickness of 50, 100, 300 and 700 μm. The energy deposited per photon within the sensor volume has been recorded into a histogram, as well as the energy of backscattered and transmitted particles. Neither primary photons transversing the sensor volume without interaction nor photons undergoing elastic scattering only have been taken into account since they do not contribute to the signal generation in the detector, although they strongly influence the detection efficiency of the detector.

Fig. 5.3 shows the fraction η of energy escaping the sensor volume normalized to the energy deposited per primary photon

$$\eta = \frac{E_{escaped}}{E_{deposited}}. \tag{5.1}$$

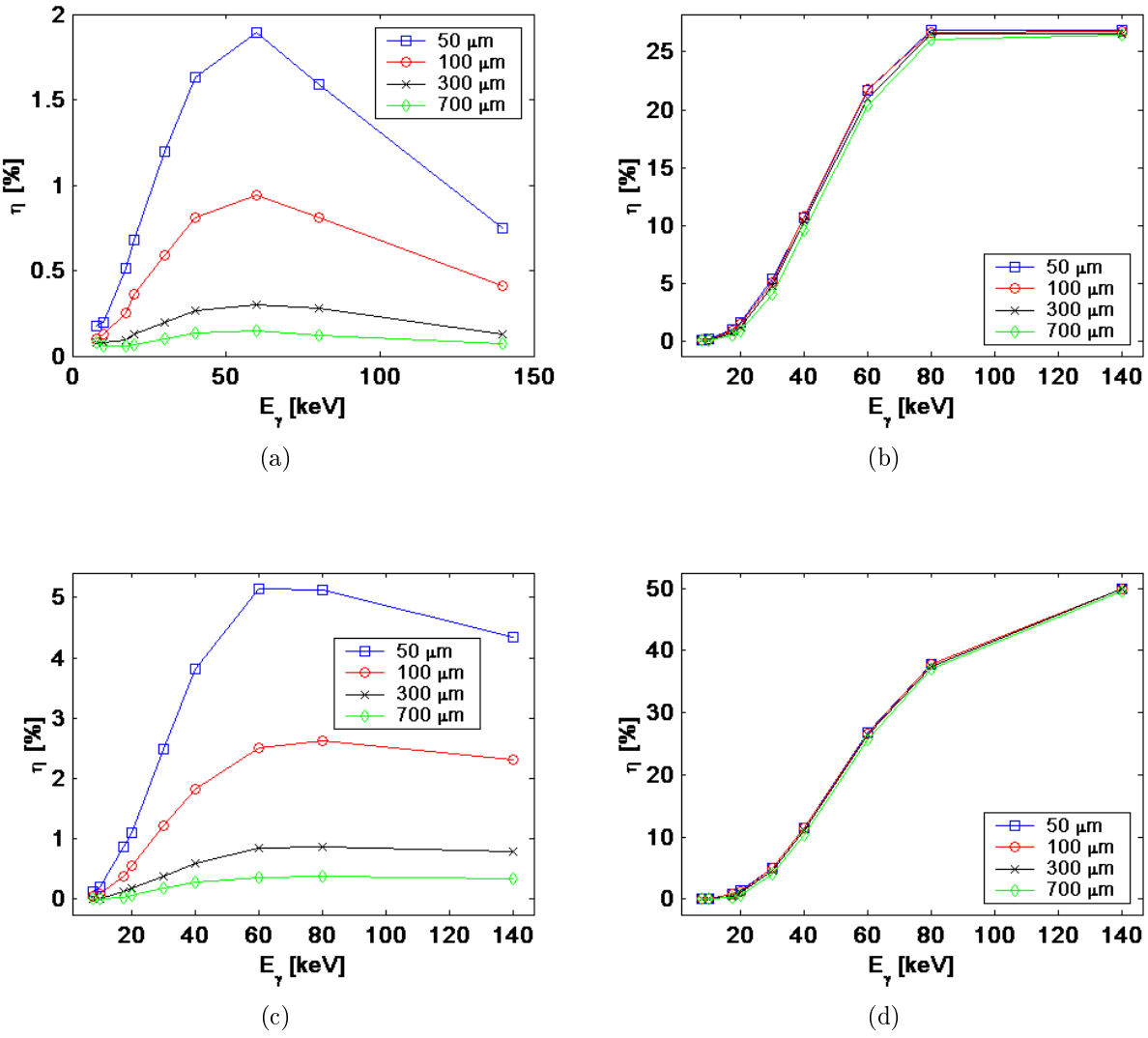


Figure 5.3: Mean energy loss per photon depositing energy in a Si sensor of 50, 100, 300 and 700 µm thickness due to a) backscattered secondary electrons, b) backscattered photons, c) transmitted secondary electrons, d) transmitted photons. The surface losses via secondary electrons becomes relatively less important above 60 keV. Less energy is transferred in average to the electrons, due to the increasing strength of Compton scattering. The thickness of the layer from with electrons can escape the sensor volume is independent of the senor thickness, therefore the surface losses are more pronounced for thin sensors. Photon losses at the other hand are essentially independent of the the sensor thickness since the mean free path of the characteristic photon is much shorter than the sensor dimensions. At photon energies where Compton scattering contributes significantly, the attenuation is very weak and the relation between mean energy deposited and mean energy escaped is independent of the sensor thickness.

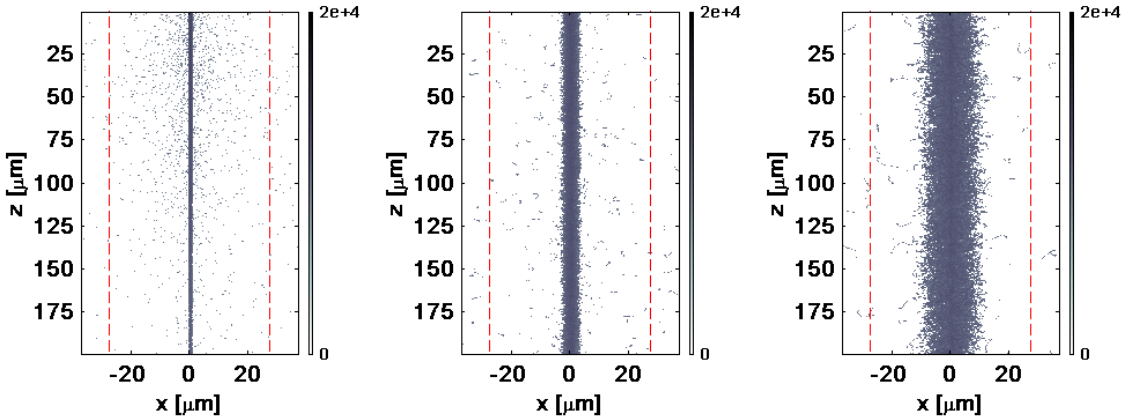
These losses mark the upper limit of the achievable energy resolution independently of the granularity of the segmentation of the sensor.

The energy out-flux by secondary electrons is always weaker than photon losses and reaches its maximum of ∼2 % at 60 keV primary photon energy in a 55 μm thick detector. The decrease in the relative importance of the energy loss via secondary electrons, Fig. 5.3(a,c), for higher energies is an effect of the increasing influence of Compton scattering. The mass attenuation coefficients of photoelectric absorption and Compton effect are equal at 57 keV photon energy whilst the energy absorption coefficients do not cross below 100 keV. Less energy is transferred from the incident photon to the secondary electron by Compton scattering than by photoelectric absorption. Therefore the mean electron range is shorter, resulting in a thinner layer below the sensor surface contributing to electron emission. The extent of this layer is independent of the sensor thickness, resulting in a relatively bigger contribution in a thinner sensor. The relatively higher out-flux of energy via transmitted electrons is a result of the energy dependence of direction of the secondary electron direction. Both Compton scattering and photoelectric absorption show increased probability of forward Compton scattering at higher energies (Fig. 1.2, Fig. 1.4).

It can be seen that the fractions of photons leaving the detector in forward and backward direction are of the same order of magnitude and roughly ten times more important than the electron escape. The average energy loss via backscattered photons, Fig. 5.3b), flattens out at ∼27 %, as a combined effect of the growing dominance of Coulomb scattering and a mean free path of the incident photon much longer than the sensor thickness. Fluorescence photons contribute very little since the florescence yield of 4.1% is very small and the mean free path of 12 μm of the characteristic X-rays is comparably short. The energy transmission by photons, Fig. 5.3d), follows the trend of the backscattered photons for the same reasons. It differs only in the increased contribution from forward escaping photons at higher energies, due to the increasing probability of forward Compton scattering. It is evident in 5.3d), that little reduction of the energy losses with sensor thickness can be expected for Si. The photonic losses are basically independent of the sensor thickness, since the mean free path of the characteristic photon is contained within the sensor thicknesses taken into account here. For higher Z materials however, as will be shown in sec. 5.1.4, losses via secondary photons depend strongly on the sensor thickness.

5.1.3 Deposition in a pixellated Si sensor

To obtain both good spatial and energy resolution in a pixel detector system it is necessary to confine the energy deposited within the pixel hit by the photon. Spectroscopic detector systems use large pixel dimensions to obtain the required energy resolution, at the expense of spatial resolution. Good spatial resolution is a prime requirement for all detector systems used in imaging applications. In a photon counting system energy resolution is an additional key factor. Though in the latter case no spectroscopic information in a narrow sense is retrieved, the number of collected charge carriers is used as a measure for the deposited energy in the discrimination process. The same mechanisms responsible for surface losses, that lead to a modification of the detected energy spectrum also introduce further changes when using a pixellated sensor. In a segmented sensor slab some photons will inevitably convert exactly on or very close to the pixel border and deposit



(a) (b) (c)

Figure 5.4: Energy deposited [$eV/\mu m^3$] of 10^5 photons of a) 8 keV, b) 20 keV, c) 40 keV in a 55 μm pixel of a 300 μm thick Si sensor. The dashed vertical lines indicate the geometric pixel borders. Note that the scaling of the x and z-axis are 2:1.

their energy in more than one pixel. The additional charge spread introduced by the diffusion processes during charge collection, c.f. sec. 5.2.2, is in general much bigger than the diameter of the initial charge cloud after photon conversion and therefore the final diameter of the charge cloud arriving at the collection electrodes is only modulated by the conversion diameter. At higher photon energies the influence of Compton scattering and fluorescence photons on the other hand exceed the effects of charge diffusion and have to be considered separately. Furthermore, secondary electrons even if to a much lesser extent, may contribute to deposition related charge-sharing between neighbouring pixels. This is the case in particular at higher energies when electron ranges become equivalent to the pixel dimension.

Fig. 5.4 gives examples for the energy deposited in the center of a 55 μm square Si pixel by 8, 20 and 40 keV photons. The 8 keV photons convert very locally and predominantly in the uppermost region of the sensor slab. The exponential shape of the attenuation law can be seen. Already 20 keV photons have a mean free path of 640 μm in Si, but the mean diameter of the charge cloud created is still well contained within the pixel. In Fig. 5.4c) it is evident that the charge deposited by 40 keV photons may be shared between two pixels if the deposition takes place within a $\sim$10 μm from the pixel border.

Simulation have been carried out in order to quantify the spectral response as a function of the pixel size and to estimate the percentage of photopeak events for different pixel geometries. One way to estimate the spectrum of the energy deposited in a given pixel geometry would be to simulate a large number of photons randomly hitting the sensor on an area exceeding the pixel size by at least several times the mean free path length of the fluorescence photons. Unfortunately this leads to very long computation times for materials with long mean free path lengths of the fluorescence photon. To derive the energy deposition spectrum including segmentation effects a different approach has been chosen. Incident photons were collimated to a square of the pixel dimensions in the center

of a laterally infinite sensor slab. The total charge deposited within the pixel borders for every individual photon was recorded into a deposition histogram. In a second histogram the energy deposited in the infinite sensor slab was tallied. The gross spectral losses to neighbouring pixels have been derived from the difference between these two data sets for each pixel size. Since all surface losses are already accounted for in the obtained out-flux spectrum, the average actual spectrum seen under uniform irradiation can been estimated as the sum of the out-flux and the initial deposition within the pixel.

Fig. 5.5(a-e) plots the calculated spectrum of the deposited charge in a single pixel for a fixed Si sensor thickness of 300 μm and different pixel sizes. The fraction of photons depositing the full energy within the hit pixel is indicated in the plot legend.

In a pixel of 1 mm^2 area the fraction of charge deposited drops to 90 % at $\sim$27 keV. For 170 μm pixel size, as in the Medipix1, photons up to 22 keV give more than 90 % signal height. In an even smaller pixel of 55 μm, as used in the Medipix2, this energy falls to 15 keV. The main mechanism causing this decrease of deposition efficiency is the out-flux of secondary photons. In Fig. 5.5f) the percentage of photons converted entirely within a given pixel size is plotted versus the photon energy. The increase of collection efficiency with pixel size is very small above 170 μm pixel pitch. An extended functionality of readout electronics as proposed in sec. 5.3 and intended mainly to correct for the effects of diffusion-related charge-sharing would therefore also correct for the biggest part of deposition related charge sharing.

At low photon energies the effect of secondary electrons leaving the pixel is negligible compared to characteristic X-rays. Starting at 20 keV the first effects of Compton scattering can be seen, Fig. 5.5a). Also visible is an increased background caused by electron losses. Both contributions grow with higher photon energies and at 80 keV the majority of photons interacting with the sensor deposit only a fraction of their energy in the pixel volume. The general rule is to set the discriminator threshold to half the energy of the incident photons [86–88] in order to obtain uniform sensor response. This is effective only for photon energies below 40 keV. Above this value thresholding will lead to a strong decrease in QE, while at the same time disregarding events providing higher spatial resolution.

From these results it can be concluded that the upper energy limit for spectroscopic pixel detectors for imaging with Si as sensor material is $\sim$20 keV, mostly due to Compton scattering. For photon energies above 40 keV applying the discrimination procedure will lead to losses in QE.

It should be noted at this point, that the effects described here do not only affect photon counting systems. In integrating systems the negative impact of partial charge deposition may even be higher, since the events are weighted by their deposited energy only. In this case contrast and information about the object is lost. At the other hand, using a counting regime all events not rejected by the discriminator are weighted equally, resulting in a increased SNR with respect to simple integration. The impact on image quality depends on the application and the photonic spectrum used. To quantify potential gain in image quality is beyond the scope of this work, but is important field for future studies.

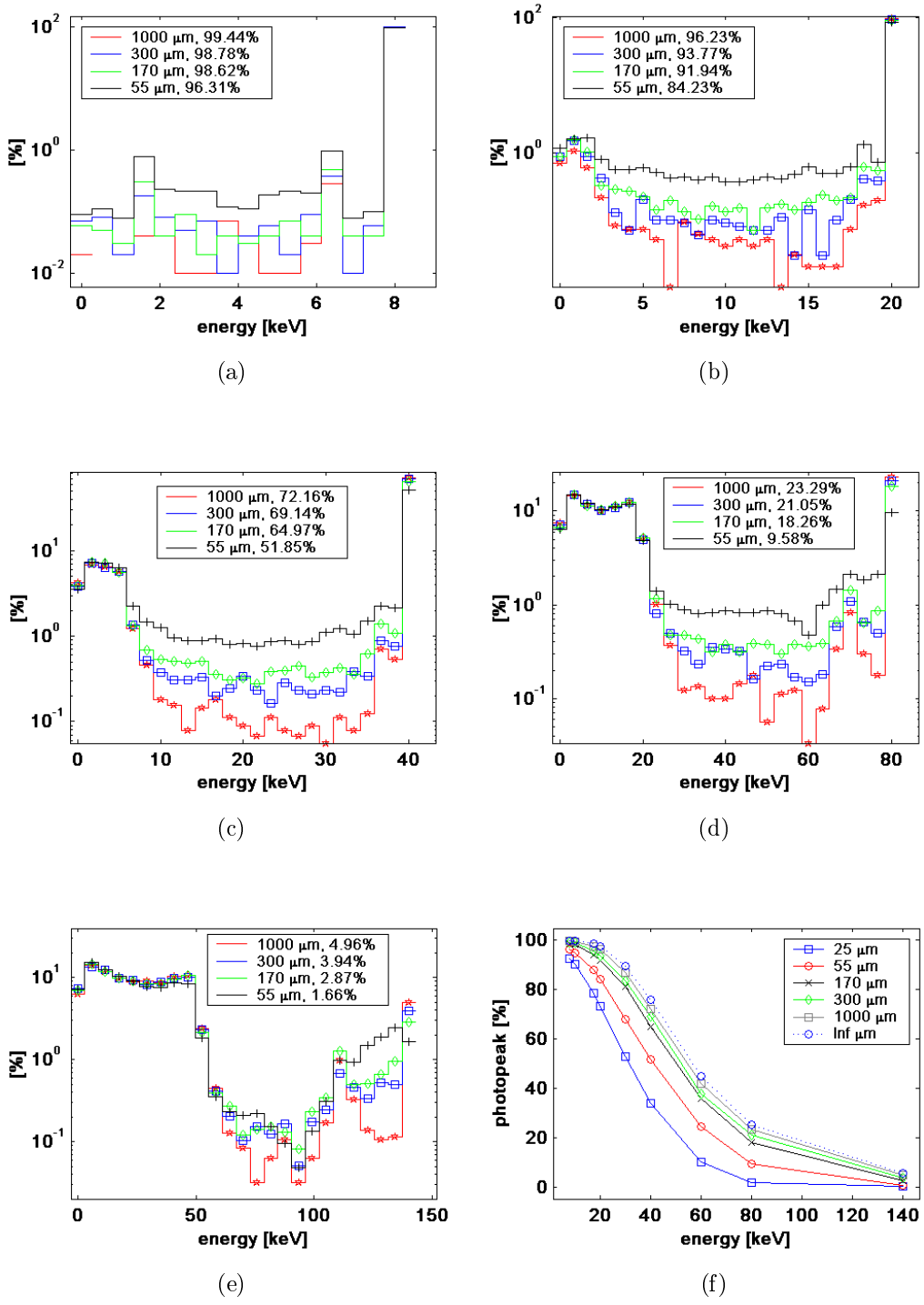
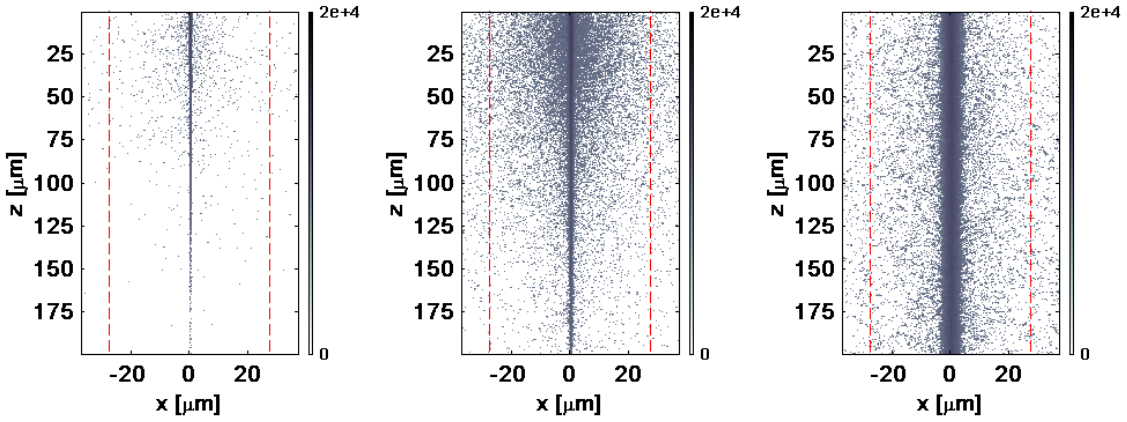


Figure 5.5: The spectrum of the energy deposited by a) 8, b) 20, c) 40, d) 80 and e) 140 keV photons in a Si sensor of 300 µm thickness within a pixel of 55, 170, 300 700 and 1000 µm width in the center of an uniformly irradiated area. The fraction of photons fully absorbed within a pixel is indicated in the plot legend. f) The percentage of photons converted entirely within a given pixel size is plotted versus the photon energy. To mark the upper limit the corresponding curve for an infinite detector slab in the legend.



(a) (b) (c)

Figure 5.6: Energy deposited [$eV/\mu m^3$] of 10^5 photons of a) 8, b) 20 and c) 40 photons in a 55 μm pixel of a 200 μm GaAs sensor. Note that the scaling of the x and z-axis are 2:1.

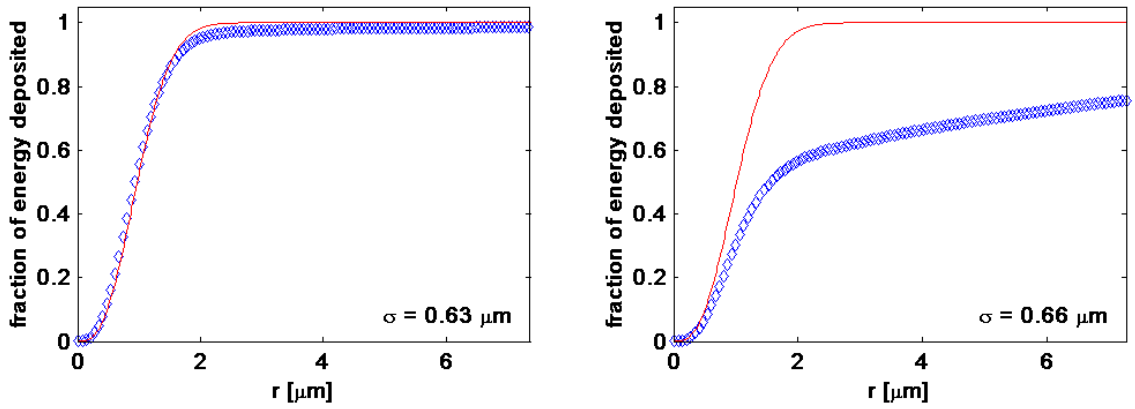
5.1.4 Other materials

The charge deposition of Si as the most common sensor material has been discussed in detail. The short mean free path of its fluorescence photons and the low fluorescence yield make for excellent sensor properties at photon energies below 20 keV. At higher energies Si suffers from substantially reduced stopping power and at the same time signal degradation due the Compton scattering. Therefore the demand for alternative, high-Z sensor material is strong. Of the various sensor materials currently under development, GaAs and CdTe, used in the Medipix1 and the Medipix2 respectively, have been simulated here. Apart from the higher stopping power the main differences in the photon conversion properties with respect to Si are the higher energies of the K-edges and the higher fluorescence yields, c.f. table 1.2. The same simulations as performed for Si have been carried out.

5.1.4.1 GaAs

Deposition in a thick sensor The energy deposition profiles for GaAs, Fig. 5.6, differ from the ones found in Si due to the presence of characteristic X-rays as well as the higher stopping power of GaAs. Fig. 5.7a) shows the radial profile of the Gaussian shaped energy deposition of 40 keV photons in GaAs with fluorescence photon emission switched off in the simulation. The emission of characteristic X-rays widens the energy deposition profile 5.7b) and only 64% of the charge is deposited within the core Gaussian profile for photons with 40 keV.

Deposition in a thin sensor The average energy deposition profiles in a thin sensor are essentially identical to the ones obtained for a thick sensor up to the energy of the K-edges of Ga and As at 10.4 keV and 11.9 keV respectively. At energies just above the K-edges, Fig. 5.8, two distinct energy deposition profiles exist concurrently, the one following



(a) (b)

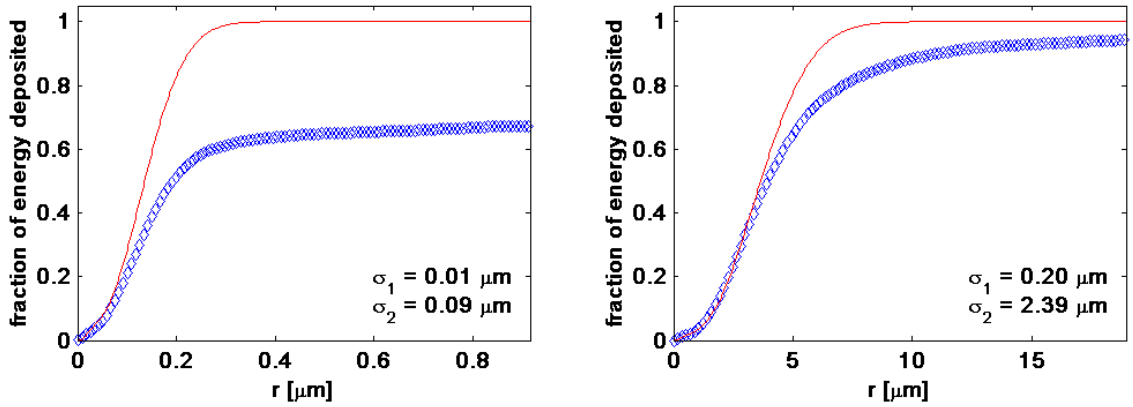
Figure 5.7: Mean radial energy deposition profiles with respect to the center of mass of the deposited charge in a GaAs sensor slab of 100 cm thickness for incident photons of 40 keV a) without and b) with fluorescence photons taken into account. Plotted is the fraction of energy contained within a sphere of a radius given on the abscissae. The solid lines mark the Gaussian distributions fitted to the simulation data without fluorescence photons.

full photo-absorption and the other including re-emission of fluorescence photons. The secondary photo-electron is emitted with very low energy and therefore is absorbed within a short range from the conversion point. The florescence photon on the other hand has a mean free path comparable to or even longer than the incident photon and may result in distant re-absorption or photo-escape. In either case only a tiny fraction of the primary photon energy is detected in a very localised region. Fig. 5.8a) indicates that only ∼63% of the charge is deposited within the Gaussian profile, since the mean free path of the As fluorescence photons is very long compared to the diameter of the charge cloud.

At even higher energies, above 60 keV, when Compton scattering becomes a relevant contribution, also two deposition widths coexist. The mechanism is the same as described above, only the secondary electron is produced in a Compton scattering event. Fig. 5.8b) illustrates the situation for 80 keV photons. The localized charges here are due to Compton scattering, ∼73% of the charges are deposited within the Gaussian profile. A second effect on the mean energy deposition profile can be seen by comparison with 5.7a). The mean diameter of the charge cloud is ∼5 % smaller as a result of secondary photon escape.

Below the K-edge energies the contribution of backscattered secondary electrons is at negligible levels of ∼0.2 % in backward and ∼0.1 % in forward direction for a 50 μm thick sensor and even less for a thicker sensor geometries. Photonic losses, Fig. 5.9(ac), are even one order of magnitude weaker for these energies.

Above the K-edges and up to 40 keV, photonic losses clearly dominate, though electron losses start to contribute as well, notably in the forward direction. The larger fraction of transmitted electrons, 5.9c), is an effect of the more and more forward emission of secondary electrons in photoelectric absorption. Like in Si, the higher probability of forward emission of the electron accounts for the more pronounced energy loss by transmitted



(a) (b)

Figure 5.8: Energy deposition profiles in a 300 μm thick GaAs sensor with incident photon energy of a) 13 keV, just above the K-edge of As and b) 80 keV. Plotted is the fraction of energy contained within a sphere of a radius given on the abscissae. The solid lines mark the Gaussian distributions fitted to the simulation data without fluorescence photons contributing. The energy deposited close to zero radial offset is due to low energy photo-electron, with the characteristic X-ray leaving the sensor volume.

electrons as compared to backscattered ones.

The minimum energy loss is found at around 40 keV. Even though the mass absorption coefficients for photoelectric absorption and Compton scattering are of equal magnitude only at ∼250 keV, the energy transported by Compton scattered photons is much higher. The parallel, almost linear increase with higher photon energies is a result of the long mean free path length for photons, e.g. 556 μm at 50 keV, since in this regime the number of absorbed or scattered particles scales linear with the sensor thickness. For energies above 80 keV the strongest loss of deposited energy is caused by the transmission of Compton scattered primary photons.

Deposition in a pixellated sensor In Fig. 5.10 the photopeak response of a 300 μm GaAs sensor is shown. The photopeak response of GaAs stays close to 100% up to the K-edge energies also in a pixellated sensor. Only photons converted in the border region between two pixels decrease the number of charges deposited within the pixel. Above these energies the dominant factor in the decrease of spectral accuracy with increasing photon energy is the emission of characteristic X-rays and re-absorption of fluorescence photons. In Fig. 5.10(b-e) the fluorescence peak and the escape peak are clearly visible. At 40 keV only for ∼59 % percent of the photon energy is collected in a pixel of 55 μm^2. At energies exceeding 80 keV Compton scattering governs the energy spectrum deposited in the sensor. At 140 keV only ∼15 % of the photons result in a photopeak signal in a 55 μm^2 pixel.

Fig. 5.10f) gives an overview of the fraction of photons fully absorbed within a pixel.

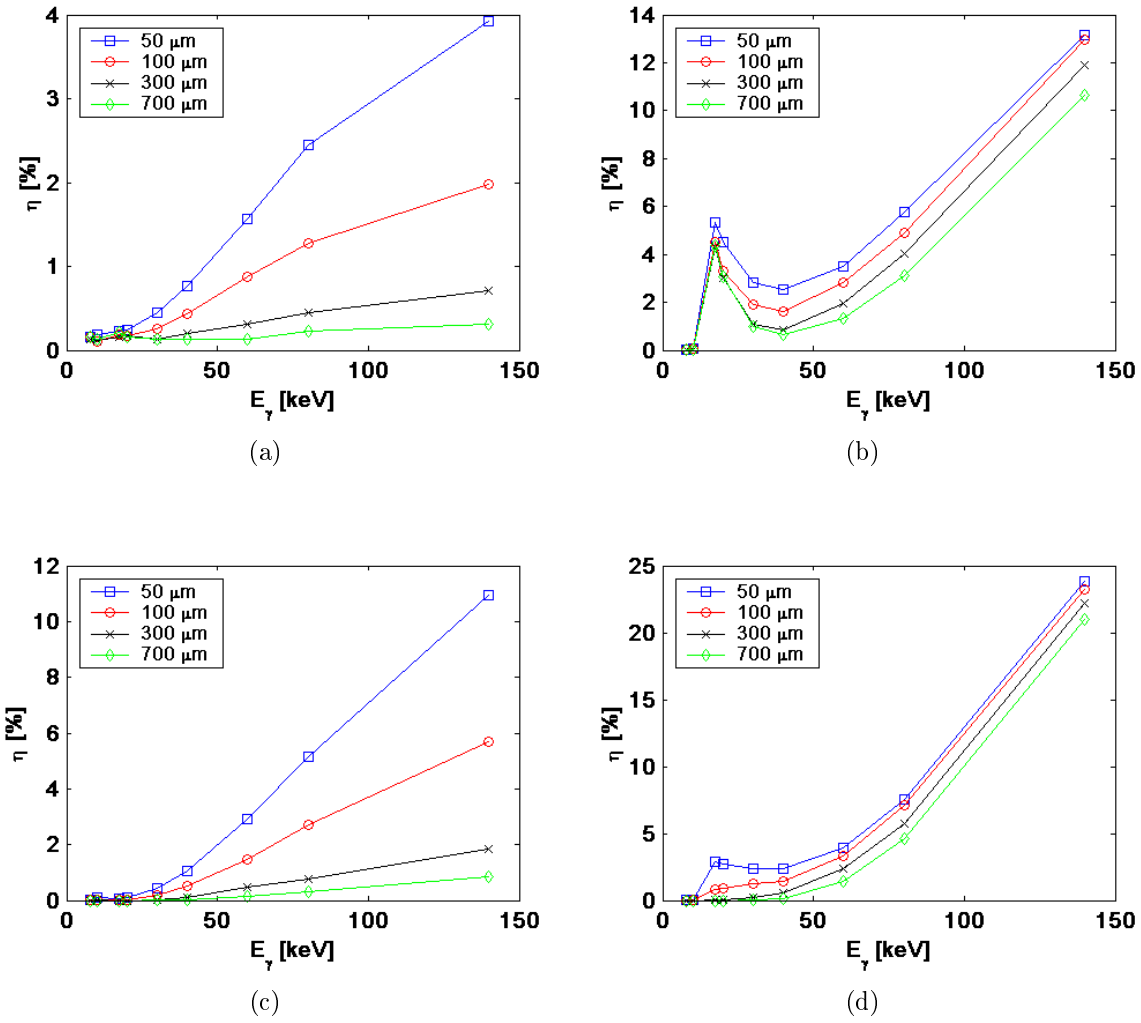


Figure 5.9: Mean energy loss per photon depositing energy in a GaAs sensor due to a) backscattered secondary electrons, b) backscattered photons, c) transmitted secondary electrons, d) transmitted photons.

The loss of secondary photons for energies above the K-edges of Ga and As is significant for pixel sizes smaller than 170 μm already for photon energies just above the K-edges. The steady decrease of the number of photons in the photopeak can be attributed to enhanced Compton scattering and growing electron ranges. The limiting factor in the energy range under investigation mainly stems from the emission of characteristic photons.

5.1.4.2 CdTe

Fig. 5.11 gives examples for the energy deposited in a 55 μm CdTe pixel of 200 μm thickness by 8, 20 and 40 keV photons. The 8 keV photons, Fig. 5.11a), are stopped almost immediately. 20 keV photons, Fig. 5.11b), with a mean free path of 76 μm still convert to 96 % and the diameter of the deposited charge cloud is contained within the pixel. In Fig. 5.4c) it is evident that the charge deposited by 40 keV photons may frequently be shared between two pixels if the deposition takes place within several microns from the pixel border.

Deposition in a thick sensor The energy deposition profiles for CdTe are also strongly modified by the emission of characteristic X-rays. Only 29% of the charge is deposited within the core Gaussian profile of photons of 80 keV due to characteristic photons. The width of the core charge cloud is increased by ∼28% with respect to the energy deposition profile with fluorescence switched off in the simulation, 5.12a).

Deposition in a thin sensor CdTe in principle shows the same behaviour as GaAs, except that the contribution of secondary photons is much higher than the one stemming from Compton scattered photons. This can be seen in Fig. 5.13(b,d), with a maximum of secondary photon losses when the mean free path of the characteristic X-rays matches the mean free path of the primary photons at ∼40 keV. Compton scattering on the other hand hardly contributes below 50 keV. Forward emission of secondary photons can be almost avoided for photon energies up to 60 keV with a sensor of 700 μm thickness. Sensor thicknesses below 300 μm suffer from strong forward escape of secondary photons for primary photon energies just above the K-edges. Of the three materials considered here, the gain in energy deposition with increasing sensor thickness is most pronounced for CdTe.

The effect of fluorescence photons on the energy deposition profiles is more pronounced since mean free path of the characteristic X-ray of Te is much longer. Fig. 5.14a) graphs the result for 30 keV photons, with localized charge deposition due to low energy secondary electrons and a tail due to reabsorbed characteristic photons. Fig. 5.14b) illustrates the situation for 80 keV photons. The shape of the energy deposition profile differs considerably from the one obtained in a thick detector, Fig. 5.12b), yielding a narrower distribution due to fluorescence photons escaping the surface. Only ∼31 % of the charge deposited is confined in the core Gaussian profile.

Deposition in a pixellated sensor In a 300 μm thick CdTe sensor the Compton effect is negligible below 80 keV, therefore the number of fully converted photons stays almost constant above the K-edge of Te, Fig. 5.15f). The main source of loss in the conversion

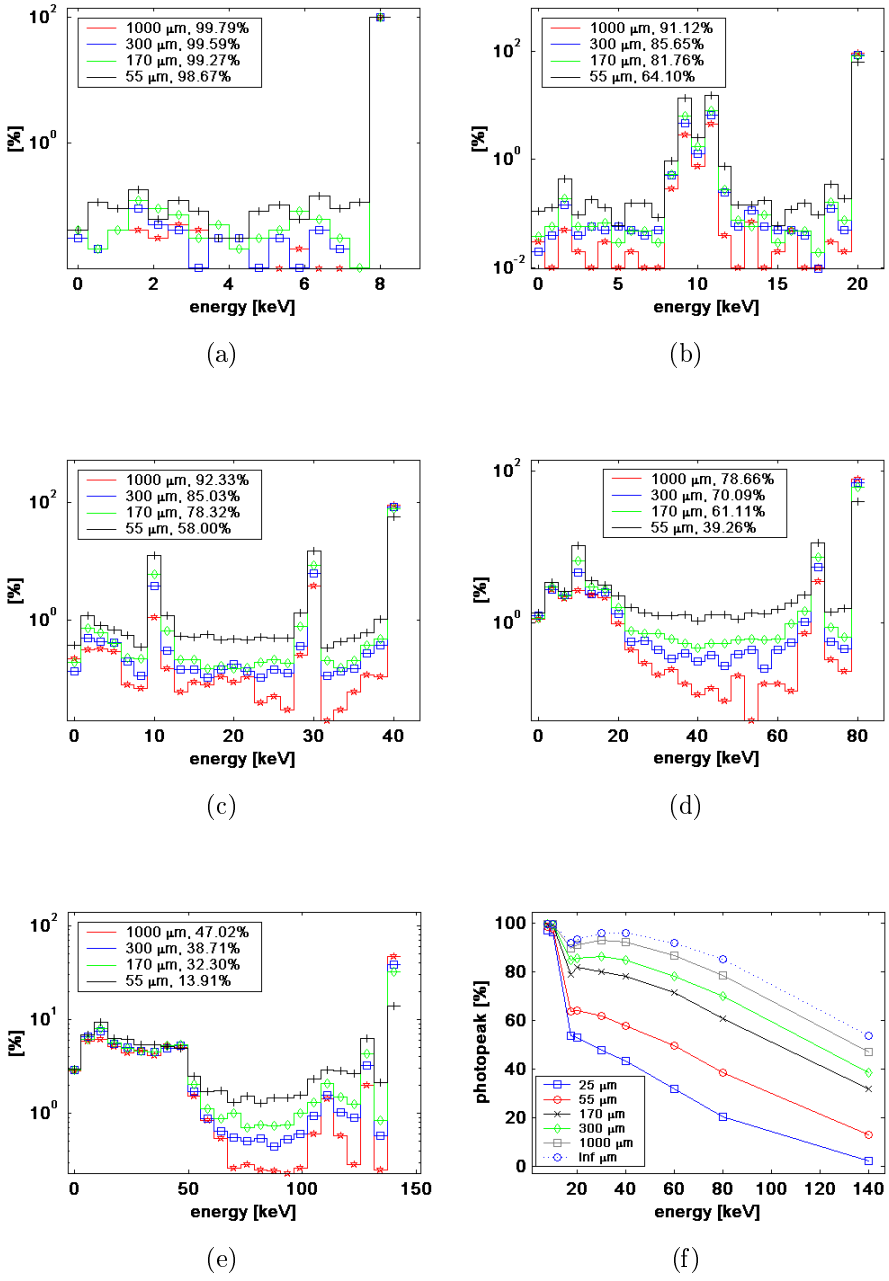
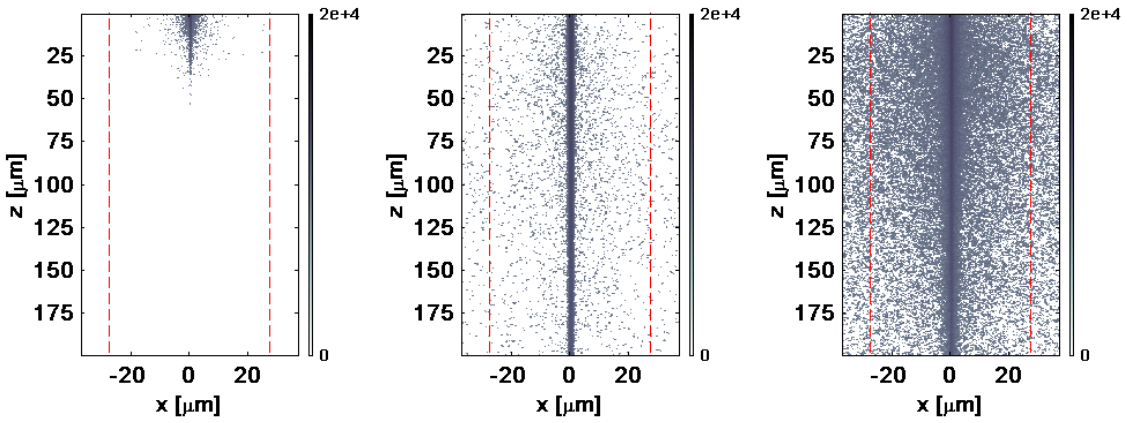
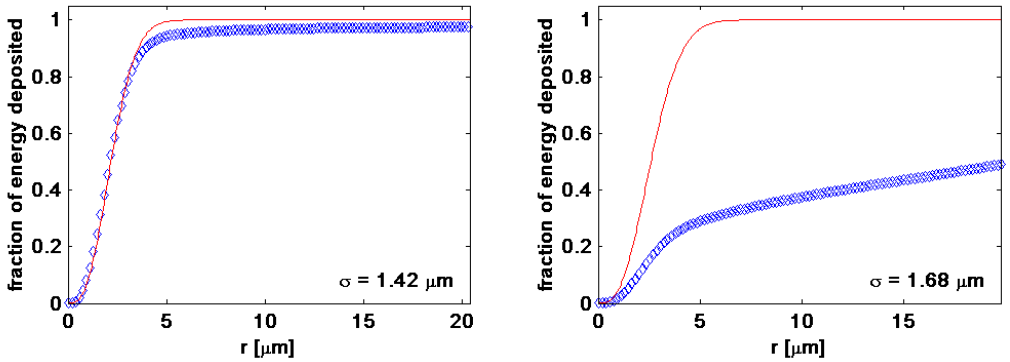


Figure 5.10: The spectrum of the energy deposited by a) 8, b) 20, c) 40, d) 80 and e) 140 keV photons in a GaAs sensor of 300 µm thickness within a pixel of 55, 170, 300, 700 and 1000 µm width in the center of an uniformly irradiated area. f) Fraction of photons fully absorbed within a pixel. To mark the upper limit the corresponding curve for an infinite detector slab is also shown.



(a) (b) (c)

Figure 5.11: Energy deposited [$eV/\mu m^3$] of 10^5 photons of a) 8, b) 20 and c) 40 photons in a 55 µm pixel of a 200 µm CdTe sensor. Note that the scaling of the x and z-axis are 2:1



(a) (b)

Figure 5.12: Mean radial energy deposition profiles with respect to the center of mass of the deposited charge in a CdTe sensor slab of 100 cm thickness for incident photons of 80 keV a) without and b) with fluorescence photons taken into account. Plotted is the fraction of energy contained within a sphere of a radius given on the abscissae. The solid lines mark the Gaussian distributions fitted to the simulation data without fluorescence photons taken into account.

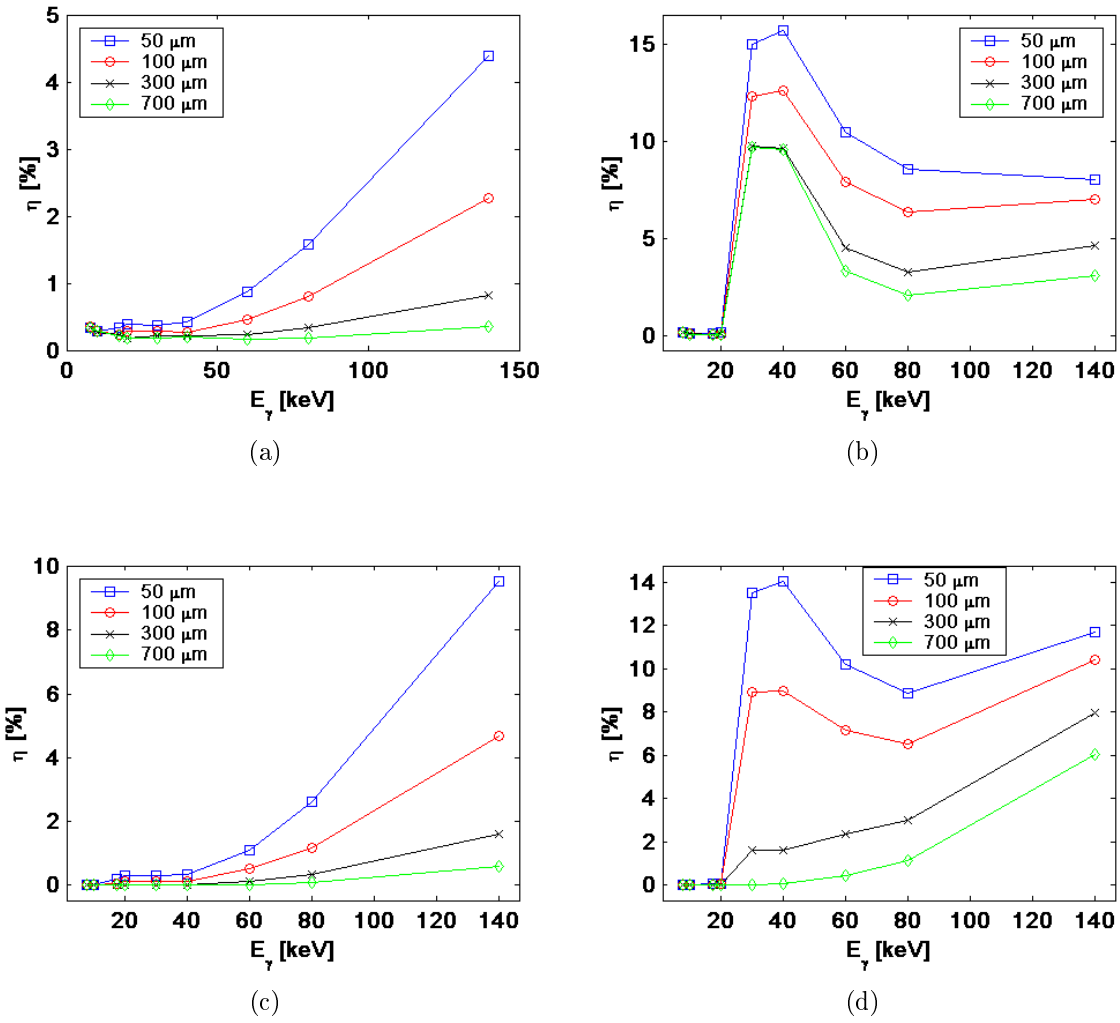
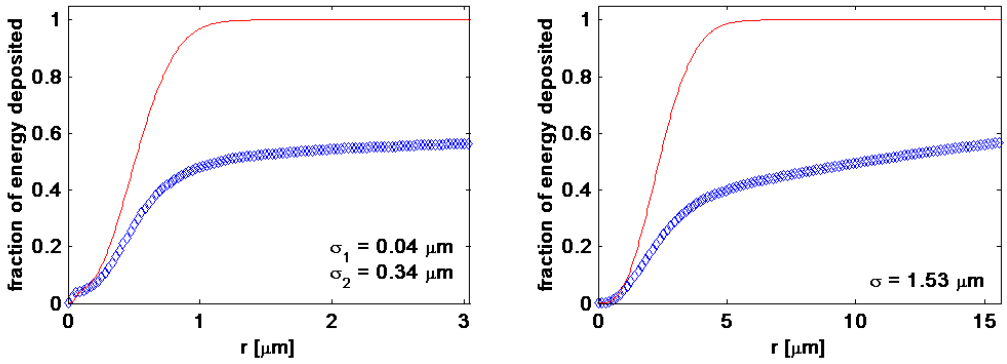


Figure 5.13: Mean energy loss per photon depositing energy in a CdTe sensor due to a) backscattered secondary electrons, b) backscattered photons, c) transmitted secondary electrons, d) transmitted photons.



(a) (b)

Figure 5.14: a) Energy deposition profiles in a 300 μm thick sensor CdTe with incident photon energy of 30 keV, just above the K-edge of Te. b) The deposition profile for 80 keV. Plotted is the fraction of energy contained within a sphere of a radius given on the abscissae. The solid lines mark the Gaussian distributions fitted to the simulation data. The energy deposited close to zero radial offset is due to low energy photo-electrons, with the characteristic X-ray leaving the sensor volume. The higher fluorescence yield leads to a stronger influence on the charge distribution as compared to GaAs, c.f. Fig. 5.8.

process is secondary photons. The maximum achievable percentage of fully converted photons is ∼85 % in a sensor of infinite pixel size.

The limiting factor in the energy range under investigation mainly stems from the emission of characteristic photons and shows a very strong decrease of photons in the photopeak. At 40 keV only ∼29 % of the converted photons lead to a full energy signal.

5.2 Charge transport and collection

5.2.1 Simulation method

After conversion of the incident X-ray, the carriers drift under the influence of the applied field towards the collection electrodes. The motion of the charge carriers generated by the converted photons has been simulated using ISE-DESSIS [89]. In Drift Diffusion mode the Poisson equation eq. 1.11 and the continuity equations eq. 1.10 for electrons and holes are solved. A 300 μm thick Si sensor with 55 μm pixel pitch was modelled as a 2D slice through the center of a pixel including its next 2 neighbours, Fig. 5.16, with a bulk doping density of $3 \cdot 10^{11} cm^{-3}$, the backside n implant $3 \cdot 10^{18} cm^{-3}$ and the front-side p implant $3 \cdot 10^{19} cm^{-3}$. A rectangular mesh grid of 1 μm and a reverse bias voltage of 100V was used. The charge deposited was modelled using the heavy ion model of DESSIS by adjusting the values for the linear energy transfer, LET, and the lateral decay length, σ_r, in accordance with the values obtained in the X-ray charge deposition simulations, c.f. sec. 5.1. The distribution of the charge cloud $G(l, r, t)$ is given by

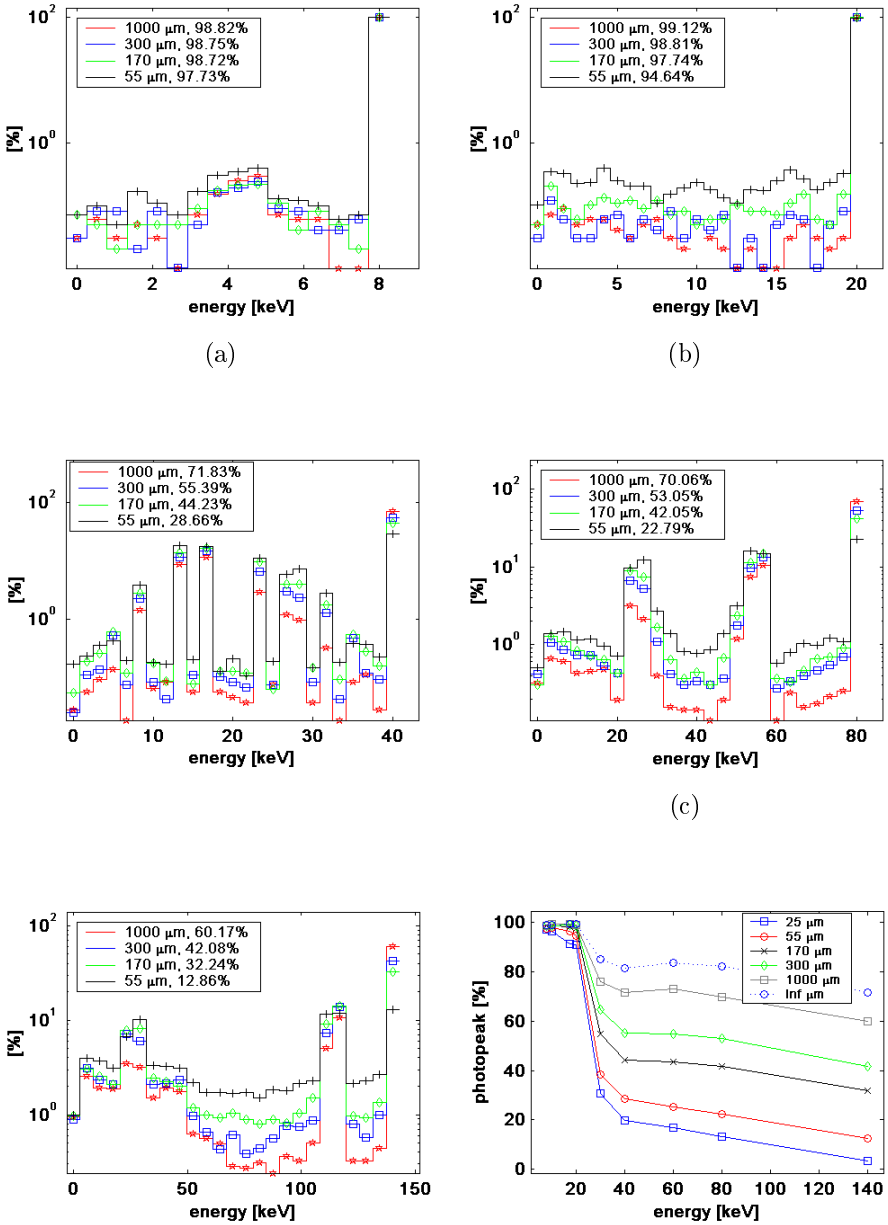


Figure 5.15: The spectrum of the energy deposited by a) 8, b) 20, c) 40, d) 80 and e) 140 keV photons in a CdTe sensor of 300 µm thickness within a pixel of 55, 170, 300, 700 and 1000 µm width in the center of an uniformly irradiated area. f) Fraction of photons fully absorbed within a pixel. To mark the upper limit the corresponding curve for an infinite detector slab is also shown.

$$
\begin{aligned}
G(l,r,t) &= LET(l)\cdot R(r)\cdot T(t) \\
T(t) &= \frac{2\exp\left(-\left(\frac{t-t_0}{\sigma_t}\right)^2\right)}{\sigma_t\sqrt{\pi}\left(1-\operatorname{erf}\left(\frac{t}{\sigma_t}\right)\right)} \\
R(r) &= \frac{1}{2\pi\sigma_r}\exp\left(-\frac{r^2}{2\sigma_r}\right)
\end{aligned}
$$

where:	LET(l)	LET as a function of longitudinal extent, l
	r	radial distance
	σ_r	lateral width of charge cloud
	t	time
	t_0	time of interaction
	σ_t	characteristic time of charge generation

The values for $LET(l)$ where chosen equal to the radial shape $R(r)$ to match the shape of the charge cloud as obtained by the PENELOPE simulations of the photon conversion. The resulting charge distribution was normalized according to the number of electron-hole pairs generated

$$\int G(l,r,t)\cdot 4\pi r^2 dr\, dl\, dt = E_\gamma/\epsilon$$

with ε the average energy necessary the create an electron hole pair, c.f. table 1.1.

In Fig. 5.17 the total current induced on the collection electrodes of a vicinity of three pixels is graphed for a X-ray energy of 27 keV. Fig. 5.17a) shows the current in the left electrode, Fig. 5.17c) in the middle electrode and Fig. 5.17e) in the right electrode for the case of a photon converting in the center of the middle pixel at distances of 30, 50, 150 and 250 μm from the plane of the collection electrodes. As expected the currents in the left and right pixel are identical. For a conversion point 50 μm from the collection electrode the current induced in the neighbours are dominated by the displacement current. No integral charge is collected in total. The swing in the displacement current does not lead to a signal in the readout electronics since the shaping time of 150 ns of the charge sensitive preamplifier is much longer than the maximum collection time. Only if the conversion takes place very close to the upper sensor surface holes arrive physically at the electrode of the neighbouring pixel and the signal in the center pixel is reduced by the number of carrier shared.

In Fig. 5.17(b,d,f) the situation for a deposition very close to the pixel border between the center and the right pixel is shown. In the left hand pixel, Fig. 5.17b), only displacement currents are induced, whereas in the center, Fig. 5.17d), and the right side, Fig. 5.17f), the current is very similar and the collected charge is almost equally shared.

To obtain realistic results for the spectrum of charge collected for a sensor under uniform irradiation a very large number of simulations would have to be run. Since very small time steps and a very dense grid is required to obtain accurate results for the charge collected this would lead to excessive computation time, even more because the whole set of simulations has to be re-run e.g. for a different bias voltage or bulk doping densities.

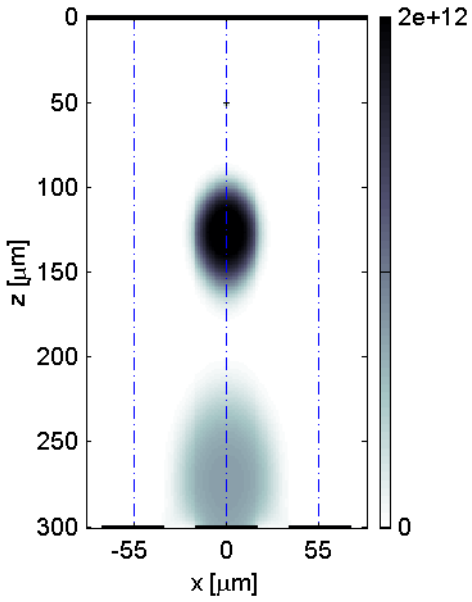


Figure 5.16: ISE-simulation geometry and charge density distribution in charges/cm^3. Plotted is the hole component of charge cloud of a 10 keV photon ∼4 ns and ∼14 ns after conversion in 50 µm depth.

3D simulations including the corner region between 4 neighbouring pixels are even more demanding. A further complication is posed by the very localized conversion of X-rays. The initial charge cloud after conversion covers only few grid points even when a very fine mesh is used. This can lead to artifacts in the simulated collection time since plasma effects may occur in the simulation

In high resistivity Si, due to its low impurity concentration, charge trapping and recombination of free carriers can be neglected. In the readout electronics used in the Medipix1 and Medipix2 the signal collected at the input electrodes is integrated with a time constant much longer than the collection time. Therefore it is sufficient to model the motion of the free carriers alone, without taking into account the exact pulse shapes.

To simulate the collection of the generated free carries in the sensor volume, a dedicated program was developed taking into account the diameter of an average initial charge cloud, conversion probabilities, K_α and K_β fluorescence photons, Compton and Rayleigh scattering, velocity saturation effects in the drift time, Coulomb repulsion and surface losses. The average spatial extent of the charge cloud generated by the photo-electron during photon conversion in the range from 8 to 40 keV has been derived from simulation data presented in sec. 5.1 by fitting a double Gaussian distribution to the simulated deposition profiles. The inferred weights and the widths of the fit are given in table **??**.

To calculate the relative weights of photoelectric effect, Compton scattering and Rayleigh scattering XCOM 1.3 [90] has been used. The probability distribution functions to determine the angle of the scattered photon after Rayleigh or Compton scattering

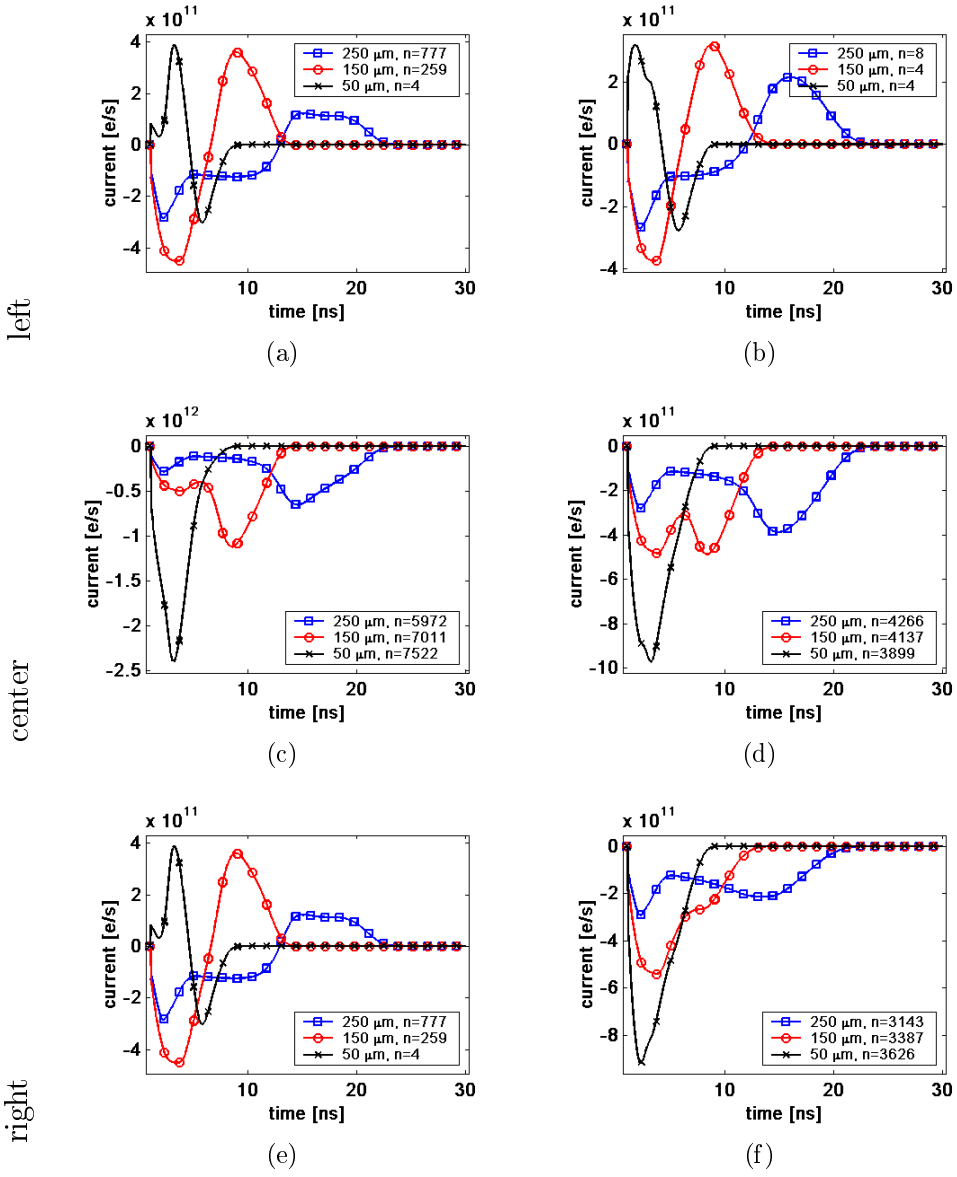


Figure 5.17: Simulated collection electrode currents for 27 keV photons converted at 250, 150 and 50 µm distance from the collection electrodes. In the first row the signal seen by the left pixel, the second row displays the situation for the center pixel and the third row the right pixel. In a), c), and e) photons convert in the in the center of the middle electrode. In b), d), and f) photons convert with a lateral offset of 27 µm to the right of the center of the middle electrode. Also indicated in the plots is the integrated collection current. The integral number of charge carriers collected is indicated in the legend.

where calculated using routines provided by PENELOPE [91]. The motion of the charge carriers has been modelled separately in radial direction and in the direction of the collecting field during the drift towards the collection electrode . In z direction, along the collecting field, therefore the one-dimensional continuity equation has been solved for the electric field given by

$$E(z) = \frac{2V_d}{D}\left(1 - \frac{z}{D}\right) + \frac{V_{bias} - V_d}{D}. \tag{5.2}$$

The z-dependent term in eq. 5.2 leads to a dispersion of the holes in the charge cloud in addition to diffusion, whilst the electron cloud is compressed in the z-direction. In the radial direction the field describing the Coulomb repulsion is given by

$$E(r) = \frac{Q(r)}{4\,\pi\,\varepsilon\,r^2}. \tag{5.3}$$

The total drift time for low electric fields of $E < 10^3\,V/cm$ is given by

$$t_{drift} = \frac{\varepsilon}{n_{eff}\cdot e\cdot\mu}\,\log\left(1 - \frac{n_{eff}\,e\,\mu\,z\,d}{\varepsilon\left(V_{bias} + \frac{n_{eff}\cdot e\cdot\mu\cdot d^2}{2\cdot\varepsilon}\right)}\right) \tag{5.4}$$

where
- e elemental electron charge
- ε dielectric permittivity of Silicon
- n_{eff} effective bulk doping density
- μ hole mobility
- d sensor thickness
- z conversion depth
- V_{bias} sensor bias voltage

For higher electric fields nonlinearities of the carrier mobilities, eq. 1.9, have to be taken into account and the collection time becomes

$$t_{coll} = \int_z^d \frac{1}{\mu(E)\cdot E(z)} dz,$$

with d denoting the sensor thickness and z the depth of the conversion point.

5.2.2 Effects of charge collection on sensor response

The spatial resolution of the sensor alone without the readout electronics is described by the point spread function PSF, that is the signal at the sensor output as a response to a delta input signal. The dependence of the intrinsic sensor resolution on the photon energy, the sensor thickness and the sensor bias voltage has been simulated by converting 10^5 photons each for energies in the range from 8 to 40 keV.

The results for the average charge distribution of 8 keV photons deposited in a 300 μm thick Si detector at 50, 100 150 and 250 μm distance from the collection electrodes is shown in Fig. 5.18a). The detector bias was 120 V, which corresponds to about four times the depletion voltage. Almost identical curves were obtained for higher photon energies, indicating that diffusion is the dominating process and the final charge spread is

almost completely independent of the initial diameter of the charge cloud after conversion. From eq. 1.18 it can be derived that the magnitude of the final width of the charge cloud scales with $\sqrt{1/V}$. This relation is valid only for collection fields below 1 V/μm. When the electric field exceeds 1 V/μm the linear correlation between electric field and drift velocity is no longer valid and velocity saturation takes place due to inelastic scattering of the charge carriers. This results in an increase in the diameter of the final charge cloud and therefore limits the obtainable benefit from increased detector bias voltage. Fig. 5.19 shows the width of the collected charge cloud for photons converted in the uppermost part of a Si sensor of 100 to 700 μm thickness, thus travelling the maximum collection time. It can be seen that the transition region between normal drift and velocity saturation starts to affect the charge cloud width already at a field strength well below 1 V/μm. It can be derived from the plot that the sensor should be operated at about 0.3 V/μm. Further increase of detector bias only leads to relatively small gains in the spatial resolution at the expense of increased leakage current.

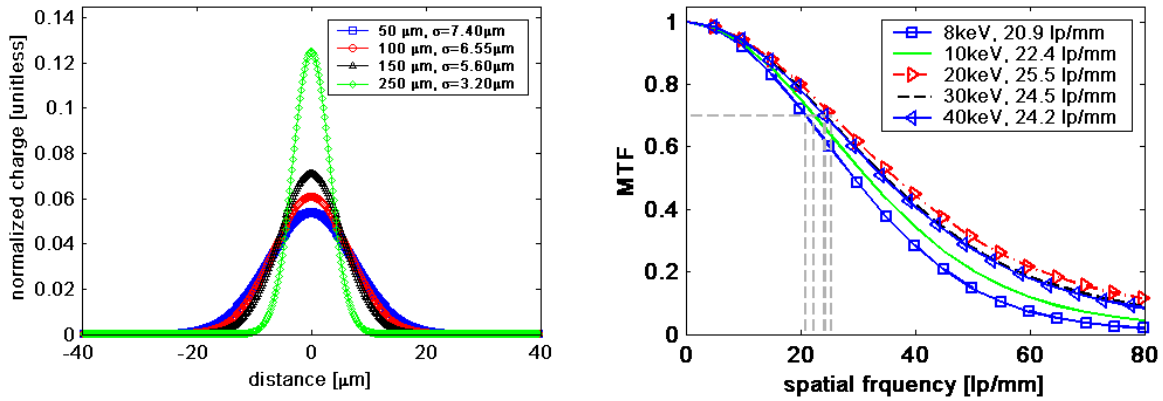
The overall spatial response of the sensor is given by the weighted sum over all conversion depths with the weights according to the linear attenuation law, c.f. eq. 1.5. For example the minimal average charge spread of 20 keV photons in a 300 μm Si sensor at 120 V bias voltage is $\sim$6 μm. A more significant measure of the spatial resolution is given by the modulation transfer function MTF. Fig. 5.18b) shows the sensor MTF for photon energies from 8 to 40keV. A characteristic figure for the spatial resolution is the spatial frequency at which the MTF drops to 70 % of its maximum value. The intrinsic sensor resolution of $>$20 lp/mm obtained for all photon energies under investigation is well above the Nyquist frequency of a 55 μm pixel pitch readout. The sensor spatial resolution also scales approximately with $\sqrt{d^2/V_{bias}}$. From this simple approximation together with the results presented in Fig. 5.19 it can be concluded, that the use of 700 μm thick Si sensors, to increase the sensor quantum efficiency QE, requires a detector bias voltage of $\sim$600 V to provide the spatial resolution.

5.2.3 Effects of readout electronics on the single pixel response

5.2.3.1 Spatial response

In pixellated detector systems the obtainable spatial resolution depends on both the sensor PSF and the pixel pitch of the readout. It is commonly described by the so-called presampling resolution, given the convolution of the sensor PSF with the aperture function of the pixellated readout. For a 300 μm thick sensor operated at 120 V the sensor resolution exceeds by far the resolution given by the Medipix2 pixel pitch, and thus the overall presampling resolution is governed by the aperture function of the readout. For photon counting system one cannot give a single figure for the presampling resolution. The reason for this is charge-sharing between adjacent pixel that leads to an effective pixel size depending on the actual applied threshold. The range of the effective pixel size in turn depends on the sensor PSF.

Fig. 5.20 gives an example for 300 μm Si sensor with a 55 μm pixel pitch and 10 keV photons. The exact geometric pixel size is obtained when setting the threshold to half the photon energy, since double counting due to charge-sharing is avoided at this threshold setting. Lower threshold values provide a higher apparent QE due to double counting, but



(a)

Figure 5.18: a) Lateral charge spread of the signal of 8 keV photons at the collection electrodes in a 300 µm Si sensor as a function of deposition depth. b) The presampling MTF for the same sensor, derived from the average deposition profile at the collection electrodes.

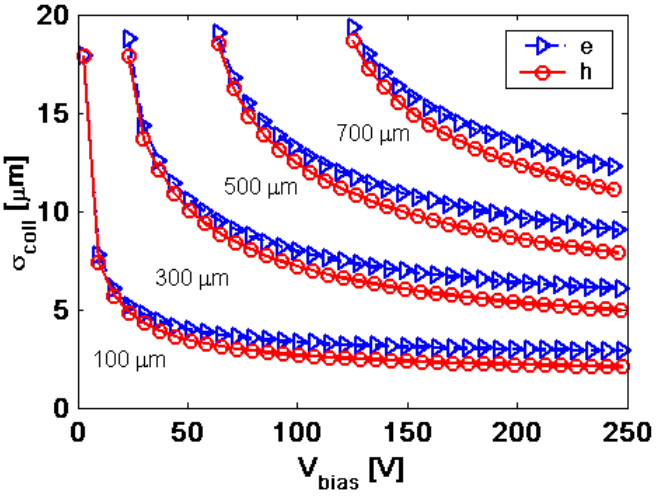


Figure 5.19: Maximal charge spread during charge collection in a Si sensor of 100-700 µm thickness as a function of the applied bias voltage.

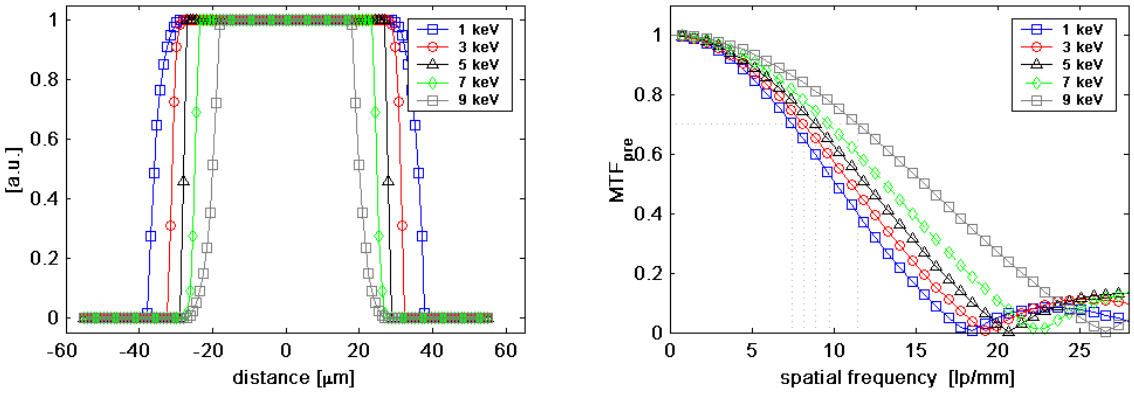


Figure 5.20: a) The effective pixel size as a function of the applied threshold value for 10 keV photons in a 300 µm Si sensor with 55 µm pixel pitch and b) the corresponding MTF curves.

at the same times decreases strongly the spatial resolution of the detector. The effective spatial resolution can be substantially increased by increasing the threshold well above the mid energy, but this is only achieved at the expense of QE and the introduction of an insensitive area around the pixel border leading to an effective fill factor of less than 100 %. On the contrary, in integrating detector systems charge-sharing always leads to an effective pixel size larger than the geometric pixel pitch, which then acts as a low pass filter on the image signal and leads to a decreased spatial resolution.

5.2.3.2 Spectroscopic response

Charge-sharing between neighbouring pixels not only affects the spatial resolution properties of the detector system but also makes the to spectroscopic response dependent on position of charge deposition. Fig. 5.21 displays the simulated spectra obtained with 55 μm pixel Si detector for 20 keV photons. In this simulation the incident beam was collimated to 10 μm width and the photons impinge on the sensor with offsets of 0 to 25 μm from the center of the pixel. For centrally converting photons the response is a sharp spectrum with a width dominated by the noise of the readout electronics, which was assumed to be 150 e^- in the simulation, The spectral information of the incident beam is preserved. At an offset of 15 μm the width of the distribution is already significant wider with going up to 1100 e^- at 25 μm offset from the center.

5.2.4 Large area detector response

The single pixel response variation described above directly affects the response properties of a large area detector. Both spatial and spectroscopic properties are changed from the ideal case.

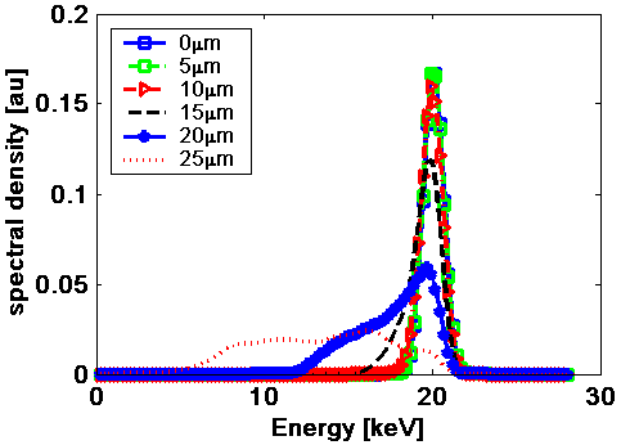


Figure 5.21: Simulated threshold scan for 10x10 µm pencil beam of 20 keV photons positioned at 0-25 µm offset from the center of 55 µm pixel in a 300 µm Si sensor. The ideal spectral information is obtained in an area of ∼100 µm² around the pixel center.

5.2.4.1 Energy resolution including readout noise

Fig. 5.22a) shows the simulated apparent spectrum of a monochromatic photon beam of 8, 10, 20 and 40 keV seen on the collection electrode of a single pixel of a 300 µm thick Si sensor with 55 µm pixel pitch. The initially mono-energetic signal is transformed into a continuous spectrum with a significant component of signal heights below 1 keV. This is due to the fact that only photons converted in the center of a pixel or very close to the collection electrode will yield the full pulse height. All other events are shared to a different extent with neighboring pixels. Signals contributing from half the photon energy to the full pulse height stem from photons converted within the pixel itself. The signals with lower energy originate from charge shared events in the direct vicinity of the pixel.

In Fig. 5.22b) the effect of the additional noise introduced by the amplification and discrimination process is illustrated, again calculated for 8, 10, 20 and 40 keV photons. In order to derive spectroscopic information from the detection data, a high peak to background ratio is desired. Fig. 5.22(c,d) show the simulated spectra of a 300 µm thick Si sensor with 170 µm pixel pitch with and without the electronic noise of the readout added.

Table 5.1 gives an overview of the simulation results for energy resolution and signal to background ratio for a 300 µm thick Si sensor with pixel size of 55-300 µm. The value for background in the calculation of the signal to background ratio was obtained by summing the spectral density from a cutoff energy of 4 keV to the beginning of the photopeak. The peak value itself was taken as the integral of the fitted Gaussian under the photopeak. The energy resolution and the peak to background ratio provide complementary information. A lower energy resolution gives results in a larger fraction of background events covered by the photopeak, giving a higher figure for the peak-to-background ratio.

The effects of charge-sharing strongly degrade the spectroscopic performance of a

		150 e^-		100 e^-	
pixel [μm]	E [keV]	resolution [%]	peak/bg	resolution[%]	peak/bg
55	8	21.7	145.4	14.0	95.7
170	8	16.9	460.7	11.2	368.3
300	8	16.4	860.1	10.9	705.6
55	20	7.5	51.3	5.0	42.9
170	20	6.6	233.2	4.4	212.7
300	20	6.5	476.3	4.3	439.0

Table 5.1: Simulated energy resolution (FWHM) and detection efficiency of the sensor signal with 150 electrons rms noise added for a 300 μm Si sensor at 120 V sensor bias and with the threshold set to 4 keV.

detector with 55 μm square pixels. A pixel size of more than 170 μm is preferable to obtain an energy resolution better than 20 %, though the target value also achievable with a readout electronic noise better than 150 e^-. The value of 20 % is a common requirement in X-ray diffraction based materials analysis to distinguish a Fe fluorescence photon background of 6.4 keV from the K_α-line of 8.0 keV of a Cu target X-ray source [44].

From the results presented in this section it can be concluded, that a satisfactory energy resolution can be reached for 8 keV photons with a pixel pitch of 55 μm, though the spectroscopic performance of a 170 μm pixel device is $\sim$22 % better.

5.2.4.2 Homogeneity of the response across pixel borders

The homogeneity of the detector response is one of the critical factors determining the achievable SNR and the maximal DQE of a detector system. Especially for applications relying on correct relative count rates, such as X-ray crystallography, the homogeneity of detector response is a key requirement. As shown in the previous section, charge-sharing between neighbouring pixels changes the pulse height distribution considerably. This can lead to count rates deviating from the real number of photon converted in the sensor depending on the actual threshold level. Especially in the border region between two neighbouring pixels photons may be counted in both pixels if the threshold is less than half the photon energy, or may be lost if the threshold is set to a higher value. It has been shown that by setting the threshold to exactly half the energy of the photons to be detected a uniform detector response between two identical neighbouring pixels can be accomplished [86]. But in a small region around the corner of a pixel however the charge may be split between four adjacent pixels. To estimate the resulting variation in detector response, simulations have been carried out with a collimated beam of 5 μm^2 stepped over 4 x 4 pixel detector surface. The varying sensitivity across the sensor area is illustrated in Fig. 5.23, where the count obtained with the threshold set to a) 25 %, b) 50 % and c) 75 % of the energy of the incoming photons are plotted. Fig. 5.23d) gives the dependency of the response homogeneity on the applied threshold for photon energies of 10, 20, 40 and 80 keV. The most uniform response is obtained for a threshold just below the half energy of the incoming photons, representing the best compromise between the extent of the

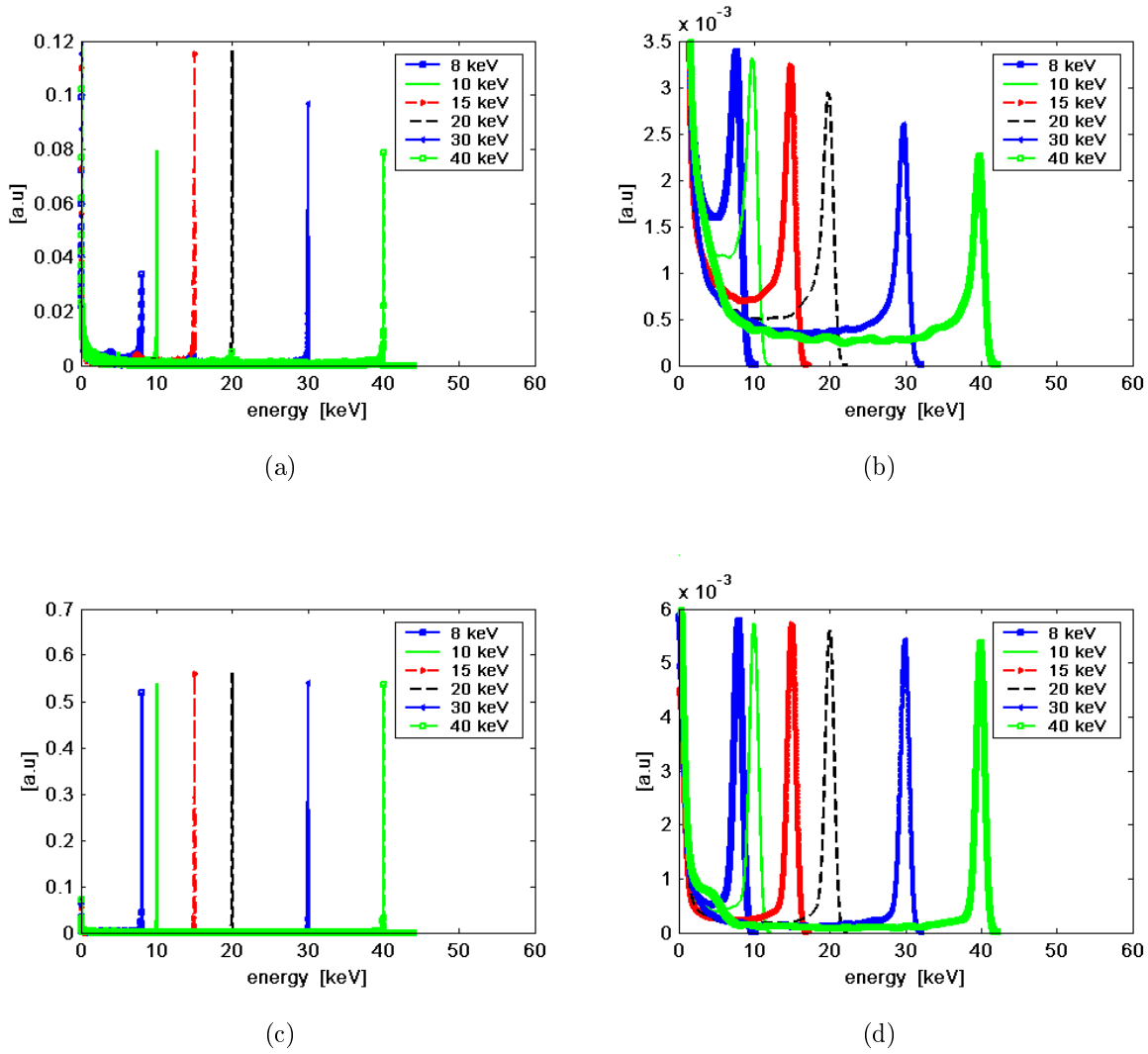


Figure 5.22: Spectral response of a 300 µm Si sensor under uniform irradiation with monochromatic X-rays of 8 to 40 keV. a) Signal spectrum seen by the collection electrodes of 55 µm pixel pitch and b) the same signal with an additional readout electronic noise of 100 e^- rms. c) Signal spectrum seen by collection electrodes of 170 µm pixel pitch and d) with a readout electronic noise of 100 electrons rms added. The reduced ratio of border region between adjacent pixel versus the center region results in an increased spectral performance of the 170 µm pixel.

charge splitting area and the maximal count loss in the border area. For 10 keV photons the count in the corner region between four adjacent pixels drops to ∼40 % and leading to a decrease of ∼4 % in mean number of counts. The best homogeneity of ∼17 % can be achieved for 20 keV photons, which provide also the best spatial resolution of the energies simulated, c.f. Fig. 5.18. For photon energies above 40 keV strong variations in the charge deposition due to increasing Compton scattering occur, as described in sec. 5.1.3, Fig 5.5. The drop of count rate in the corner therefore is much more pronounced since almost all Compton scattered photons will be missed.

5.2.4.3 SNR and DQE

Charge sharing also changes the detected signal variance of the photon beam. Two cases have to be considered, namely the variance of the summed counts of all pixels in the matrix in repeated measurements and the variance across the pixel matrix for a single acquisition.

The statistics for total number of counts recorded by the detector for a series of measurements can be calculated from the probabilities for a photon being counted only in one pixel or resulting in multiple counts. The number of photons detected in one pixel follows Poisson statistics with $q = QE \cdot N_{photon}$ being average count, QE the quantum efficiency and $N_{phototn}$ the number of incident photons. α_n is the probability that a detected photons is counted n-fold (in other words in n neighbouring pixels) and α_0 denotes the probability of not counting at all a converted photon. The probability of recording n photons in a pixel is given by

$$p(n) = \frac{q^n e^{-q}}{n!}. \tag{5.5}$$

The mean value and the variance can be derived from the moment generating function, which is given by

$$H(t) = \Sigma_n e^{nt} p(n) = e^{q(\Sigma_i \, \alpha_i e^{i\,t} - 1)}$$

The mean value and the variance of the resulting distribution then is calculated from the first and second derivative of moment generating function H at $t = 0$.

$$\mu = H'(0) = q\Sigma_i i \, \alpha_i$$

$$\sigma^2 = H''(0) - H'(0)^2 = \Sigma_n n^2 \, \alpha_i.$$

With $\alpha_1 = 1 - \alpha_0 - \Sigma_{n=2} \, \alpha_n$ one obtains

$$\sigma^2 = q(1 - \alpha_0 + \Sigma_{n=2}(n^2 - 1)\alpha_n).$$

The resulting SNR is given by

$$SNR = \sqrt{q} \frac{1 - \alpha_0 + \Sigma_{n=2} \, (n-1)\alpha_n}{\sqrt{1 - \alpha_0 + \Sigma_{n=2}(n^2 - 1)\alpha_n}}. \tag{5.6}$$

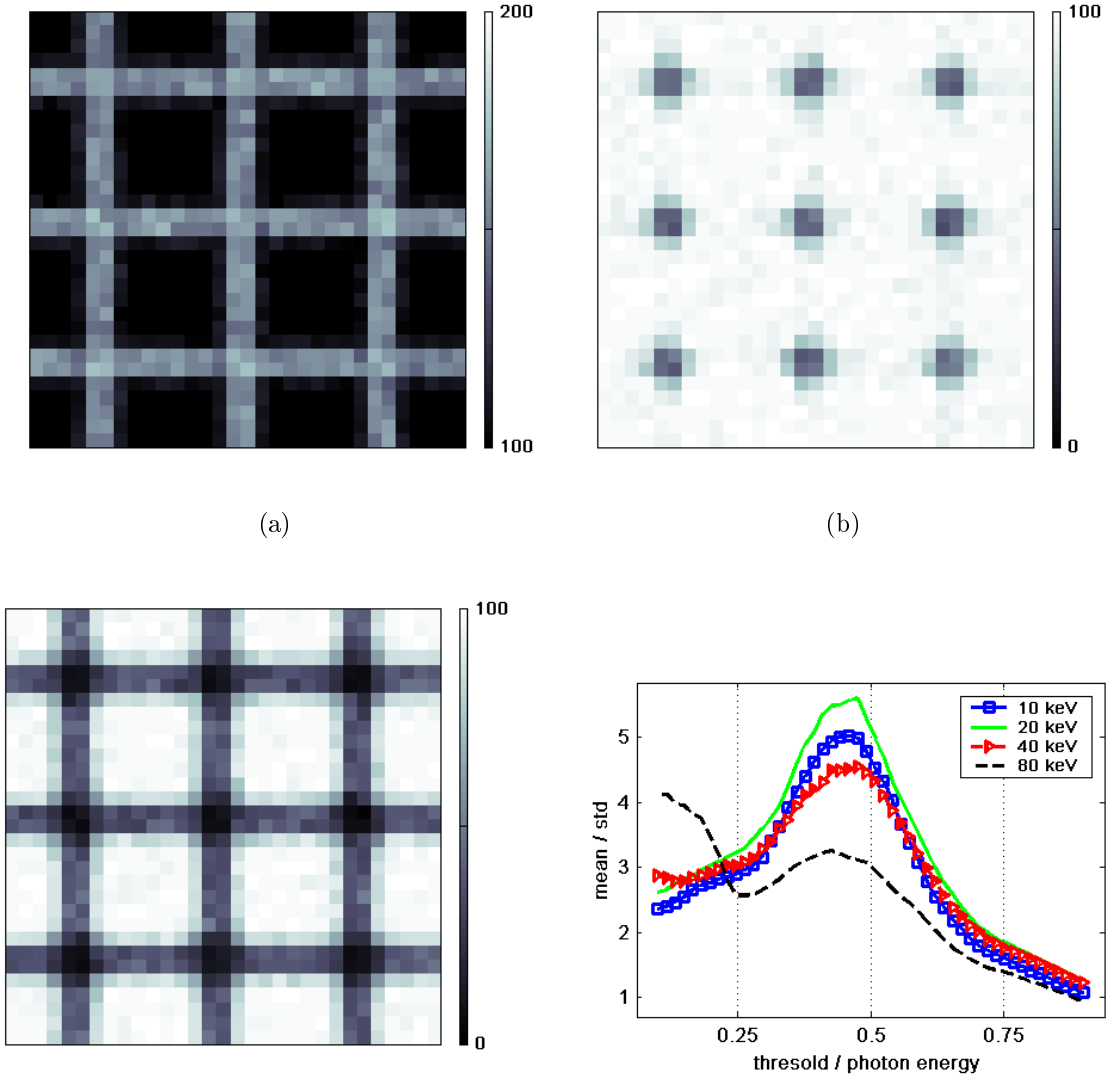


Figure 5.23: Detector response variations as a function of the energy threshold. The count rates obtained in an 4 x 4 pixel area with the threshold set to a) 25%, b) 50% and c) 75% of the energy of the incoming photons are shown. d) The homogeneity of the detector in terms of mean count rate over standard deviation as a function of the applied threshold for photon energies of 10, 20 , 40 and 80 keV.

It is evident from eq. 5.6 that the SNR decreases due to the multiple counts. Taking only into account double counts and neglecting higher multiple hits, one obtains for the DQE

$$DQE = \frac{SNR^2}{N_{photon}} = QE\frac{(1-\alpha_0+\alpha_2)^2}{1-\alpha_0+3\alpha_2}.$$

For reasonable detector operation modes one can assume that less then half the recorded photons are counted twice, in other words $\alpha_2/(1-\alpha_0) < 1/3$, leading to an approximate expression for DQE

$$DQE = QE(1-\alpha_0-\alpha_1). \tag{5.7}$$

In other words charge shared events rejected by the discriminator and double counted events decrease the DQE to the same extent. It should be noted however, that eq. 5.7 does not represent the DQE(0) of an individual image, but rather describes the statistics of the summed up total count of the pixel array.

To obtain the corresponding expression for the spatial distribution of counts in a single acquisition one has to start again from eq. 5.5. The probability of counting in the same pixel n charge shared events originating in a direct neighbour is given by

$$p_s(n) = \frac{(\alpha q)^n e^{-\alpha q}}{n!}$$

with

$$\alpha = \frac{N_{double}}{N_{single}} + 2\,\frac{N_{triple}}{N_{single}} + 3\,\frac{N_{quatriple}}{N_{single}}$$

the fraction of events leading to a count in a neighbouring pixel. Then the probability to record exactly n counts in a pixel is

$$h(n) = \Sigma_{m=0}^{n} p(n-m)p_s(m).$$

For the moment generating function one obtains

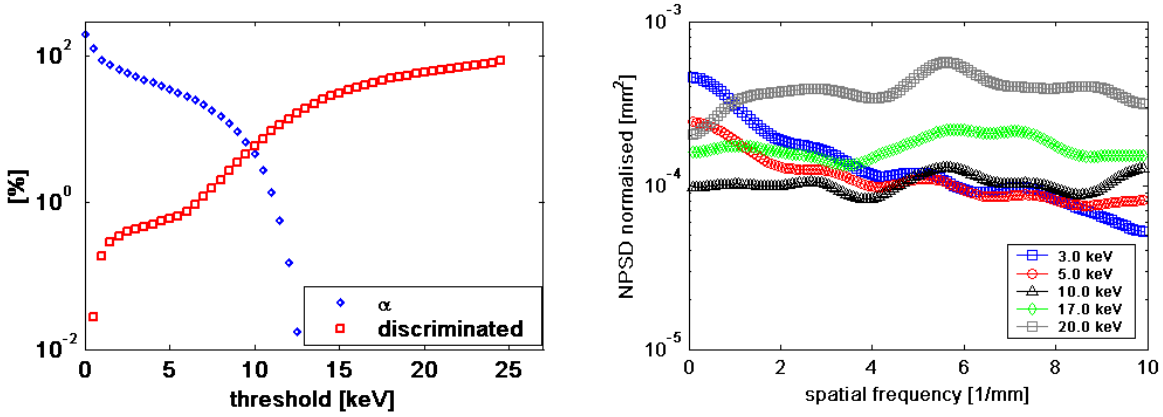
$$\begin{aligned} H(s) &= \Sigma_n\, e^{nt}\Sigma_{m=0}^{n}\,\frac{e^{-q}q^{n-m}}{(n-m)!}\frac{e^{-\alpha q}(\alpha q)^m}{m!} \\ &= \Sigma_n\, e^{nt}e^{-q(\alpha+1)}q^n(1+\alpha)^n \end{aligned}$$

leading to the following expressions for the mean and variance of the pixel array response

$$\mu = H'(0) = q(1+\alpha)$$

$$\begin{aligned} \sigma^2 &= H''(0) - H'(0)^2 = q^2(1+\alpha)^2 + q(1+\alpha) - \mu \\ &= q(1+\alpha). \end{aligned}$$

The DQE(0) finally is given by



(a) (b)

Figure 5.24: a) The average number of charge shared events in a 300 µm Si sensor of 55 µm pixel pitch as a function of the threshold applied. The spectrum of a W-tube operated at 25 keV with 2.5 mm Al prefiltering was used in the simulation. b) The NPS derived from simulated data from the same sensor as in a) over an area of 20x20 pixels. The minimum noise levels are obtained at 10 keV threshold, which marks the crossing point of the spectrum of single counted and double counted events.

$$DQE = QE\,(1+\alpha).$$

This apparent increase of DQE above the level of Poisson statistics is not an expression of increased image quality but rather is a consequence of the blurring effect of the charge shared events acting as a low-pass filter on the image, with the penalty of decreased contrast resolution. The effects on the NPS are illustrated in Fig. 5.24(a,b) for spectral X-ray source, which is the more common case in imaging applications. In this simulation $5 \cdot 10^4$ photons from a of a W-tube at 25 keV with 2.5 mm Al prefiltering have been converted into a matrix 20x20 pixels of a 300 µm Si sensor with 55 µm pixel pitch and 120 V sensor bias. Fig. 5.24a) shows the fraction of charge shared events per detected photons α, which strongly decreases with the threshold applied. Also plotted is the fraction of photons discriminated. Fig. 5.24b) illustrates the NPSD for threshold values of 3, 5, 17 and 20 keV. For the lowest threshold of 5 keV the increased fraction of charge sharing leads to a decrease of the NPSD at higher frequencies due to the low pass filtering effect of the multiple counts. The minimal variance is obtained for a threshold of 10 keV with a flat NPS power spectrum. This minimum is reached at the crossing point of the spectrum of single counted and multiple counted events, which marks the optimal compromise between discriminating charge shared events and reduction of count rate, Fig. 5.25. A further increase of threshold does not improve image quality but leads to increasing noise levels due to loss of count rate.

5.3 Charge sharing correction

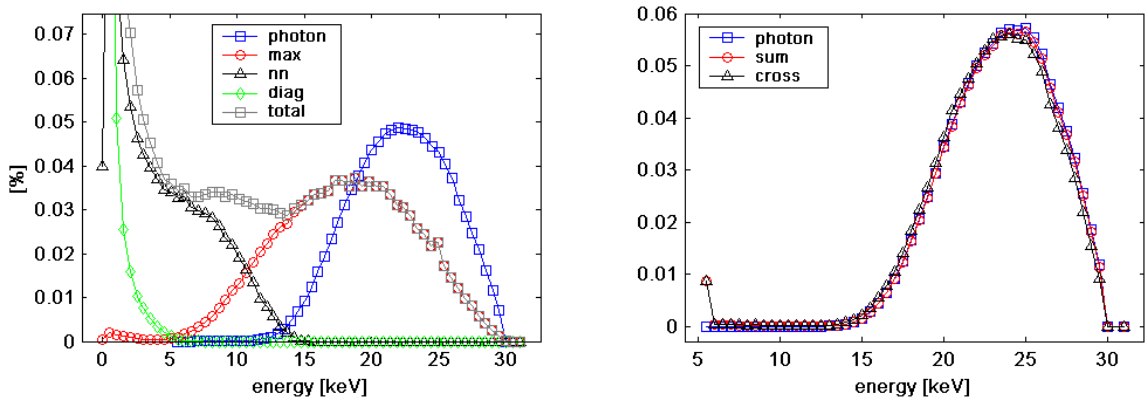
The influence of charge sharing on the spectral response is particularly evident when using spectral X-ray sources. Fig. 5.25a) illustrates the incident spectrum observed in a single pixel when using a W-tube operated at 30 kV and with 2.5 mm Al prefiltering after passing trough a 2 cm Perspex layer. The photonic spectrum is already widened considerably in single pixel spectrum, i.e. just signal from photons converted in the pixel itself, without any contribution from charge shared events from neighbouring pixels. Additional contributions from charge shared signals from the four direct neighbours and the 4 diagonal neighbours further modify the spectrum. The counts recorded correctly within the hit pixel itself show an energy range down to ∼5 keV, whereas the charge shared events stemming from neighbouring pixels contribute up to ∼14 keV. The low energy tail of the maximum pulse spectrum is a result of Compton scattering in the energy deposition. Obviously it is impossible to discriminate double counts by adjusting the threshold without losing correctly counted photons at the same time. This leads to increased noise levels and effectively limits the achievable SNR and dose efficiency in imaging applications.

A possible solution to this limitations is to include a winner-takes-all logic in the readout electronics. In this way it is feasible to determine the highest concurrent signal in a neighbourhood of 3x3 pixels. The smaller pulses are disregarded and only the maximum signal is compared against the discriminator threshold. In a more sophisticated version of this readout electronics a summing of the coincident signals could be done, with the sum assigned to the pixel with the maximum individual contribution prior to further processing. In this case it has to be kept in mind that the noise on the summed signal scales with the square-root of the number of pixels taken into account. Therefore it may be advantageous to treat the summing logic from the corner with 4 neighbours rather than the pixel itself. A charge sharing correction on the single pixel level corrects not only for the position dependent spectroscopic response but also removes inhomogeneities in detector response and provides a correct effective pixel size regardless the threshold applied.

5.4 Energy weighting

A further option of treating the charge shared signal is to take advantage of the possible additional information. One can envisage to put a DAC and several counters inside every pixel. By calculating the center of mass from the signal heights in a cluster, sub-pixel resolution could be achieved. In an similar approach, using N counter per pixel the signal can be tested against N thresholds, creating N bins for the spectral information. In this way the X-ray image can be split into several "colors", providing extra information about the absorbing material. As already described in sec. 3.4 the SNR ratio can be improved by weighting the individual photon according to its energy.

To quantify the possible gains of this technique a low contrast case has been studied, represented by a 1 cm thick water object in 4 cm thick block of Perspex. The spectrum used for the calculations was a W-target X-ray tube operated at 30 kV and prefiltered with 0.5 mm Al before transmission through the object and a Si sensor of 300 μm thickness was



(a) (b)

Figure 5.25: a) The spectrum of a W-tube at 30 keV with 2.5 mm Al prefiltering seen by the collection electrodes. The overall spectrum has been split in to the contributions from the maximum signal per photons (labelled max), the charge shared signal from the 4 direct neighbours (labelled nn) and the signal from the diagonal neighbours (labelled diag). The signal from diagonal neighbours is negligible for thresholds above 6 keV, whereas the the contributions from the direct neighbours extends up to 15 keV. b) The spectrum obtained for the same incident photon spectrum, but in this case the signal of neighbouring pixel is preprocessed before being compared against the energy threshold. The spectrum of all pixel in a 3x3 neighbourhood (labelled sum) and the one obtained of a of a cross shaped neighbourhood around the main signal pixel (labelled cross) is plotted. The contribution of diagonal vicinity is small compared to the next neighbours, apart from very low energies. The spectrum of the summed signal presents an excellent approximation for the real photonic spectrum.

assumed. The results given here represent the ideal case and no additional noise from the readout is added to the Poissonian photonic noise. The effective spectra used to calculate the SNR are derived from the simulated photon spectra by convolution with the results for the spectroscopic response presented in sec. 5.2.4.1.

Fig. 5.26 shows the results for the SNR as a function of the applied threshold. Included in the graphs are the values for the SNR obtained by weighting the incident spectrum with the optimal weights as given in eq. 3.7. This curve is meant to give the reference value of the maximum SNR possible, since it only can be reached with an a-priory exact knowledge of the examined object.

Fig. 5.26a) illustrates the situation for an hypothetical energy-discriminating but still integrating detector system. In this case the signal height is compared against an energy threshold and only integrated if the pulse height exceeds the threshold. The use of signal preprocessing of the pixel signals as described in sec. 5.3 can provide significant improvements also for this hypothetical integrating scheme. The SNR can be improved to up to 74 % of the ideal case by summing all signals of a cluster of responding pixels. Basically the same result can be achieved by summing a cross shaped neighbourhood (the signal of the four direct next neighbours and the pixel with highest signal itself). This is not surprising, since the spectrum recovered from a cross shaped neighbourhood is already an excellent approximation for the full sum of all pixel involved, c.f. Fig. 5.25b), since the majority of events does not include the diagonal neighbours. Also by selecting only the maximum signal of an event yields a SNR of about 69 % of the ideal one can be achieved. Analogue simulations of higher contrast objects and objects including K-edge absorption give very similar results.

Fig. 5.26b) shows the SNR obtained when simulating a counting system, which corresponds to applying uniform weights to valid signals. The gain in SNR for the charge shared signal is $\sim$10 % higher than in integrating systems. For the maximum signal, the sum and the cross-sum signal the SNR is about 90 % for thresholds well below the respective effective signal spectrum.

In Fig. 5.26c) finally the signals are weighted by a factor E^{-3}. Applying this technique on the charge shared signal without further preprocessing, the resulting SNR is strongly degraded. Since the original photonic energy spectrum is substantially altered, the resulting mis-weighting of the charge shared signals increases the noise dramatically. On the other hand weighting the maximum signal increases the SNR to over 70 %. But it still does not exceed the results obtained by simply counting the maximum signal. Again the deviation from the real spectrum in combination with a strong weighting of the recorded spectrum reduces the performance. When applying a E^{-3} weighting function to the summed and cross summed signal, the SNR approaches the theoretical limit and yields up to 98 % of the maximal achievable SNR, provided the threshold is set in a way that the contributions from Compton scattered events are disregarded .

The gain in SNR by weighting the individual photon by E^{-3} is most pronounced if the object contrast is very low, as in the example described above. This is a consequence of the fact that the weighting by E^{-3} is the first order approximation for the ideal weighting factors, c.f. Eq. 3.7, assuming low contrast setup. Energy weighting still offers improvements also for higher contrast objects, though the relative increase in SNR is smaller. The weighting by E^{-3} in fact becomes counter-productive if K-edge absorption takes

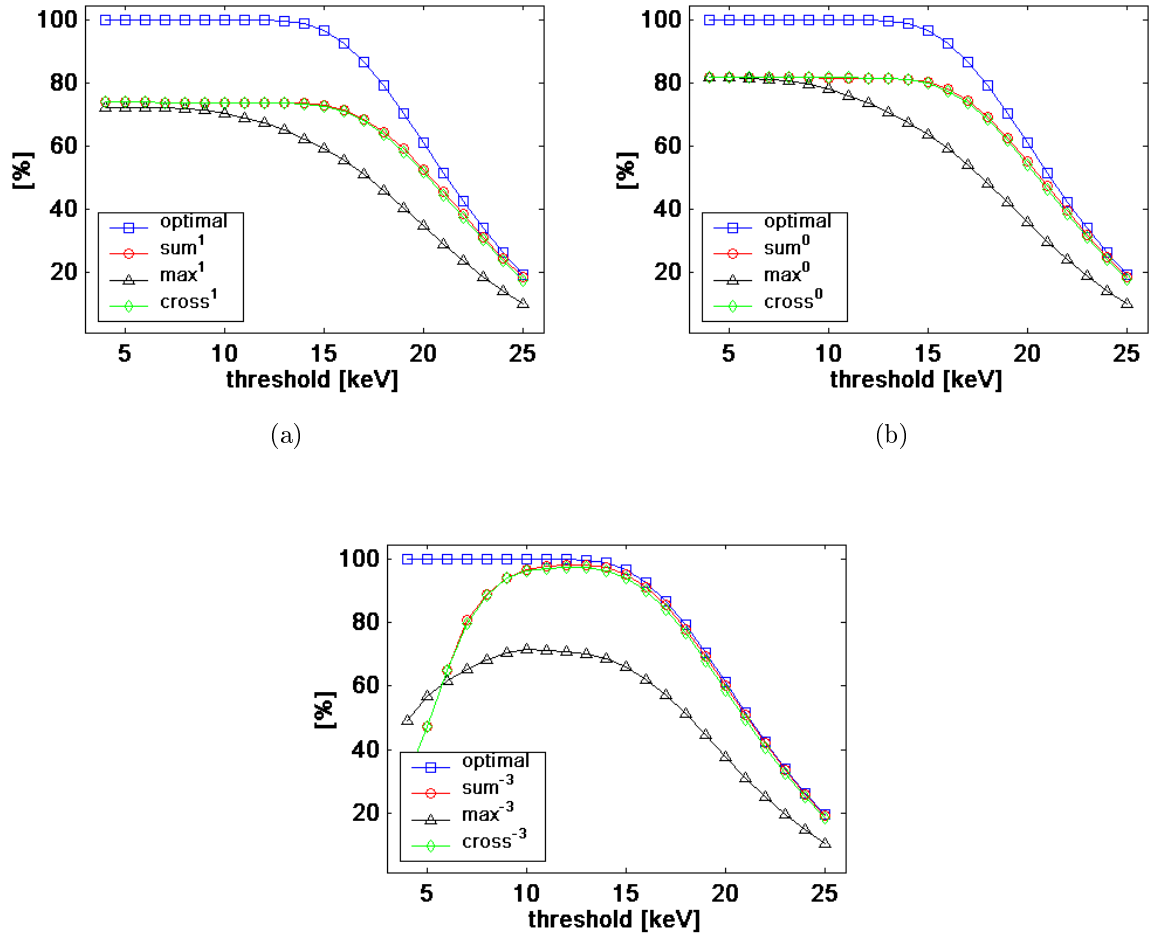


Figure 5.26: Comparison of the SNR obtained with a) hypothetical energy discriminating but integrating detector system, b) with a counting and c) with an energy weighting systems. The values graphed represent the ideal case of no electronic noise added to the sensor signal. In all three curves the SNR obtained by weighting the incident spectrum with the optimal weights as given in eq. 3.7 is also plotted as a reference value.

place in the object under investigation. The discontinuity in the energy dependence of the linear absorption coefficient leaves photons above the K-edge overly weighted. The E^{-3} dependence of the weighting factors therefore is not an universal schema, but needs to be adapted to the object examined if the maximum gain from energy weighting is to be obtained.

Most of the benefits of energy weighting can already be obtained by using few energy bins for the recorded spectrum and to apply uniform weighting factors to the tallied spectrum. For example in the case of a smooth photon spectrum a five energy-bin counting electronics provides up to 97 % of the effect of weighting the continuous spectrum. For spectra including discontinuities the efficiency of a five-bin weighing is still ∼77 %. A readout chip offering three to five energy bins therefore would open the possibility to apply weights offline after image acquisition and tailor the weighting functions to the object under investigation.

5.5 Summary

Monte Carlo simulations have been carried out for Si, GaAs and CdTe for detector thicknesses of 50, 100, 300, 700 μm and pixel sizes of 25, 55, 170, 300, 700 and 1000 μm for photon energies from 8 keV up to 140 keV. The diameter of the initial charge cloud after conversion in the range of 8 to 40 keV photon energy depends almost linearly on the photon energy and ranges from 0.1 μm to 5.2 μm rms in Si, in GaAs from 0.04 μm to 2.2 μm and in CdTe from 0.04 μm to 1.7 μm.

In Si losses in deposited energy due to surface escape are almost independent of the sensor thickness in the range investigated. In a 300 μm thick Si sensor with 55 μm pixel pitch photons with energies up to 20 keV deposit more than 90 % of their energy within the pixel. Above this energy the fraction of photopeak events drops quickly with increasing photon energy. An increase in pixel size hardly improves the spectral response of the sensor, since the dominant mechanism for the energy losses is surface escape of Compton scattered primary photons. Surface losses due to escaping secondary electrons are negligible compared to photonic losses for a sensor thickness >50 μm. In a 170 μm pixel pitch sensor the photon energy limit for 90 % deposition rises only to 27 keV. The QE of a 300 μm thick detector on the other hand is only about 27 % for 20 keV photons. It can be concluded that Si as a sensor material for a photon counting system gives best results in the energy range up to ∼20 keV.

In GaAs the influence of the Compton effect is of minor importance for energies lower than 60 keV. The principal mechanism resulting in a deformation of the recorded energy spectrum is fluorescence photon emission, with a pronounced local maximum at photon energies just above the K-edges. The same is true for CdTe, apart from stronger surface losses via fluorescence photons. The main difference between the two materials is found in their spectroscopic responses. In general in GaAs a higher fraction of photons contribute to the photopeak signal. The respective numbers for 80 keV photons converting in a 170 μm pixel pitch sensor of 300 μm thickness are 60 % for GaAs and 45 % for CdTe. For photon energies above the K-edge, both materials show a strong influence of the sensor and pixel geometry on the spectrum recorded. In the energy range below 20 keV CdTe should provide the best spectroscopic performance, whilst Si and GaAs give a comparable

response.

A further broadening of the spectral response is introduced by the additional charge spread after charge transport and collection and by the readout noise. The energy resolution better than 20 % can be obtained with a 300 μm thick Si sensor with 55 μm pixels using a Medipix2 readout electronics. The best presampling spatial resolution of $\sim$25 lp/mm and the most homogeneous area response for such a device is expected for 20 keV photons. Both spatial resolution and image noise have been found to depend on the fraction of charge shared photons.

It should be noted, that all the effects described in this chapter are not exclusively present in photon counting systems, but also affect integrating detectors. Especially if Compton scattering is not negligible in the sensor, a counting scheme may offer advantages over simple integration of the charge deposited.

Spatial and spectroscopic performance can be improved by correcting for the charge split introduced by the energy deposition and the charge transport. A good approximation of the real photonic spectrum can be obtained by using the signal of the four direct neighbours in a pixel matrix to calculate a sum signal and to determine the pixel with the highest individual signal via a WTA logic. By applying appropriate weighting to the obtained spectral information the SNR in imaging application can be increased with respect to conventional energy integrating detection techniques. The most substantial improvements can be obtained for very low contrast objects.

The gain of such energy weighting schemes depends strongly on the object contrast, and the weighting factors have to be chosen very carefully. In the presence of deviations in the recorded spectrum from the real photon spectrum, the energy weighting technique can degrade the image SNR. On the other hand a simple photon counting scheme that uses a corrected spectrum gives a slightly lower SNR, but proves to be more robust against deviations from the true energy spectrum.

Chapter 6

Experimental Detector Performance Characterisation

Extensive measurements have been performed to evaluate the detector performance. The first part of the chapter describes measurements performed with the Medipix2 detector using monochromatic X-rays at the European Synchrotron Radiation Facility, ESRF. Threshold scans were used to measure the apparent spectrum of the individual pixel signal, to determine the pixel threshold and the energy resolution and to investigate the effects of charge-sharing. These scans were made for different X-ray energies in the range of 8 keV to 40 keV. The influence of charge-sharing was studied by using both pencil beam irradiation and wide area irradiation. In order to estimate the homogeneity of the detector response mesh scans were performed by scanning the pencil beam in steps of 5 and 7 μm over the border region of adjacent pixels with 8, 10 and 20 keV photon energy.

In section 6.2 detector response homogeneity and the effectivity of flat-field correction techniques are investigated, using both generations of the Medipix and different X-ray spectra from conventional generators. In section 6.3 the experimental determination of the modulation transfer function (MTF) is presented. The noise of the detector is characterised in terms of the noise power spectrum (NPS) and the detective quantum efficiency (DQE) is derived from the measurements. Section 6.4 discusses the influence of applied dose on the image quality. In the last part of the chapter the first results using the energy window mode of the Medipix2 detector are presented.

6.1 Synchrotron beam measurements

Electronic noise, sensor homogeneity, threshold dispersion and linear energy response are key figures of merit for detector performance. Electronic noise may dominate the spectral resolving power. Sensor inhomogeneity and energy threshold dispersion limit the maximum SNR in imaging applications, whilst the linearity of the energy threshold is directly linked to the efficiency of the fine tuning of the threshold dispersion. An absolute energy calibration of the detector therefore is imperative, in order to set the detector to the optimal working point for a given application.

Charge-sharing leads to a complex interplay of photon energy, energy threshold and energy resolution. Therefore the individual contributions are difficult to separate in mea-

surements using broad energy spectra. The tunable and intense monochromatic X-ray radiation provided by synchrotron radiation facilities is best suited to investigate the detector performance. Measurements have been performed to determine the detector response under both highly collimated pencil beams and the irradiation covering a large number of pixels. In this way one can separately study the effects of sensor homogeneity and readout electronics on the one hand and charge-sharing on the other hand.

For reasons of clarity all plots in the chapter displaying threshold scan measurements have the abscissae converted from the external DAC setting for the discriminator into photon energy in keV using the calibration results presented in sec. 6.1.2.

6.1.1 Experimental setup

The measurements were performed on the multipurpose BM5 beam-line at the ESRF, Grenoble. The machine mode was 2x1/3 filling, with 200 mA nominal ring current. The photon beam energy was tuned from 8 keV to 40 keV with a double crystal Si (111) monochromator at 27.2 m from the bending magnet providing $2 \cdot 10^{-4}$ relative energy resolution and a typical beam intensity 10^{10} photons/mm^2/s at 25 keV at the detector. To avoid detector dead-time effects in the measurements the very high beam intensity was reduced to $\sim 1 - 2 \cdot 10^6$ photons/mm^2/s by detuning the second monochromator mirror. Upstream attenuators before the monochromator were not used to adjust beam intensity in order to keep the monochromator in a stable thermal state. The beam intensity was monitored with a Si photo-diode. The largest beam size obtainable at the BM5, ~6x3 mm^2 wide, is not completely uniform. Therefore a double set of horizontal and vertical slits was placed 20 cm upstream of the detector to collimate the incident photon beam to about 1 mm^2 for area irradiation, covering ~300 pixels. To perform sub-pixel resolution measurements the collimator opening was set to the minimum width of 10x10 μm^2.

The Medipix2 detector was placed in a protective metallic housing with a low X-ray absorption light-proof entrance window, a black polymer foil of 50 μm thickness, to exclude light induced leakage current in the sensor. The metallic housing was positioned on a bench with 4 motorized axes, XYZ translations and vertical rotation, providing submicron positioning precision in order to perform pencil beam scans to measure detector response with sub-pixel precision. The step sizes used in a scan were 5 or 7 μm.

In all threshold scans presented in this section, the external DAC was used to control the low energy threshold. As mentioned in sec. 4.2.2, the external 12-bit DAC offers a much finer resolution than the on-chip internal DAC. It should be noted that energy threshold rises with increasing internal DAC value, whereas the relation between external DAC and threshold is inverse.

6.1.2 Energy calibration

In order to obtain uniform detector response and optimal SNR in imaging the energy threshold has to be set accurately. In the case of mono-energetic X-rays one uses a value of half the photon energy. For spectral X-ray sources the optimal point depends both on the actual spectrum used and on the extent of charge-sharing between adjacent pixels, cf. section 5.2.4.3.

To measure the threshold linearity the X-ray beam was collimated to an area of 10x10 μm^2 and positioned in the center of a pixel to ensure charge collection of the deposited energy as much as possible within the targeted pixel only. The monochromator was set to 7.9 keV, leaving the second monochromator crystal only weakly detuned. In this way contaminations from higher harmonics can pass the monochromator, providing a set of well defined X-ray lines that can be used in a single experiment to calibrate the DAC value-energy correlation. Fig. 6.1a) shows the result of the threshold scan, plotting the measured counts versus the values of the external DAC controlling the energy threshold. The presence of higher harmonics is clearly visible and the plateaus in the threshold scan indicate the absence of charge-sharing effects. The position of the steps in the count correspond to at 7.9 the right hand side and 23.7, 31.6 and 39.5 keV at decreasing values for the external DAC. The first harmonics line of 15.8 keV is a quasi forbidden reflection of the Si(111) monochromator and is therefore missing in the sequence.

The derivative of the threshold scan gives the recorded photon spectrum. The position of the X-ray line and its width in terms of threshold DAC value is calculated by fitting the derivative with a Gaussian distribution. As the intensity decreases with the order of the reflection and the detection efficiency of Si drops rapidly with increasing photon energy, the height of the peaks also decreases. Therefore also the obtained values for position and width of the photopeaks are less precise for energies higher than 24 keV.

The energy calibration curve is plotted in Fig. 6.1b). The correlation coefficient for a linear fit of the mean threshold values is 0.9997, indicating excellent linearity. This is an important parameter for the chip functionality in connection with the procedure to reduce the spread of the threshold energy across the active matrix using a so-called threshold adjustment map, c.f. section 4.2.3. Provided a linear threshold-energy correlation it is sufficient to determine the threshold adjustment mask only once for all threshold values within the linear range. The same map then can be used at any other threshold without broadening the threshold distribution.

This energy calibration is based on the response of one single pixel only. The final calibration was obtained using the results from the average response of a large number of pixels under area irradiation. This measurement will be described in detail in sec. 6.1.4. The so obtained energy calibration for the external DAC is

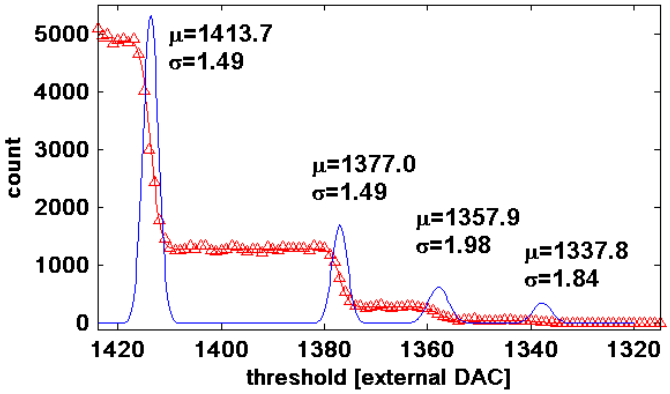
$$DAC_{extern} = 1430.8 - 2.455 \cdot E\,[keV], \tag{6.1}$$

also shown in Fig. 6.1b). The main difference to the calibration obtained by the single pixel is given by a small offset, which is a result of a remaining non zero threshold dispersion after fine tuning. The deviation in constant of proportionality is less than 2%. A calibration for the internal DAC can be found in sec. 6.3.1.

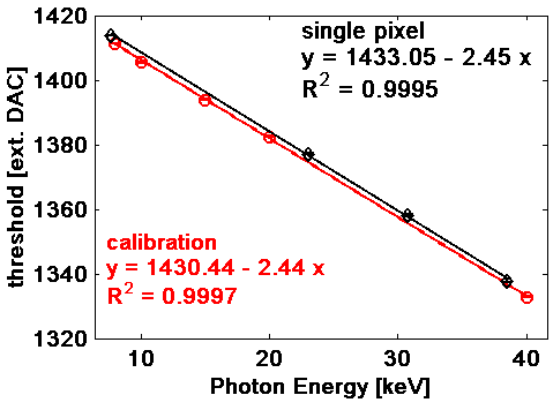
6.1.3 Single pixel response

6.1.3.1 Pixel response profile and detector response homogeneity

In the ideal case a pixel responds only to photons converting within its geometrical limits and the spatial resolution is determined only by the pixel aperture. In reality the effective pixel geometry is given by the convolution of the geometric pixel dimension with the



(a)



(b)

Figure 6.1: a) Threshold scan, performed by stepping the discriminator level from 2 keV up to 43 keV. Plotted are the measured counts versus the values of the external DAC controlling the energy threshold . The presence of higher harmonics at 23.7, 31.6 and 39.5 keV is clearly visible. The constant count rate between the energy lines indicates the absence of charge-sharing effects as the photons hit the center of a single pixel. The count rate for threshold DACs approaching 1425 starts to rise due to increasing frequency of noise hits for threshold level very close to the single pixel noise floor of ∼2.2 keV. b) The energy calibration obtained from the single pixel measurement graphed in (a) together with the results extracted from area irradiation measurements involving 330 pixels. The constants of proportionality differ by less than 2% and the offset of the single pixel calibration is in compliance with the threshold spread of the electronics.

sensor PSF. As pointed out in sec. 5.2.3, the effective pixel size is threshold dependent in a photon counting system. Further deviation from the ideal pixel response may be caused by sensor inhomogeneities or variations in bump bonding quality. Especially around the junction of four neighbouring pixels charge sharing will cause increased charge splitting and subsequently may lead to missed photons or photons counted in more than one pixel, depending on the threshold levels.

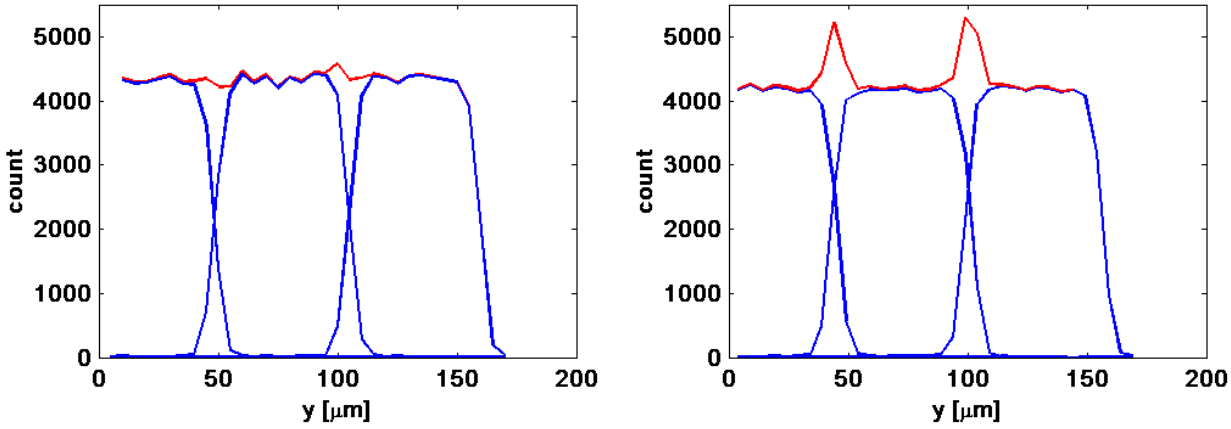
Pencil beam scans have proven to be a useful tool to test for inhomogeneities in detection efficiency [86, 92]. Several sub-pixel mesh scans with a highly collimated beam were performed. They allowed to evaluate the single pixel response, the homogeneity of the detector response and to quantify local inhomogeneities in the detection efficiency. An area covering 3x3 pixels was probed in 5 μm steps in x and y direction using a 10 keV photon beam collimated to the minimal possible area of 10x10 μm^2. Two acquisitions with 4 sec shutter time were taken at each position, one with the global discriminator threshold set to 4.3 and the other with 5 keV threshold. The spatial resolution of this measurements is limited by the minimal width of the collimator opening and the measured pixel profiles are a convolution of the beam profile with the pixel response function.

Fig. 6.2 shows the measured single pixel response profiles in y direction for a threshold set to half the photon energy, 5 keV, and just below to 4.3 keV. When trimming the threshold accurately to half the photon energy the sum of all three pixel counts shows excellent uniformity, Fig. 6.2a). On the other hand even relatively small offsets from that working point lead to double counting of photons in the border region between two pixels, Fig. 6.2b). Due to overlapping pixel dimensions. The observed fraction of double counted photons per pixel obtained for 4.3 keV threshold is 3.5%. Though this is a relatively small effect, it has to be carefully corrected for if objects of very low contrast have to be resolved.

Fig. 6.3a) shows the 2-dimensional result of the mesh scan. On each position of the pencil beam the sum of all counts in the vicinity of the targeted pixel is plotted. The variations of recorded counts in the border regions between pixels depend on the difference of threshold levels of the respective pixels. The sudden increase of ~25 % of the number of counts in the last row is due to a refill of the electron storage ring during the measurement.

Fig. 6.3b) shows the number of counts in the corner region between four pixels. The recorded count drops to ~40 % with respect to the one in the pixel center, which is in excellent accordance with the simulation results presented in sec. 5.2.4.2. The Gaussian width of the dip in count is of 6.5 μm. Since the diameter of the low count region is independent of the pixel size, the detection homogeneity strongly depends on he pixel size. Previous measurements [86] using the Medipix1 chip with 170x170 μm^2 pixel size also showed that the sensitivity profile across the pixel borders is flat and displays neither counting losses nor double counting. The sensitivity drop in the corner region however only accounted for 15 % of the count. This indicates that for hypothetical pixel sizes smaller than the current 55 μm reasonable detection uniformity is possible only with extended readout functionality, such as charge-sharing correction electronics as proposed in sec. 5.3.

In practice this variation in sensor response is corrected for by applying a so-called flat-field correction if the feature size in the recored image is much larger than the measured



(a) (b)

Figure 6.2: a) Single pixel response profile in y-direction measured with a 10x10 μm^2 pencil beam of 10 keV photons with the threshold set to 5 keV. When trimming the threshold accurately to half the photon energy the sum of all three pixel counts shows excellent uniformity. b) Lowering the threshold to 4.3 keV leads to double counting of photons converting in the border region between two pixels due to overlapping pixel response. The observed fraction of double counted photons per pixel obtained is 3.5 %.

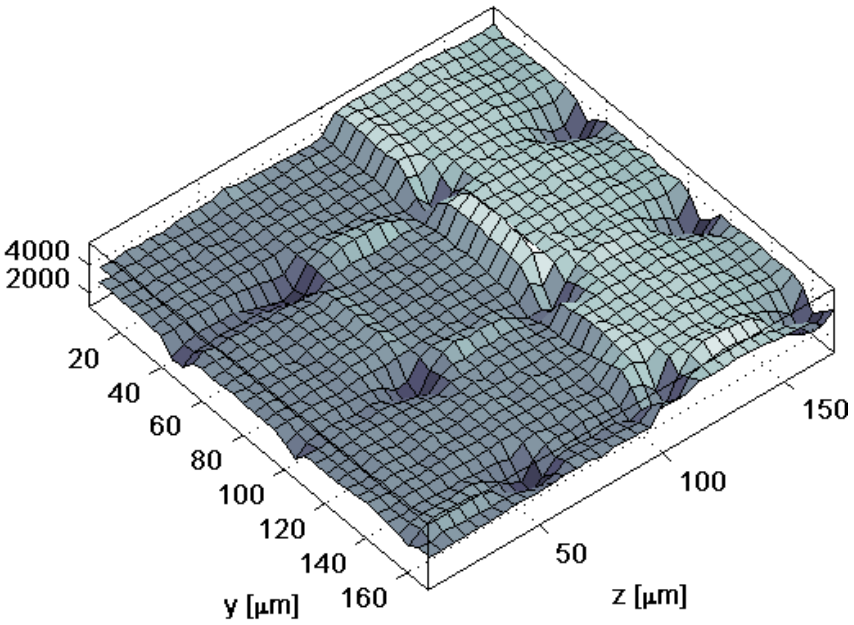
6.5 μm diameter of the region of reduced sensitivity. In crystallographic applications however, care has to be taken when diffraction spot sizes are comparable to the pixel size, since flatfield correction techniques rely on the fact that neighbouring pixels receive comparable signals. A detailed discussion of the flatfield correction technique is given in sec. 6.2.

6.1.3.2 Electronic noise

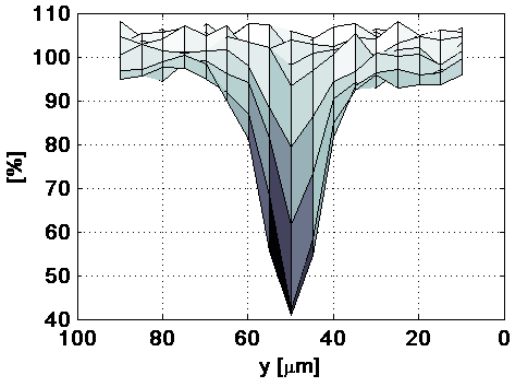
The determining factor for the energy resolution of a semiconductor detector system is the electronic noise. The term electronic noise refers to the overall noise including contributions from the input capacitance and leakage current in the sensor part as well as e.g. baseline and shaper noise in the readout electronics. It is generally expressed as of Equivalent Noise Charge ENC [23, 29, 93] and measured in units of electron charge or eV to provide a direct comparison to the level of the input signal.

To study the electronic noise, threshold scans with a pencil beam of 10x10 μm^2 aligned to the pixel axis were performed with photon energies of 8 and 20 keV. The second monochromator mirror was detuned in order to prevent higher harmonics from passing the monochromator.

As for the energy calibration the photon beam was aligned with the central pixel axis. In this way the energy deposition was limited to a region within the targeted pixel where complete charge collection takes place. Offsetting the beam from the pixel axis leads to charge losses to the neighbouring pixels and subsequently to lower signal heights. By measuring the width of the error function shaped s-curve at several pencil beam positions the influence of charge-sharing on the energy resolution can be assessed.



(a)



(b)

Figure 6.3: a) Pencil beam mesh-scan over the area of 3 neighbouring pixels with 5 µm step size using a 10 keV photon beam collimated to 10x10 µm², the global threshold was set to 5 keV. The sum of the number of counts of all nine pixels per pencil beam position is plotted versus the beam position. The increase of count in the third row of pixels is due to a refill of the electron storage ring. b) Drop in count for 10 keV photons in the corner region due to charge sharing, again with the threshold set to 5 keV.

	experiment		simulation	
offset	threshold [keV]	σ_{rms}[keV]	threshold [keV]	σ_{rms}[keV]
0 μm	7.92	0.51	7.99	0.54
7.5 μm	7.89	0.52	7.91	0.55
15 μm	7.34	0.77	7.23	0.74
20 μm	-	-	5.67	1.20
22.5 μm	5.70	1.35	4.28	1.46

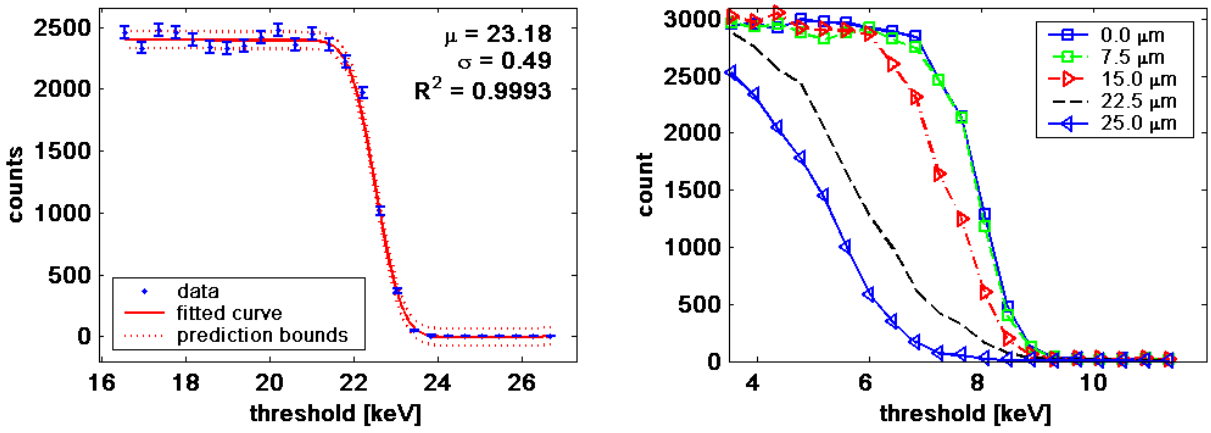
Table 6.1: The apparent threshold and the energy resolution derived from the simulated data and from 10x10 μm^2 pencil beam measurements with 8 keV photons, shown in Fig. 6.4d). The deviation for larger offsets are due to the limited positioning precision during the experiment. Close to the pixel border the energy resolution changes rapidly with the beam position.

Fig. 6.4a) shows the s-curves of a 20 keV photon beam threshold scan with the pencil beam correctly positioned in the pixel center, showing an ENC of 136 e^- rms corresponding to 0.49 keV rms in a Si sensor. Fig. 6.4b) illustrates the response at various offsets from the pixel center, measured with a 8 keV pencil beam. Already small offsets in the order of 10 μm change the shape of the s-curve significantly, rendering the measurement of the energy resolution very susceptible to the beam position. The exact position of the pencil beam within the pixel can only be determined up to a precision of several μm, since only the pixels borders, themselves probed with a pencil experiment cf. section 6.1.3.1, can be used a reference point.

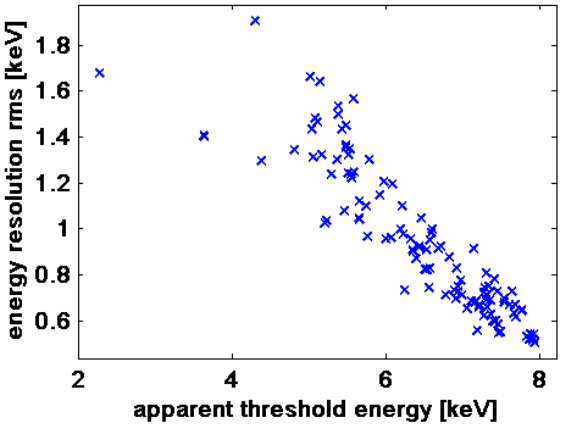
Fig. 6.4c) illustrates the dependence of both the apparent threshold and the energy resolution on the actual position of the collimated beam within a pixel. The values for the apparent threshold and the width of the s-curve where calculated by fitting the measured data with error-functions. The minimum value for the energy resolution of $\sim$0.49 keV rms, is obtained only at beam positions very close to the center of the pixel. This value matches very well the design value for the ENC of 120 e^- rms, c.f. sec. 4.2.

Table 6.1 gives a comparison of values for the threshold and the energy resolution derived from the simulated data and from the experiment. The deviation at larger offsets are due to the limited positioning precision during the experiment. Close to the pixel border the energy resolution changes rapidly with the beam position.

Under wide area irradiation, as it is the case in imaging applications, the energy resolution is the result of a weighted average of the s-curves presented in Fig. 6.4b). The ENC of the readout electronics therefore fixes only the lower limit of the obtainable overall energy resolution. The system energy resolution is determined by the ENC and by the systematic fluctuations in the charge collection in the sensor. Another effect of charge sharing is to shift apparent threshold position to lower values, since the photons impinging close to the pixel borders lead to a shallower shape of the measured s-curves.



(a) (b)



(c)

Figure 6.4: a) The s-curve of a 20 keV photon beam threshold scan with the pencil beam positioned at the pixel center, indicating an ENC of 0.49 keV rms respectively. b) The detector response at increasing offset from the pixel center, measured with a 8 keV pencil beam collimated to 10x10 μm^2. At 15 μm offset from the pixel center the shape of the s-curve is already significantly deformed, the resulting ENC is 0.77 keV as compared to 0.49 keV closer to the pixel center. c) The apparent energy resolution versus the apparent threshold for different positions of the collimated beam within a pixel. The minimum value for the width of the s-curve of ∼0.49 keV rms, corresponding to 140 e^- rms, is observed only at beam positions very close to the center of the pixel.

6.1.4 Pixel array response

As already mentioned, an accurate setting of the energy threshold and the smallest possible spread in threshold is of particular importance when it is used to reject parts of an incident X-ray spectrum under wide area irradiation. To assess the performance of the detector system for imaging applications it is therefore necessary to understand the response to wide area irradiation. The pencil beam experiments described in the previous section suggest deviations from ideal detector response related to charge-sharing effects. To determine the apparent threshold and the energy resolution of individual pixels under wide area irradiation, threshold scans with a 1 mm^2 beam covering 330 pixels were carried out. These scans were performed for different X-ray energies in the range of 8 to 40 keV.

To extract values for threshold position and energy resolution from a threshold scan, each of the 330 s-curves was processed in two different ways. First the derivative of the s-curve, representing the apparent spectrum seen by the pixel, was fitted with a Gaussian distribution. Alternatively, each s-curve was fitted with a theoretical s-curve, stemming from the simulations described in sec. 5.2. The amplitude, the position and the noise were used as free fit-parameters in both cases. The main difference between the two approaches is, that the fit with a Gaussian distribution does not take into account the effects of charge sharing and therefore gives the apparent width of the recorded photopeak and is a measure for the energy resolution of the system. The s-curve fit on the other hand is more suited to assess the noise performance of the read-out electronics, since the effects of charge-sharing in the sensor are already included in the fit function. From this analysis supplementary measures for the threshold linearity and the uniformity of the energy calibration can be derived. The results were also used to complement energy calibration measurements performed with pencil beam geometry.

6.1.4.1 Threshold position and dispersion

Fig. 6.5 shows the results of the area irradiation threshold scans performed with monochromatic photons of 20 keV. The results are representative also for the other photon energies used. In Fig. 6.5a) the raw data s-curves are plotted, indicating both a spread in actual threshold as well as a dispersion in signal height. The divergence in the tail of the s-curves is due to residual beam inhomogeneities, giving rise to steeper slope for higher absolute number of counts.

The individual s-curves were analyzed as described above. The Gaussian fit to the derivative of the s-curves results in strongly varying values for the threshold from pixel to pixel. This is a combined effect of the Poissonian noise on the individual points of the s-curve and the fact that only $\sim$5 points lie within the width of the photopeak. The derivative amplifies the Poissonian variations and therefore renders the Gaussian fit an unreliable measure, especially for 8 and 10 keV photons. Using the modelled s-curves as fit function avoids both problems since the measured data has not to be differentiated and also points outside the photopeak contribute in the fitting procedure. Additionally, in order to countercheck the results obtained with the model fit-functions, the threshold dispersion was deduced by a pattern matching algorithm. This analysis was performed iteratively: first all s-curves were averaged, i.e. for each threshold value the average count was calculated resulting in a reference curve. Then each individual s-curve was offset

photon energy [keV]	8	10	15	20	40
μ_{thresh} s-curve [DAC]	1411.2	1405.3	1393.9	1382.3	1332.7
$\sigma_{thresh}^{s-curve}$ [keV] rms	0.45	0.44	0.39	0.44	0.47
$\sigma_{thresh}^{matching}$ [keV] rms	0.40	0.44	0.42	0.43	0.54

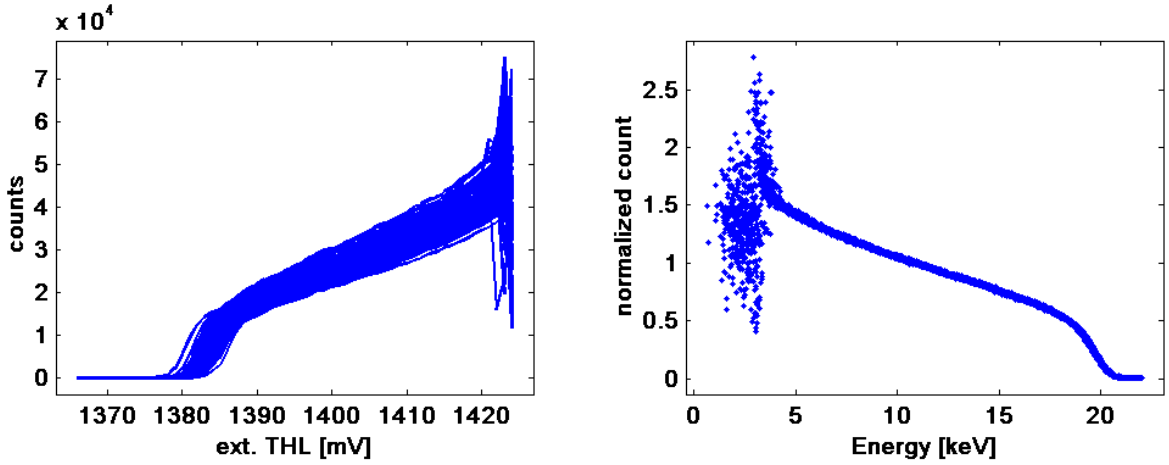
Table 6.2: The mean threshold position μ_{thresh} and threshold dispersion $\sigma_{thresh}^{s-curve}$ for the measured photon energies derived by fitting the measured data with model s-curves. The threshold dispersion $\sigma_{thresh}^{matching}$ obtained using a pattern matching algorithm are also given as comparison.

along the x-axes and scaled on the y-axes to match this average curve by minimizing r-square to the reference. The final offset and scaling factors were obtained after three iterations, each using the average s-curve of previous iteration as reference. An excellent compression of the dispersion in both threshold spread as well as very good uniformity in s-curve height and slope could be obtained, Fig. 6.5b). This indicates that the spread in the slope of the unprocessed s-curves is due to the interplay of charge-sharing and threshold dispersion at the one side and beam inhomogeneities in the other side. Inhomogeneities in the linearity of the threshold settings would in fact result in deviating slope steepness of the realigned s-curves. The linear increase in count for threshold values around the midpoint of the photon energy is the result of an almost constant background of charge shared events. This results in an constant increase of count with decreasing threshold. The slope of the s-curve around the midpoint therefore can be used to estimate the spread of the proportionality factor in the energy calibration. The uniformity of the threshold linearity was estimated to be 1.6% by fitting the linear slope of the realigned s-curves for each pixel.

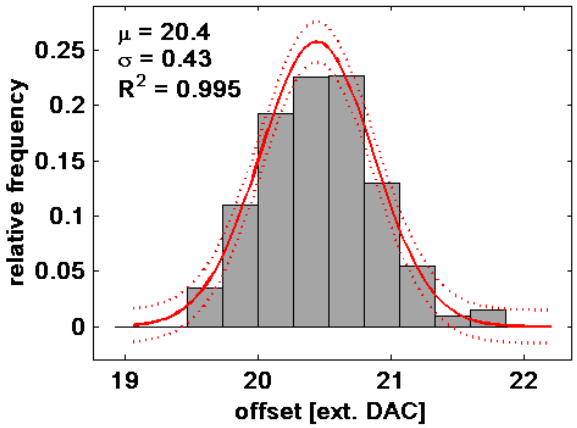
Fig. 6.5c) graphs the derived threshold distribution for a 20 keV photon beam with an threshold dispersion of 0.44 keV rms, corresponding to 122 e^- rms. The obtained values for other photon energies measured give similar results and are given in table 6.2. A related figure is the position of noise floor of the individual pixel. From the single pixel energy calibration a value for 2.2 keV for noise floor has been found, which fits very well the expected value equal to 4-5 times the ENC. For area irradiation the observed level of the noise floor is slightly higher at ∼3 keV. This is due to noise transmitted from active electronics in neighbouring pixels, which have been inactive during the measurement with pencil beam irradiation.

6.1.4.2 Energy resolution and electronic noise

Energy resolution When analyzing the derivative of individual pixel response it is difficult to extract values for threshold position and the width of the photopeak by fitting a Gaussian distribution to the photopeak. To calculate the mean spectral response and to quantify the mean energy resolution of the detector system the derivative of the sum of the re-aligned s-curves, Fig. 6.5b), has been used instead. Gaussian distributions were fitted to the photopeaks of the spectra, Fig. 6.6. The obtained results for the photopeak



(a) (b)



(c)

Figure 6.5: Results of a threshold scans under 1mm^2 area irradiation with a 20 keV photon beam. a) The raw threshold scan data from the measurements. b) The threshold dispersion derived from realignment procedure described in the text. c) The distribution of the threshold position of the individual pixels. Similar results were obtained for 8, 10, 15 and 40 keV.

photon energy [keV]	8	10	15	20	40
resolution [%] FWHM	18.5	18.1	10.3	7.9	4.7
peak / background [%]	164.4	145.4	82.1	53.1	24.1

Table 6.3: A breakdown of the measured energy resolution properties under area irradiation.

energies are in good agreement with the expected values from the energy calibration, eq. 6.1, whereas the energy resolution of 180 to 220 electrons rms exceeds the one obtained by pencil beam measurements by ∼50 %, indicating that charge-sharing is a significant contribution to the readout ENC. Therefore the commonly used method to estimate the ENC from area irradiation using radioactive sources is only a good approximation for pixel geometries with a much lower aspect ratio than the Medipix2.

The spectroscopic performance often is expressed normalized to the photon energy: the energy resolution as the ratio of photopeak FWHM to photopeak energy, and the peak-to-background ratio, given by the ratio of the total count under the photopeak versus the sum of background counts. Table 6.3 shows the obtained values for the energies investigated.

Electronic noise variations In addition to the mean apparent electronic noise also the dispersion of the noise over the active matrix can be estimated. It has to be kept in mind still, that the numbers obtained from an area irradiation measurement represent an upper limit. It includes all contributions from the variations of the proper electronics noise as well as the variations induced by the charge sharing. Even in the case of a completely uniform beam intensity, Poissonian variations in the relative numbers of photons converted in the border region of a pixel with respect to the number converted in the center region would lead to varying modulation of the apparent electronic noise.

To estimate the electronic noise variations model derived s-curve fit functions have been fitted to the individual pixel s-curves. Table 6.4 lists the results for mean electronic noise and noise dispersion. Fig. 6.7 shows the noise distribution for 20 keV photons representatively for the other photon energies measured. The mean values of the electronic noise fit very well the noise figure extracted from pencil measurements, since the effects of charge sharing on the pulse height distribution is already taken into account in the fit functions and the width of the noise distribution is estimated be be 0.06 keV or 17 electrons rms.

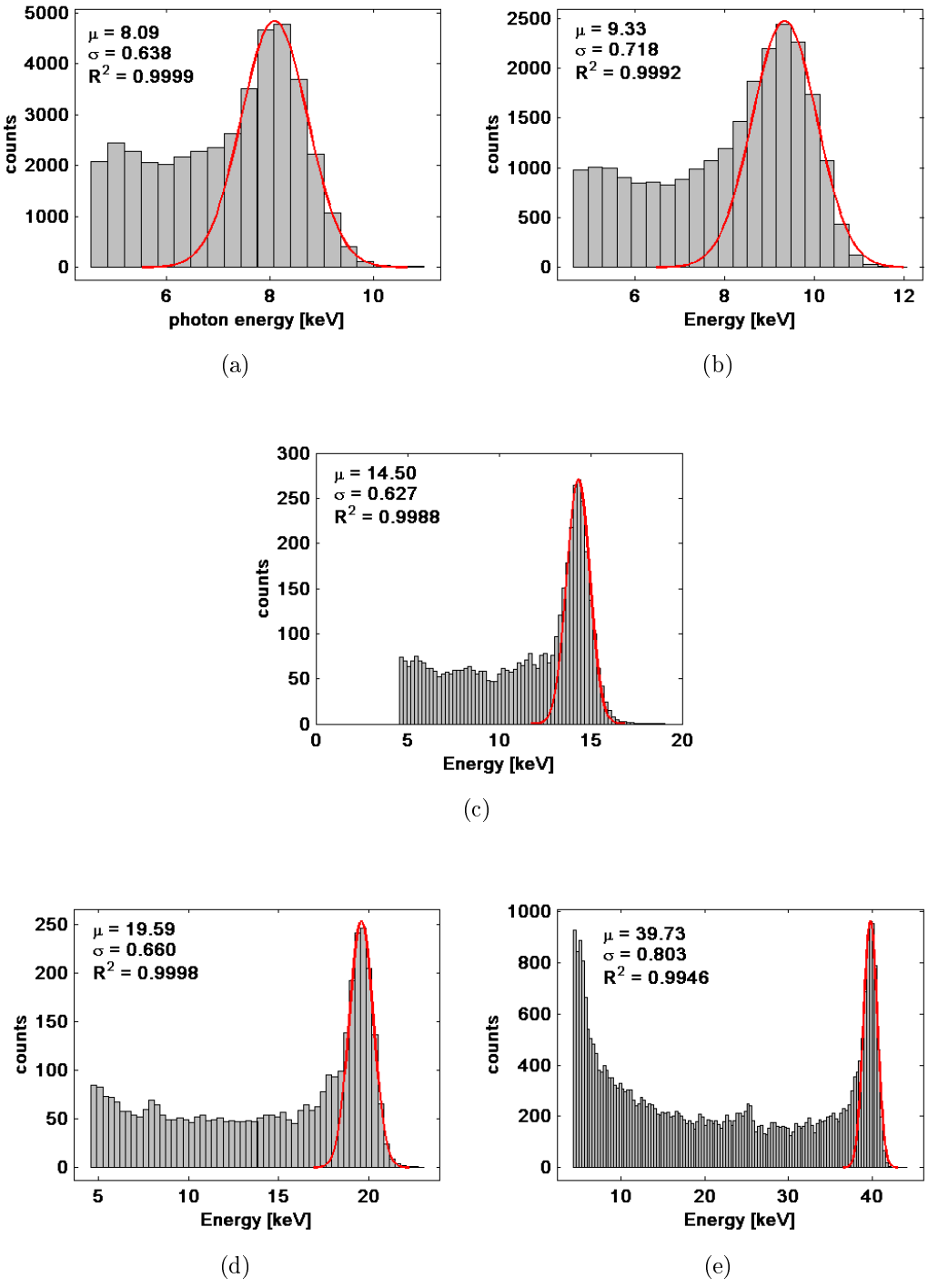


Figure 6.6: Results for the spectra derived from threshold scans under area irradiation of 1 mm^2 for a) 8 keV, b) 10 keV, c) 15 keV , d) 20 keV and e) 40 keV. Also indicated in the plots is the mean energy of the photopeak in keV according to the energy calibration given in eq. 6.1, the with of the photopeak in keV rms and the coefficient of determination for the Gaussian fit.

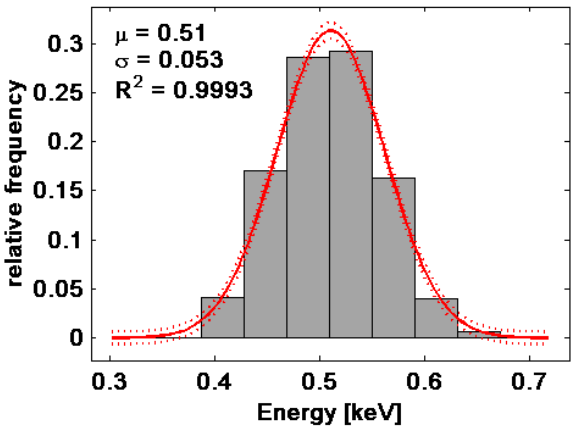


Figure 6.7: The distribution of the electronic noise calculated from 20 keV photons area irradiation data. Measurements with other photon energies give similar results.

E [keV]	8	10	15	20	40
μ_{noise} [keV] rms	0.51	0.55	0.46	0.48	0.41
σ_{noise} [keV] rms	0.07	0.07	0.05	0.07	0.04

Table 6.4: Mean electronic noise and electronic noise dispersion for different photon energies.

6.2 Flat-field-correction

Low image noise and high spatial resolution are common requirements for most imaging applications since the image signal-to-noise ratio imposes fundamental limitations to object perceptibility. The two major contributions to image noise are the statistical fluctuation in the number of photons per unit area and the noise added by the imaging system. Whilst the photonic noise is entirely random, the contributions from the detector can be both stochastic and non-stochastic. The non-stochastic, time constant parts are referred to as fixed-pattern noise and can be further divided in to contributions from the sensor and from the readout electronics.

The most important source of non-uniform response of the sensor part is material inhomogeneities, especially for compound semiconductor materials. These inhomogeneities introduce non-uniform field distributions, local variations in leakage current and locally reduced charge collection efficiency. The noise introduced by leakage currents, one of the main noise sources in integrating detectors, is removed in both generations of the Medipix2 via a leakage current compensation, cf. sec 4.

The main source of readout-related sensitivity variations are CMOS-process related transistor mismatches introduced during chip production. In the case of photon counting pixel detectors this translates into inter-pixel variation in the effective threshold energy. The magnitude of this variation in the Medipix readout chips is $\sim$400 e^- rms and is reduced to $\sim$100 e^- rms by an on-chip correction circuitry, which fine-tunes the threshold level for each pixel individually, c.f. chapter 4.

Residual sensitivity fluctuations in the electronics or the sensor over the active area can be corrected for by applying a so-called flat-field correction. This calibration is obtained by taking a large number of flood-field images using a uniform open-field illumination and calculating the ratio of the mean count over the whole sensitive area to the accumulated count of the individual pixel. The coefficients for the individual pixels constitute the flat-field correction map. Theoretically fixed pattern noise is removed by applying such a correction map. It has to be kept in mind that the effectiveness of this procedure depends strongly on the statistical base of the correction map as well as the intensity distribution in the raw image. By dividing the raw data by the highly averaged flat-field map, fixed-pattern noise in areas of higher count is reduced, while the stochastic noise in areas of lower sensitivity is amplified. Non-stochastic, time-dependent noise will not be reliably removed either.

To study the origins of residual sensitivity variations and to investigate the effectiveness of flat-field correction techniques, extensive measurements have been carried out using both generations of the Medipix and using different X-ray spectra. In sec. 6.2.1 measurements are presented that identify threshold dispersion and charge sharing as the main source of fixed pattern noise. In the same section the implications on the image quality achievable in application using a spectral X-ray source are described. In sec. 6.2.1 the sensor homogeneity is studied by probing the field distribution in the sensor by varying the detector bias voltage.

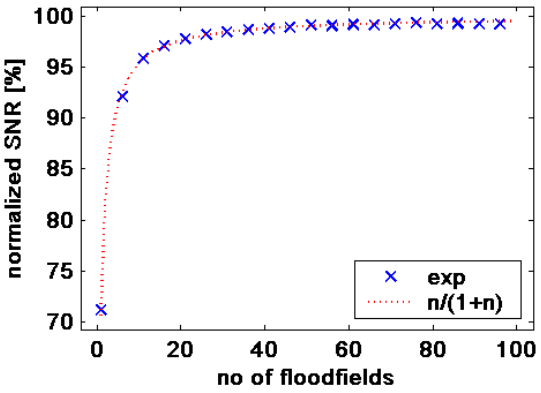


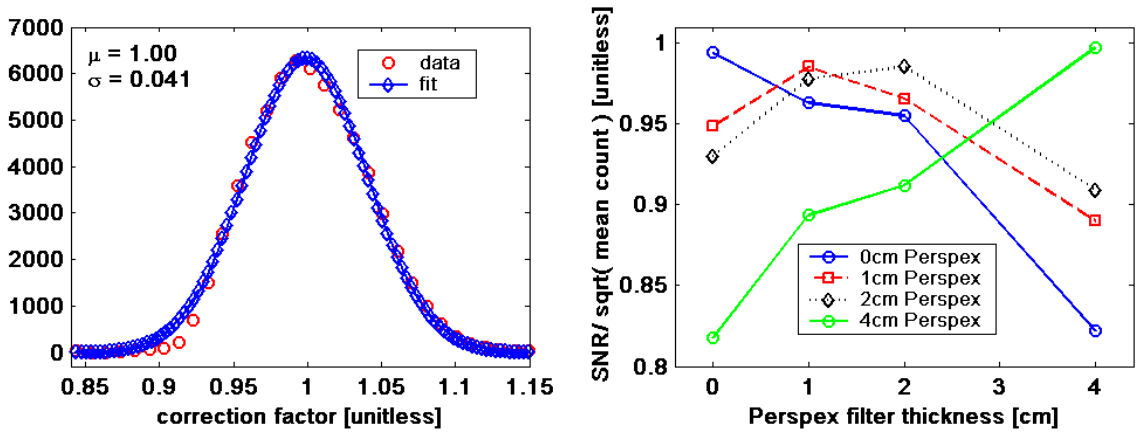
Figure 6.8: SNR of a uniform exposure corrected with a flat-field correction map calculated from increasing number of flood-fields, as indicated on the abscissa. The values are normalized to Poisson noise, the square root of the mean number of counts. The SNR approaches the Poisson limit when increasing the statistical base of the flat-field correction.

6.2.1 Threshold dispersion

All measurements presented in this section were carried out using a Seifert FK61-04x12 W-target X-ray source with 35 kV, 2.5 mm Al equivalent filtering. If the fixed pattern noise is, as assumed, an effect of multiple counting only, then it can be removed using a flat-field correction map as described above. Simulations in sec. 5.2 indicate that the threshold variations in combination with charge sharing effects lead to such a multiplicative modulation of count. To test the assumption that the fixed pattern noise stems from these sources only, the increase in SNR with the number of flood-fields taken into account for the calculation of the flat-field correction map has been investigated. In the case that no additive or additional time dependent noise contributions are present the variance of the corrected image can be expressed as the ratio of two independent random variables and is given by

$$\sigma^2 = \sigma_0^2(1 + \frac{1}{n}), \tag{6.2}$$

where σ_0^2 denotes the variance of the raw image and n the number of frames compiled into the correction map. In eq. 6.2 it is assumed that all flood-fields and the data yet to be corrected were recorded under the same conditions and have the same mean number of counts. 101 flood-field acquisition with the threshold set to 10 keV were taken and the correction maps were calculated from an increasing number of flood-fields. Fig 6.8 shows the obtained SNR normalized to square root of the mean number of counts in the corrected image. The measured curve follows closely the curve predicted by eq. 6.2, indicating that other noise sources are negligible. It also shows that the Poisson limit for the SNR can be reached given a sufficiently high number of photons contributing to the correction map. Fig. 6.9a) shows the histogram of correction factors for such a map for a dose of 296 mGy air kerma. The distribution follows as expected a Gaussian shape, with an rms of $\sim$4%.



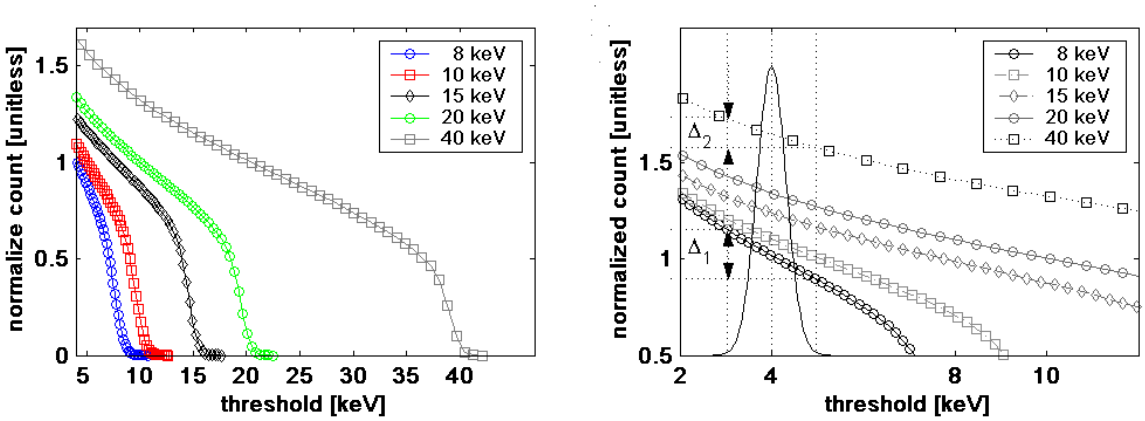
(a) (b)

Figure 6.9: a) Histogram of factors in the flat-field correction map obtained with a W-target X-ray source with 35 kV and 2.5 mm Al equivalent filtering, together with a fitted Gaussian distribution of 4.1% rms. b) SNR normalized to Poisson limit when combining different acquisition conditions for image and correction map. The individual curves represent the normalized SNR of a single acquisition with 0,1,2 and 4 cm prefiltering, which then is corrected with correction maps obtained with Perspex prefiltering denoted on the abscissa. The Poisson limit, which is given by the square root of the mean number of counts, only can be approached when using identical photon spectra for acquisition and flat-field correction.

To remove fixed-pattern noise efficiently by means of flat-field correction it is required that the acquisition conditions of the raw image data to be identical to those used when measuring the correction map. In absorption imaging contrast is achieved by attenuating photons out of the incident beam. Since low energy photons have a much higher probability to be absorbed in matter, the transmitted beam is subject to beam hardening when spectral X-ray sources are used. The flat-field correction map on the other hand represents an average calibration over the spectrum of the incoming photons. Hence the required correction map would change if the incoming spectrum changes.

Fig. 6.9b illustrates the effects of beam hardening on the achievable SNR. Again a W-tube with 35 kV, 2.5 mm Al equivalent filtering was used with additional layers of 1,2 and 4 cm of Perspex. 100 flood-fields were taken for each thickness of Perspex and used to calculate the corresponding correction maps for each configuration. Then the resulting four correction maps were applied to an additional single flood-field acquisition of the same thickness of Perspex, as well as "wrongly" applied to a flood-field obtained with a different thickness. With increasing deviation of the object thickness from the one used to measure the correction map, the SNR degrades from the maximum value, which as mentioned before is close to the Poisson limit. The loss of SNR goes up to 20%.

Fig. 6.10 illustrates the origin of this decrease in SNR. Fig. 6.10a) shows simulation results for the number of recorded counts a count as a function of the energy threshold. The curves are normalized to the number of counts recorded at half the photon energy.



(a) (b)

Figure 6.10: a) The range of flat-field correction factors depends on the actual spread of pixel threshold and the incoming photon spectrum. b) The curves for 8 to 40 keV photons are a zoom into a). Superimposed is a Gaussian distribution of pixel thresholds with 100 electrons rms dispersion. Note the difference in the resulting spread of correction factors Δ_2 for 40 keV and Δ_1 for 8 keV.

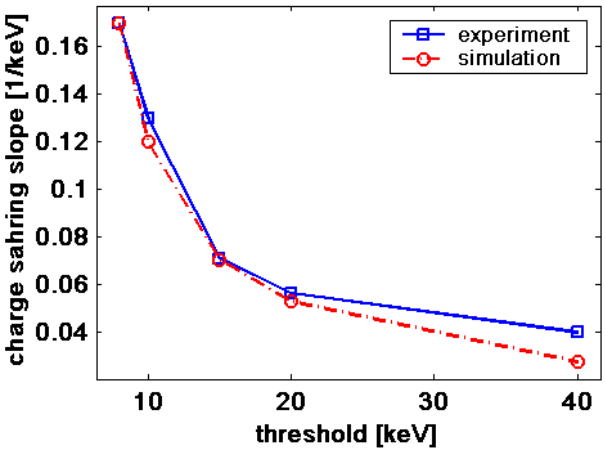


Figure 6.11: Measured and simulated charge sharing slope for photon energies form 8 to 40 keV with the threshold set to half the photon energy.

At this point the background of charge shared events in the spectrum seen by the pixel is almost constant, c.f. 5.22, and the number of counts represents best the true number of correctly counted photons. Fig. 6.10b) illustrates the effects of the threshold dispersion on the flat-field correction map. The plot is a zoom into Fig. 6.10a) at low energies. The Gaussian distribution represents a typical threshold dispersion of the Medipix2 with 100 electrons rms and centered around 4 keV, again a typical value for the lowest achievable threshold with the full matrix active. The fraction of double counted photons is lower for higher photon energies, resulting in a close to linear increase of counts recorded with decreasing threshold values. Therefore higher energy photons produce a narrower distribution of the factors in the flat-field correction map. The resulting spread in correction factors Δ_1 for 8 keV and Δ_2 for 40 keV photons respectively are indicated in Fig. 6.10b). For both, measured and simulated data, the slope in the linear part of the count versus threshold curves has been fitted with a line using an energy range of ± 1 keV around the threshold of half the photon energy. Fig. 6.11 shows results for the measured and simulated slopes.

The total noise due to charge-sharing and threshold dispersion in the region of constant increase of count now can be written as

$$\sigma = \sqrt{N \cdot (1 + \alpha)}$$

where

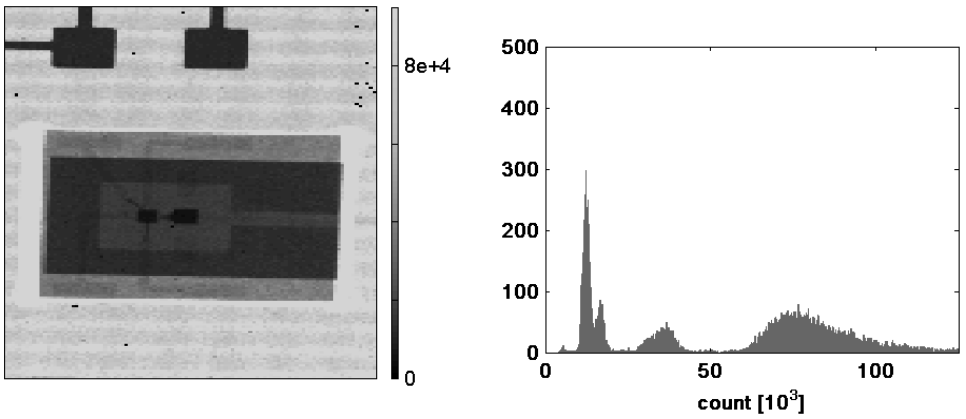
$$\alpha = k_{slope} \cdot \sigma_{thresh}$$

This corresponds to a maximum obtainable SNR of the raw image

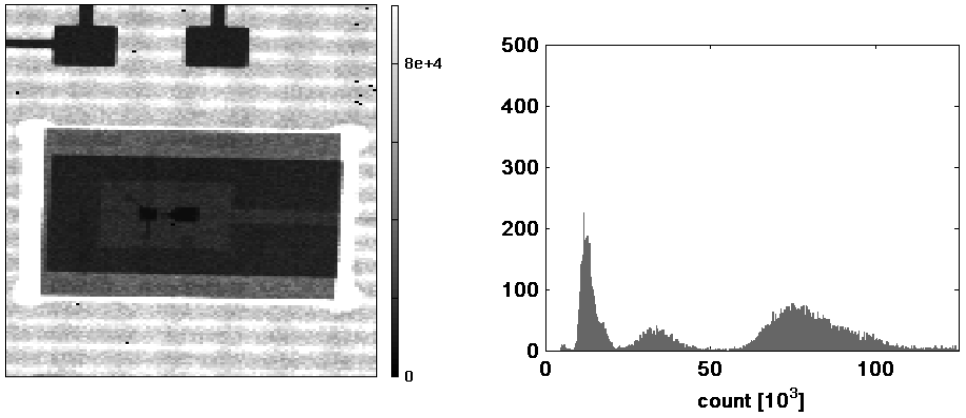
$$SNR = \frac{N}{\sigma} = \alpha, \tag{6.3}$$

or in other words, for uncorrected data the contribution of fixed pattern noise exceeds the one of photonic noise already at less than 1000 counts in average for 20 keV photons.

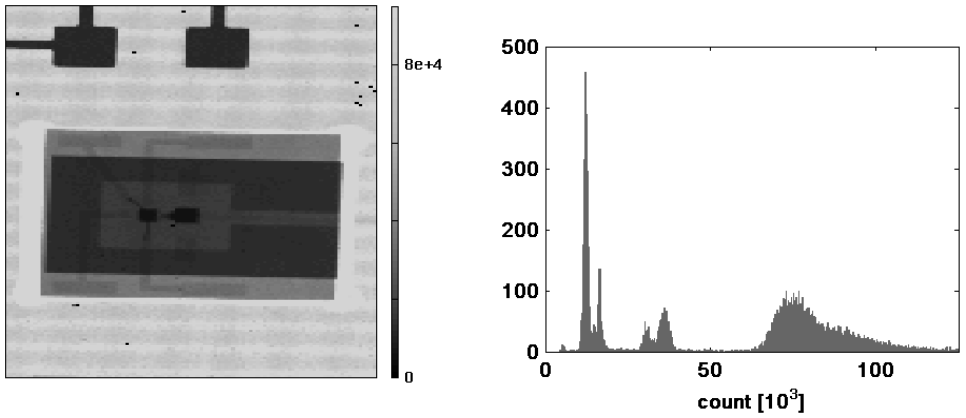
The most pronounced change in charge-sharing slope, Fig. 6.11, occurs for photons below $\sim$15 keV. This means that imaging with a spectral content lower than $\sim$15 kV needs special considerations when significant beam hardening occurs. This is illustrated in Fig. 6.12. The object shown is an encapsulated laser-diode mounted on a printed circuit board. In order to maximize the image contrast a W-tube was used with 0.125 mm Al filter and 20 kV tube voltage. In Fig. 6.12a) the uncorrected image and its histogram are shown. In Fig. 6.12b) the image is a flat-field corrected. The correction map was calculated using the standard procedure with no attenuating object placed in the beam. The effects of beam hardening in the correction efficiency are clearly visible by comparison with Fig. 6.12a). The application of a conventional flat-field correction leads to a strong increase of image noise, masking even details visible in the uncorrected image and the separation of components with high absorption in the histogram is lost. Fig. 6.12c) shows the same data, but this time corrected with a flat-field correction obtained with a prefiltering of 5 mm Perspex in order to include the effects of beam hardening also in the correction map. The resulting image shows a clear improvement with respect to both the uncorrected data and the one with the standard correction map applied. The



a)

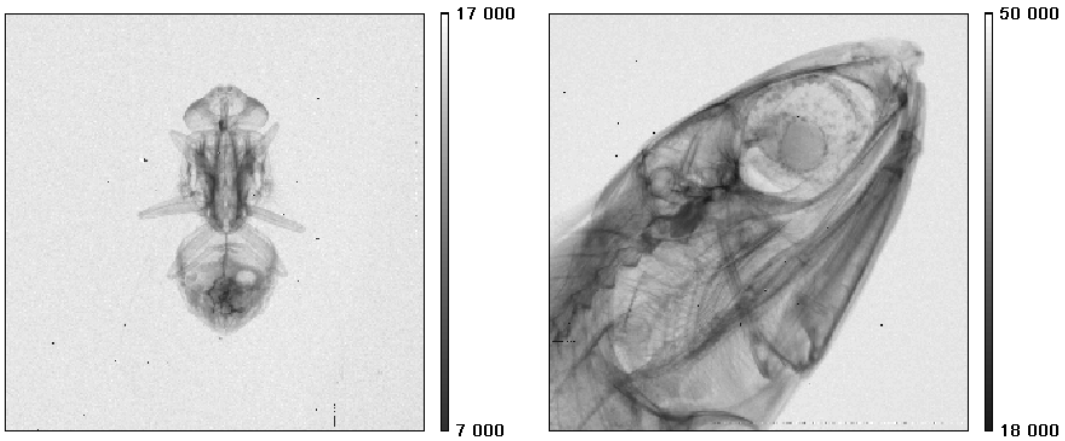


b)



c)

Figure 6.12: a) Images of an encapsulated laser diode and the corresponding histogram taken with a W-tube, 20 kV, 0.125 mm Al filter. a) No flat-field correction is applied. A number of counts higher than $5 \cdot 10^4$ represent the area of the printed circuit board. b) A simple flat-field correction, calculated from unfiltered photon spectrum, is applied. The image noise is amplified with respect to the uncorrected image and the separation of components with high absorption is lost in the histogram. c) The correction map was derived from data obtained with additional 5 mm Perspex filtering. The improvement of image quality is clearly visible and the separation of the components in the histogram is improved.



(a) (b)

Figure 6.13: a) Example of a low absorption object, the spectrum of the incident photons is changed very little. Acquisition settings: W-tube, 14 kV, 0.125 mm Al and 5 mm Perspex prefiltering. b) Anchovy, acquisition settings: W-tube, 35 kV, 2.5 mm Al equivalent prefiltering. In this case almost the entire spectrum is above 15 keV. The charge-sharing slope is almost constant in this energy range (Fig. 6.10a) and therefore the flat-field correction is insensitive to beam hardening.

improvement of the contrast between the different components of the laser diode is also evident in the histograms.

The standard correction map remains sufficient when the incident photon spectrum is hardly changed or the spectrum is confined to an energy range where the charge-sharing slopes depend less strongly on the photon energy. Fig. 6.13a) illustrates the situation for a very low attenuation object, a fly. In order to obtain contrast the W-tube voltage was set to 14 kV and the prefiltering was 0.125 μm Al and 5 mm Perspex. The image shown was obtained using conventional flat-field correction and the anatomical features of the fly are clearly visible. In Fig. 6.13b) the W-tube settings were 35 kV and 2.5 mm Al, resulting in an X-ray spectrum almost entirely above 15 keV. The correction factors are almost identical for the photon energies present, since the charge-sharing slopes in this range change very little with energy, Fig. 6.10. The image obtained with standard flat-field correction again gives very high contrast and resolution.

It can be concluded that the fixed pattern noise visible in the current generations of the Medipix detectors is introduced predominantly by an interplay of charge sharing and threshold dispersion. Whilst it can be corrected for easily by means of flat-field corrections in the case of monochromatic photons, the correction becomes more complicated when used with spectral X-ray sources. To maximize the SNR, the correction map should be measured with a photon spectrum as close as possible to the one impinging on the detector when the object to be examined is placed in the beam. As an alternative the flatfield correction map can generated from detector response simulations if the exact threshold position of each individual pixel is known from electrical measurements.

In order to reduce the magnitude of the fixed pattern noise already during image formation either the lateral diffusion during charge collection in the sensor has to be reduced or the threshold dispersion in the readout has to be further compressed. Unfortunately neither of the two sources can be suppressed completely. Also here a possible remedy is given by summing the signals of neighbouring pixels, c.f. 5.3. In this way the charge split is entirely corrected for and the increase of count with lower thresholds is removed. As a consequence the threshold spread would not add any noise if it is set below the lowest energy in the photon spectrum.

6.2.2 Sensor homogeneity

In the previous section charge sharing has been identified as one of the main causes of fixed pattern noise. The lateral extent of the collected charge cloud, and therefore also the fraction of multiply counted photons, depends also on the collecting field in the sensor. Bulk doping inhomogeneities have been found to degrade detector performance in silicon drift detectors (SDD), even though highly uniform neutron transmutation doped (NTD) Si is used as a sensor material. The doping variations in NTD Si in the order of 2 % rms [94] are substantially lower than the one found in high resistivity float-zone (FZ) Si used here. The measured particle impact position in large SDD showed systematic offsets from the real interaction point [94–96] in both directions, parallel and perpendicular to the drift direction.

To investigate the effects of detector bias voltage on the charge collection properties of the Si sensor, a large number of flood field acquisitions (150-1000) were taken using the Medipix1/Si assembly operated at different detector bias voltages. The X-ray sources used were a Mo and W target tubes with various filter and tube voltage combinations. The results proved to be independent of the spectrum used. All results presented here were obtained using a Seifert FK61-04x12 X-ray Mo target tube operated at 20 kV with a 30 μm Mo filter and are representative for those obtained with the other spectra.

First the depletion voltage of the sensor was estimated by measuring the average number of counts per pixel time as a function of the applied detector bias voltage. The saturation in the number of counts was reached at detector bias voltages higher than 24 V, which is consistent with the 20 V depletion voltage announced by the manufacturer.

Then the bias voltage of the detector was increased in powers of 2 from 4 V to 128 V, with additional intermediate steps at 12, 24, 48, 80, 100 V, in order to step the depth of the depletion layer through the sensor thickness. For each detector voltage the X-ray tube current was adjusted to give a count rate of $\sim$10 kHz/pixel. The number of flood field images taken was adjusted to obtain an accumulated total count of about $2.5\,10^6$ per pixel for each detector bias.

In Fig. 6.14 shows the image of 16, 24 and 64 V sensor bias voltage, normalized to the mean count and corrected with the flatfield correction map for 128 V bias. In the under-depleted regime V_{bias} <24 V a wave pattern is evident. Increasing the bias voltage above depletion makes the pattern less pronounced, but still is faintly visible even at 64 V bias voltage. The structure in the image becomes clearer if single row profiles are plotted. In Fig. 6.15 these profiles, calculated along the horizontal center row of the detector, are presented. Figures 6.15a and 6.15b) show the profile of the raw data, where the low spatial

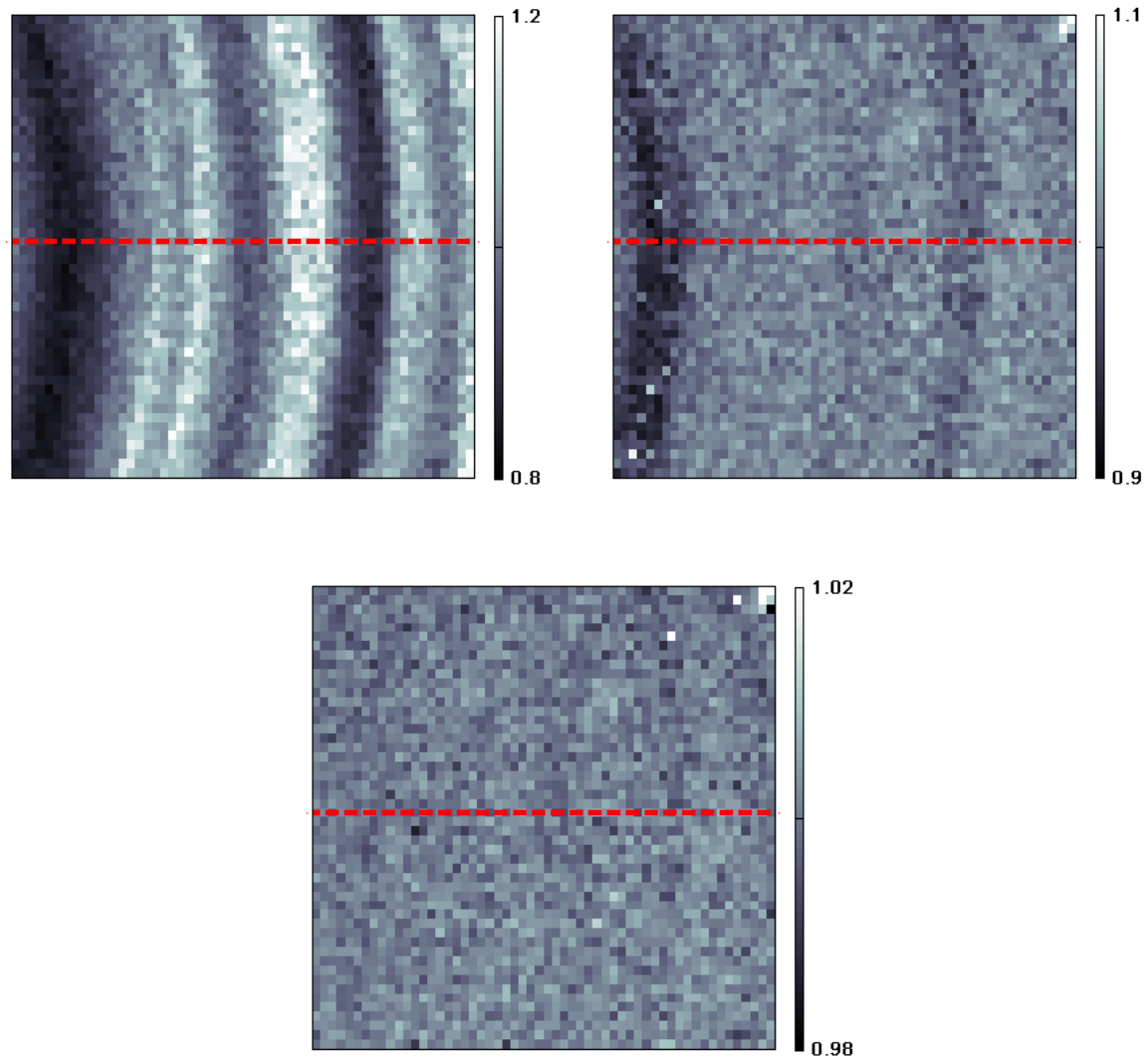


Figure 6.14: Floodfield data taken with a Medipix1/Si detector with the sensor biased at a) 16 V, b) 24 V and c) 64V, corrected with a flatfield correction map obtained from data measured with 128V sensor bias and normalized to the mean count. The nominal depletion voltage of the sensor is 20 V.

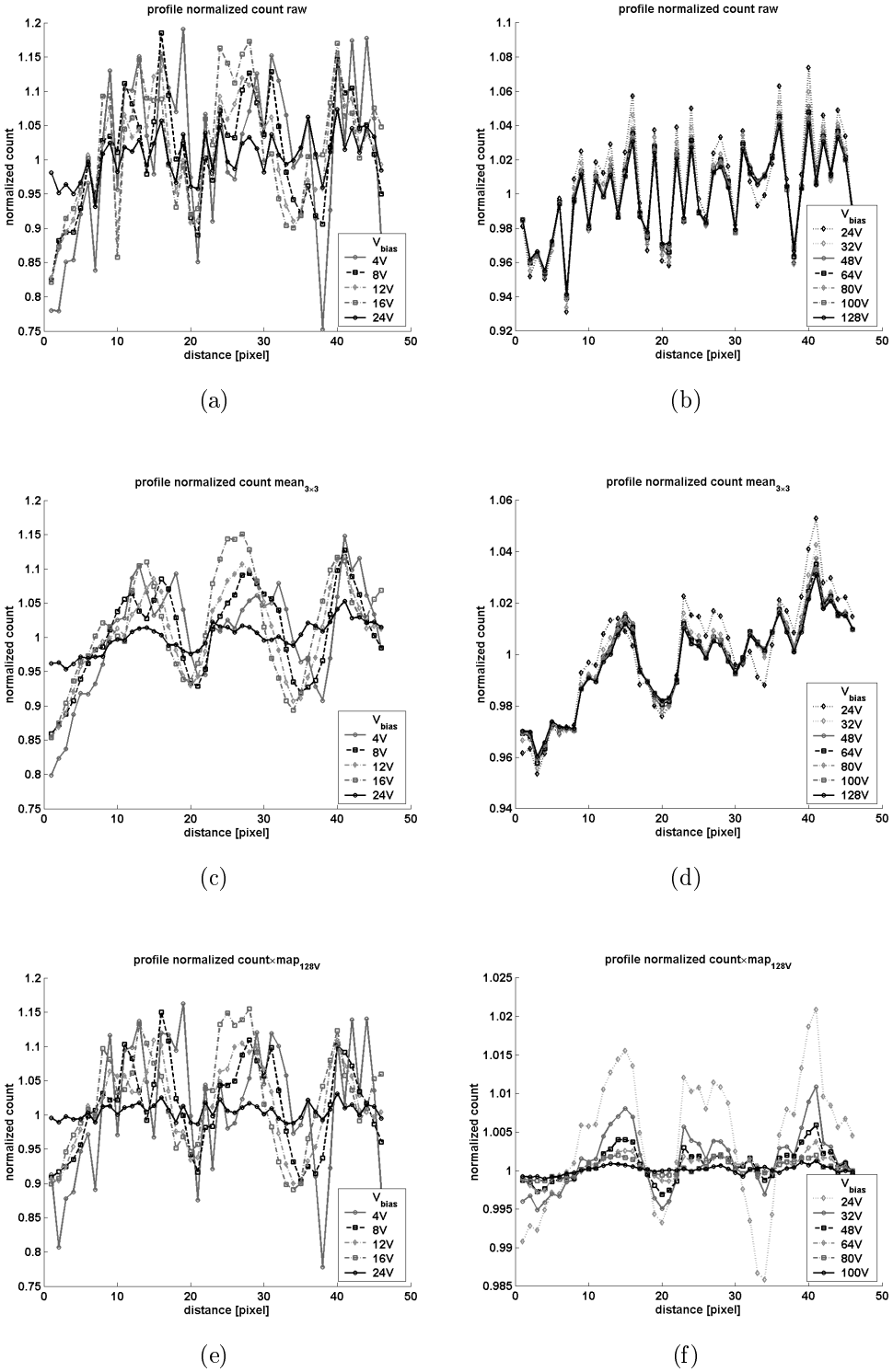


Figure 6.15: (a,b) Profile taken from centre row of raw uncorrected flood-field data. (c,d) Profile taken from centre row of flood-field data smoothed with a 3x3 mean filter. (e,f) Profile taken from centre row of flood-field data corrected with flat-field correction calculated at 128V detector bias.

frequency structure of the wave pattern is strongly masked by the local variations of the count between neighbouring pixels. This high frequency variation in count is caused by threshold mismatch between adjacent pixels, see sec. 6.2.1. Figure 6.15c) and 6.15d)show the profiles taken from the same data after applying a 3x3 pixel mean filter to accentuate the low frequency pattern. The magnitude of the fluctuations increases rapidly up to +- 10 % with the detector bias just under full depletion. The position of the pattern moves by up to a several pixels (several hundred μm) between 4 V and 16 V detector bias. For voltages >24 V the position of the waves remains fixed and also the magnitude of the low frequency variation stays well below 5 %. The systematic left-right increase in counts is due to beam inhomogeneity. In figures 6.15e) and 6.15f) the same profiles with the 128 V flat-field correction applied are graphed. The high frequency variation is almost completely removed leaving only the smoothed wave pattern. Again the shifting of the pattern is visible.

The dependence on the magnitude and position of the low frequency wave pattern points to detector bulk doping inhomogeneities. These waves have a different orientation on different detector assemblies. Put together, they appear to constitute rings originating at the centre of the detector wafer, Fig. 6.16. The low frequency fluctuations seen are compliant with doping striations introduced during float zone wafer processing [97], both in magnitude and spatial frequency. For bias voltages below the depletion voltage, a variation in the bulk doping density n_{bulk} leads to changes in the depth of the depleted layer in the sensor scaling with $1/\sqrt{n_{bulk}}$. For a mean effective bulk doping density of $3 \cdot 10^{11}\, cm^{-3}$ and a maximal range of 20 % in doping density [97] the resulting theoretical variation in the attenuation of the photon beam of is 16 % . This corresponds very well with the observed amplitudes in Fig. 6.14. Above 32 V however the detector is fully depleted, even in the regions with higher doping densities, and a differing absorption length has to be disregarded as a possible explanation. Generation/recombination centres due to crystal defects caused by oxygen precipitations which are associated with bulk impurities were found for low-resistivity Si [98]. Here this seems to be less probable, since it would cause fluctuation in the leakage current in the sensor. In this case the transition from columns completely situated within a high-count region to columns completely in low- count region should result in discontinuities in the image, since the Medipix1 chip is provided with a column wise-leakage current compensation.

The smooth and continuous shape of the flat-field corrected profiles measured here, Fig. 6.14(e,f), suggest that variations of the effective pixel geometry introduce deviations in the charge collection. A parasitic field induced by a locally differing potential distribution due to doping inhomogeneities gives rise to field components perpendicular to the charge collection direction. The impact of the parasitic fields is reduced with with increasing detector bias voltage. As opposed to the high frequency variations described in the previous section, no correction for doping-inhomogeneity related sensitivity variations can be be envisaged in the readout electronics. The deviations account for up to 15 % of the total number of counts in the raw image data if a sensor bias in close vicinity to the depletion voltage is used. The signal variations can be reduced by one order of magnitude by strongly over-depleting the sensor. The deviations can be reduced by another order of magnitude by flat-filed correcting the raw data.

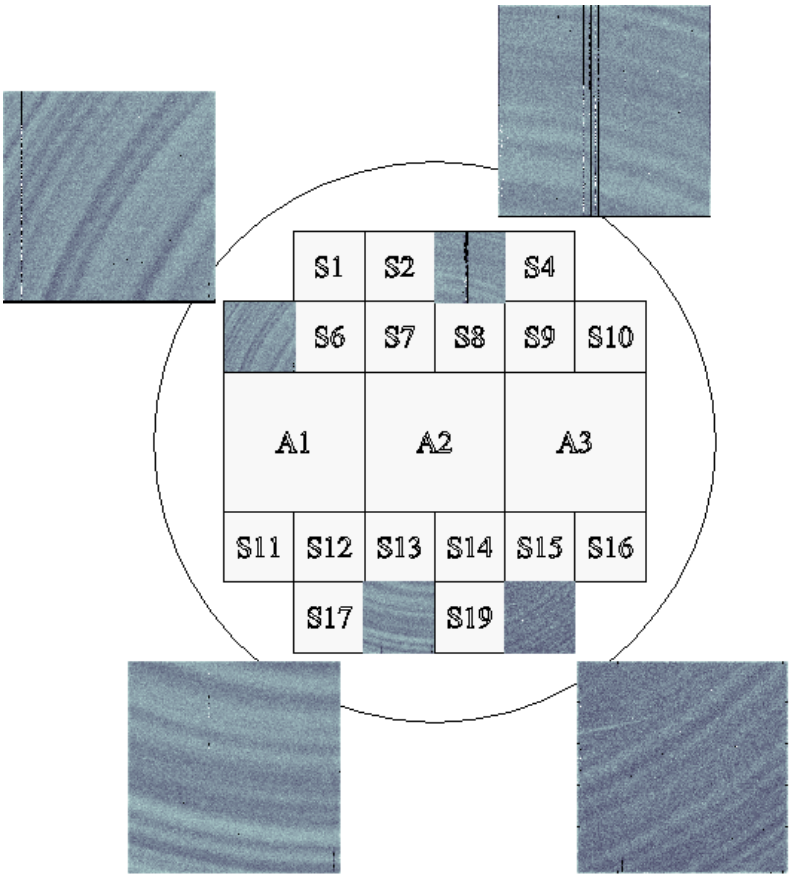


Figure 6.16: Count variations found in four different Medipix2/Si assemblies, K8_S18, K7_S20, J3_S5 and D3_S3, measured with 16V sensor bias. The naming convention for a detector assembly puts the readout chip position first, followed by the sensor wafer position. Placed on the corresponding position on the detector wafer-map measured inhomogeneities constitute rings originating at the centre of the detector wafer. The position on the readout electronics map, on the other hand is entirely uncorrelated to the ring pattern.

6.3 MTF, NPS and DQE

Image quality can be characterised by various parameters amongst which the most important are image sharpness, contrast and noise level. Several figures of merit describe different aspects of detector performance and image quality [36, 37, 99–101]. The significance of the respective figure strongly depends on the application. In medical imaging the image noise is the limiting factor, because the detectable feature size and contrast is directly linked to the dose applied, which has to be kept as low as possible. The minimum possible noise levels therefore are crucial to reduce the necessary patient dose for a given examination [102]. In other applications, e.g. baggage inspection, spatial resolution and contrast may be the key requirement, whereas dose efficiency is of lesser importance.

In the following sections the influence of the energy threshold on the imaging performance as well as the influence of the applied dose will be investigated. In sec. 6.3.2 the experimental determination of the MTF will be described. The MTF is the quantity most frequently used to measure the spatial resolution and the degradation in image quality caused by system unsharpness. It takes into account only the characteristics of the signal transfer in the imaging system but gives no information about the noise characteristics, which itself is characterised by the NPS, described in sec. 6.3.3. The most significant and widely used single measure of detector performance is the DQE. It describes the degradation of information in the signal while being processed in the detector system, by relating the inherent noise of the incident photon flux to the noise contained in the output signal. It therefore is best suited to compare the internal noise performance of different detector systems, independent from the input signal. In sec. 6.4 finally the impact of applied dose on the image quality will be studied.

6.3.1 Experimental setup and parameters

All measurements were performed using a Seifert FK61-04x12 W-target X-ray source with 2.5 mm Al equivalent filtering. For the MTF and DQE measurements the tube voltage was set to 25 keV and 45keV and the distance between detector and focal spot was 65 cm.

In these experiments the coarser, but more temperature stable internal DAC for THL was used. The external, finer adjustable Muros2 controlled DAC could not be used since this requires stable temperature conditions. The cooling of the Seifert FK61 caused significant variations in ambient temperature of the laboratory room resulting in a slow drift of the threshold level controlled by the external DAC. The internal, on-chip DAC controllers are designed to internally compensate for temperature variations of 10-15 °C.

Energy calibration:

In order to accurately determine the position of the lower energy threshold in terms of photon energy the detector had to be calibrated with respect to the internal DAC for the lower energy threshold THL_{int}. The calibration threshold scans were carried out with the X-ray tube voltage set to 20, 24, 28, 35 and 40 keV. The spectra were derived from the measurements by taking the gradient of each threshold scan. The DAC value for THL_{int} at the endpoint of the measured spectra was used as reference value for the highest photon energy present in the spectrum, determined by the respective tube voltage.

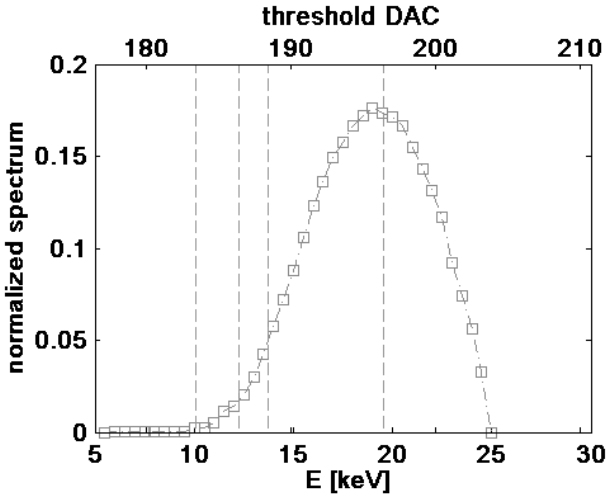


Figure 6.17: Threshold settings with respect to calculated spectrum of a W-target X-ray tube operated at 25 keV tube voltage.

After correction for the cutoff energy offset, introduced by the convolution of the photonic spectrum with the threshold dispersion, the obtained energy calibration for the internal DAC, THL_{int}, was computed

$$E_\gamma = -122.5 + 0.723 * THL_{int} \tag{6.4}$$

with a coefficient of determination of 0.9998.

Fig. 6.17 illustrates the position of the lower energy thresholds used in the experiments with respect to the tube spectrum.

The dose applied per acquisition was adjusted in such a way that the mean number of counts in the image was kept approximately constant for the different thresholds. The dose values were monitored using a semiconductor dosimeter[1]. For each threshold setting 80 additional flood field acquisitions were recorded to calculate the flatfield correction. Table 6.5 gives an overview of the experimental parameters used together with some key-figures calculated from the measurements.

6.3.2 Modulation Transfer Function

From a theoretical point of view the MTF is given by the Fourier transform of the system response to a delta function as input. Commonly applied techniques to measure the MTF are the slit-method, the edge-method and bar-pattern mask. The latter method does not measure strictly the MTF but rather the contrast transfer function CTF, but is still widely used as a measure for the MTF due to its experimental simplicity. The CTF measures the overall reduction in contrast obtained when imaging a pattern of square waves with increasing frequency. It therefore also includes the effects of higher harmonic terms introduced by the bar pattern, which are not present in the MTF. All methods have

[1]Diados, PTW-Freiburg Physikalisch-Technische Werkstätten, 79115 Freiburg, Germany

Spectrum	W-25 keV				W-45 keV
THL_{int}	182	185	187	195	182
E [keV]	9.1	11.3	12.7	18.6	9.1
dose [mGy]	1.05	1.26	1.43	3.99	3.62
Resolution [μm]	8.1	8.7	9.1	11.0	7.8
Effective pixel size [μm]	54.0	50.5	48.2	39.5	57.4
DQE(0) [%]	25	22	20	5	9

Table 6.5: Overview of the parameters and results of the measurements of the MTF and NPS. Also indicated is the DQE at zero spatial frequency computed from the MTF and NPS measurements.

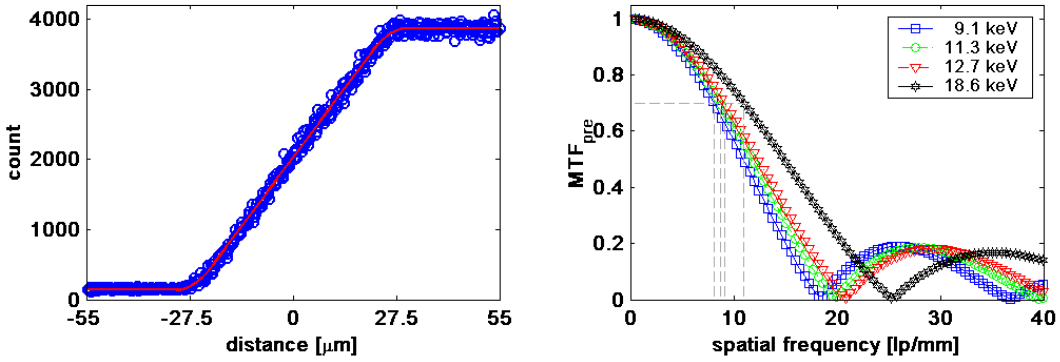
in common that the measured response of digital systems depends on the orientation of the test pattern with respect to the detectors pixel axes, since the effect of aliasing is not equal in all directions. It is common practice to measure the MTF only in the detectors natural x/y directions. Methods have been developed to measure a two dimensional MTF directly using circular test mask geometries, but the deviation from one dimensional methods have been found to be in the order of only few percent [103, 104].

Here the edge method was applied to measure the MTF, which gives a good approximation to a delta function input if a sufficiently sharp edge is available. The sharp edge of the 4 mm wide opening of a 50 μm thick lead bar mask[2] has been used. It was placed at an angle θ of ~2-3 ° with respect to the pixel row and column axis, directly on top of the detector to avoid blurring due to geometric unsharpness. By placing the edge inclined by a very small angle the fraction of area covered per pixel increases slowly along the edge until the full pixel was covered by the lead attenuator. To obtain the edge spread function (ESF) from the measured data, the pixel count values were projected along the edge direction. In this way an oversampling of ESF with a frequency of $a \cdot sin(\theta)$, with a denoting the pixel pitch is achieved. The position and angle of the edge in the recored image was found using a simple edge detection algorithm. The 2-dimensional Laplacian of the median filtered edge image was calculated and then the zero crossing point in each column was detected. The so obtained x and y coordinates for the zero-crossings were then fitted with a line to calculate the slit angle needed for the resampling. Fig. 6.18a) shows an example of a re-sampled ESF. A deformation of the measured edge-spread function ESF due to scattered radiation as reported in [105] has not been observed.

Fig. 6.18b) displays the results for the MTF, calculated by taking the Fourier transform of the gradient of the ESF. The value used as characteristic figure for the spatial resolution is the spatial frequency at which the MTF drops to 70 % of its maximum value. The theoretical value for the resolution of an ideal unblurred pixel response with 55 μm pixel pitch is 9.1 lp/mm. The observed effect of increasing the threshold was to diminish the equivalent size of the pixel and therefore enables an improvement in MTF beyond the value predicted by Nyquist sampling theory.

In addition to the measurements with 25 keV tube voltage the same procedure was

[2]Manufactured by PTW Freiburg, Lörracherstr. 7, 79115 Freiburg, Germany.



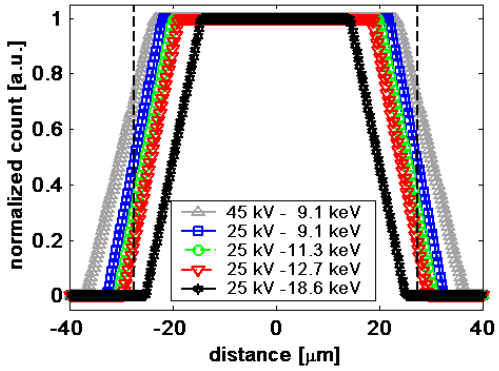
(a) (b)

Figure 6.18: a) The measure oversampled edge spread function measured with the lower energy threshold set to 11.3 keV. b) The presampling MTF_{pre} for the different energy thresholds. The spatial resolution, given by the spatial frequency at which the MTF drops to 70 % of its maximum value ranges from 8.1 to 11 lp/mm. The nominal resolution of a 55 μm pixel pitch detector is 9.1 lp/mm.

followed with the tube voltage set to 45 keV while keeping the threshold fixed to 9.1 keV. The aim was to study the detector response in the case of the threshold put well below half the mean photon energy. The outcome is an increase of effective pixel size to 57.4 μm, exceeding the geometrical limits of the pixel pitch and as a consequence a reduction of spatial resolution to 7.8 lp/mm.

The effect on the effective pixel geometry is illustrated in Fig. 6.19. Displayed are the pixel profiles derived from the fitted ESF. The effective pixel size ranges from 57.4 μm at 9.1 keV threshold to only 39.51 μm at 18.6 keV energy threshold. The increase in resolution with the threshold is explained by the increasing rejection of charge shared counts. Further increase of the threshold progressively leaves photons converting close to the pixel border discarded, creating a region of reduced sensitivity. The observed gain in resolution is compensated for by a decrease in recorded counts, as can be seen in the dose necessary to obtain a constant number of counts per acquisition.

After having determined the presampling resolution properties of the system it is instructive to study the impact of digitalization on the presampling signal. The measure chosen to describe the digital MTF was the expectation MTF or EMTF, described in detail in chapter 2. It takes into account the dependence of the digital MTF on the offset of the edge from the pixel border. Fig. 6.20 shows for the relative position of the MTF_{pre} and the EMTF measured with the threshold set to 9.1 keV representatively for the other threshold settings. The side-effects of an excellent MTF_{pre} extending well above the Nyquist frequency is the origin of the big discrepancy between the two curves. The presampling MTF represents the system response to single-frequency sinusoidal input, being the extreme case of a narrow bandwidth signal. The EMTF describes better the other extreme of an infinite bandwidth input, with extensive signal aliasing present. The real frequency transfer in a given application will lie in between the two extremes, depending



(a)

Figure 6.19: The pixel profiles derived from the fitted ESF measured with a 25 kV W-tube spectrum and energy threshold ranging from 9.1 to18.6 keV. Also shown is the resulting pixel profile for the threshold set well below half the mean photon energy.

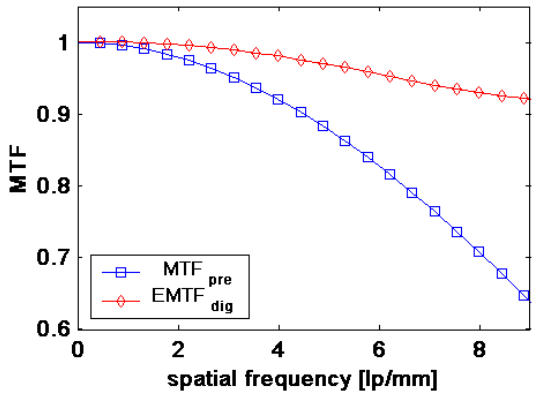


Figure 6.20: The measured MTF_{pre} and the corresponding digital EMTF for the energy threshold set to 9.1 keV up to the Nyquist frequency.

on the frequency content of the signal.

6.3.3 Noise Power Spectrum

The NPS represents the noise power present at given spatial frequencies in the output signal. The theoretical NPS of an ideal system, with a MTF determined only by the pixel pitch, is flat without a decrease at higher frequencies. A decrease in NPS amplitude with frequency would indicate a correlated response of individual pixels. In practice the measurement of noise power spectrum consists of recording a large number of flat field acquisition under normal operation conditions. For each of the energy thresholds listed in table 6.5, 20 frames were recorded as raw data for the NPS calculations.

To remove additional noise stemming from time-constant fixed patter inhomogeneities in the recorded image flatfield correction map were applied. These inhomogeneities originate from non-homogeneous detector response or residual beam inhomogeneities. 80 additional flood-field acquisition were taken to calculate the correction map for each threshold. Widely used additional correction methods such as subtracting dark-field images or taking the difference of two open-field acquisitions to remove time dependent structural noise were not employed. These corrections are not necessary in a photon counting system since they are result of an integration of a background noise signal, which is entirely discarded in the discrimination process.

The NPS was derived from the data by calculating both the two dimensional NPS directly from the corrected images and by computing the 1-dimensional approximation in x and y direction using the Welch method [106]. An inherent property of the one dimensional method is to give a much smoother estimate for the NPS. To compare the results of the two methods an average of the two dimensional NPS along the main axes was computed by by radially averaging a slice of four pixels on either side of the axes. The computed estimates yielded essentially identical results, apart from the Welch method, which yielded slightly smoother results, an inherent property of the method.

Fig. 6.21 shows the results for the one dimensional NPS normalized to the mean count in the image. Apart from the 9.1 keV threshold NPS, all spectra are flat, which is an effect of the MTF reaching far beyond the Nyquist frequency. Furthermore it can be concluded that the threshold variations across the pixel matrix are randomly distributed and do not show any spatial correlations.

The highest threshold at 18.6 keV displays elevated noise since the threshold is placed very close to the maximum of the photon spectrum. At this position the translation of the threshold dispersion into additional image noise is most pronounced. Apart from this higher noise level the progression with frequency still displays white noise characteristics.

For the lowest setting of the energy threshold a slightly different situation has been found. The fact, that it appears to have elevated noise values with respect to 11.3 and 12.7 keV threshold, is a consequence of a 3 % lower mean count as compared to the higher thresholds. The main difference however is the decrease in noise power with increasing frequency, introduced by the low-pass filtering effect of the charge shared events.

The above described characteristics have been found to be identical in the NPS in x and y direction. This illustrated in Fig. 6.22 displaying the results for the two dimensional NPS, which too shows no deviation from the flat shape. The one dimensional spectra therefore can be used for the calculation of the DQE without introducing artifacts.

Also displayed is the relative order of magnitude for the not flatfield-corrected data with respect to the one with the correction map applied. The higher noise in the uncorrected image is governed by the threshold dispersion, as discussed in sec. 6.2. The necessity to apply flatfield corrections could be removed by readout electronics implementing the charge-sharing correction logic suggested in sec. 5.3. Efforts to develop such a readout are currently undertaken in the microelectronics group at CERN.

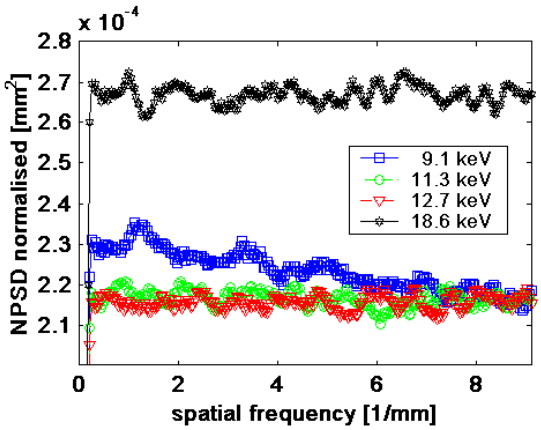


Figure 6.21: The one dimensional NPS normalized to the mean count in the image. All threshold settings show a white power spectrum, only at 9.1 keV the low-pass filtering effect of increased charge-sharing can be seen.

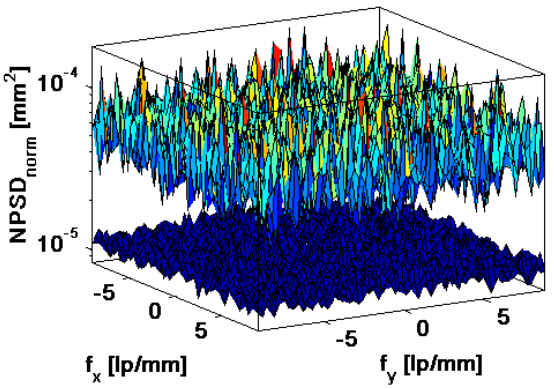


Figure 6.22: The 2-dimensional NPS for the energy threshold set to 11.3 keV with and without flatfield correction applied.

6.3.4 Detective Quantum Efficiency

As already pointed out before, the DQE represents the most significant single figure of merit to compare detector performance for imaging applications. One input parameter to the calculation of the DQE is the MTF. The question, whether it is more appropriate to use the EMTF or as most frequently done, to take the MTF_{pre} to derive the DQE has already been discussed in sec. 2.3. Both alternatives have been found to have weak points in providing a realistic measure for achievable SNR. The most complete way to characterize the detector performance is to provide both versions, since the two approaches offer complementary information, c.f. Fig. 6.20. The MTF, the derived DQEs will describe the situations for the extreme cases of a sinusoidal input and an infinite bandwidth input. The observed DQE in real applications therefore will lie within these limits. Only if both versions of the DQE are given together is the detector performance described accurately. For this reason both versions of the MTF will be used for the calculation of the DQE.

The third input parameter to calculate the DQE is the incident quantum fluence. The calculated emission spectrum of the X-ray tube has been used together with the measured dose per acquisition to compute the photon flux.

Fig. 6.23 shows the computed DQEs for the different threshold settings. A characteristic value of the DQE is its value at zero spatial frequency, which is a measure of the effective quantum efficiency QE of the system. The lowest threshold gives the highest QE of ∼25-26 %. This approaches very closely the maximum value of 27 %, given by the total attenuation of a 25 keV W-tube spectrum in a 300 μm Si sensor. The penalty for the increased spatial resolution obtained at higher energy thresholds is the reduction of the DQE(0). The most pronounced decrease was observed for 18.6 keV threshold with ∼5 % at zero spatial frequency. The reason for this very low DQE is the lowered impact of the flatfield correction for this energy threshold. A larger number of flood-field acquisitions has to be compiled into the correction map to remove the fixed pattern noise effectively.

From the results presented in this section it can be concluded that both the spatial resolution and the noise level in the image depend on the threshold setting of the detector system. The threshold has to be carefully chosen depending on the incident photon spectrum in order to optimize SNR. If the working point is chosen appropriately the nominal pixel pitch resolution and minimal noise level can be obtained at the same time. As a result the DQE at zero frequency approaches attenuation limit, indicating that the detector system is basically only Poisson noise limited.

6.4 Imaging performance and applied dose

The DQE for the MPX2-Si detector has been evaluated in the previous sections, displaying excellent imaging performance, even approaching the theoretical Poissonian limit. Measurements using different X-ray tubes tube have been performed with the Medipix1-Si detector to investigate the dependence of resolution and DQE on the dose applied without changing the energy threshold held fixed at ∼10 keV.

The Medipix1 detector was tested with a Planmeca Prostyle Intra[3] dental tube, a W-target X-ray designed for dental application, operated at 60 kV and at 70 keV. The distance

[3]Manufacturer: Planmeca Oy, Asentajankatu 6, 00880 Helsinki, Finland.

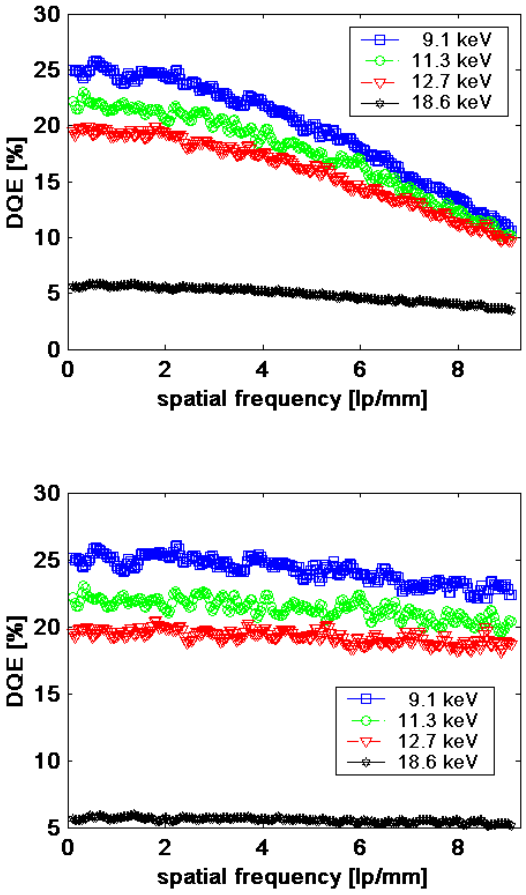


Figure 6.23: The DQE computed using the a) the presampling MTF_{pre} and b) the EMTF.

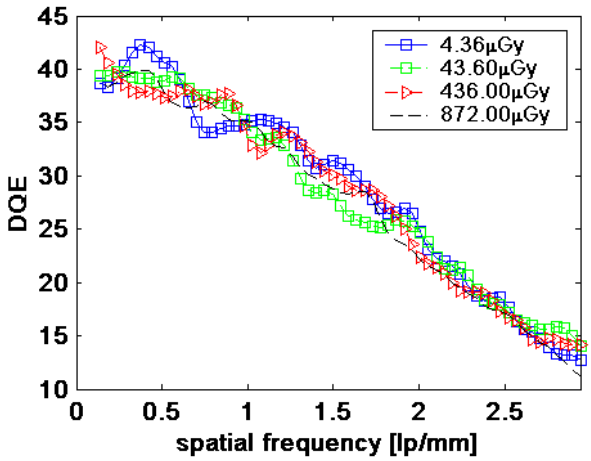


Figure 6.24: Dose dependence of the DQE measured with the Medipix1 using a Mo-target at 28 keV.

between the detector and the focal spot was 59 cm. The applied dose was varied from ∼11 μGy to ∼501 μGy. Both the MTF_{pre} and the NPS proved to be entirely unaffected by changes in the applied dose. The resulting DQE also remained dose independent. The observed spatial resolution was 2.35 lp/mm and the extrapolation of the DQE to zero spatial frequency matched very well the theoretical QE of 5.7 % for the 60 kV spectrum and 4.9 % for the 70 kV spectrum.

Fig. 6.24 shows the dependence of the DQE of the Medipix1 detector tested with a Seifert FK61-04x12 Mo-target X-ray source with 30 μm Mo filtering, providing a bremsstrahlung spectrum with strong $K_{\alpha,\beta}$ lines at 17.4 and 19.6 keV. This is a typical spectrum used in mammographic examinations. The dose ranged from 4.4 to 872 μGy. The spatial resolution in this case was found to be slightly lower with 2.3 lp/mm, but independent of the dose. Again the system response was constant over the dose range investigated and the DQE(0) approached the theoretical maximum of 46 %. The measured values for the DQE(0) are summarized in Fig. 6.25.

This is an important result since it highlights the potential of photon counting devices for medical applications as it may offer significant patient dose reduction. In CMOS imagers and CCD devices the DQE generally decreases with the dose since contributions from leakage currents, TFT switching noise and external noise sources becomes stronger with respect to the signal level.

The normal dose in dental examinations is around 0.5 mGy for CCD detectors and even higher with ∼2 mGy for conventional film. In mammographic examinations the typical doses are in the range between 1-3 mGy. The principal improvement offered by photon counting pixel detectors is the potential to work at significantly lower dose compared to other imaging system. In both cases investigated the Medipix1 showed equally excellent dose efficiency for doses well below the current standard values.

This is illustrated in Fig 6.26, showing an anchovy X-rayed with increasing acquisition time using the Seifert Mo-target X-ray source operated at 17 kV. The tube voltage was chosen below the K-lines of Mo to optimize the contrast by using the bremsstrahlung

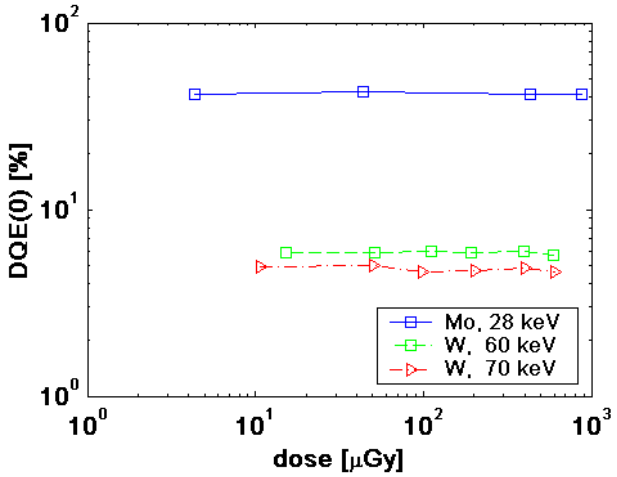


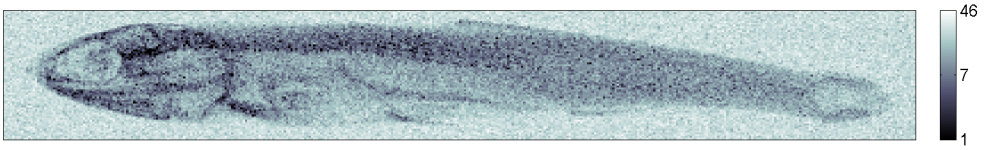
Figure 6.25: Dose dependence of the DQE(0) measured with the Medipix1 using a Mo-target X-ray source at 28 kV and a W-target X-ray source at 60 and 70 kV.

spectrum only. The distance between focal spot of the tube and detector was 51 cm. The image was tiled together from individual 2x7 frames to cover the whole anchovy. For Fig 6.26b) 2 mA tube current and 30 ms acquisition time was used, resulting in ∼46 recorded photons in the background of the image. The shape of the anchovy is clearly visible. In Fig. 6.26d) 330 ms acquisition time was used with the same settings as in b). Most of the anatomical features of the anchovy are already visible. As a comparison the image obtained using the full counter depth of the Medipix1 is shown in Fig. 6.26e). The acquisition parameters here were 10 mA tube current and 4 sec.

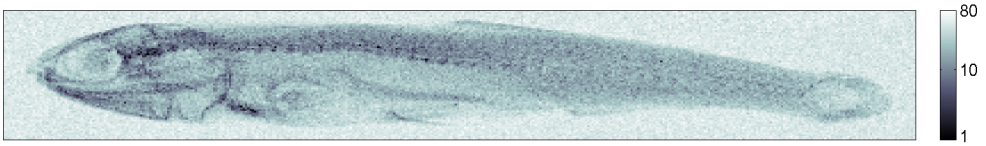
It can be concluded, that one of the limiting factors for the application of direct detection photon counting systems in the medical field is posed by the sensor part of the assembly. Si as sensor material, as used in the measurements presented here, offers outstanding properties in terms of availability and homogeneity but does not provide a sufficiently high stopping power to meet the requirements posed in the medical radiography. One way to overcome this limitation is to bump-bond higher Z-material to the photon counting readout. The other option is to increase the thickness of the Si sensor to more than 2 mm to provide a QE of >70 % required for mammography. In both cases new challenges are posed to the readout electronics. Higher Z-materials dramatically increase the QE but suffer from characteristic X-ray emission. A GaAs sensor for example requires only 150 μm thickness to provide the same stopping power. At the same time fluorescent photons of ∼10 keV are emitted with a fluorescence yield of more than 50 % which lead to conversion related charge-sharing with a mean free path of the secondary photon of ∼40 μm. On the other hand a very thick Si sensor inevitable leads to long collection times, here resulting in elevated charge-collection related charge-sharing. In both cases it is necessary to implement a charge-sharing correction in the readout electronics if the resolution goals are to be achieved. For applications using lower energy photons the current generation of Medipix in combination with a Si sensor already offers unmatched properties, namely high resolution and Poissonian noise limit over almost the full dynamic range.



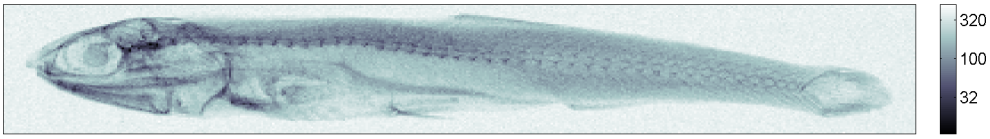
(a)



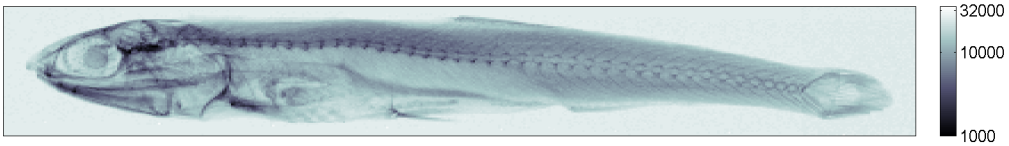
(b)



(c)



(d)



(e)

Figure 6.26: Images of an anchovy X-rayed with increasing acquisition time using the Seifert Mo-target X-ray source operated at 17 kV. b) 2 mA tube current and 30 ms c) 50 ms and d) 330 ms acquisition time. d) The same anchovy using the full counter depth of the Medipix1 with 10 mA tube current and 4 sec acquisition time.

6.5 Spectrocopic imaging

In all measurements presented so far throughout the thesis only the lower energy threshold was used. In this section the first measurements exploiting the second, upper threshold of the Medipix2 are presented.

Threshold tuning: First the behaviour of the system using both energy thresholds concurrently had been examined. Both the lower and the upper threshold have to be tuned as described in chapter 4 to give the minimal threshold dispersion, in order to obtain the narrowest possible window and to bin the detected photons accurately. The threshold dispersion and electronic noise determine the minimum width of the energy window, which has been found to be 2 internal DAC values difference between the upper and the lower thresholds. Later tests with a 109 Cd radioactive source (peaks at ∼22 keV and ∼25 keV) confirmed that value, which corresponds ∼1.4 keV window width. The lowest possible value for the low threshold in window operation mode was 4.4 keV.

Energy spectrum and backscattered radiation: After having fine tuned both thresholds, the tallied energy spectrum of W-target X-ray tube with 2.5 mm Al filter and a tube voltage of 50 kV was measured by moving the lower and the upper threshold level concurrently from the minimum value of 4.4 keV over the range of the photon spectrum. Different energy window widths (1.4, 2.8 and 4.2 keV) have been used and the total number of counts was recorded as a function of the lower threshold of the window.

Fig. 6.27 graphs the observed spectrum, which includes two fluorescence peaks at ∼22 keV and at ∼25 keV. The number of counts increases with the width of the energy window, but the energy resolution decreases, as can be seen by the distinction of the fluorescence peaks.

The peaks were associated with fluorescence photons from Sn (K_α 25.2 keV, K_β 28.5 keV), Ag (K_α22.1 keV, K_β 24.9 keV) and Pb (L_α 10.5 keV, L_β 12.6 keV) by comparison with simulations. The bump bonds are made of eutectic Sn-Pb bump (63% Sn, 37% Pb) and Ag is contained in the conductive glue used to mount the assembly on the PCB. The radiation transmitted through the sensor is subject to backscattering and creates fluorescence photons of which in turn a fraction is reabsorbed in the sensor. In order to estimate the contributions from the radiation entering the sensor via the backside, the photons emitted backward from the geometry depicted in Fig. 6.28a) has been simulated for the same incident spectrum as used in the measurement. The simulated spectrum of the backscattered photons is depicted in Fig. 6.28b). In total ∼0.9 % of the incoming photons are backscattered and about 1.4 % create backward emitted secondary photons. Taking into account the absorption probabilities of the primary and the backscattered photons the contribution of the backscattered photons account to up to 8.4 % of the number of actually detected photons in a 300 μm Si sensor.

Imaging: As the fluorescence photons observed come from behind the sensor they should also contribute during image acquisition. A plastic Swatch watch was placed near to the entry of the sensor and images were taken with an energy window of 3.5 keV at various energy thresholds with the same tube spectrum. Some of these images are

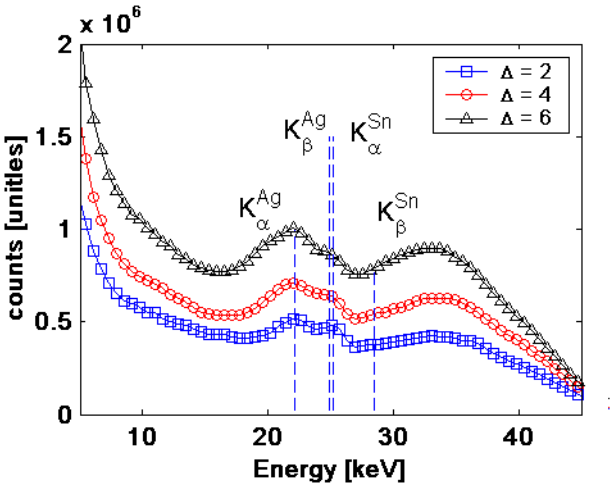


Figure 6.27: The tallied energy spectrum of W-target X-ray tube operated at a tube voltage of 50 kV and with 2.5 mm Al filter, measured by moving the lower and the upper threshold level concurrently from the minimum value of 4.4 keV over the range of the photon spectrum. Plotted is the number of counts over the position of the lower threshold of the energy window with a width of 2, 4 and 6 DAC values (corresponding to 1.4 keV, 2.8 keV and 4.2 keV).

shown in Fig. 6.29. With the windows around 18 keV the image in a) is rather clear although, as expected, the higher density components of the watch are rather opaque as the lower energy photons are easily absorbed. In Fig. 6.29b) the effect of the fluorescence photons is quite evident as the energy windows is centered at around 23.3 keV. Even if selecting harder photons here there is an evident blurring of the image probably due to the fluorescence photons coming from underneath the chip. In Fig. 6.29c) the image becomes much clearer. In this case the energy window is above the emission lines of Sn and Ag. Finally in Fig. 6.29d,e) as the photon energy further increases more objects hidden behind the denser components of the watch are revealed. Although a much more systematic and quantitative study is needed to evaluate the effects on spatial resolution and image noise, these results may be the first images taken using such a spectroscopic imager. It gives a first indication of the potential of such devices to improve image quality where only broadband X-ray sources are readily available.

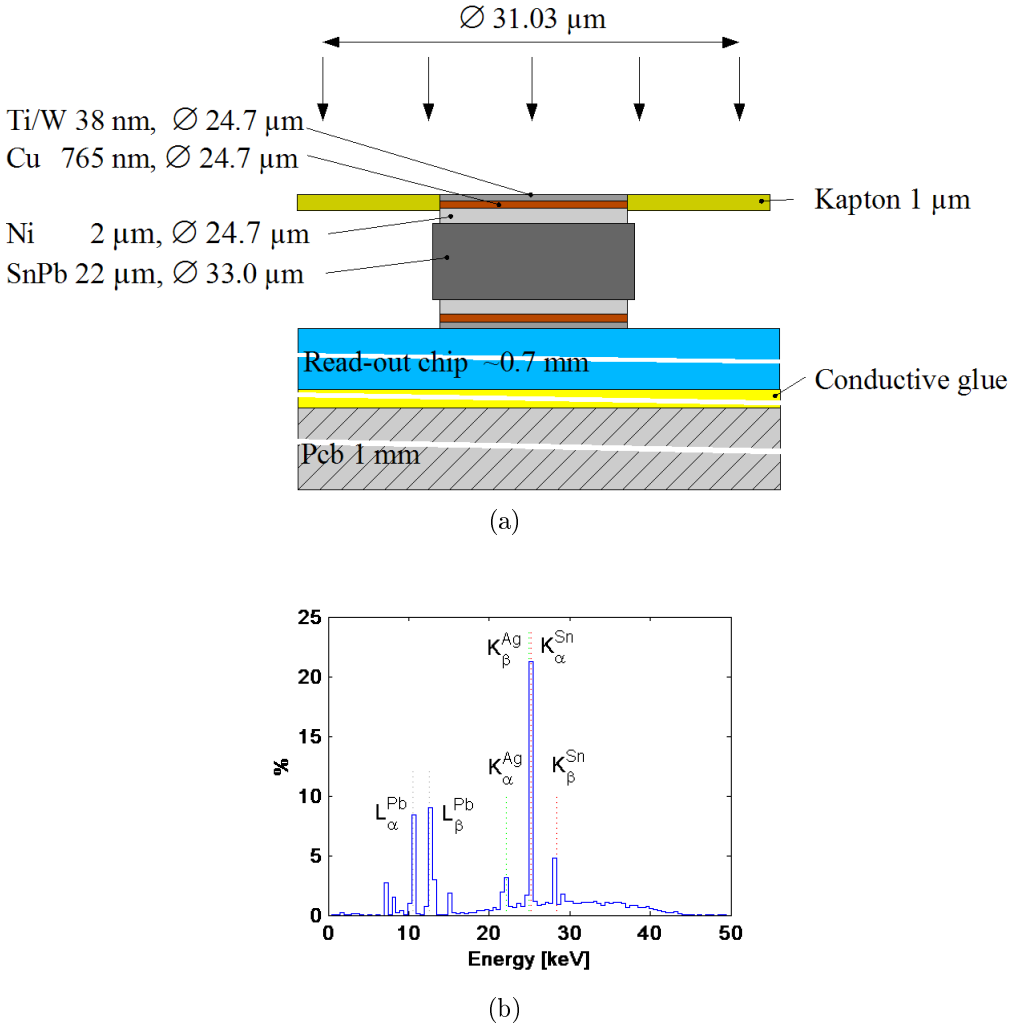


Figure 6.28: a) Model of the bump bond connection between sensor and read-out electronics. The bump bond is made of eutectic SnPb (63/37) solder, the silver content of the conductive glue between the readout chip and the PCB board is about 3 %. The indicated thicknesses for the under bump metalization are given on the top side of the bump only. The metal layers are symmetric on both sides of the SnPb solder bump. b) The spectrum of the backscattered photons of an incident beam of W-tube at 50 kV and 2.5 mm Al filter after passing through a 300 µm thick Si sensor on top of the simulated geometry in Fig. a). The position of K-lines of Sn (K_α 25.2 keV, K_β 28.5 keV) and the L-Lines of Pb (L_α 10.5 keV, L_β 12.6 keV) in the solder and the k-lines of Ag (K_α 22.1 keV, K_β 24.9 keV) in the conductive glue are indicated .

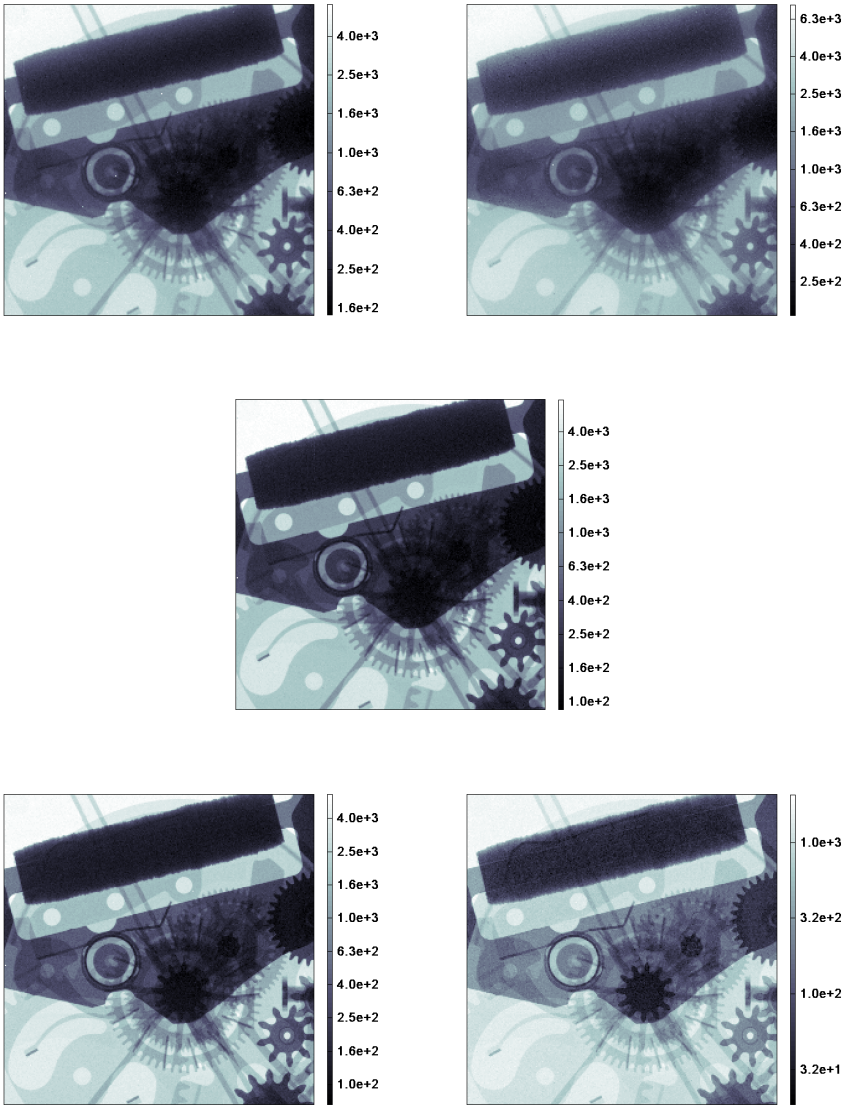


Figure 6.29: Images of a plastic Swatch taken using the energy window at different values of the energy threshold. A W-target X-ray tube with 2.5 mm Al filter operated at 50 kV tube voltage was used. a) 16.1-19.6 keV b) 21.6-25.1 keV c) 29-33.5 keV d) 36.9-40.4 keV e) 43.1-46.6 keV.

6.6 Summary

In this chapter a quantitative characterization of the detector performance has been presented. Figures of merit for single pixel response were presented as well as characteristic values for imaging performance.

- An energy calibration has been performed for both internal and external DAC, which control the energy threshold. The increase in energy per external DAC step has been found to be 0.407 keV/THL_{ext} with a coefficient of determination of 0.9997. The corresponding values for the internal DAC are measured to be 0.773 keV/THL_{int} and 0.9998.

- Uniform detector response across pixel borders can be achieved if the energy threshold values of neighbouring pixels are identical. In case of an offset of the order of one step in THL_{int} an excess in counts of ∼3.5% was observed.
  At the corner of four neighbouring pixels a region of reduced sensitivity of Gaussian shape with 6.5 μm width and a minimum in count in the order of 40 % of the mean detector response has been measured with 10 keV photons.

- The ENC has been determined to be ∼0.49 keV rms (corresponding to 136 e^- in Si) with single pixel pencil beam measurements using 8 and 20 keV photons. Similar values could be derived from area irradiation measurements with a dispersion of the electronic noise of 0.06 keV rms or 17 e^- rms.

- The single pixel energy resolution has been found to depend in the position of the incident beam in the pixel area and range from 0.5 keV rms at the center of the pixel to 1.35 keV rms close to the pixel borders. The mean system energy resolution under large area irradiation has been determined to be ∼0.69 keV rms for photon energies in the range of 8-40 keV.

- The threshold dispersion after fine tuning is 0.44 keV rms or 120 e^- rms. Threshold dispersion and charge sharing together introduce systematic fluctuations in the recorded count leading to fixed pattern noise in the image. Such fixed pattern noise can be efficiently corrected for if the incoming photon beam is monochromatic. In the case of broadband spectral X-ray beams, the application of a simple flat-field correction may reduce the image SNR by up to 20 %, depending on the extent of beam hardening in the examined object. To obtain results comparable to monochromatic X-ray, careful prefiltering of the beam is necessary when calculating the correction map from flood-field exposures. For narrow spectrum X-ray beams

or low contrast objects excellent results can be obtained using conventional flat-field correction maps.

- Doping inhomogeneities have been found to introduce count variations of up 2 % in fully depleted 300 μm Si sensors and even much stronger ones in under-depleted regime. By operating the sensor in strong overdepletion, i.e. with a bias voltage higher than four times the depletion voltages, the fluctuations in the number of recorded counts can be reduced to less than 0.1 %.

- The MTF and the NPS have been measured for the Medipix2/Si detector using two different W-tube spectra. The spatial resolution has been found to change with threshold position, increasing from 8.1 lp/mm to 11 lp/mm with increasing threshold. The NPS show a flat shape, except for very low threshold values. At low thresholds the shape is ascribed to the low pass filtering effects of the increased contributions of charge sharing.

- The DQE derived from MTF and NPS measurements for both the Medipix1 and the Medipix2 have shown the potential of photon counting systems to provide a SNR close to the theoretical limit posed by Poisson statistics. Moreover the DQE proved to be unaffected by the applied dose in the range investigated, from 4 μGy to 832 μGy.

- The energy window mode has been successfully applied to measure the approximate energy spectrum of a W-target X-ray source. A contribution of backscattered photons from structures underneath the sensor could be identified. These photons lead to a blurring in imaging in the photon energy range from 22-28 keV. By excluding these photon energies from the final image, the image quality can be enhanced. Note that such phenomena can not precisely be identified integrating imaging devices, but also there contribute to image degradation. This indicates the potential for an energy resolving imaging detector to extract currently hidden information from a single broad spectrum radiographic image.

Chapter 7

Conclusion and Outlook

7.1 Conclusion

Single photon counting in high granularity pixel detectors represents a new technique for X-ray imaging. The work carried out for this thesis seeks to contribute to the understanding of the advantages and limitations of this new imaging modality. The effects of charge sharing in high granularity pixel detectors have been investigated. The underlying physical phenomena have been modelled and simulations have been carried out. These have been compared with measured data.

Charge deposition simulations showed that charge is shared between adjacent pixels at the stage of photon conversion in the sensor chip. Though Si provides only weak stopping power it still offers excellent detection characteristics for low energy photons up to 20 keV. The QE of a 300 μm thick Si sensor is >99 % for photons of up to 8 keV but drops steeply thereafter reaching 27 % at 20 keV. In Si, simulations demonstrate that surface losses due to photon escape are practically independent of the sensor thickness and escaped electrons make a negligible contribution to the loss of energy resolution. A higher QE can be achieved by increasing the Si sensor thickness, but the larger contribution of Compton scattering limits the achievable energy resolution at photon energies higher than 40 keV.

The two other materials investigated, GaAs and CdTe provide significantly increased stopping power compared to Si, in a 300 μm thick sensor the respective quantum efficiencies for 20 keV photons are 99.8% and 98.1 %. On the other hand, when the photon energies exceed the respective material K-edge energies, ∼11 keV in GaAs and ∼27 keV in CdTe, both the spatial resolution and the energy resolution are strongly affected by the presence of fluorescence photons. Although CdTe offers the highest stopping power of the three materials for high energy photons, much larger pixel volumes would be needed to obtain the same energy resolution as in GaAs, due to the much larger mean free path, of the fluorescence photons (∼110 μm cf. ∼40 μm in GaAs). For a typical sensor geometry of 300 μm thickness and 170 μm pixel pitch epitaxial GaAs as sensor material offers better spatial resolution and energy resolution than CdTe for photon energies up to 80 keV.

After the photon conversion the generated charge cloud is subject to lateral diffusion while being transported towards the collection electrodes by the electric field in the sensor.

The effects of charge diffusion which leads to charge sharing have been investigated during the detector performance characterisation of the Medipix2. A consequence of this is the appearance of a low energy tail on the spectrum seen by the individual pixel. An energy calibration has been performed using both the internal and the external DACs, which set the energy threshold. The energy calibration has been found to be linear with the DAC value, the coefficient of determination being >0.999 for both alternatives. The linearity of the threshold energy relation is of particular importance for the fine tuning of the energy threshold dispersion over the whole pixel array.

The combined effects of pixel-to-pixel threshold dispersion and charge sharing introduce systematic fluctuations in the recorded count in each pixel leading to fixed pattern noise in the image. The threshold dispersion after fine tuning has been found to be $\sim$0.44 keV. It has been shown that uniform detector response across pixel borders can be achieved if the energy threshold values of neighbouring pixels are identical. It has been confirmed that the correct number of photons is recorded if the threshold is set to half of the photon energy of an incoming monochromatic beam. In the region of the corner of four neighbouring pixels in a 300 μm Si thick sensor with 55 μm pixel pitch an area of reduced number of counts of 6.5 μm width has been measured with 10 keV photons. A Gaussian shaped decrease in count to 40 % of the center pixel count has been observed. The result is that $\sim$4 % of the converted photons are not counted. An increase of $\sim$3.5% in mean number of counts per pixel was observed with the energy threshold set 0.7 keV below half the photon energy.

The effectiveness of flat-field corrections in removing fixed pattern noise has been studied. For monochromatic photon beams the fixed pattern noise due to threshold dispersion can be effectively removed. In the case of broadband spectral X-ray beams, the application of an inappropriately measured flat-field correction may even worsen the image SNR. When calculating the correction map from flood-field exposures, the spectrum used should be similar to the one expected in the image acquisition. The application of a well matched flat-field correction results in a strong suppression of fixed pattern noise. In order to obtain results comparable to monochromatic X-rays, careful prefiltering of the beam is necessary. An alternative way to calculate the correction map from electrical characterisation of the readout electronics and simulated sensor response will be the subject of further research. For narrow spectrum X-ray beams or low contrast objects excellent results can be obtained using simple flat-field correction maps.

Doping inhomogeneities have been observed to be another source of fixed pattern noise in high resistivity Si-sensors and can produce variations of up to 2% in the number of counts per pixel. The application of a flat-field correction suppresses the influence of pixel-to-pixel threshold variation and this source of fixed pattern noise can be reduced by two orders of magnitude in a strongly over-depleted sensor. The pattern observed is compliant with the typical striation pattern present in FZ-Si.

The ENC of the readout electronics has been determined to be 140 e^- rms with single pixel pencil beam measurements using 8 and 20 keV photons. Similar values could be derived from area irradiation measurements with a dispersion of the electronic noise of

16 e^- rms. The spectroscopic response of the Medipix2 with a 300 μm thick Si sensor was found to depend on the point of incidence of the pencil beam in the pixel area. In the pixel center, the energy resolution is given by the ENC only, corresponding to ~1.2 keV FWHM. Already at an offset of 15 μm from the pixel center an additional broadening of the photopeak equivalent to 140 e^- rms is introduced by charge sharing effects. The mean system energy resolution under large area irradiation is ~1.62 keV FWHM for photon energies in the range of 8-40 keV. These measured results have been confirmed in simulations.

The MTF and the NPS have been measured for the Medipix2/Si detector using two different W-tube spectra. Both spatial resolution and image noise depend on the fraction of multiply counted photons. As a consequence, the spatial resolution alters with the threshold position, increasing from 8.1 lp/mm to 11 lp/mm with increasing threshold. This increase in spatial resolution beyond the value given by pixel aperture is obtained at the cost of QE. By discriminating charge shared events in the border region the effective pixel size falls below the geometric pixel pitch.

The high inherent spatial resolution of the 300 μm Si sensor used results in a MTF closely following the curve given by the pixel aperture. As a result the NPS showed a flat shape and a decrease with higher frequencies was only found when using a very low energy threshold. This decrease is attributed to the low pass filtering effect of an effective pixel size exceeding the geometric pixel pitch of the readout. Such a behaviour of the NPS is typical in integrating, indirect detection systems, when the intrinsic sensor resolution is less than the one given by the pixel pitch.

The DQE derived from MTF and NPS measurements for both the Medipix1 and the Medipix2 have shown the potential of photon counting systems to provide a SNR close to the theoretical limit imposed by Poisson statistics. It has been demonstrated experimentally and in simulations, that with appropriate threshold setting and flatfield correction applied the DQE at zero spatial frequency approaches the theoretical maximum value of the sensor QE. Moreover the measured DQE proved to be unaffected by the applied dose in the range investigated, from 4 μGy to 832 μGy, highlighting the enormous potential of single photon counting for low dose imaging.

The energy window mode has been successfully applied to measure the approximate energy spectrum of a W-target X-ray source. A contribution of fluorescent photons emitted from structures underneath the sensor could be identified. These photons lead to imaging blurring in the photon energy range from 22-28 keV. By excluding these photon energies from the final image, the image quality can be enhanced. This gives a first indication of the potential of energy resolving imaging detectors. One can obtain spectral information even when only a broadband spectrum X-ray source is used. This information is not accessible using an integrating detection scheme.

In spite of the limitations mentioned above the existing Medipix2 presents an excellent X-ray detector, in particular in the low count rate environment as images are not distorted by electronic noise. The focus of this thesis has been on the X-ray detection properties of

the system, but the same device has found applications in other areas such as transmission electron microscopy, neutron imaging and adaptive optics in astronomy.

7.2 Outlook

The Medipix1 and the Medipix2 detectors are founding members of a new generation of X-ray imagers based on single photon processing. This new modality of image acquisition promises big improvements over integrating detection schemes. This is highlighted by the constant DQE found over a wide range of dose per acquisition. Lateral charge diffusion is an inherent property of the detection process and cannot be avoided in planar sensor geometries. Although the threshold dispersion in the readout electronics cannot be reduced infinitely, the ever increasing component density in microelectronics may allow in future imagers to introduce functionality that not only corrects for the effects of charge sharing but even uses its additional information.

Spatial resolution and spectroscopic performance can be improved by developing readout electronics, which corrects for the charge sharing introduced by energy deposition and charge transport. Calculations suggested that in a 300 μm thick Si sensor with 55 μm pixel pitch, a good approximation of the real photon spectrum could be obtained if the sum of the signals of adjacent pixels was assigned to the pixel with the highest individual signal via a winner-takes-all (WTA) logic. The summed signal would be compared to the energy threshold, in this way correcting for the effects of charge sharing. Such readout electronics would provide the spectral information necessary to apply energy weighting techniques to optimize the SNR in the resulting image.

By weighting each detected photon appropriately the SNR can be substantially increased with respect to conventional energy integrating detection techniques. The most substantial improvements in SNR can be obtained for very low contrast objects. Calculations for a low contrast object showed that a theoretical SNR of more than twice the one of a simple integrating device could be achieved. The same simulation also showed that such an energy weighting scheme is very susceptible to additional noise introduced by wrongly weighted Compton scattered photons. A photon counting scheme that uses a charge sharing corrected spectrum on the other hand gives a slightly lower SNR than a E^{-3} weighting function, but proves to be more robust against deviations from the true energy spectrum.

A first step in this direction is currently taken within the microelectronics group at CERN. A next generation of the Medipix chip is being developed in which neighbouring pixels exchange information about the deposited charge. In this way the charge sharing can be almost completely corrected for, at least in a Si sensor. With this readout the spectroscopic response is expected to be limited only by the conversion losses in the sensor chip.

Further shrinking of the minimum dimension in CMOS processes together with improvements in the quality of semiconductor material should ensure continuing progress in future in the field of X-ray imagers based on single photon processing.

List of Figures

1.1 Energy band diagrams of a) Si and b) GaAs [25]. The lower band edge of the conduction bands in Si are the boundaries of the Brillouin zone, whereas for GaAs it is in the centre of the Brillouin zone aligned with the upper edge of the valence band. 7
1.2 a) The total mass attenuation coefficient of Si and its contributions from photoelectric effect, Rayleigh scattering, Compton scattering and pair production in the energy range up to 2 MeV. b) The total mass attenuation coefficient of Si, GaAs and CdTe in the energy range up to 200 keV. . . . 10
1.3 a) The fluorescence yields $\omega_{K,L}$ for the K and L-shell as a function of the atomic number and the fractions $P_{K,L}$ of all photo-effect interactions that occur in the K and L-shell [28]. b) The mean free path of photons in common semiconductor detector materials. 12
1.4 a) The angular distribution of the Compton scattered photon and b) angular distribution of the recoil electron for energies of the incident photons of 20 keV, 80 keV, 140 keV and 511 keV. 14
1.5 Relative attenuation Compton effect as a percentage of the total attenuation. 15
1.6 Relative attenuation Rayleigh scattering as a percentage of the total attenuation 15
1.7 Bragg curve of an alpha particle of several MeV [29]. 17
1.8 The extrapolated range for electrons in Si, GaAs and CdTe 17
1.9 The electron μ_e and hole μ_h mobilities and the respective diffusivities $D_{e,h}$ for in Si and GaAs as a function of impurity concentration. [25]. 19
1.10 The dependence of the drift velocity on the electric field for electrons and holes in Si, Ge, GaAs and InP. Electron in GaAs and InP show a velocity overshoot above the saturation velocity [30]. 20

3.1 Induced charge on the p^+ electrode of a p^+n diode for a 10 keV photon converted in 150 μm distance from the pixel collection electrode in a 300 μm thick Si sensor of 55 μm pixel size. 34
3.2 The weighting potentials for three different pixel sizes in dependence of the normalized detector depth [29]. 35
3.3 Schematic of a hybrid pixel detector with the sensor chip and the electronics chip connected via bump bonds. 38

4.1 a) The functional block diagram of the Medipix1 pixel cell. b) The CAD layout of the pixel cell. 40

4.2 A photograph of a Medipix1 chip without the sensor chip mounted. The 64x64 pixel array in the upper part is the active chip area that will be connected to the sensor chip. Two pixel row at the lower end of the array are not used for particle detection purposes but serve for leakage-current sensing and connect the sensor guard-ring to the chip ground. The bottom part of the chip contains the I/O functionality. 41

4.3 A typical result of a V_{bias}/V_{comp} scan to find the optimal working point for a given application. Plotted are a) the number of counting pixels, b) the number of noisy pixels, c) the mean threshold , c) the standard deviation of the threshold plotted against the bias voltage. 45

4.4 The Medipix1 3-bit threshold adjustment. Plotted are the threshold distribution with the adjustment value set to 0 in all pixels and the one with the adjustment value set to 7 (the distributions for the intermediate adjustment values are not plotted for reason of clarity). To obtain the best compression of the threshold dispersion, these two curves should overlap by $1/8^{\text{th}}$ of their full width. The adjustment mask is generated by selecting for each pixel the adjustment value which results in the threshold closest to the midpoint between the two curves. The fine tuned threshold distribution then is centered at this midpoint and can be shifted to lower mean threshold values by lowering the global bias voltage V_{th}. 46

4.5 A photograph of the Medipix2 readout chip. The zoom shows the area implementing the five lateral I/O wire-bonding pads that can be used to form a daisy-chain of multiple chips. 47

4.6 Medipix2 pixel cell layout [17]. a) Functional block diagram. b) 1: Preamplifier. 2: High threshold Discriminator. 3: Low threshold discriminator. 4: 8-bit configuration register. 5: Double discriminator logic. 6: Shift register and control logic. The octagonal bump bond opening has a diameter of 20 μm. 49

4.7 Example for the Medipix2 threshold tuning using the noise floor method [79]. Plotted are the threshold distribution with the adjustment value set to 0 in all pixels and the one with the adjustment value set to 7. The fine tuning is achieved by selecting for each pixel the adjustment value which results in the threshold closest to the midpoint between the two curves. . 53

5.1 Mean radial energy deposition profiles (circles) with respect to the center of mass of the deposited charge in a laterally infinite Si sensor slab of 100 cm thickness for photons of 10 keV. Plotted is the fraction of energy contained within a sphere of a radius given on the abscissa. The solid line marks the Gaussian distribution fitted to the simulation data with a width 0.14 μm in both cases, representing the situation without fluorescence photons present. a) No fluorescence photons are taken into account and b) . The effects of the 4.1% fluorescence yield in Si result in the offset on the right hand side. 57

5.2 a) The energy deposition profiles in a 300 μm thick Si sensor of 10 keV photons impinging perpendicular on the sensor surface. The solid line marks the Gaussian distribution fitted to the simulation data. b) The deposition profile in the case of 80 keV photons. Plotted is the fraction of energy contained within a sphere of a radius given on the abscissae. The very localized deposition for 80 keV photons stems from Compton recoil electrons, since almost all Compton scattered photon leave the detector without depositing their total energy. The solid line is a fitted double Gaussian distribution. 58

5.3 Mean energy loss per photon depositing energy in a Si sensor of 50, 100, 300 and 700 μm thickness due to a) backscattered secondary electrons, b) backscattered photons, c) transmitted secondary electrons, d) transmitted photons. The surface losses via secondary electrons becomes relatively less important above 60 keV. Less energy is transferred in average to the electrons, due to the increasing strength of Compton scattering. The thickness of the layer from with electrons can escape the sensor volume is independent of the senor thickness, therefore the surface losses are more pronounced for thin sensors. Photon losses at the other hand are essentially independent of the the sensor thickness since the mean free path of the characteristic photon is much shorter than the sensor dimensions. At photon energies where Compton scattering contributes significantly, the attenuation is very weak and the relation between mean energy deposited and mean energy escaped is independent of the sensor thickness. 59

5.4 Energy deposited [eV/μm^3] of 10^5 photons of a) 8 keV, b) 20 keV, c) 40 keV in a 55 μm pixel of a 300 μm thick Si sensor. The dashed vertical lines indicate the geometric pixel borders. Note that the scaling of the x and z-axis are 2:1. 61

5.5 The spectrum of the energy deposited by a) 8, b) 20, c) 40, d) 80 and e) 140 keV photons in a Si sensor of 300 μm thickness within a pixel of 55, 170, 300 700 and 1000 μm width in the center of an uniformly irradiated area. The fraction of photons fully absorbed within a pixel is indicated in the plot legend. f) The percentage of photons converted entirely within a given pixel size is plotted versus the photon energy. To mark the upper limit the corresponding curve for an infinite detector slab in the legend. . . 63

5.6 Energy deposited [eV/μm^3] of 10^5 photons of a) 8, b) 20 and c) 40 photons in a 55 μm pixel of a 200 μm GaAs sensor. Note that the scaling of the x and z-axis are 2:1. 64

5.7 Mean radial energy deposition profiles with respect to the center of mass of the deposited charge in a GaAs sensor slab of 100 cm thickness for incident photons of 40 keV a) without and b) with fluorescence photons taken into account. Plotted is the fraction of energy contained within a sphere of a radius given on the abscissae. The solid lines mark the Gaussian distributions fitted to the simulation data without fluorescence photons. . . 65

5.8 Energy deposition profiles in a 300 μm thick GaAs sensor with incident photon energy of a) 13 keV, just above the K-edge of As and b) 80 keV. Plotted is the fraction of energy contained within a sphere of a radius given on the abscissae. The solid lines mark the Gaussian distributions fitted to the simulation data without fluorescence photons contributing. The energy deposited close to zero radial offset is due to low energy photo-electron, with the characteristic X-ray leaving the sensor volume. 66

5.9 Mean energy loss per photon depositing energy in a GaAs sensor due to a) backscattered secondary electrons, b) backscattered photons, c) transmitted secondary electrons, d) transmitted photons. 67

5.10 The spectrum of the energy deposited by a) 8, b) 20, c) 40, d) 80 and e) 140 keV photons in a GaAs sensor of 300 μm thickness within a pixel of 55, 170, 300, 700 and 1000 μm width in the center of an uniformly irradiated area. f) Fraction of photons fully absorbed within a pixel. To mark the upper limit the corresponding curve for an infinite detector slab is also shown. 69

5.11 Energy deposited [eV/μm^3] of 10^5 photons of a) 8, b) 20 and c) 40 photons in a 55 μm pixel of a 200 μm CdTe sensor. Note that the scaling of the x and z-axis are 2:1 70

5.12 Mean radial energy deposition profiles with respect to the center of mass of the deposited charge in a CdTe sensor slab of 100 cm thickness for incident photons of 80 keV a) without and b) with fluorescence photons taken into account. Plotted is the fraction of energy contained within a sphere of a radius given on the abscissae. The solid lines mark the Gaussian distributions fitted to the simulation data without fluorescence photons taken into account. 70

5.13 Mean energy loss per photon depositing energy in a CdTe sensor due to a) backscattered secondary electrons, b) backscattered photons, c) transmitted secondary electrons, d) transmitted photons. 71

5.14 a) Energy deposition profiles in a 300 μm thick sensor CdTe with incident photon energy of 30 keV, just above the K-edge of Te. b) The deposition profile for 80 keV. Plotted is the fraction of energy contained within a sphere of a radius given on the abscissae. The solid lines mark the Gaussian distributions fitted to the simulation data. The energy deposited close to zero radial offset is due to low energy photo-electrons, with the characteristic X-ray leaving the sensor volume. The higher fluorescence yield leads to a stronger influence on the charge distribution as compared to GaAs, c.f. Fig. 5.8. 72

5.15 The spectrum of the energy deposited by a) 8, b) 20, c) 40, d) 80 and e) 140 keV photons in a CdTe sensor of 300 μm thickness within a pixel of 55, 170, 300, 700 and 1000 μm width in the center of an uniformly irradiated area. f) Fraction of photons fully absorbed within a pixel. To mark the upper limit the corresponding curve for an infinite detector slab is also shown. 73

5.16 ISE-simulation geometry and charge density distribution in charges/cm^3. Plotted is the hole component of charge cloud of a 10 keV photon ∼4 ns and ∼14 ns after conversion in 50 μm depth. 75

5.17 Simulated collection electrode currents for 27 keV photons converted at 250, 150 and 50 μm distance from the collection electrodes. In the first row the signal seen by the left pixel, the second row displays the situation for the center pixel and the third row the right pixel. In a), c), and e) photons convert in the in the center of the middle electrode. In b), d), and f) photons convert with a lateral offset of 27 μm to the right of the center of the middle electrode. Also indicated in the plots is the integrated collection current. The integral number of charge carriers collected is indicated in the legend. 76

5.18 a) Lateral charge spread of the signal of 8 keV photons at the collection electrodes in a 300 μm Si sensor as a function of deposition depth. b) The presampling MTF for the same sensor, derived from the average deposition profile at the collection electrodes. 79

5.19 Maximal charge spread during charge collection in a Si sensor of 100-700 μm thickness as a function of the applied bias voltage. 79

5.20 a) The effective pixel size as a function of the applied threshold value for 10 keV photons in a 300 μm Si sensor with 55 μm pixel pitch and b) the corresponding MTF curves. 80

5.21 Simulated threshold scan for 10x10 μm pencil beam of 20 keV photons positioned at 0-25 μm offset from the center of 55 μm pixel in a 300 μm Si sensor. The ideal spectral information is obtained in an area of ∼100 μm^2 around the pixel center. 81

5.22 Spectral response of a 300 μm Si sensor under uniform irradiation with monochromatic X-rays of 8 to 40 keV. a) Signal spectrum seen by the collection electrodes of 55 μm pixel pitch and b) the same signal with an additional readout electronic noise of 100 e$^-$ rms. c) Signal spectrum seen by collection electrodes of 170 μm pixel pitch and d) with a readout electronic noise of 100 electrons rms added. The reduced ratio of border region between adjacent pixel versus the center region results in an increased spectral performance of the 170 μm pixel. 83

5.23 Detector response variations as a function of the energy threshold. The count rates obtained in an 4 x 4 pixel area with the threshold set to a) 25%, b) 50% and c) 75% of the energy of the incoming photons are shown. d) The homogeneity of the detector in terms of mean count rate over standard deviation as a function of the applied threshold for photon energies of 10, 20 , 40 and 80 keV. 85

5.24 a) The average number of charge shared events in a 300 μm Si sensor of 55 μm pixel pitch as a function of the threshold applied. The spectrum of a W-tube operated at 25 keV with 2.5 mm Al prefiltering was used in the simulation. b) The NPS derived from simulated data from the same sensor as in a) over an area of 20x20 pixels. The minimum noise levels are obtained at 10 keV threshold, which marks the crossing point of the spectrum of single counted and double counted events. 87

5.25 a) The spectrum of a W-tube at 30 keV with 2.5 mm Al prefiltering seen by the collection electrodes. The overall spectrum has been split in to the contributions from the maximum signal per photons (labelled max), the charge shared signal from the 4 direct neighbours (labelled nn) and the signal from the diagonal neighbours (labelled diag). The signal from diagonal neighbours is negligible for thresholds above 6 keV, whereas the the contributions from the direct neighbours extends up to 15 keV. b) The spectrum obtained for the same incident photon spectrum, but in this case the signal of neighbouring pixel is preprocessed before being compared against the energy threshold. The spectrum of all pixel in a 3x3 neighbourhood (labelled sum) and the one obtained of a of a cross shaped neighbourhood around the main signal pixel (labelled cross) is plotted. The contribution of diagonal vicinity is small compared to the next neighbours, apart from very low energies. The spectrum of the summed signal presents an excellent approximation for the real photonic spectrum. 89

5.26 Comparison of the SNR obtained with a) hypothetical energy discriminating but integrating detector system, b) with a counting and c) with an energy weighting systems. The values graphed represent the ideal case of no electronic noise added to the sensor signal. In all three curves the SNR obtained by weighting the incident spectrum with the optimal weights as given in eq. 3.7 is also plotted as a reference value. 91

6.1 a) Threshold scan, performed by stepping the discriminator level from 2 keV up to 43 keV. Plotted are the measured counts versus the values of the external DAC controlling the energy threshold . The presence of higher harmonics at 23.7, 31.6 and 39.5 keV is clearly visible. The constant count rate between the energy lines indicates the absence of charge-sharing effects as the photons hit the center of a single pixel. The count rate for threshold DACs approaching 1425 starts to rise due to increasing frequency of noise hits for threshold level very close to the single pixel noise floor of $\sim$2.2 keV. b) The energy calibration obtained from the single pixel measurement graphed in (a) together with the results extracted from area irradiation measurements involving 330 pixels. The constants of proportionality differ by less than 2% and the offset of the single pixel calibration is in compliance with the threshold spread of the electronics. 98

6.2 a) Single pixel response profile in y-direction measured with a 10x10 μm^2 pencil beam of 10 keV photons with the threshold set to 5 keV. When trimming the threshold accurately to half the photon energy the sum of all three pixel counts shows excellent uniformity. b) Lowering the threshold to 4.3 keV leads to double counting of photons converting in the border region between two pixels due to overlapping pixel response. The observed fraction of double counted photons per pixel obtained is 3.5 %. 100

6.3 a) Pencil beam mesh-scan over the area of 3 neighbouring pixels with 5 μm step size using a 10 keV photon beam collimated to 10x10 μm^2, the global threshold was set to 5 keV. The sum of the number of counts of all nine pixels per pencil beam position is plotted versus the beam position. The increase of count in the third row of pixels is due to a refill of the electron storage ring. b) Drop in count for 10 keV photons in the corner region due to charge sharing, again with the threshold set to 5 keV. 101

6.4 a) The s-curve of a 20 keV photon beam threshold scan with the pencil beam positioned at the pixel center, indicating an ENC of 0.49 keV rms respectively. b) The detector response at increasing offset from the pixel center, measured with a 8 keV pencil beam collimated to 10x10 μm^2. At 15 μm offset from the pixel center the shape of the s-curve is already significantly deformed, the resulting ENC is 0.77 keV as compared to 0.49 keV closer to the pixel center. c) The apparent energy resolution versus the apparent threshold for different positions of the collimated beam within a pixel. The minimum value for the width of the s-curve of $\sim$0.49 keV rms, corresponding to 140 e^- rms, is observed only at beam positions very close to the center of the pixel. 103

6.5 Results of a threshold scans under 1mm^2 area irradiation with a 20 keV photon beam. a) The raw threshold scan data from the measurements. b) The threshold dispersion derived from realignment procedure described in the text. c) The distribution of the threshold position of the individual pixels. Similar results were obtained for 8, 10, 15 and 40 keV. 106

6.6 Results for the spectra derived from threshold scans under area irradiation of 1 mm^2 for a) 8 keV, b) 10 keV, c) 15 keV , d) 20 keV and e) 40 keV. Also indicated in the plots is the mean energy of the photopeak in keV according to the energy calibration given in eq. 6.1, the with of the photopeak in keV rms and the coefficient of determination for the Gaussian fit. 108

6.7 The distribution of the electronic noise calculated from 20 keV photons area irradiation data. Measurements with other photon energies give similar results. 109

6.8 SNR of a uniform exposure corrected with a flat-field correction map calculated from increasing number of flood-fields, as indicated on the abscissa. The values are normalized to Poisson noise, the square root of the mean number of counts. The SNR approaches the Poisson limit when increasing the statistical base of the flat-field correction. 111

6.9 a) Histogram of factors in the flat-field correction map obtained with a W-target X-ray source with 35 kV and 2.5 mm Al equivalent filtering, together with a fitted Gaussian distribution of 4.1% rms. b) SNR normalized to Poisson limit when combining different acquisition conditions for image and correction map. The individual curves represent the normalized SNR of a single acquisition with 0,1,2 and 4 cm prefiltering, which then is corrected with correction maps obtained with Perspex prefiltering denoted on the abscissa. The Poisson limit, which is given by the square root of the mean number of counts, only can be approached when using identical photon spectra for acquisition and flat-field correction. 112

6.10 a) The range of flat-field correction factors depends on the actual spread of pixel threshold and the incoming photon spectrum. b) The curves for 8 to 40 keV photons are a zoom into a). Superimposed is a Gaussian distribution of pixel thresholds with 100 electrons rms dispersion. Note the difference in the resulting spread of correction factors Δ_2 for 40 keV and Δ_1 for 8 keV. 113

6.11 Measured and simulated charge sharing slope for photon energies form 8 to 40 keV with the threshold set to half the photon energy. 113

6.12 a) Images of an encapsulated laser diode and the corresponding histogram taken with a W-tube, 20 kV, 0.125 mm Al filter. a) No flat-field correction is applied. A number of counts higher than $5 \cdot 10^4$ represent the area of the printed circuit board. b) A simple flat-field correction, calculated from unfiltered photon spectrum, is applied. The image noise is amplified with respect to the uncorrected image and the separation of components with high absorption is lost in the histogram. c) The correction map was derived from data obtained with additional 5 mm Perspex filtering. The improvement of image quality is clearly visible and the separation of the components in the histogram is improved. 115

6.13 a) Example of a low absorption object, the spectrum of the incident photons is changed very little. Acquisition settings: W-tube, 14 kV, 0.125 mm Al and 5 mm Perspex prefiltering. b) Anchovy, acquisition settings: W-tube, 35 kV, 2.5 mm Al equivalent prefiltering. In this case almost the entire spectrum is above 15 keV. The charge-sharing slope is almost constant in this energy range (Fig. 6.10a) and therefore the flat-field correction is insensitive to beam hardening. 116

6.14 Floodfield data taken with a Medipix1/Si detector with the sensor biased at a) 16 V, b) 24 V and c) 64V, corrected with a flatfield correction map obtained from data measured with 128V sensor bias and normalized to the mean count. The nominal depletion voltage of the sensor is 20 V. 118

6.15 (a,b) Profile taken from centre row of raw uncorrected flood-field data. (c,d) Profile taken from centre row of flood-field data smoothed with a 3x3 mean filter. (e,f) Profile taken from centre row of flood-field data corrected with flat-field correction calculated at 128V detector bias. 119

6.16 Count variations found in four different Medipix2/Si assemblies, K8_S18, K7_S20, J3_S5 and D3_S3, measured with 16V sensor bias. The naming convention for a detector assembly puts the readout chip position first, followed by the sensor wafer position. Placed on the corresponding position on the detector wafer-map measured inhomogeneities constitute rings originating at the centre of the detector wafer. The position on the readout electronics map, on the other hand is entirely uncorrelated to the ring pattern. 121
6.17 Threshold settings with respect to calculated spectrum of a W-target X-ray tube operated at 25 keV tube voltage. 123
6.18 a) The measure oversampled edge spread function measured with the lower energy threshold set to 11.3 keV. b) The presampling MTF_{pre} for the different energy thresholds. The spatial resolution, given by the spatial frequency at which the MTF drops to 70 % of its maximum value ranges from 8.1 to 11 lp/mm. The nominal resolution of a 55 μm pixel pitch detector is 9.1 lp/mm. 125
6.19 The pixel profiles derived from the fitted ESF measured with a 25 kV W-tube spectrum and energy threshold ranging from 9.1 to18.6 keV. Also shown is the resulting pixel profile for the threshold set well below half the mean photon energy. 126
6.20 The measured MTF_{pre} and the corresponding digital EMTF for the energy threshold set to 9.1 keV up to the Nyquist frequency. 126
6.21 The one dimensional NPS normalized to the mean count in the image. All threshold settings show a white power spectrum, only at 9.1 keV the low-pass filtering effect of increased charge-sharing can be seen. 128
6.22 The 2-dimensional NPS for the energy threshold set to 11.3 keV with and without flatfield correction applied. 128
6.23 The DQE computed using the a) the presampling MTF_{pre} and b) the EMTF. 130
6.24 Dose dependence of the DQE measured with the Medipix1 using a Mo-target at 28 keV. 131
6.25 Dose dependence of the DQE(0) measured with the Medipix1 using a Mo-target X-ray source at 28 kV and a W-target X-ray source at 60 and 70 kV. 132
6.26 Images of an anchovy X-rayed with increasing acquisition time using the Seifert Mo-target X-ray source operated at 17 kV. b) 2 mA tube current and 30 ms c) 50 ms and d) 330 ms acquisition time. d) The same anchovy using the full counter depth of the Medipix1 with 10 mA tube current and 4 sec acquisition time. 133
6.27 The tallied energy spectrum of W-target X-ray tube operated at a tube voltage of 50 kV and with 2.5 mm Al filter, measured by moving the lower and the upper threshold level concurrently from the minimum value of 4.4 keV over the range of the photon spectrum. Plotted is the number of counts over the position of the lower threshold of the energy window with a width of 2, 4 and 6 DAC values (corresponding to 1.4 keV, 2.8 keV and 4.2 keV). 135

6.28 a) Model of the bump bond connection between sensor and read-out electronics. The bump bond is made of eutectic SnPb (63/37) solder, the silver content of the conductive glue between the readout chip and the PCB board is about 3 %. The indicated thicknesses for the under bump metalization are given on the top side of the bump only. The metal layers are symmetric on both sides of the SnPb solder bump. b) The spectrum of the backscattered photons of an incident beam of W-tube at 50 kV and 2.5 mm Al filter after passing through a 300 μm thick Si sensor on top of the simulated geometry in Fig. a). The position of K-lines of Sn (K_α 25.2 keV, K_β 28.5 keV) and the L-Lines of Pb (L_α 10.5 keV, L_β 12.6 keV) in the solder and the k-lines of Ag (K_α 22.1 keV, K_β 24.9 keV) in the conductive glue are indicated 136
6.29 Images of a plastic Swatch taken using the energy window at different values of the energy threshold. A W-target X-ray tube with 2.5 mm Al filter operated at 50 kV tube voltage was used. a) 16.1-19.6 keV b) 21.6-25.1 keV c) 29-33.5 keV d) 36.9-40.4 keV e) 43.1-46.6 keV. 137

List of Tables

1.1 Properties of common semiconductors in radiation detection, data taken from [23–25] 6

1.2 The fluorescence properties of some semiconductor detector material. For comparison two common scintillator materials are listed as well. The energies for the K_1, L_1 and L_2 absorption edge energies and the characteristic $K_{\alpha 1}$, $K_{\alpha 2}$ energies are given in [keV]. The mean free path $d_{\alpha 1}$ and $d_{\alpha 2}$ of the $K_{\alpha 1}$ and $K_{\alpha 2}$ photons are given in $[\mu m]$. η is the total fluorescent yield for the K-shell fluorescence. As a comparison the values for two scintillator materials, GdSO and CsI, are also given. 13

3.1 Example of detector requirements in HEP, radiography and protein crystallography. [8, 44, 45, 47–50] 33

4.1 A breakdown of the system and performance parameters of the MPX2 . . . 48

5.1 Simulated energy resolution (FWHM) and detection efficiency of the sensor signal with 150 electrons rms noise added for a 300 μm Si sensor at 120 V sensor bias and with the threshold set to 4 keV. 82

6.1 The apparent threshold and the energy resolution derived from the simulated data and from 10x10 μm^2 pencil beam measurements with 8 keV photons, shown in Fig. 6.4d). The deviation for larger offsets are due to the limited positioning precision during the experiment. Close to the pixel border the energy resolution changes rapidly with the beam position. . . . 102

6.2 The mean threshold position μ_{thresh} and threshold dispersion $\sigma_{thresh}^{s-curve}$ for the measured photon energies derived by fitting the measured data with model s-curves. The threshold dispersion $\sigma_{thresh}^{matching}$ obtained using a pattern matching algorithm are also given as comparison. 105

6.3 A breakdown of the measured energy resolution properties under area irradiation. 107

6.4 Mean electronic noise and electronic noise dispersion for different photon energies. 109

6.5 Overview of the parameters and results of the measurements of the MTF and NPS. Also indicated is the DQE at zero spatial frequency computed from the MTF and NPS measurements. 124

Bibliography

[1] S. Gruner, M. Tate, and E. Eikenberry. Charge-coupled device area x-ray detectors. *Rev. Sci. Instrum.*, 73(8):2815–2842, Aug. 2002.

[2] A. Goertzen, V. Nagarkar, R. Street, M. Paulus, J. Boone, , and S. Cherry. A comparison of x-ray detectors for mouse CT imaging. *Phys. Med. Biol.*, 49:5251–5265, 2004.

[3] A. R. Faruqi, H. N. Andrews, D. M. Cattermole, and S. Stubbings. A tiled CCD detector with 2x2 array and tapered fibre optics for electron microscopy. *Nucl. Instr. Meth. A*, 477:137–142, January 2002.

[4] D.S. Evans, A. Workman, and M. Payne. A comparison of the imaging properties of CCD-based devixes used for small field digital mammography. *Phys. Med. Biol.*, 47:117–135, 2002.

[5] L. Lachaine, E. Fourkal, and B. Fallone. Detective quantum efficiency of a direct-detection active matrix flat panel imager at megavoltage energies. *Med. Phys.*, 28:1364–1372, 7 2001.

[6] M. Maolinbay, Y. El-Mohri, L.E. Antonuk, K.W. Jee, S. Nassif, X. Rong, and Q. Zhao. Additive noise properties of active matrix flat panel imagers. *Med. Phys.*, 27(8):1841–1854, 8 2000.

[7] J.H. Siewerdsen, L.E. Antonuk, Y. El-Mohri, J. Yorkston, W. Huang, J.M. Boudry, and I.A. Cunningham. Empirical and theoretical investigation of the noise performance of indirect detection, active matrix flat-panel imagers for diagnostic radiology. *Med. Phys.*, 24(1):71–89, 1 1997.

[8] L Blanquart, V Bonzom, G Comes, P A Delpierre, P Fischer, J C Hausmann, M Keil, M Lindner, S Meuser, and N Wermes. Pixel readout electronics for LHC and biomedical applications. *Nucl. Instrum. Methods Phys. Res. A*, 439:403–412, 2000.

[9] N. Pavel. Particle detectors for biomedical applications - demands and trends. *Nucl. Instr. Meth. A*, 478:1–12, 2002.

[10] S. Bachmann, S. Kappler, B. Ketzer, T. Müller, L. Ropelewski, F. Sauli, and E. Schulte. High rate X-ray imaging using multi-GEM detectors with a novel readout design. *Nucl. Instr. Meth. A*, 478:104–108, February 2002.

[11] E. Auffray, P. Bruyndonckx, O. Devroede, A. Fedorov, U. Heinrichs, M. Korjik, M. Krieguer, C. Kuntner, C. Lartizien, P. Lecoq, S. Leonard, C. Morel, J. B. Mosset, C. Pedrini, A. Petrosian, U. Pietrzyk, M. Rey, S. Saladino, D. Sappey-Marinier, L. Simon, M. Streun, S. Tavernier, J. M. Vieira, and K. Ziemons. The ClearPET project. *Nucl. Instr. Meth. A*, 527:171–174, July 2004.

[12] J. Jakubek, S. Pospisil, D. Vavrik, and J. L. Visschers. Resolution and stability tests of a Medipix-1 pixel detector for X-ray dynamic defectoscopy. *Nucl. Instr. Meth. A*, 509:294–301, August 2003.

[13] J. Jakubek, S. Pospisil, J. Uher, J. Vacik, and D. Vavrik. Properties of the single neutron pixel detector based on the Medipix-1 device. *Nucl. Instr. Meth. A*, 531:276–284, September 2004.

[14] J. Jakubek, T. Holy, S. Pospisil, and D. Vavrik. Tomography for XRDD. *Nucl. Instr. Meth. A*, 531:307–313, September 2004.

[15] L. Blanquart and P. Fischer. Pixel readout electronics for LHC and biomedical applications. *Nucl. Instr. Meth. A*, 439:403–412, dec 1999.

[16] M. Campbell, E. Heijne, G. Meddeler, E. Pernigotti, and W. Snoeys. Readout for a 64 x 64 pixel matrix with 15-bit single photon counting. *IEEE Trans.Nucl.Sci.*, 45(3):751–753, 1998.

[17] X. Llopart, M. Campbell, R. Dinapoli, D. San Segundo, and Pernigotti E. Medipix2, a 64k pixel readout with 55 um square elements working in single photon counting mode. *IEEE Trans. Nucl. Sci.*, 49:2279–2283, 2001. Proc. Conf. Rec. IEEE Nuclear Science Symp. and Medical Imaging Conf. (San Diego, CA, 4-10 November 2001).

[18] A.R. Faruqi, R. Henderson, and L. Tlustos. Noiseless Direct Detection of Electrons in Medipix2 for Electron Microscopy. *Nucl. Instr. Meth. A*.

[19] S. R. Amendolia, A. Annovazzi, A. Bigongiari, M. G. Bisogni, F. Catarsi, F. Cesqui, A. Cetronio, M. Chianella, P. Delogu, M. E. Fantacci, D. Galimberti, C. Lanzieri, S. Lavanga, M. Novelli, G. Passuello, M. Pieracci, M. Quattrocchi, V. Rosso, A. Stefanini, A. Testa, and L. Venturelli. A prototype for a mammographic head and related developments. *Nucl. Instr. Meth. A*, 518:382–385, February 2004.

[20] J. V. Vallerga, J. B. McPhate, A. S. Tremsin, O. H. W. Siegmund, B. Mikulec, and A. G. Clark. A noiseless, kHz frame rate imaging detector for AO wavefront sensors based on MCPs read out with the Medipix2 CMOS pixel chip. *American Astronomical Society Meeting Abstracts*, 205:–+, December 2004.

[21] G. Mettivier, M.C. Montesi, and P. Russo. Tritium digital autoradiography with a Medipix2 hybrid silicon pixel detector. *Nucl. Instr. Meth. A in Physics A*, 516(137):554–563, 2004.

[22] C. Ponchut and F. Zontone. Evaluation of medipix-1 in X-ray scattering and X-ray diffraction applications. *Nucl. Instr. Meth. A*, 510:29–34, September 2003.

[23] G. Lutz. *Semiconductor radiation detectors.* Springer, 1999.

[24] P.J. Sellin, W. Cunningham, M. Rahman, J. Vaitkus, E. Gaubas, D. Hoxley, A. Lohstroh, and A. Simon. First results from epitaxial GaN detectors. IWORID2003, 2003.

[25] S.M. Sze. *Semiconductor Devices, Physics and Technology.* John Wiley & Sons, 1985.

[26] M. Balkanski and R.F. Wallis. *Semiconductor Physics and Applications.* Oxford University Press, 2000.

[27] F. Salvat, J.M. Fernandez-Varea, E. Acosta, and J. Sempau. *PENELOPE, A Code System for Monte Carlo Simulation of Electron and Photon Transport.* OECD/NEA.

[28] Ervin B. Podgorsak, editor. *Review of Radiation Oncology Physics: A Handbook for Teachers and Students.* IAEA, 2003.

[29] G.F. Knoll. *Radiation Detection and Measurement.* John Wiley and Sons, 2000.

[30] J. Singh. *Semiconductor Devices, Basic Principles.* John Wiley & Sons, 2001.

[31] R.C. Gonzalez and R.E. Woods. *Digital Image Processing.* Addison Wesley Publishing, 1993.

[32] L. Rutz, D. Ergun, and J.T. Dobbins. Effects of undersampling on the proper interpretation of modulation transfer function, noise power spectrua, and noise equivalent quanta of digital imaging systems. *Med. Phys.*, 22(2):171–181, 2 1995.

[33] H. Fujita, D.Y. Tsai, T. Itoh, K. Doi, J. Morishita, K. Ueda, and A. Ohtsuka. A simple method for determining the modulation transfer function in digital radiology. *IEEE Transactions-on-Medical-Imaging*, 11:34–39, 4 1992.

[34] MJ Tapiovaara and RF Wagner. SNR and noise measurements for medical imaging: I. A practical approach based on statistical decision theory. *Phys Med Biol*, 38(1):71–92, Jan 1993.

[35] A. R. Cowen. Digital X-ray imaging . *Measurement Science and Technology*, 2:691–707, August 1991.

[36] ICRU Report 54. Medical Imaging - The Assessment of Image Quality. 1996.

[37] M.J. YAffe and J.A. Rowlands. X-ray detecors for digital radiography. *Phys. Med. Biol.*, 42:1–39, 1997.

[38] H. Wieczorek. Physical aspects of detector design. *Radiation Measurements*, 33:541?545, 2001.

[39] G. Borasi, A. Nitrosi, and D. Ferrari, P.and Tasson. On site evaluation of three flat panel detectors for digital radiography. *Med. Phys.*, 30:1719–1731, 2003.

[40] D. C. Hunt, O. Tousignant, and J.A. Rowlands. Evaluation of the imaging properties of an amorphous selenium-based flat panel detector for digital fluoroscopy. *Med. Phys.*, 31:1166–1175, 2004.

[41] G. Harding and B. Schreiber. Coherent X-ray scatter imaging and its applications in biomedical science and industry. *Radiation Physics and Chemistry*, 56:229–245, August 1999.

[42] S. Singh and S. Maneesha. Explosives detection systems (eds) foraviation security. *Signal Processing*, 83:31–55, 2003.

[43] V. Kogan, K. Bethke, and R. D. Vries. Applying X-rays in material analysis. *Nuclear Instruments and Methods in Physics Research A*, 509:290–293, August 2003.

[44] E. Gerndt and L Brügemann. Detectors for X-ray diffraction and scattering: a users overview. *Nucl. Instr. Meth. A*, 531:292–301, 2004.

[45] R. Lewis. Position sensitive detectors for synchrotron radiation studies: the tortoise and the hare? *Nucl. Instr. Meth. A*, 513:172–177, 2003.

[46] J. Plaisier, R. Koning, H. Koerten, A. van Roon, J. Thomassen, M. Kuil, J. Hendrix, C. Broennimann, N. Pannu, , and J. Abrahams. Area detectors in structural biology. *Nucl. Instr. Meth. A*, 509:274–282, 2003.

[47] N. Wermes. Trends in Pixel Detectors: Tracking and Imaging. *IEEE Trans. Nucl. Sci. Vol.*, 51(3):1006–1015, 2004.

[48] R. Remillard. X-ray detectors for astrophysics. *Nucl. Instr. Meth. A*, 531:285–291, 2004.

[49] H. Spieler. Imaging detectors and electronics: a view of the future. *Nucl. Instr. Meth. A*, 531:1–17, 2004.

[50] Bätz L. Hoheisel, M. Requirements on amorphous semiconductors for medical X-ray detectors. *Thin Solid Films*, 383:132–136, 2001.

[51] S. Ramo. Currents induced by electron motion. *Proceedings of the IRE*, 27:584–585, 1939.

[52] P. J. Sellin. Modelling of the small pixel effect in gallium arsenide X-ray imaging detectors. *Nucl. Instr. Meth. A*, 434:75–81, September 1999.

[53] E. Manach and O. Gal. Experimental and simulation results of gamma imaging with hybrid pixel detectors. *Nucl. Instr. Meth. A*, 531:38–51, September 2004.

[54] H. H. Barrett, J. D. Eskin, and H. B. Barber. Charge Transport in Arrays of Semiconductor Gamma-Ray Detectors. *Physical Review Letters*, 75:156–159, July 1995.

[55] P.N. Luke, M. Amman, T.H. Prettymann, P.A. Russo, and D.A. Close. Electrode design for coplanar-grid detectors. *IEEE Trans. Nucl. Sci.*, 44:713–720, 1997.

[56] W. Zhao, G. DeCrescenzo, and J. A. Rowlands. Investigation of lag and ghosting in amorphous selenium flat-panel x-ray detectors. In *Proc. SPIE Vol. 4682, p. 9-20, Medical Imaging 2002: Physics of Medical Imaging, Larry E. Antonuk; Martin J. Yaffe; Eds.*, pages 9–20, May 2002.

[57] D. Lepori, P. Monnin, D. Gutierrez, S. Bulling, J.-F. Valley, and F. R. Verdun. Performance comparison of an active matrix flat panel imager, computed radiography system, and a screen-film system at four standard radiation qualities. *Med. Phys.*, 32:343–350, 2005.

[58] R. N. Cahn, B. Cederström, M. Danielsson, A. Hall, M. Lundqvist, and D. Nygren. Detective quantum efficiency dependence on x-ray energy weighting in mammography. *Medical Physics*, 26:2680–2683, December 1999.

[59] M. Tapiovaara and R. Wagner. SNR and DQE analysis of broad spectrum x-ray imaging.

[60] J. Giersch, D. Niederlöhner, and G. Anton. The influence of energy weighting on X-ray imaging quality. *Nuclear Instruments and Methods in Physics Research A*, 531:68–74, September 2004.

[61] M. Bettuzzi, S. Cornacchia, M. Rossi, E. Paltrinieri, M. P. Morigi, R. Brancaccio, D. Romani, and F. Casali. A new linear array detector for high resolution and low dose digital radiography. *Nucl. Instr. Meth. B*, 213:227–230, January 2004.

[62] M. Partridge, B.-M. Hesse, and L. Müller. A performance comparison of direct- and indirect-detection flat-panel imagers. *Nucl. Instr. Meth. A*, 484:351–363, May 2002.

[63] Michael Overdick. Flat X-ray Detectors for Medical Imaging. IWORID 2002.

[64] M. Campbell, E. H. M. Heijne, P. Jarron, F. Krummenacher, C. C. Enz, M. Declercq, E. Vittoz, and G. Viertel. A 10 MHz micropower CMOS front end for direct readout of pixel detectors. *Nuclear Instruments and Methods in Physics Research A*, 290:149–157, May 1990.

[65] F. et al. Anghinolfi. A 1006 element hybrid silicon pixel detector with strobed binary output,. *IEEE Trans. Nucl. Sci.*, NS-39:654–661, 1992.

[66] F. et al Antinori. First Results from the 1994 Lead Beam Run of WA97. *Nuclear Physics A*, 590:139–146, feb 1995.

[67] D. et. al. di Bari. Performance of 0.5 x 10e6 sensitive elements pixel telescope in the WA97 heavy ion experiment at CERN. *Nucl. Instr. Meth. A*, 395:391–397, feb 1997.

[68] Medipix Collaboration. http://medipix.web.cern.ch/MEDIPIX/.

[69] E. Heijne et al. LHC1: A semiconductor pixel detector readout chip with internal, tunable delay providing a binary pattern of selected events. *Nucl. Instr. Meth. A*, 383:55–63, 1996.

[70] P. J. Sellin, G. Rossi, M. J. Renzi, A. P. Knights, E. F. Eikenberry, M. W. Tate, S. L. Barna, R. L. Wixted, and S. M. Gruner. Performance of semi-insulating gallium arsenide X-ray pixel detectors with current-integrating readout. *Nucl. Instr. Meth. A*, 460:207–212, March 2001.

[71] P. Horowitz and W. Hill. *The Art of Electronics*. Cambridge University Press, 1980.

[72] S. R. Amendolia, E. Bertolucci, M. G. Bisogni, U. Bottigli, A. Ceccopieri, M. A. Ciocci, M. Conti, P. Delogu, M. E. Fantacci, P. Maestro, V. Marzulli, E. Pernigotti, N. Romeo, V. Rosso, P. Rosso, A. Stefanini, and S. Stumbo. MEDIPIX: a VLSI chip for a GaAs pixel detector for digital radiology. *Nucl. Instr. Meth. A*, 422:201–205, February 1999.

[73] G. Bardelloni, E. Bertolucci, A. Boerkamp, D. Calvet, M. Conti, M. Maiorino, P. Russo, and J. Visschers. A new Read-out System for an Imaging Pixel Detector. *IEEE Trans. Nucl. Sci.*, 2001.

[74] B. Mikulec. *Single photon detection with semiconductor pixel arrays for medical imaging applications*. PhD thesis, University of Vienna, Austria, Cern-Thesis-2000-021.

[75] A. Fornaini, T. Boerkamp, R. de Oliveira, and J. Visschers. A multi-chip board for X-ray imaging in build-up technology. *Nucl. Instr. Meth. A*, 509:206–212, August 2003.

[76] D. San Segundo Bello, M. van Beuzekoma, P. Jansweijera, H. Verkooijena, and J. Visschers. An interface board for the control and data acquisition of the Medipix2 chip. *Nucl. Instr. Meth. A*, 509:164–170, 2003.

[77] D. San Segundo Bello. Muros2 user manual. http://www.nikhef.nl/ dbello/txts/muros2/muros2.html, 2003.

[78] M. Conti, M. Maiorino, G. Mettivier, M. Montesi, and P. Russo. Preliminary Test of Medisoft 4: Control Software for the Medipix2 Readout Chip. *IEE Trans. Nucl. Sci.*, 50:869–877, 2003.

[79] X. Llopart, K. Bethke, M. Campbell, A. Fornaini, H. Graafsma, E. Heijne, M. Mitschke, C. Ponchut, P. Russo, L. Tlustos, J. L. Visschers, and R. de Vries. Performance of the 65536 pixel Medipix2 assembly operating in single photon counting mode. IWORD 2003, 2003.

[80] J. Baró, J. Sempau, F. Salvat, and J. M. Fernández-Varea. PENELOPE: An algorithm for Monte Carlo simulation of the penetration and energy loss of electrons and positrons in matter. *Nucl. Instrum. Methods B*, 100(136):31–46, May 1995.

[81] A.F. Bielajew, H. Hirayama, W.R. Nelsony, and D. Rogers. History, overview and recent improvements of EGS4. Technical report, SLAC, 1994.

[82] MCNP - A General Monte Carlo N-Particle Transport Code.

[83] H. Zaidi. Comparative evaluation of photon cross-section simulations . *IEEE Trans. Nucl. Sci.*, 47:2722–2735, 2000.

[84] S.J. Ye, I. A Brezovich, P. Pareek, and S. A Naqvi. Benchmark of PENELOPE code for low-energy photon transport: dose comparisons with MCNP4 and EGS4. *Phys. Med. Biol*, 49:387–397, 2004.

[85] S. et al Agostinelli. GEANT4: A Simulation Toolkit. *Nucl. Instr. Meth. A*, 506:250–303, 2003.

[86] C. Ponchut, J.L. Visschers, A. Fornaini, H. Graafsma, and M. Maiorino. Evaluation of a photon-counting hybrid pixel detector array with a synchrotron X-ray source. *Nucl. Instr. Meth. A*, 484:397–406, 2002.

[87] B. Mikulec, M. Campbell, G. Dipasquale, C. Schwarz, and J. Watt. Characterisation of a single photon counting pixel system for imaging of low-contrast objects. *Nucl. Instr. Meth. A*, 458:352, 1999.

[88] Ch. Schwarz. *Digital X-ray Imaging Using Hybrid Semiconductor Pixel Detectors in Single Photon Counting Mode.* PhD thesis, Albert Ludwigs Universität Freiburg i. Brsg., 2001.

[89] ISE Integrated Systems Engineering AG, Zürich, Switzerland. *DESSIS 6.1 Reference Manual.*

[90] M J Berger, J H Hubbell, S M Seltzer, J S Coursey, and D S Zucker. XCOM: Photon Cross Sections Database, NIST Standard Reference Database 8 (XGAM). http://physics.nist.gov/PhysRefData/Xcom/.

[91] J. Baró, M. Roteta, J. M. Fernández-Varea, and F. Salvat. Analytical cross sections for Monte Carlo simulation of photon transport. *Rad. Phys. Chem.*, 44:531–552, November 1994.

[92] A. Owens, M. Bavdaz, S. Kraft, A. Peacock, R. Strade, S. Nenonen, H. H. Andersson, M. Gagliardi, T. Gagliardi, and H. Graafsma. Synchrotron characterization of deep depletion epitaxial GaAs detectors. *J. Appl. Phys.*, 86:4341–4347, 1999.

[93] H. Spieler and E. Haller. Assesment of present and future large scale semiconductor systems. *IEEE Trans. Nucl. Sc.*, 32:419–426, 1985.

[94] S. Beole, V. Bonvicini, P. Burger, G. Casse, P. Giubellino, M. Idzik, A. Kolojvari, A. Rashevsky, L. Riccati, A. Vacchi, and N. Zampa. Study of the uniformity of high resistivity neutron doped silicon wafers for silicon drift detectors. *Nucl. Instr. Meth. A*, 473:319–326, 2001.

[95] Correction of dopant concentration fluctuation effects in silicon drift detectors. Nouais, D and Bondila, M and Bonvicini, V. and Cerello, P. and Crescio, E. and Giubellino, P and Hernandez-Montoya, R. and Kolojvari, A. and Montano, L. M. and Nilsen, B. S. *Nucl. Instr. Meth. A*, 461:222–225, 2001.

[96] E. Crescio, M. Bondila, P. Cerello, P. Giubellino, A. Kolozhvari, S. Kouchpil, G. Mazza, D. Montano, L.M.and Nouais, and S. Piano. Results from beam tests of large area silicon drift detectors. *Nucl. Instr. Meth. A*, 539:250–261, 2005.

[97] W. Ammon and H. Herzer. The production and availability of high resistivity silicon for detector application. *Nucl. Instr. Meth. A*, 226:94–102, 1984.

[98] A. Rantzer and C. Svensson. Bulk wafer defects observable in vision chips. ESSDERC 2002.

[99] J.C. Dainty and R. Shaw. *Image Science*. Academic Press, 1974.

[100] J.A. Rowlands. The physics of computed radiography. *Phys. Med. Biol.*, 47:123–126, 2002.

[101] *Assessment of objective image quality in digital radiography: noninvasive determination of the detective quantum efficiency*, volume 2708. SPIE, 12 1996.

[102] C.J. Martin, D.G. Sutton, and P.F. Sharpc. Balancing patient dose and image quality. *Applied Radiation and Isotopes*, 50:1–19, 1999.

[103] M. Bath, M Hakanson, and L. Mansson. Determination of the two-dimensional detective quantum efficiency of a computed radiography system. *Med. Phys.*, 30:3172–3182, 12 2003.

[104] K. Fetterly, N. Hangiandreou, and Schueler B. Measurement of the presampled two-dimensional modulation transfer function of digital imaging systems. *Med. Phys.*, 29:913–921, 5 2002.

[105] E. Same, M. Flynn, and D. Reimann. A method for measuring the presampled MTF of digital radiographic systems using an edge test device. *Med. Phys.*, 25:102–113, 1 1998.

[106] P.D Welch. The use of fast fourier transform for the estimation of power spectra:a method based on time averaging over short, modified periodograms. *IEEE Trans. Audio Electroacoust.*, Vol. AU-15:70–73, 1967.

Acknowledgements

First of all I would like to thank my supervisors Prof. H. Aiginger at the Atominstitut der Österreichischen Universitäten for accepting to supervise this thesis. My special thanks go to my CERN supervisors, Michael Campbell and Erik Heijne for their help and encouragement during the last years. I thank Mike Letheren and Pierre Jarron for their kind reception in the MIC group.

Thanks go to Georg Vorlaufer for a list of things too long to write. Roberto Dinapoli deserves special thanks for some emergency tutorials in electronics. So does Xavier Llopart for lessons in applied Catalan and repeated change of phone extension, Rafael Ballabriga for his unsuccessful but continuing efforts to talk me into salsa dancing and Bettina Mikulec for support in the beginning of the thesis. Furthermore I would like to thank my colleagues in the Medipix collaboration. In particular Wasi Faruqi for his welcome in Cambridge and Cyril Ponchut for his continuous help at the ESRF. Thanks also go to the group at the University of Napoli for providing the readout software and to Jan Visschers and his colleagues at NIKHEF. Ian McGill always responded rapidly to last minute wire-bonding requests. And of course Bert van Koningsveld for timely and cheerful help with all IT matters.

I am very grateful to Johannes Bethke, Klaus Bethke and Roelof de Vries at PANalytical for their help at the end of the thesis.

Finally I would like to thank my family and my friends for their continuous support and to Adriana amongst countless other things for her patience and fearless proof-reading.

This work was performed within the Austrian Doctoral Student Programme at CERN, by the Austrian Federal Ministry for Education, Science and Culture.